NATIONAL AKADEMY OF SCIENCES OF UKRAINE
INSTITUTE FOR SINGLE CRYSTALS

Vol.2, No.2 1995

FUNCTIONAL MATERIALS

Kharkov

National Academy of Sciences of Ukraine
Department of Physical and Technical Problems of Materials Science

Institute for Single Crystals

Functional Materials

Founded in September 1993
(4 numbers per year)

Address:

60, Lenin Ave., 310001, Kharkov, Ukraine
Phone: +380 (572) 307 411, +380 (572) 307 960;
Fax: +380 (572) 320 273
E-mail: shcherbina@isc.kharkov.ua

Reports

from Summer School on Chemistry and Physics of Surfaces

CPS'94

September 4 – 10, 1994, Kiev, Ukraine

Part II

Works presented by CPS'94 International Program Commitee

Contents

Functional Materials 2, No.2 (1995)

Multiphonon processes of defect creation in surface regions of semiconductors, initiated by electron excitations decay

L.G.Grechko, V.G.Levandovskii and G.E.Chaika*

Institute for Surface Chemistry, National Academy of Sciences of Ukraine,
31 Nauki Ave., 252028 Kiev, Ukraine

*Kiev Branch of Odessa Communication Institute,
7 Solomenskaya St., 252022 Kiev, Ukraine

The probability of lattice site-intersite transition of an impurity atom initiated by heated-up exciton plasma in surface layers of semiconductors with non-homogeneous electrical field is calculated by quantum mechanical methods. This transition is accompanied by exciton decay and the hole capture onto the level of the created defect. The final result shows that heating of exitons may stimulate to a significant measure the formation of electrically active centers in materials.

З використанням квантово-механічного підходу розраховано ймовірність переходу домішкового атома у міжвузля, ініційованого розігрітою екситонною плазмою у поверхневих областях напівпровідників з неоднорідним електричним полем.Цей перехід може супроводжуватись розпадом екситона та захопленням дірки на енергетичний рівень утвореного дефекту. В результаті проведених досліджень показано, що розігрів екситонів може значно стимулювати формування електрично активних центрів у матеріалі.

Introduction

It was noted in number of recent papers [1] that an electric field $E \approx 10^5$ to 10^7 V/cm promotes essentially the formation of new local electron states. One can observe this effect both in the dark and (in a more pronounced form) in the presence of ionizing radiation, particularly near the surface region of the crystal or at the interface. There are several energy dissipation channels of electron excitations decay leading to formation of electrically active centers in nonmetallic materials as it is known from [1–5]. One must differ in multithermic [1,2] and multiphonons [3–5] types of processes. The last one is essentially nonlinear because it is accompanied by self-consistent electron (or hole) capture at the energy level of created electrically active defect. Mechanisms of such phenomena have been proposed in [3]. They are based on the polyaron theory which is a conceptual theory where the system with many degrees of freedom is phonons subsystem. It was shown that some probability exists for an electron in the conduction band of giving rise to a defect generation associated with electron transition from conduction band to a lower energy level of that defect, so that free energy of the system «crystal having a defect plus an electron» would reach its minimum value. The probability of the elementary act of defect creation assisted by electron excitation depends particularly on the quantum number labelling of such excitations and on the wave vector for nonlocalized excitations. Thus, external factors (electrical field, light exposure, etc.) acting on the excitation partition function must change also the observed efficiency of defect creation. But, as far back as in [3], it was noted that electrons (holes) are not the sole «light» subsystem for effective process of defect formation. Exciton gas is the other such one. We have already analyzed in [6] the inhomogeneous electrical field influence on exciton plasma heat-

ing up in surface layers of semiconductors. That is why we think it would be expedient to estimate the excitons heating-up influence on defect formation in inhomogeneous regions of nonmetalic crystals.

Approximate quantum mechanical treatment

In the present report, we calculate transition probability between two following states of the system «nonmetallic crystal plus exciton»: 1) all the host crystal atoms are located in lattice sites, more light-weight impurity atom is substitutional (*i*-state), exciton has the wave vector $\vec{k_i}$; 2) impurity atom is located in a lattice intersite (*f*-state), the lattice site occupied by it before is now, empty exciton decays into a hole, localized at the vacancy quantum level, and an electron that moves to a conduction band. To calculate the transition probability W_{if}, we use the following coordinates: q_χ – normal coordinates for description of the lattice vibrations, coordinates $\vec{R}$ for impurity atom *f* which transition is accompanied by wave of displacements of surrounding atoms, $\vec{r}, \vec{r_1}, \vec{r_2}$ – coordinates of the exciton, electron, and hole, respectively. The probability of the process is calculated by nonadiabatic operator for electron and defect atom introduced in [4].

$$\hat{H}_{\text{int}} = -\frac{\hbar}{2M}\,\Psi_{l\ldots n_\chi}\,\frac{\partial\Psi_{si}(\vec{r_1})}{\partial\vec{R}}\,\frac{\partial\varphi_l(\vec{R})}{\partial\vec{R}}. \qquad (1)$$

Here, $\Psi_{si}(\vec{r_1})$, $\varphi_l(\vec{R})$, $\Psi_{l\ldots n_\chi}(q_\chi)$ – are eigenfunctions of exciton, the impurity atom in the initial state and normal vibrations with quantum number n_χ, respectively. The eigenfunction of exciton in the initial state is defined as the product $\Psi_{si} = \chi(r)\,\psi_1(r_{12})$, where $\psi_1(r_{12})$ is hydrogen-like exciton eigenfunction in bound state, $\chi(\vec{r})$ describes the exciton translation movement, $\vec{r} = (m_n\vec{r_1} + m_p\vec{r_2})/(m_p + m_n)$, $r_{12} = |\vec{r_1} - \vec{r_2}|$, m_n and m_p are effective masses of the electron and the hole. In the final state, the exciton eigenfunction has also the form of a product $\Psi_{s_f} = \psi_g(\vec{r}_R)\,\psi_k(\vec{r})$, where $\psi_g(\vec{r}_R)$ is the hydrogen-like eigenfunction for electron localized at the defect, and $\psi_k(\vec{r})$ is a Bloch function for electron in conduction band with wave vector $\vec{k}$. Eigenfunctions of the displacing atom are harmonic oscillator type and vary in $q^0_{\chi i}$ and $q^0_{\chi f}$ equilibrium positions for *i* and *f* states. Transition probability into new quantum state is calculated by summation with respect over all changes of states, when energy conservation law being satisfied:

$$\sum_k (n_k' - n_k) = p \qquad (2)$$

where $p = (\varepsilon_s - \varepsilon_k + \varepsilon_g - W)/\hbar\omega$, $\hbar\omega$ is phonon energy, ε_s is exciton energy including energy of translation movement and an interior energy, ε_g is energy of the bound electron the localized at the defect, ε_k is the electron kinetic energy in conduction band, W is the height of potential barrier for electron transition between states, n_k are the quantum numbers for normal oscillations of the host crystal atoms.

With the help of results from [4,5], one can transform the expression for transition probability to the following form:

$$W_{if} = \frac{\pi\hbar^2}{2M\omega}\left|G_{l_f, g, \vec{k}, l_i, \vec{k_i}, s}\right|^2 (1 + 1/\bar{n})^p \times \times I_p(z)\exp(-a\,(\bar{n} + 1/2)). \qquad (3)$$

Here, l_f, l_i are the quantum numbers of transiting atom, *g* is the quantum number of hole been localized, *s* is the quantum number of exciton state, I_p is the first-kind Bessel function of imaginary argument, $z = a\,[\bar{n}\,(\bar{n} + 1)]^{1/2}$, $a = \sum\left(q_{\chi i} - q_{\chi f}\right)^2$; $q_{\chi i}$, $q_{\chi f}$ are coordinates for atomic normal vibrations, $\bar{n}$ is the number of equilibrium phonons.

It is necessary to note that the preexponential integral *G* in (3) depends on ε_k also but, as the estimations that based on [5] demonstrate, this dependence is less strong than exponential. In this report, we are interested first of all in the dependence of defect formation efficiency on the electrical field *E*, therefore, we assume this integral to be constant.

Field influence on quantum transition probability

For comparison our results with experimental ones, we must average (3) over vectors $\vec{k_i}$ and $\vec{k}$: $\gamma = \iint W_{if} f_{\vec{k_i}} f_{\vec{k}} d^3\vec{k_i}\, d^3\vec{k}$. When the free electron has energy near the conduction band bottom, and exciton partition function is the equilibrium one, we obtain

$$\gamma \approx C\exp[-(W - \Delta\varepsilon + p_m)/kT_0], \qquad (4)$$

where $p_m = (z/2)\ln(1 + 1/\bar{n})$, T_0 is the equilibrium temperature of exciton gas, $\Delta\varepsilon$ is the difference in bound energy between the hole at local level and

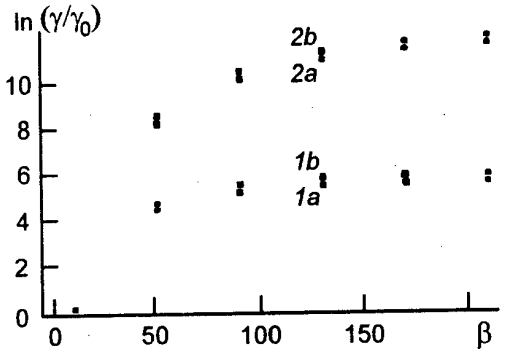

Fig.1. The natural logarithm ($\ln(\gamma/\gamma_0)$) dependence on the electric field parameter β for $(W-\varepsilon_v)/kT_0$ = 20 (1), 30 (2) and $\hbar\omega/kT_0 = 0.1$ (*a*), 0.5 (*b*).

the exciton. Now we account properly for the influence of factors distorting the exciton partition function on the defect creation probability. Let an external nonuniform electrical field will be one of such factors. We have considered in [6] the heating-up of exciton gas by inhomogeneous electrical field E. It had been shown that exciton partition function may be written as

$$f(\varepsilon,\beta) = \frac{n(x)\,(\beta + (\varepsilon_s/kT_0))^{\beta}\exp(-\varepsilon_s/kT_0)}{(2\pi mkT_0)^{3/2}\,\beta^{\beta+3/2}\,\psi(3/2,\,\beta+5/2,\,\beta)}, \quad (5)$$

where $n(x)$ is excitons concentration and $\beta = (\alpha E\,(dE/dx))\,l_x^2/8$, α is the exciton polarizability, l_x is an exciton free path length. According to [6] the heating-up of exciton plasma byelectrical field leads to increasing of exciton concentration in regions where β tends to maximal value; that can change the exciton luminescence intensity. At the same time, the defect creation process may be initiated also.

Substituting the partition function obtained in [6] into expression for γ, and calculating the integral approximately, we obtain

$$\gamma \approx C_\beta\left(1+\frac{t_1}{\beta}\right)\left(1+\frac{t_2^2}{\beta}\right)^{-\beta} \times$$
$$\times \exp\left[-t_2 - \frac{(W-\Delta\varepsilon-t_1kT_0)^2}{2\hbar\omega kT_0}\right], \quad (6)$$

where

$$t_1 = \frac{W+\Delta\varepsilon-\hbar\omega}{kT_0}\left(1+\frac{\hbar\omega(W-\delta\varepsilon)}{(W-\Delta\varepsilon+kT_0-\hbar\omega)kT_0}\right),$$

$t_2 = 1/4\,[1+(1+8\beta)^{1/2}]$. C_β is the constant including all preexponential factors which are weakly dependent on β.

The result of numerical integration in expression for γ for nonequilibrium partition function (5) is shown at Fig.1 for $(W-\Delta\varepsilon)/kT_0$ = 20 (1), 30 (2) and $\hbar\omega/kT_0$ = 0.1 (a), 0.5 (b). One can see that formula (6) is qualitatively valid for γ(β) dependence. The final result shows that $\gamma/\gamma_0 = f(\beta)$ ($\gamma = \gamma_0$ when $\beta = 0$) is an abrupt function for β values from 1 to 100. Increasing of the defect formation probability by the factor 10^2 to 10^3 in this interval requires β to be magnified by 10 times only. Thus, the heating by nonuniform electrical field, causing the increase of exciton density in the high energy tail region, may enhance appreciably the defect creation efficiency.

Conclusion

The probability of lattice site-intersite transition of impurity atoms initiated by exciton plasma heating-up in semiconductors is calculated by quantum mechanical methods. Such defect may be due to impurity atoms capable of occurring at intersites, the latter being acceptors. This transition is accompanied by capture the electron at the level of the created defect. When calculating by quantum mechanical methods, the impurity atomic mass is supposed to be smaller than those of the host atoms. Such an assumption makes it possible to apply the double-adiabatic approximation for the system host atoms - impurity atom – exciton and to calculate the probability of multiphonon transition process. As a result, the upper value of the above transition probability corresponds to higher exciton energy. Thus, the activating of exciton subsystem by an electric field or by radiation causing the exciton density to increase in the high energy tail region may stimulate the defect formation in material. The results of the investigation make it possible to predict the dependence of defect formation probability on some parameters of subsystems taking part in the transition and electrical field (β).

References

1. M.K.Sheikman, *Pisma v ZhETF*, **38**, 278 (1983).
2. M.L.Klinger, Ch.B.Lushchik, T.V.Mashovets, G.A.Kholodar, M.K.Sheikman, M.A.Elango, *Usp. Fiz. Nauk*, **147**, 523 (1985).
3. V.L.Vinetsky, *Fiz.Tv.Tela*, **10**, 867 (1968).
4. G.E.Chaika, V.L.Vinetsky, *Phys.Stat.Sol.(b)*, **98**, 727 (1980).
5. V.L.Vinetsky, G.E.Chaika, *Fiz.Tv.Tela*, **28** 3389 (1986)
6. G.E.Chaika, L.G.Grechko, V.G.Levanovsky, V.P.Siomik, S.E.Vavilov, in Nonlinear World, Proc.IV International Workshop on Nonlinear and Turbulent Processes in Physics [in Russian], Naukova Dumka, Kiev (1989) V.1, p.37.

Многофононные процессы создания дефектов в поверхностных слоях полупроводников, инициированные распадом электронных возбуждений

Л.Г.Гречко, И.Г.Левандовский, Г.Е.Чайка

С применением квантово-механического подхода рассчитана вероятность перехода примесного атома в междоузлие, инициированного разогретой экситонной плазмой в поверхностных областях полупроводников с неоднородным электрическим полем. Этот переход может сопровождаться распадом экситона и захватом дырки на энергетический уровень образовавшегося дефекта. В результате проведенных исследований показано, что разогрев экситонов может стимулировать значительным образом формирование электрически активных центров в материале.

Functional Materials 2, No.2 (1995)

Surface spin-reorientational transition in rare-earth orthoferrites and orthochromites

E.A.Gan'shina, G.S.Krinchik and E.A.Balykina

M.V.Lomonosov Moscow State University,
117234 Moscow, Russian Federation

Magnetooptical effects of reflection were investigated in rare-earth orthoferrites and orthochromites in the temperature range 10–295 K. In some orthoferrites and LuCrO3, the character of phase SRT is found to be different from that observed by magnetic experiments. Decreasing the temperature to 50 K for $TbFeO_3$ and to 33 K for $SmFeO_3$, magnetooptical effects were found to fall to zero sharply. This fact indicates that the weak ferromagnetism vector disappears in a surface layer (the Morin transition). Temperature of the SRT onset on the surface of $SmFeO_3$ is found to shift to the high-temperature region as compared to the bulk. Hence, there is a transitional surface layer similar to the domain boundary with the gradual reorientation of the antiferromagnetism vector about 90 °.

Приведено результати дослідження магнітооптичних ефектів відбиття у рідкоземельних ортоферритах (РЗОФ) та ортохромітах. Для виявлення явищ поверхневого магнетизму вивчались температурні польові та поляризаційні залежності екваторіального ефекту Керра в області температур 10–295 К при накладанні магнітного поля вздовж різних кристалографічних осей. Виявлено, що в ряду РЗОФ та в $LuCrO_3$ характер поверхневих спін-переорієнтаційних переходів (СПП) відрізняється від тих, що відбуваються в об'ємі. Виявлено, що при зниженні температури до 50 К в $TbFeO_3$ і до 33 К в $SmFeO_3$ екваторіальний ефект Керра зменшується до нуля, що свідчить про зникнення вектора слабого феромагнетизму в поверхневому шарі (перехід типу Моріна). Для $ErFeO_3$ виявлено зсув у високотемпературну область початку СПП $\Gamma_4 - \Gamma_2$ на поверхні порівняно з об'ємом, т.т. на поверхні $ErFeO_3$ існує перехідний поверхневий шар типу доменної межі, в якому відбувається поступовий поворот вектора антиферомагнетизму на 90 °.

A transitional microscopic layer on the magnetic crystals surface having the magnetic state different from that of bulk material was first revealed at weak ferromagnetics. During investigations of magnetooptical reflection effects on the hematite non-base faces, it was found that surface layer behaves as a single-axial weak ferromagnet while hematite itself is a crystal having "light plane" anisotropy [1]. This phenomenon was explained as a result of the competition of two anisotropy types, i.e. magneto-dipole and single-ionic ones. In rare-earth orthoferrites (REOF) which belong to the weak ferromagnetics, various spin reorientational transitions (SRT) are observed at temperature variation due to competitive interactions between the rare-earth and the ferric sublattices [2]. In the SRT area where the first anisotropy constant is small, the contribution of surface anisotropy can result in various manifestations of the surface magnetism.

The existence of the surface magnetism can be revealed by the study of magnetooptical reflection effects controlled by the magnetic state of the thin surface layer.

This work describes the magnetooptical effects of reflection studied on rare-earth orthoferrites and orthochromites (REOC). To reveal the surface magnetism phenomena, dependences of the equatorial Kerr effect (EKE) on temperature, field and polarization were studied in the temperature range 10-295 K under a magnetic field being imposed along various crystallographic axes. For a number of REOF, the SRT character was found to be substantially different from that in the bulk material.

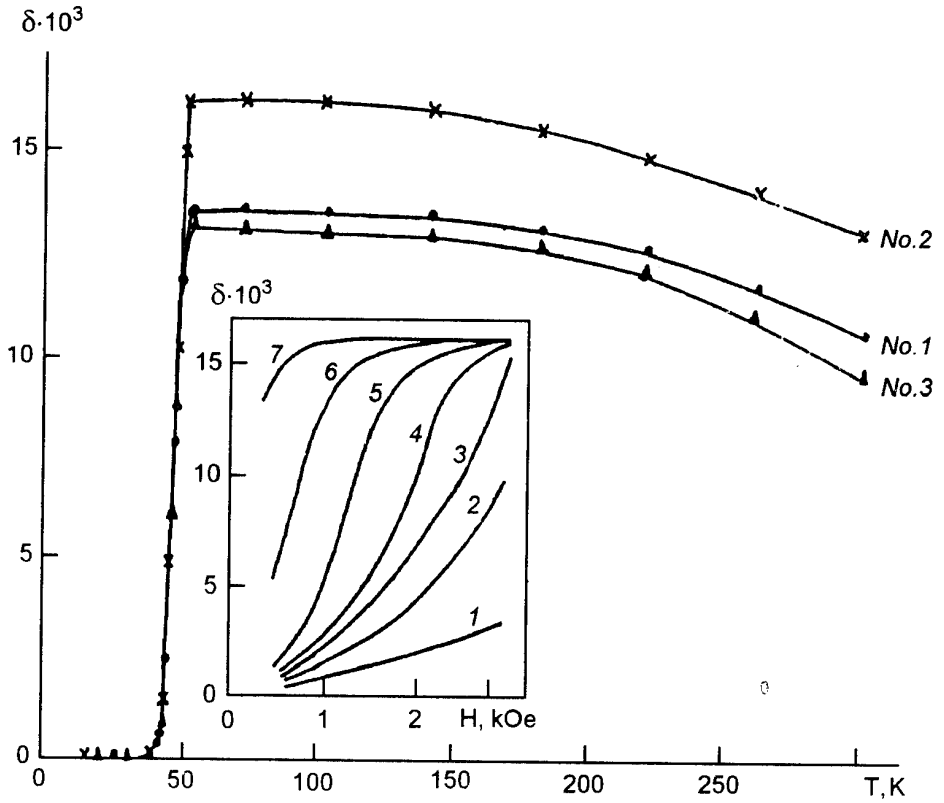

Fig.1. $\delta(T)$ in $TbFeO_3$, $\hbar\omega$ = 3.0 eV, H = 0.5 kOe, light incidence angle φ = 65 °, $H \parallel c$. Specimens: No.1 – (110), No.2 – (010), No.3 – (100). Inset: $\delta(H)$ for specimen No.2 at T = 25 K (1), 30 K (2), 33 K (3), 37 K (4), 40 K (5).

a) $TbFeO_3$

The temperature and field dependences of EKE (δ) for $TbFeO_3$ were measured on three specimens. Specimen No.1 represented the mirror face (110) of a single crystal. Two other plates oriented in (010) (specimen No.2) and (100) (specimen No.3) planes were cutted out of $TbFeO_3$ single crystal growed by the zone melting method with the optical heating. Measurements on the specimen No.1 were made without surface pretreatment (on the natural mirror face) and after annealing in air at T = 1200 °C for 5 h. The plates of specimens No.2 and No.3 were polished mechanically and then annealed in air for 3 h at T = 1200 °C. The specimen No.2 after reference measurements was etched by orthophosphoric acid at 300 °C for two minutes.

Fig.1 shows the temperature dependences of EKE, $\delta(T)$, in the area of spectral maximum 3 eV measured in the magnetic field of 0.5 kOe parallel to C axis. At the temperature decrease to (50±1) K, a sharp drop of the effect to zero was observed for all specimens within a narrow temperature range. Increasing the magnetic field intensity resulted it a shift of the knee on $\delta(T)$ curves toward low temperatures by about 6 K/kOe. On the inset of Fig.1, the field dependences of EKE, $\delta(H)$, are shown for specimen No.2 at various temperatures. The additional surface treatment of the specimens No.1 and No.2 (annealing and chemical etching) did not cause any change of $\delta(T)$ and $\delta(H)$ dependences type.

To elucidate the type of the spin-reorientational transition observed, the EKE measurements in the magnet field $H \parallel a$ were performed for the specimen No.2. In Fig.2, polarization dependences of the magnetooptical effect, $\delta(\theta)$, for various temperatures are shown. At elevated temperatures, the polarization dependencies pattern corresponds to the intensitive meridional Kerr effect (IMKE) which is due to the presence of a longitudinal magnetization component F_z. The specimen remagnetization occurs at the cost of small component of the magnetic field projection on the C axis. At the temperature lowering to 50 K, the IMKE disappeared by jump. The imposing of a magnetic field $H \parallel a$ caused the appearance of EKE which was increased with temperature lowering. The inset of Fig.2 shows

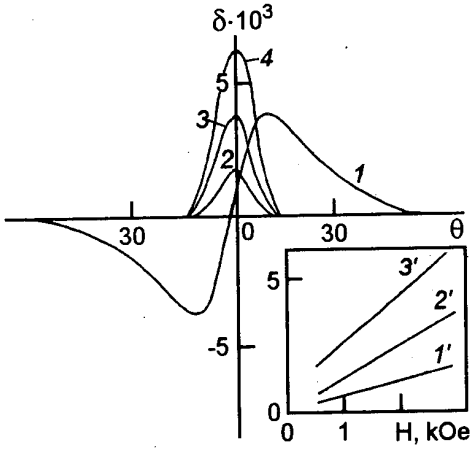

Fig.2. δ(θ) for the specimen No.2. θ is the light polarization azimuth, $\hbar\omega$ = 3.0 eV, φ = 65 °, H = 3 kOe,

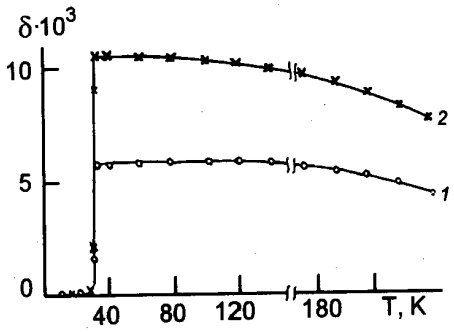

Fig.3. δ(T) in $SmFeO_3$, $\hbar\omega$ = 3.1 eV, H = 0.5 kOe. Specimens: No.1 – (110), No.2 – (010)

the field dependencies of that effect for several temperatures. For the specimen No.3, none magnetooptical effects were observed at temperatures lower than 50 K in magnetic field up to 5 kOe directed along the b axis.

For the terbium orthoferrite, a rather intricate magnetic behaviour was observed in the low-temperature range [2]. At T > 6.5 K, spins of Fe^{3+} ions are in the phase $\Gamma_4(G_xF_z)$ (where G is the antiferromagnetism vector; F, ferromagnetism one) and, at T_{R1} = 6.5 K, change to $\Gamma_2(G_xF_x)$ arranging the magnetic moments of Tb^{3+} ions along a axis of the crystal according to $\Gamma_4(G_xF_y)$ mode. It is the R–Fe interaction which is the cause of that transition and results in the splitting of the main Tb^{3+} quasidoublet in the Γ_2 phase. At T_N = 3.3 K, an antiferromagnetic ordering occurs in the rare-earth subsystem ($\Gamma_2 \rightarrow \Gamma_{82}$) which causes a decrease of the terbium ions susceptibility along the a axis what renders the Γ_2 phase to become energetically disadvantageous and gives rise to a reverse $\Gamma_2 \rightarrow \Gamma_4$ reorientation of Fe^{3+} ions spins at T_{R2} = 3.1 K [3,4]. Rare-earth ions pass therewith into a purely antiferromagnetic configuration $\Gamma_8(a_xg_y)$.

It follows from the results obtained by us that, at temperatures lower than 50 K, no spontaneous turning of spins into $\Gamma_2(G_xF_x)$ state occurs in surface layer of $TbFeO_3$. Thus, it should be supposed that the SRT observed is a $\Gamma_4 \rightarrow \Gamma_1$ transition of Morin type and, in the absence of magnetic field, a transitive layer exists on the $TbFeO_3$ surface where the antiferromagnetism vector turns to 90 °C $G_x \rightarrow G_y$ and ferromagnetism vectors changes itself from F_z to 0. A relatively weak magnetic field (up to 3 kOe) imposed along c axis causes the complete "erasement" of the surface magnetism in the temperature range 35–50 K (see Fig.1, inset). The EKE increase with temperature lowering in the magnetic field $H \parallel a$ is associated with the magnetic moment F_x rise as the critical temperature of bulk phase transition is approached. As it follows from the experimental phase diagram of threshold field (H_x^n,T) given in [5], at T = 10 K, a magnetic field of H_x ~ 3 kOe is sufficient to induce the $\Gamma_4 \rightarrow \Gamma_2$ SRT. Our results (Fig.2) show that, at 10 K in the magnetic field H_x = 3 kOe, the SRT does not attain its maximum value, i.e. the critical field of surface SRT $\Gamma_1 \rightarrow \Gamma_2$ has a larger value than the threshold one of $\Gamma_4 \rightarrow \Gamma_2$ transition in the bulk crystal. The increase of δ with the $H \parallel a$ growing indicates to a diminution of the surface magnetic layer depth.

b) $SmFeO_3$

The EKE in $SmFeO_3$ was measured on the mirror growth face (110) of a single crystal (specimen No.1) and on a plate oriented in (010) plane made from a crystal of the same growth batch (specimen No.2). The specimen No.1 surface was not treated, specimen No.2 was undergone an annealing and chemical etching. Fig.3 shows temperature dependences of EKE for both specimens in the 0.5 kOe magnetic field directed along [110] axis for specimen No.1 and along [100] one for specimen No.2. The temperature lowering to T ~ 33 K caused a knee on the δ(T) plot and subsequent sharp drop of the Kerr effect. On the specimen No.2, the field EKE dependences were measured for several temperatures in the transition range; the results obtained are shown on

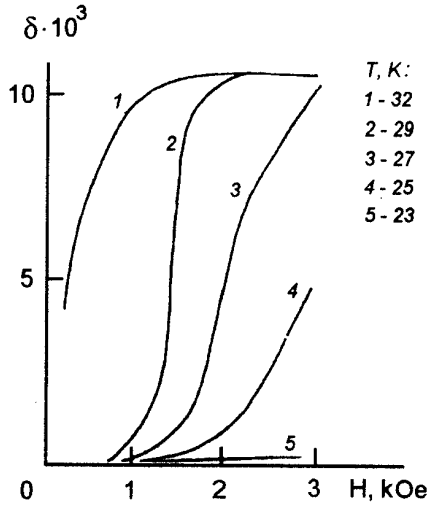

Fig.4. $\delta(H)$ in $SmFeO_3$ (specimens: No.2), $\hbar\omega$ = 3.1 eV, $H \parallel a$, T = 32 K (1), 29 K (2), 27 K (3),

Fig.4. Measurements performed on both specimens in a magnetic field $H \parallel c$ have shown that, within the limit of experimental accuracy, the EKE in $SmFeO_3$ is absent. The absence of Kerr effect at $T < 33$ K indicates the disappearance of the weak ferromagnetic moment vector in the surface layer of $SmFeO_3$, thus, it can be supposed that the surface transition observed is a SRT of Morin type $\Gamma_2(G_zF_x) \rightarrow \Gamma_1(G_y)$.

On the specimen No.1 of samarium orthoferrite, the magnetization was measured at temperature being varied from 300 K to 4.2 K (see Fig.5). In the temperature range studied, no bulk phase transitions were observed what confirms our supposition that the SRT observed takes place in a thin surface layer having the thickness comparable to the depth of light penetration into crystal. Thus, at $T < 33$ K, a situation occurs when the $\Gamma_2(G_zF_x)$ phase is the magnetic state of the bulk $SmFeO_3$ while surface spins are ordered according to $\Gamma_1(G_y)$ mode, i.e. the surface is a transitional layer of the domain boundary type, where a progressive turn of the iron ions spin system $G_zF_x \rightarrow G_y$ takes place.

c) $ErFeO_3$

In $ErFeO_3$, the initial temperature of $\Gamma_4(G_xF_z) \rightarrow \Gamma_2(G_xG_z)$ reorientation on the surface (T_{2S}) was observed to be shifted largely (by 40 K) toward the high-temperature area as compared to that in volume (T_{2V}). For Tm and Ho, orthoferrites, critical SRT temperatures on the surface and in the volume were the same (see Fig.6). That experimental fact leads inevitably to

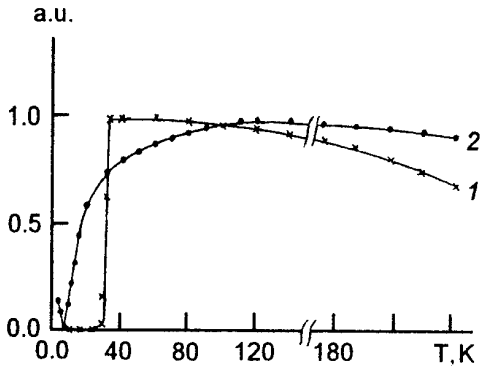

Fig.5. Temperature dependences of EKE (1) and magnetization (2) in $SmFeO_3$

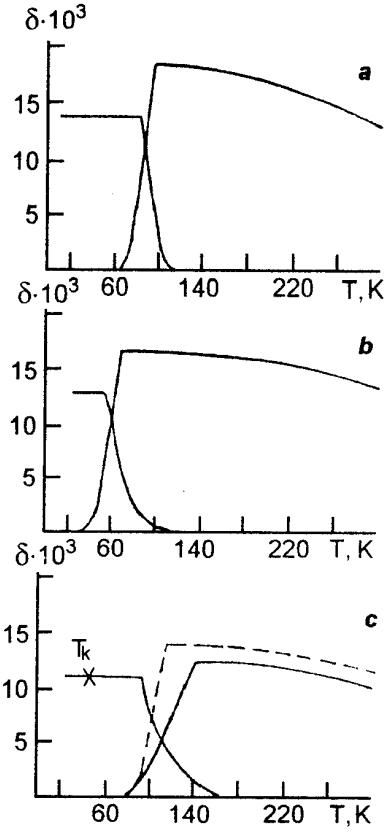

Fig.6. $\delta(T)$ in $TmFeO_3$ (a), $HoFeO_3$ (b), $ErFeO_3$ (c), $\hbar\omega$ = 3.25 eV, H = 1 kOe

the conclusion that there is a surface magnetism in erbium orthoferrite on (010) face.

Based on the results obtained, we can state that, in the temperature range from T_{2S} = 140 K to T_{2V} = 100 K with magnetic field being oriented along c axis, the bulk magnetic moment is oriented exactly along that axis while on the surface it is deflected from c axis by a certain angle ϑ

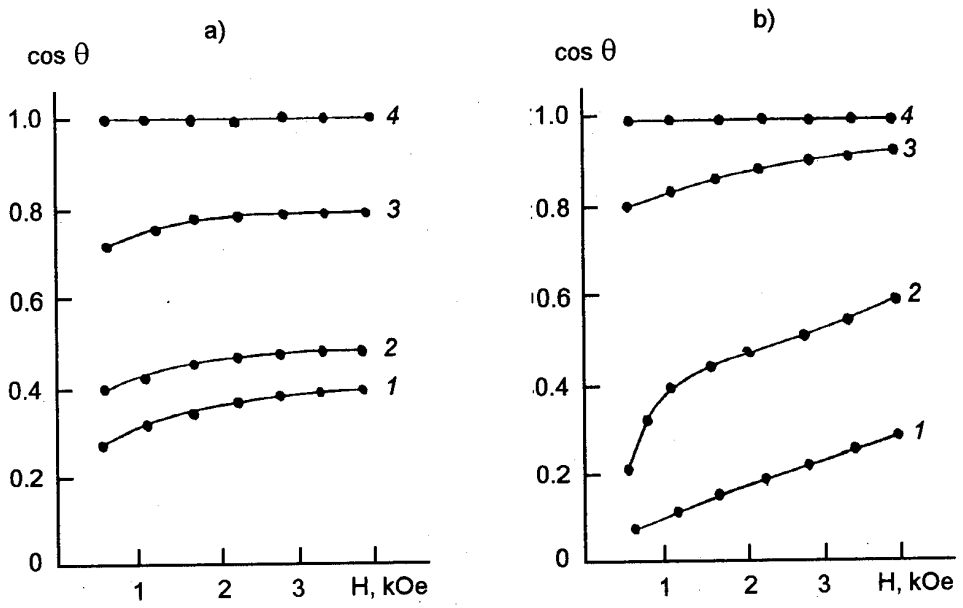

Fig.7. Field dependences of cos θ: for $ErFeO_3$ (a) at T = 95 K (1), 100 K (2), 120 K (3), 140 K (4); for $HoFeO_3$ (b) at T = 50 K (1), 55 K (3), 65 K (4). In both case, $H \parallel c$, (010)

increasing with lowering temperature and attaining 90 ° at temperature T_{2V}. The angle ϑ can be determined from the relationship $\cos \vartheta = \delta_T/\delta_S$ where δ_T is the EKE value at $T > T_{2S}$. Our experiments showed that ϑ does not depend essentially on the magnetic field when the latter varies from 2 to 4 kOe. In Fig.7, field dependences of the EKE are presented for $ErFeO_3$ in the temperature range T_{1S} -T_{2S} and for $HoFeO_3$ in the SRT range. The EKE value for $HoFeO_3$ is seen to vary significantly when H increases. For $ErFeO_3$, on the contrary, the EKE independence from H is observed after the monodomain state is attained. That result can be explained as follows. The angle ϑ takes the equilibrium value due to action of the surface anisotropy localized in few surface atomic layers. But to rearrange the structure of the transitional layer, its energy in a magnetic field must be comparable to that of bulk anisotropy which increases significantly at $T > T_2$. For example, the value of the first magnetic anisotropy constant, K_1, for erbium orthoferrite at T = 130 K is $3.2 \cdot 10^5$ erg/cm^3 i.e. the effective anisotropy field amounts to $H_K = 2K_1/m_S$ = 64 kOe [5] what exceeds substantially the external magnetic field.

The following experiment supports to some extent the contention that, as in the case of hematite [6], the physical cause of the surface magnetism rise in the erbium orthoferrite lies in a symmetry decrease of the environment of surface magneto-active ions and not in casual effects like the strain hardening during polishing or surface admixtures. From an $ErFeO_3$ single crystal of the same growth batch, using the same technology, a plate was made having the plane turned by about 40 °C relatively to initial one (010) around [001] axis (let it by designated as the plane *a*). For that plane, T_{2S} is found to be shifted toward the low-temperature area to T_2 = 113 K (the $\delta(T)$ curve obtained for that specimen at $H \parallel c$ is showed by a broken line on Fig.6).

The studies performed show that the surface magnetism is a rather common phenomenon for rare earth orthoferrites manifesting itself in the rise of surface orientations ($SmFeO_3$, $TbFeO_3$), shifting of SRT critical temperatures for the surface as compared with those for the bulk crystal ($ErFeO_3$) and being due to more fundamental causes than surface defects or contaminations.

Phenomenologically, the appearance of surface magnetic transitions of the spin reorientation type can be explained by a difference in the character of temperature dependences of the magnetic anisotropy constants near the surface and in the bulk crystal. The qualitative distinction of results obtained for $TmFeO_3$ and $HoFeO_3$, on the one hand, and $ErFeO_3$, $TbFeO_3$, and $SmFeO_3$, on the other, can be understood if we take into account that the rise of the surface magnetism is, in a sense, a threshold process [6] occurring when a gain at the cost of the surface anisotropy energy, K_S, exceeds the characteristic energy of the domain boundary formation in the surface layer, $\sigma = (AK)^{1/2}$. If $K_S < \sigma_0$, the magnetic moments of

iron ions have the same orientation both on the surface and in the crystal volume (that is the case of $TmFeO_3$, $HoFeO_3$).

According to current views, the spin-reorientation type transitions in REOF do not occur because of a variation of the iron sublattices anisotropy constant under temperature influence, but are due to rare-earth sublattices effect intensifying when temperature decreases. At low temperatures, rare-earth ions exhibit a great anisotropy of magnetic properties which is due, to a large extent, to the presence of a low-symmetrical crystal field. Pecularities of the interaction between RE ions and Fe ones are responsible for the variety of SRT in REOF and define the mechanisms of the orientation transitions. The symmetry lowering of the crystalline surrounding of magneto-active ions in the REOR surface layer causes changes in RE–Fe and Fe–Fe interactions what may result in the surface magnetism appearance.

Thus, we get the conclusion that, along with the usual SRT, a diversity of surface phase SRTs exists in REOFs, and to explain them, account must be taken for variations of different RE–Fe and Fe–Fe interaction in surface layer.

A specific surface magnetic phase state was found also at the investigation of the temperature dependence of magnetooptical effects in the $LuCrO_3$ orthocromite, for which the EKE drop to zero was observed at $T < 50$ K [7].

The experimental data presented here provide strong evidence that the presence of the surface magnetism is the rule rather than the exception for weak ferromagnetics.

References

1. G.S.Krinchik, V.E.Zubov, *Pis'ma v ZhETF*, **20**, 307 (1974).
2. K.P.Belov, A.K.Zvezdin, A.M.Kadomtseva, R.Z.Levitin, Orientation Transitions in Rare-Earth Magnetics [in Russian], Nauka, Moscow (1979).
3. R.Belaux, J.E.Bouree, J.Hammann, *J.Physique*, **36**, 803 (1975).
4. K.P.Belov, A.K.Zvezdin, A.A.Mukhin, *ZhETF*, **76**, 1100 (1979).
5. K.P.Belov, A.M.Kadomtseva, N.M.Kovtun et al, *Phys.Stat.Sol.(a)*, **36**, 415 (1976).
6. G.S.Krinchik, V.E.Zubov, *ZhETF*, **69**, 707 (1975).
7. E.A.Gan'shina, V.V.Zotov, M.M.Nishanova, V.M.Milov, *FTT*, **35**, 343 (1993).

Поверхностные спин-переориентационные переходы в редкоземельных ортоферритах и ортохромитах

Е.А.Ганьшина, Г.С.Кринчик, Е.А.Балыкина

Приведены результаты исследования магнитооптических эффектов отражения в редкоземельных ортоферритах (РЗОФ) и ортохромитах. Для обнаружения явлений поверхностного магнетизма изучались температурные, полевые и поляризационные зависимости экваториального эффекта Керра в области температур 10–295 K, при приложении магнитного поля вдоль различных кристаллографических осей. Обнаружено, что в ряде РЗОФ и в $LuCrO_3$ характер поверхностных спин-переориентационных переходов (СПП) отличается от происходящих в объеме. Обнаружено, что при понижении температуры до 50 K в $TbFeO_3$ и до 33 K в $SmFeO_3$ экваториальный эффект Керра уменьшается до нуля, что свидетельствует об исчезновении вектора слабого ферромагнетизма в поверхностном слое (переход типа Морина). Для $ErFeO_3$ обнаружено смещение в высокотемпературную область начала СПП $\Gamma_4 - \Gamma_2$ на поверхности по сравнению с объемом, т.е. на поверхности $ErFeO_3$ существует переходный поверхностный слой типа доменной границы, в котором происходит постепенный поворот вектора антиферромагнетизма на 90 °.

Functional Materials 2, No.2 (1995)

Surface shear modes in piezoelectric superlattice with additional layer

A.N.Podlipenets and L.P.Zinchuk

Institute of Mechanics, National Academy of Sciences of Ukraine,
3 Nesterov St., 252057 Kiev, Ukraine

The results on theoretical studies of the surface phonons (shear modes) existence in a system of piezoelectric superlattice and additional thin layer are presented. The additional layer that modifies the surface wave properties of the superlattice is considered as a planar defect or as a piezoelectric or metallic coating. The superlattice is assumed to be formed by two or more materials and to have the geometry which exhibits Bleustein-Gulyaev wave existence in a single surface problem. The long-wavelength phonon propagation is studied for the case when the layers are considered as elastic continuous media. The dispersion equations are derived by the mathematical formalism of periodic Hamiltonian system. The relations for surface modes are discussed as functions of the nature and the relative parameters of additional film.

Викладено результати теоретичних досліджень умов існування поверхневих фононів (мод зсуву) в системі "п'єзоелектрична надрешітка – додатковий тонкий шар". Додатковий шар, що модифікує хвильові властивості надрешітки, розглядається як планарний дефект або п'єзоелектричне (металеве) покриття. Вважається, що надрешітка створена двома (або більше) різними матеріалами і має геометрію, при якій існують хвилі Блюстейна-Гуляєва в задачі з однією поверхнею. Вивчається поширення довгохвильових фононів у випадку, коли всі шари розглядаються як пружні суцільні середовища. Дисперсійні рівняння одержано за допомогою математичного формалізму періодичних гамільтонових систем. Співвідношення для поверхневих мод досліджуються в залежності від природи та відносних параметрів додаткової плівки.

1. Introduction

With the considerable advances in thin-film techniques that enable high-quality crystalline multilayer structures – superlattices – to be fabricated, researches exploring the various properties of such heterostructures attract the increasing attention. In addition to extensive investigation of the electronic quantum states and transport properties, a number of works, both theoretical and experimental, have been dealt with the study of vibrational characteristics of superlattices [1–3]. Particularly, as noted in [4], the phonon propagation consideration can provide much information on the composition, periodicity, interfaces, defectness, strain field and, generally speaking, on the quality of the superlattices. Among the numerous works devoted to the acoustical properties of infinite and semi-infinite superlattices we must mention the studies on bulk and surface waves in piezoelectric CdS–ZnO systems [5–11]. In these studies, the dispersion equations have been obtained and investigated using different mathematical approaches, namely, the transfer matrix method [1,5], Green's function method [2,6,7], and Hamiltonian system formalism [8–11] (see also the reviews [1–3,12]).

This paper has the aim to present detailed computer simulation study of dispersion equations for shear horizontal modes, propagating in systems consisting of a superlattice and an additional layer. This layer that modifies the acoustical properties of superlattice may be considered either as a technological planar defect or as an artificial piezoelectric or metallic coating.

2. Dispersion equations

2.1. Field representation within superlattice

We assume that the superlattice occupies the semi-infinite region $x_2 > 0$ and is formed by the repetition of a unit cell of thickness h, consisting of R piezoelectric layers with thicknesses h_r: $h = h_1+h_2+...+h_R$, $R \geq 2$. The additional layer of thickness h_0 is bonded to superlattice along the plane $x_2 = 0$ and is contiguous to vacuum along the plane $x_2 = -h_0$. The superlattice layers are of hexagonal symmetry belonging to the 6*mm* class with their sixth-order symmetry axis along the x_3 axis of a reference orthonormal coordinate system; the superlattice axis, perpendicular to the layers, is along x_2 and the propagation wavevector **k**, parallel to the layers, is along x_1. In this particular geometry, the transverse vibration (parallel to x_3), in which we are interested here, is accompanied by an electric potential and decouples from pure elastic sagittal vibrations (polarized in the x_1x_2 plane). It can be shown [13] that, if we seek the simultaneous solutions of electroelastodynamics equations for transverse vibration within superlattice in the form

$$\{D_2(x_1,x_2,t),\sigma_{23}(x_1,x_2,t),\varphi(x_1,x_2,t),u_3(x_1,x_2,t)\} = \{q_1(x_2),q_2(x_2),p_1(x_2),p_2(x_2)\}\exp(ikx_1 - i\omega t), \quad (1)$$

where D_2, σ_{23}, φ, and u_3 are the normal component of electric displacement, the stress component, the electric potential and the displacement vector component, respectively, then for determination of column vectors $\mathbf{q} = \mathrm{col}(q_1,q_2)$ and $\mathbf{p} = \mathrm{col}(p_1,p_2)$ we obtain h-periodic Hamiltonian system of linear differential equations

$$\frac{d}{dx_2}\begin{bmatrix}\mathbf{q}\\ \mathbf{p}\end{bmatrix} = \mathbf{A}(x_2)\begin{bmatrix}\mathbf{q}\\ \mathbf{p}\end{bmatrix}, \quad \mathbf{A}(x_2) = \begin{bmatrix}0 & \mathbf{Q}(x_2)\\ -\mathbf{P}(x_2) & 0\end{bmatrix} \quad (2)$$

with Hamilton function

$$H(x_2, \mathbf{q}, \mathbf{p}) = \left[\mathbf{q}^{\mathrm{T}}\mathbf{P}(x_2)\,\mathbf{q} + \mathbf{p}^{\mathrm{T}}\mathbf{Q}(x_2)\,\mathbf{p}\right]/2. \quad (3)$$

The symmetrical matrices-functions $\mathbf{Q}(x_2)$ and $\mathbf{P}(x_2)$ have the following structure

$$\mathbf{Q}(x_2) = \begin{bmatrix}-\varepsilon_{11}(x_2)k^2 & e_{15}(x_2)k^2\\ e_{15}(x_2)k^2 & c_{44}(x_2) - \rho(x_2)\omega^2\end{bmatrix},$$
$$\mathbf{P}(x_2) = \begin{bmatrix}c_{44}(x_2)d(x_2) & -e_{15}(x_2)d(x_2)\\ -e_{15}(x_2)d(x_2) & -1/\bar{c}_{44}(x_2)\end{bmatrix}, \quad (4)$$
$$\bar{c}_{44}(x_2) = c_{44}(x_2) + [e_{15}(x_2)]^2/\varepsilon_{11}(x_2),$$
$$d(x_2) = 1/[\varepsilon_{11}(x_2)\,\bar{c}_{44}(x_2)],$$

where $\rho(x_2)$, $c_{ij}(x_2)$, $e_{ij}(x_2)$ and $\varepsilon_{ij}(x_2)$ are the mass density, the elastic, the piezoelectric and the dielectric characteristics of the superlattices, respectively, k is the wavenumber, ω is the circular frequency. Here, the superlattice characteristics are assumed to be arbitrary, absolutely integrable, periodic functions

$$\rho(x_2) = \rho(x_2 + h), \quad c_{ij}(x_2) = c_{ij}(x_2 + h), \quad (5)$$
$$e_{ij}(x_2) = e_{ij}(x_2 + h), \quad \varepsilon_{ij}(x_2) = \varepsilon_{ij}(x_2 + h).$$

The surface wave solution of system (2) for the n-th unit cell $(n-1)h \leq x_2 \leq nh$ can be represented [11,13] as

$$\begin{bmatrix}\mathbf{q}(x_2 + nh - h)\\ \mathbf{p}(x_2 + nh - h)\end{bmatrix} = \sum_{l=1}^{2} K_l\kappa_l^n\mathbf{U}(x_2)\mathbf{Y}_l, \quad (6)$$
$$0 \leq x_2 \leq h, \quad |\kappa_l| < 1, \quad n = 1,2,3,...,$$

where K_l are the unknown coefficients, $\mathbf{U}(x_2)$ is a matrixant of system (2), i.e. the fundamental matrix satisfying the condition $\mathbf{U}(0)=E$ (E is the 4×4 unit matrix), κ_l and $\mathbf{Y}_l$ are eigenvalues and their corresponding eigenvectors of the monodromy matrix $\mathbf{U}(h)$. According to Lyapunov-Poincare theorem [14], the characteristic equation of the monodromy matrix has the form

$$\kappa^4 + a_1\kappa^3 + a_2\kappa^2 + a_1\kappa + 1 = 0. \quad (7)$$

Equation (7) admits reciprocal roots and upon substitution by $\kappa+\kappa^{-1}=2b$ is reduced to equations

$$\kappa^2 - 2b_j\kappa + 1 = 0,$$
$$2b_j = -\frac{a_1}{2} - (-1)^j\left(\frac{a_1^2}{4} - 2a_2 + 2\right)^{1/2}, \quad j = 1,2.$$

Among the four eigenvalues κ_l associated to a given ω and k only two may have their moduli less than unity to ensure the decrease of the wave amplitude with increasing distance into the superlattice. It is just these eigenvalues that are used in the solution representation (6).

In the most general case of arbitrary periodicity along x_2 direction, the matrixant $\mathbf{U}(x_2)$ is constructed either with the use of numerical methods (for every value of frequency and wavenumber it is necessary to solve four Cauchy problems for the set (2) on the interval $0 \leq x_2 \leq h$), or on the basis of its representation in the form of converging matrix series [12,15]. For superlattices with properties described by piecewise-constant functions (5), the matrixant may be written in analytical form [13].

The acoustical field (6) in the superlattice should satisfy the boundary conditions at the in-

terface $x_2 = 0$ between the superlattice and the additional film. We shall distinguish two types of boundary conditions depending on whether the film is of piezoelectric or metallic material.

2.2. Additional piezoelectric layer

When the additional layer is of piezoelectric homogeneous material with the same 6*mm* symmetry as the superlattice layers, the solution of set (2) can be represented in the form [13]

$$\mathbf{M}_0(x_2) = \begin{bmatrix} \alpha_4\cosh(ky) & 0 & \alpha_4\sinh(ky) & 0 \\ \alpha_3\cosh(ky) & \alpha_1\,\mathbf{Cs}(\Omega_0 y) & \alpha_3\sinh(ky) & \gamma_0\alpha_1\mathbf{Ss}(\Omega_0 y) \\ \sinh(ky) & \alpha_2\,\mathbf{Ss}(\Omega_0 y) & \cosh(ky) & \alpha_2\mathbf{Cs}(\Omega_0 y) \\ 0 & \mathbf{Ss}(\Omega_0 y) & 0 & \mathbf{Cs}(\Omega_0 y) \end{bmatrix};$$

$$\mathbf{B}_0 = \mathrm{col}\left[B_0^{(1)}; B_0^{(2)}; B_0^{(3)}; B_0^{(4)}\right], \quad y = x_2 + h_0;$$

$$\alpha_1 = \bar{c}_{44,0}\Omega_0, \quad \alpha_2 = e_{15,0}\varepsilon_{11,0}^{-1}, \quad \alpha_3 = ke_{15,0},$$

$$\alpha_4 = -k\varepsilon_{11,0}, \quad \bar{c}_{44,0} = c_{44,0} + e_{15,0}^2\varepsilon_{11,0}^{-1};$$

$$[\gamma_0; \mathbf{Ss}(\cdot); \mathbf{Cs}(\cdot)] = \begin{cases} [-1; \sin(\cdot); \cos(\cdot)], & \rho_0\omega^2/\bar{c}_{44,0} > k^2, \\ [+1; \sinh(\cdot); \cosh(\cdot)], & \rho_0\omega^2/\bar{c}_{44,0} < k^2, \end{cases}$$

$$\mathrm{col}[\mathbf{q}(x_2); \mathbf{p}(x_2)] = \mathbf{M}_0(x_2)\mathbf{B}_0, \tag{8}$$

where

The unknown coefficients K_1 and $B_0^{(i)}$ of (6) and (8) can be determined, except for a multiplicative factor, by using the boundary conditions at $x_2 = 0$ and $x_2 = -h_0$. The usual interface conditions expressing the continuity of the mechanical displacement, the normal stress, the normal electric displacement and the potential are assumed to be fulfilled at $x_2 = 0$. We suppose that the free surface $x_2 = -h_0$ is either metallized or non-metallized. For the first case, when the boundary conditions express the vanishing of the stress and of the electric potential at the surface, we obtain the dispersion equation

$$\begin{vmatrix} \alpha_1\alpha_2^{-1}C_1 & \alpha_3 S_1 & Y_1^{(1)} & Y_2^{(1)} \\ \alpha_1(C_2 - C_1) & \gamma_0\alpha_1 S_2 - \alpha_2\alpha_3 S_1 & Y_1^{(2)} & Y_2^{(2)} \\ \alpha_2 S_2 - \alpha_1\alpha_3^{-1}S_1 & \alpha_2(C_2 - C_1) & Y_1^{(3)} & Y_2^{(3)} \\ S_2 & C_2 & Y_1^{(4)} & Y_2^{(4)} \end{vmatrix} = 0, \quad |\kappa_1| < 1, \quad |\kappa_2| < 1, \tag{9}$$

where $C_1 = \cosh(kh_0)$, $C_2 = \mathbf{Cs}(\Omega_0 h_0)$, $S_1 = \sinh(kh_0)$, $S_2 = \mathbf{Ss}(\Omega_0 h_0)$.

For the second case, when the boundary conditions express the vanishing of the normal stress at

$$\begin{vmatrix} -\varepsilon_{11,0} & 0 & 0 & 0 & \varepsilon_0 \\ \alpha_2^{-1}C_1 & \alpha_2^{-1}\alpha_3 S_1 & Y_1^{(1)} & Y_2^{(1)} & 0 \\ \alpha_3(C_2 - C_1) & \gamma_0\alpha_1\alpha_2^{-1}S_2 - \alpha_3 S_1 & Y_1^{(2)} & Y_2^{(2)} & -\gamma_0\alpha_1\alpha_2^{-1}S_2 \\ \alpha_1^{-1}\alpha_2\alpha_3 S_2 - S_1 & C_2 - C_1 & Y_1^{(3)} & Y_2^{(3)} & -C_2 \\ \alpha_1^{-1}\alpha_3 S_2 & \alpha_2^{-1}C_2 & Y_1^{(4)} & Y_2^{(4)} & -\alpha_2^{-1}C_2 \end{vmatrix} = 0,$$

the surface and the continuity of the normal electric displacement and the electric potential, we have

$$|\kappa_1| < 1, \quad |\kappa_2| < 1, \tag{10}$$

where ε_0 is the dielectric permittivity of vacuum.

2.3. Additional metallic layer

When the additional layer is of isotropic metallic material, the solution of motion equations can be represented in the form [16]

$$\begin{bmatrix} \sigma_{23} \\ u_3 \end{bmatrix} = L_m(x_2)\mathbf{A}_0\exp(ikx_1 - i\omega t), \tag{11}$$

where

$$L_m(x_2) = \begin{bmatrix} d_m\mathbf{Cs}(\Omega_m y) & \gamma_m d_m\mathbf{Ss}(\Omega_m y) \\ \mathbf{Ss}(\Omega_m y) & \mathbf{Cs}(\Omega_m y) \end{bmatrix},$$

$$\mathbf{A}_0 = \mathrm{col}[A_0^{(1)}; A_0^{(2)}], \quad y = x_2 + h_0, \quad \nu_m^2 = c_{44,m}/\rho_m,$$

$$d_m = c_{44,m}\Omega_m, \qquad \Omega_m^2 = \begin{cases} \omega^2\nu_m^{-2} - k^2, & \omega^2\nu_m^{-2} > k^2; \\ k^2 - \omega^2\nu_m^{-2}, & \omega^2\nu_m^{-2} < k^2, \end{cases}$$

$$[\gamma_m; \mathbf{Ss}(\cdot); \mathbf{Cs}(\cdot)] = \begin{cases} [-1; \sin(\cdot); \cos(\cdot)], & \omega^2\nu_m^{-2} > k^2; \\ [+1; \sinh(\cdot); \cosh(\cdot)], & \omega^2\nu_m^{-2} < k^2. \end{cases}$$

Satisfying the boundary conditions at $x_2 = 0$ and $x_2 = -h_0$, we can write the dispersion equation for the surface modes as

$$\begin{vmatrix} \gamma_m d_m\mathbf{Ss}(\Omega_m h_0) & Y_1^{(2)} & Y_2^{(2)} \\ 0 & Y_1^{(3)} & Y_2^{(3)} \\ \mathbf{Cs}(\Omega_m h_0) & Y_1^{(4)} & Y_2^{(4)} \end{vmatrix} = 0, \quad |\kappa_1| < 1, \quad |\kappa_2| < 1, \tag{12}$$

The dispersion equations (9),(10), and (12), derived in this section, represent the implicit relations between the frequency ω and wave number k and are valid for any relative value of the wavelength as compared to the period h of the superlattice (assuming that we remain in the range of

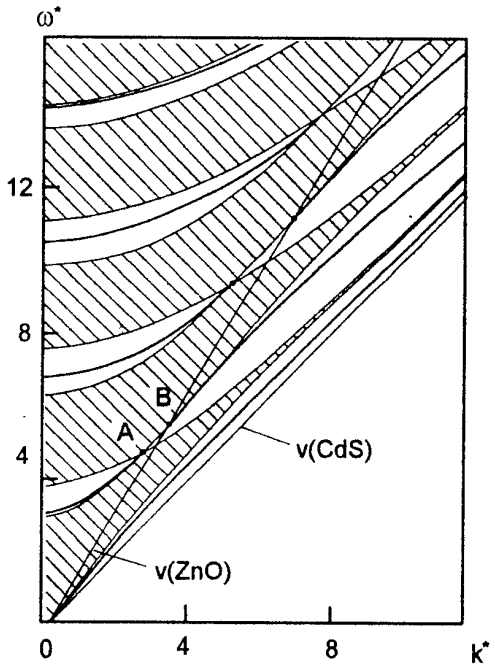

Fig.1. Bulk bands (shaded areas) and surface wave dispersion curves (solid lines) for a CdS–ZnO superlattice with h_1(ZnO)/h_2(CdS) = 3/7 and additional layer of thickness h_0(CdS) = h_2 (the case of perfect superlattice [8–11]).

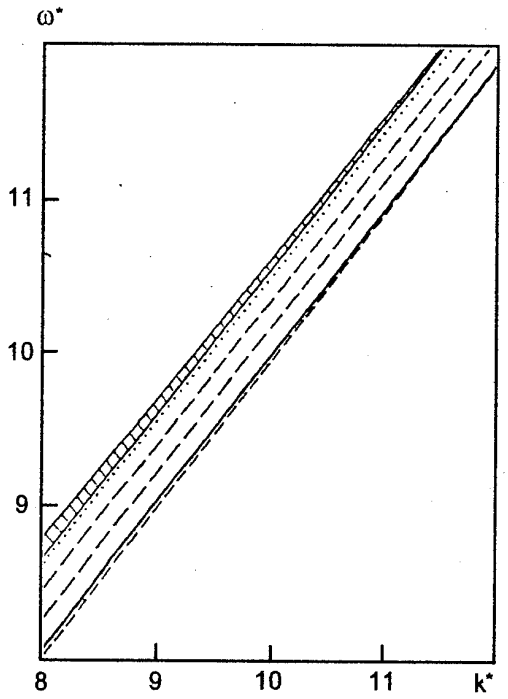

Fig.2. The lowest surface mode at the different values of the thickness h_0(CdS): h_0/h_2 = 1/2 (dotted curve), 4/7, 5/7 (dashed curves), 1 (solid curve), 8/7 (dashed curves). As functions of h_0, all dispersion curves are arranged in a decreasing order.

the elasticity theory where the atomic character of the vibrations does not play a role [5]).

3. Computer results and discussion

In this section we present a few illustrations of the dispersion curves of the surface waves in a CdS–ZnO superlattice and discuss their behaviour as functions of the nature and thickness of the additional layer.

Fig.1 shows the bulk bands and the surface modes for the perfect superlattice when the superlattice is terminated by ZnO layer, the additional layer is of CdS and has the same thickness as in the superlattice bulk. Here we assumed that the free surface is metallized and thus used the equation (9) at $h_0 = h_2$. For a non-metallized surface $x_2 = -h_0$, when the equation (10) has to be taken, the results for surface modes are slightly different but cannot be distinguished from the preceding ones at the scale of the figure [5,9,11]. The straight lines v(CdS) and v(ZnO) correspond to the shear wave velocity in CdS and ZnO, respectively. The dimensionless quantities $k^*=kh$ and $\omega^* = \omega h(\rho_0/c_0)^{1/2}$ are used on both axes, $\rho_0 = 3\cdot10^3$ kg/m^3, $c_0 = 10^{10}$ N/m^2. Here, as in the case of pure elastic shear waves [17–21], we recognize two kinds of critical points: the points at which the bulk band boundaries intersect (indicated by **A**) and the points at which lower band boundary and the fast velocity line meet (indicated by **B**).

Figs.2–5 represent the different types of surface wave behaviour occuring for the first two branches of the imperfect superlattice when the additional layer is of CdS as in Fig. 1, but has a different value of the thickness h_0. The free surface remains to be metallized. At $h_0 > h_2/2$, the lowest surface mode (Fig.2) exists for all values of k and ω below the bulk bands. In Fig.2, the particular range of k and ω is chosen on an enlarged scale for clarity. Figs.3–5 illustrate the variations of the second surface mode within the first frequency gap at different values of h_0. Within the inner part of the gap (to the left of point A) this mode exists only if $h_0 \geq h_2/2$. When $h_2/2 \leq h_0 \leq h_2$, all dispersion curves extend from k=0 to the point **A**. At $h_0 > h_2$, the curves terminate on the lower band edge, as shown by the lowest curve (h_0/h_2 = 8/7) in the Fig.3. Within the outer part of the gap (to the right of point **A**) the second mode curve in Fig.4 starts in the vicinity of a point **B** and extends to $k \to \infty$, when $h_0 = h_2$. As the thick-

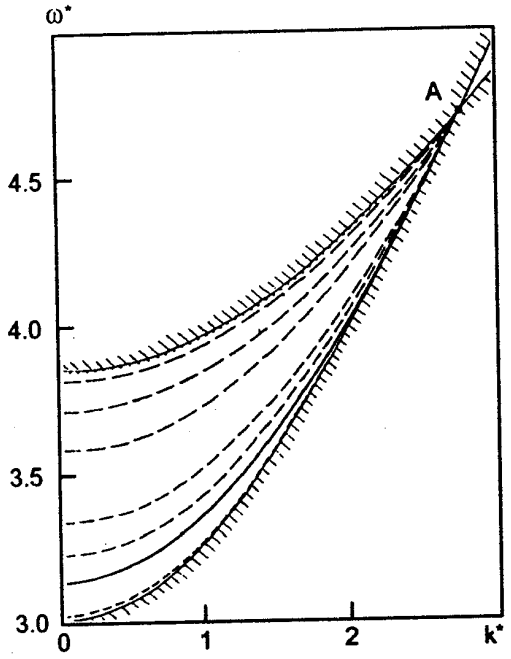

Fig.3. Variations of the second surface mode into the left part of the gap: h_0/h_2 = 1/2 (dotted curve), 4/7, 9/14, 5/7, 6/7, 13/14 (dashed curves), 1 (solid curve), 8/7 (dashed curve). All curves are in a decreasing order as functions of h_0.

ness h_0 is decreased ($h_2/2 < h_0 < h_2$), the starting point of the curve moves to larger values of k on the band edge. At $h_0 > h_2/2$ (Fig.4) and $0 < h_0 < h_2/2$ (Fig.5), the dispersion curves start at the point **A**. Some of them terminate on the upper bulk band edge at a finite value of k, as shown by the top curve in the Fig.5, and some do not.

Fig.6 represents the situation when the superlattice ($x_2 > 0$) is terminated by CdS layer and the additional layer ($-h_0 < x_2 < 0$) is of the ZnO. Previously, we have shown that in the case of perfect superlattice terminated by ZnO layer, the dispersion curves exist practically only between the points **A** and **B** inside every gap, but these curves are very close to the corresponding bulk band boundaries [9,11]. The similar behaviour is demonstrated by the considered system when the additional ZnO layer has the thickness $h_0 > h_2/2$, as shown in the inset of Fig.6. At $0 < h_0 < h_2/2$, the surface wave exists practically over all frequency range considered (Fig.6) and as the additional layer thickness h_0 approaches zero, the dispersion curves tend to those of Fig.1.

Figs.7–9 illustrate the case of additional metallic layer on the CdS–ZnO superlattice terminated by CdS layer. One can see from Fig.7 that in the case of Al layer (v(Al) > v(ZnO) > v(CdS)),

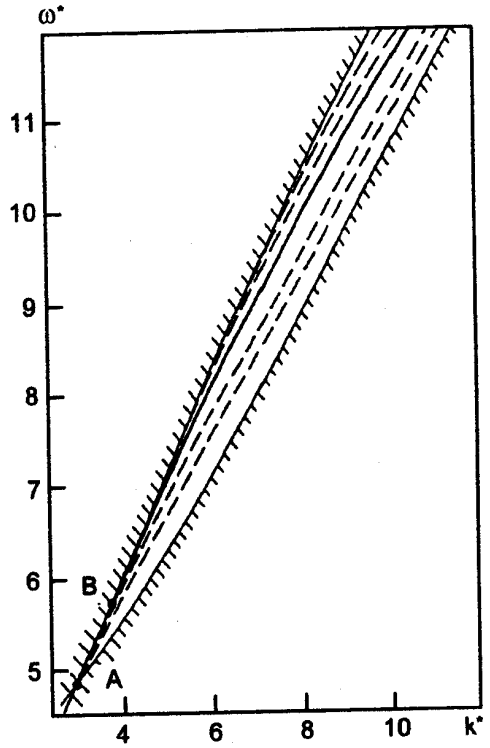

Fig.4. Variations of the second surface mode into the right part of the gap at h_0(CdS) > $h_2/2$: h_0/h_2 = 6/7, 13/14 (dashed curves), 1 (solid curve), 8/7, 9/7 (dashed curves). As functions of h_0, all curves are in a decreasing order.

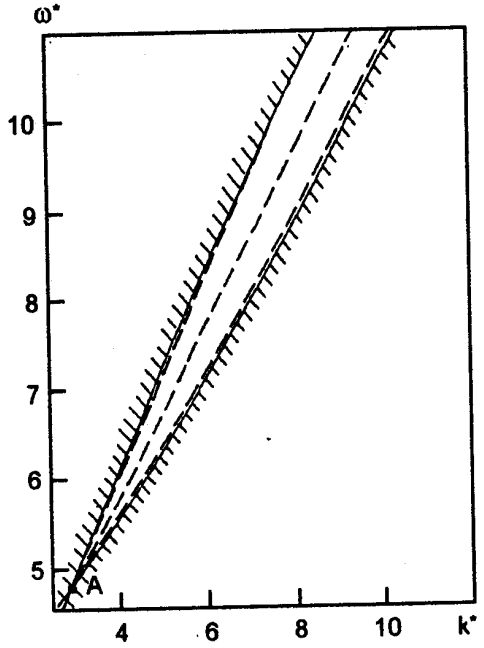

Fig.5. Variations of the second surface mode into the right part of the gap at $0 < h_0$(CdS) < $h_2/2$: h_0/h_2 = 1/7, 2/7, 3/7. All dashed curves are in a decreasing order as functions of h_0.

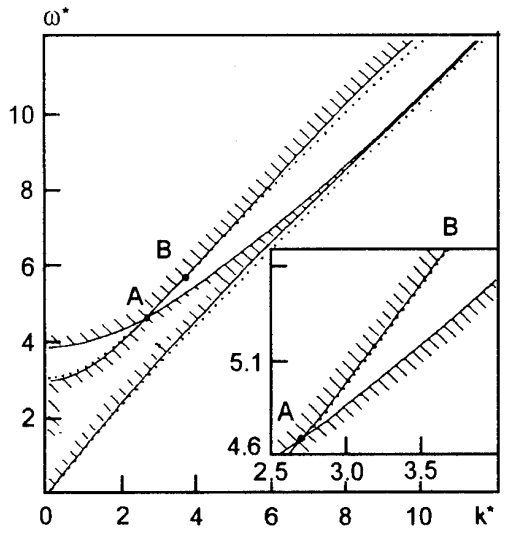

Fig.6. Existence of surface modes when the additional layer is of ZnO at $h_0/h_2 = 1/6$. As function of h_0, the possible dispersion curves at other values of h_0 ($0 < h_0 < h_2/2$) would be arranged in an increasing order inside the outer part of the gap and below the bulk bands whereas they would be in a decreasing order within the inner part of the gap. In inset: the same but $h_0/h_2 = 2/3$, curves at other values h_0 ($h_0 > h_2/2$) would be in increasing order.

the fundamental surface mode is quasibulk one and deeply penetrated into the superlattice at the sufficiently large values of additional layer thickness as shown in Figure for $h_0 = h/5$ and $h/10$ (the corresponding dispersion curves are close to the bulk band). As Al layer thickness approaches zero, the dispersion curve approaches to the fundamental mode of Fig.1 from above. In the case of Ag layer (v(Ag) < v(CdS) < v(ZnO)), the fundamental mode is more localized one and tends to that of Fig.1 from below with decreasing layer thickness. Figs.8 and 9 show the variations of the second mode within the frequency gap. Within the inner part of the gap the corresponding dispersion curves fall in the range between the perfect superlattice mode of Fig.1 and the lower bulk band. The curves start at $k = 0$ and terminate either at the the point **A** (for Al layer) or on the lower band edge (for Ag layer). Within the outer part of the gap the dispersion curves start either at the point **A** (for Ag layer) or on the upper bulk band boundary above a point **B** (for Al layer) and extends to $k \to \infty$.

4. Concluding remarks

In this paper, the long-wavelength surface phonon (acoustic shear wave) propagation in the

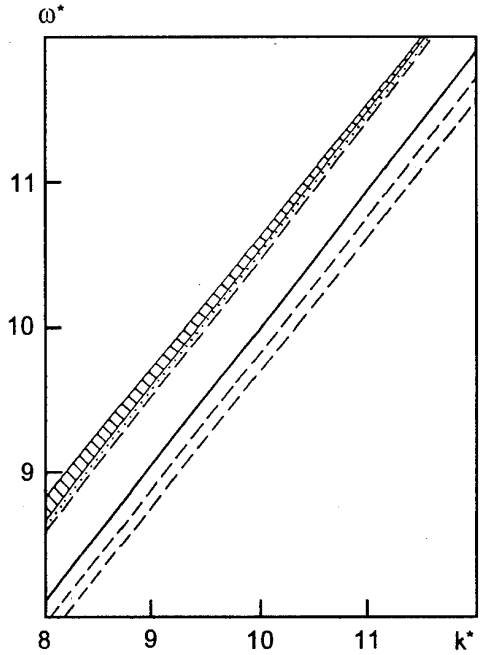

Fig.7. The lowest surface mode of a CdS–ZnO superlattice with additional metallic layer. The curves near bulk band are for the case of Al layer: $h_0/h = 1/5$ (dotted) and 1/10 (dashed). Solid line corresponds to the surface mode of perfect superlattice as in Fig.1. The dashed curves below it are for the case of Ag layer: $h_0/h = 1/20$ and 1/10 (in a decreasing order).

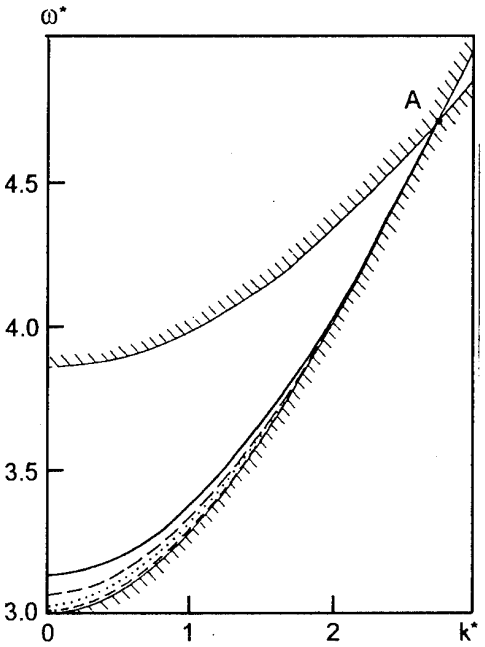

Fig.8. The second mode dispersion within the inner part of the gap when, from above to below, $h_0 = 0$ (solid curve), h_0(Al)/h = 1/10 (dashed) and 1/5 (dotted), h_0(Ag)/h = 1/20 (dashed) relatively.

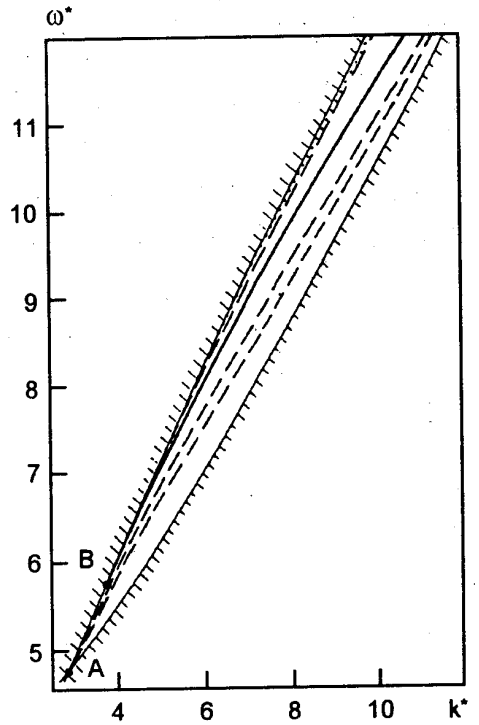

Fig.9. The second mode dispersion within the outer part of the gap when, from above to below, $h_0(Al)/h$ = 1/5 (dotted curve) and 1/10 (dashed), h_0 = 0 (solid), $h_0(Ag)/h$ = 1/20 and 1/10 (dashed curves) relatively.

semi-infinite piezoelectric superlattice with additional piezoelectric or metallic layer has been investigated within the mathematical formalism of periodic Hamiltonian system. The dispersion equations have been derived and corresponding dispersion curves have been calculated for the CdS–ZnO superlattice and different additional layers. In particular cases the obtained equations and numerical results are transformed into outcomes of works [5–11]. The small contradiction between [5] and [9,11], concerning surface mode existence in the perfect superlattice terminated by ZnO layer is explained by the fact that the authors of [5] limited themselves to the representation of dispersion curves at the scale of the figures and did not use a very fine mesh to search surface waves very near to the bulk band boundaries [22]. The existence of such quasibulk modes has been again confirmed by this work (Fig.6), but it should be agreed that these waves are probably less interesting than those situated in the middle of the gaps because they penetrate deeper into the superlattice [22].

We have shown here that, in any case, all surface modes of perfect superlattice, more or less localised, are very sensitive to the appearing the additional layer (as defect or artificial coating) and its nature and the relative parameters.

Acknowledgement

The research described in this publication was made possible in part by Grant No. UB5000 from the International Science Foundation. This work was also supported in part by the Ukraine State Committee on Science and Technology through the projects Nos. 13.3/56 and 13.3/62, and by two Soros Foundation Grants awarded by the American Physical Society. We thank Profs. B.Djafari Rouhani, L.Dobrzynski, N.A.Shulga, and V.R.Velasco for stimulating communications and useful discussions.

References

1. J.Sapriel, B.Djafari Rouhani, *Surf.Sci.Repts*, **10**, 189 (1989).
2. F.Garcia-Moliner, V.R.Velasco, *Surf.Sci.*, **299/300**, 332 (1994).
3. L.Dobrzynski, *Surf.Sci.*, **299/300**, 1008 (1994).
4. E.M.Khourdifi, B.Djafari Rouhani, *J.Phys.: Condens. Matter*, **1**, 7543 (1989).
5. A.Nougaoui, B.Djafari Rouhani, *Surf.Sci.*, **185**, 154 (1987).
6. L.Fernandez, V.R.Velasco, *Surf.Sci.*, **185**, 175 (1987).
7. L.Fernandez, V.R.Velasco, F.Garcia-Moliner, *Surf.Sci.*, **188**, 140 (1987).
8. L.P.Zinchuk, A.N.Podlipenets, N.A.Shulga, *Elektronnaya Tekhnika*, Ser.6, No.2 (278), 95 (1988).
9. L.P.Zinchuk, Cand.Sci.Thesis, Kiev (1989).
10. A.N.Podlipenets, N.A.Shulga, in: Proc. II Intern. Symp. on Surf. Waves in Solids and Layered Structures, Varna, Bulgaria (1989), v.2, p.289.
11. L.P.Zinchuk, A.N.Podlipenets, N.A.Shulga, *Sov.Appl. Mech.*, **26**, 1092 (1990).
12. N.A.Shulga, A.N.Podlipenets, in: Mechanics of Composites [in Russian], A.N. Guz, ed., Naukova Dumka, Kiev (1993), v.2, p.35.
13. L.P.Zinchuk, A.N.Podlipenets, N.A.Shulga, *Sov. Appl. Mech.*, **24**, 245 (1988).
14. V.A.Yakubovich, V.M.Starzhinskii, Linear Differential Equations with Periodic Coefficients, Vol.1, Wiley, New York (1975).
15. L.P.Zinchuk, A.N.Podlipenets, *Sov.Appl.Mech.*, **27**, 775 (1991).
16. L.P.Zinchuk, A.N.Podlipenets, *Sov.Appl.Mech.*, **25**, 1107 *(1989)*.
17. V.G.Savin, N.A.Shulga, *Akust.Zhurn.*, **21**, 260 (1975).
18. B.A.Auld, G.S.Beaupre, G.Herrmann, in: Modern Problems in Elastic Wave Propagation, ed. by J.Miklowitz and J.D.Achenbach, Wiley, New York (1978), p.459.
19. N.A. Shulga, Principles of Mechanics of Layered Media with Periodic Structure [in Russian], Naukova Dumka, Kiev (1981).
20. A.N.Podlipenets, *Mech.Compos.Mater.*, **18**, 734 (1982).

21. R.E.Camley, B.Djafari Rouhani, L.Dobrzynski, A.A.Maradudin, *Phys.Rev. B*, **27**, 7318 (1983).

22. B.Djafari Rouhani, private communication.

Поверхностные сдвиговые моды в пьезоэлектрической сверхрешетке с дополнительным слоем

А.Н. Подлипенец, Л.П.Зинчук

Представлены результаты теоретических исследований существования поверхностных фононов (сдвиговых мод) в системе "пьезоэлектрическая сверхрешетка – дополнительный тонкий слой". Дополнительный слой, модифицирующий волновые свойства сверхрешетки, рассматривается как плоский дефект или пьезоэлектрическое (металлическое) покрытие. Предполагается, что сверхрешетка образована двумя (или больше) различными материалами и имеет геометрию, при которой существуют волны Блюстейна-Гуляева в задаче с одной поверхностью. Изучается распространение длинноволновых фононов для случая, когда все слои рассматриваются как упругие сплошные среды. Дисперсионные уравнения получены с помощью математического формализма периодических гамильтоновых систем. Соотношения для поверхностных мод исследуются в зависимости от природы и относительных параметров дополнительной пленки.

Functional Materials 2, No.2 (1995)

Light scattering on the surface superlattices in ferromagnetic semiconductors produced by coherent light beams

A.Yu.Semchuk

Institute for Surface Chemistry, National Academy of Sciences of Ukraine,
31 Nauki Ave., 252028 Kiev, Ukraine

Effect of surface superlattice of electron density on the light propagation in the ferromagnetic semiconductors (FMSC) is studied. A wide-gap FMSC of EuO-type under constant electric field in the spin-wave temperature range is considered. The nonequilibrium state in FMSC is created by an external field. Phonons serve as a thermostat. Under such conditions, the action of CLBs give rise to the formation of surface superlattices in FMSC with certain concentration of electrons, electric field strength, electron and magnon temperatures. The light reflection coefficient for a FMSC with surface superlattices is determined. It is also shown that, by varying the magnitude of an external electric field, one can decrease this coefficient, i.e. make FMSC "antirefractive", as well as increase it up to the case of total reflection.

Досліджено вплив поверхневої надрешітки електронної густини на розповсюдження світла у ферромагнітних надпровідниках (ФМНП). Розглянуто широкощілинний ФМНП в постійному електричному полі і в температурному діапазоні спінової хвилі. Нерівноважний стан в ФМНП створюється зовнішнім полем. Термостатом є фонони. В цих умовах вплив когерентних світлових пучків викликає утворення в ФМНП поверхневих надрешіток з певною концентрацією електронів, напруженістю електричного поля, електронною та магнонною температурами. Визначено коефіцієнт відбиття світла для ФМНП з поверхневими надрешітками. Показано також, що, змінюючи напруженість зовнішнього електричного поля, можна зменшити цей коефіцієнт, тобто перетворити ФМНП в "невідбиваючий", а також збільшити його до випадку повного відбиття.

1. Introduction

During the last few years the semiconductors with spatial periodic structures (superlattices) have been a subject of intensive studies. Firstly, in connection with the appearance of high-power nano- and picosecond lasers as well as corresponding recording facilities, experimental studies of such structures have considerably grown. Secondly, there has been a significant increase of interest in different spatial periodic structures in view of intensive development of electronics, holography and semiconductor technology. The FMSC with surface superlattices of nonequilibrium electrons and magnons may become objects which completely meet the needs. Superlattices in FMSC can be formed using CLBs. Such FMSCs with superlattices of nonequilibrium electrons and magnons were described for the first time in [1,2]. The electrical conduction and refractive index of such FMSCs were studied in [3–6].

In this work, we consider the influence of a surface superlattice of electron density on the light propagation in FMSC. We have determined the light reflection coefficient for a surface of FMSC with a superlattice. It is also shown that varying the magnitude of an external electric field one can decrease the light reflection coefficient, i.e. make FMSC "antirefractive", as well as increase that coefficient until the total reflection occurs.

2. FMSC with a surface superlattices

Let us consider a wide-gap FMSC of EuO type with mean carrier density n_0 in an external constant electric field $E_0 \| 0Z$ and in the spin-wave temperature range. Let several CLB be incident on the outer surface $x = 0$ of the FMSC, the vector-potential of the beam in the material is given as:

$$A(r, t) = \sum A_j \cos(\omega t - k_j r - \varphi_j) \qquad (1)$$

and its frequency ω satisfying the inequality $\varepsilon << \hbar\omega << \varepsilon_g$ (ε is the mean carrier energy, ε_g is the energy-gap width). Therefore, the CLB does not change the total number of carriers and only causes their spatial redistribution.

A non-equilibrium state in the electron-magnon system of the FMSC is produced both by heating-up electrons by the external constant electric field E_0 and as a result of absorption of light quanta by free carriers, followed by energy transfer from electrons to magnons.

There are phonons which play the role of a thermostat. Under such conditions, as was shown in [1,2], the CLB gives rise to the formation of surface superlattices in the FMSC with electron concentration n, electric field strength F, electron θ_e and magnon θ_m effective temperatures, which at $A_j \perp F_0$ and in the case of incidence on a FMSC surface of only two symmetrically oriented beams with $A_1 \| A_2$, $k_{1x} = k_{2x}$, $k_{1z} = -k_{2z}$, are described by the following expression

$$n(z) = n_0 + n_1 = n_0(1 + \xi_1 \cos 2k_{1z}z + \xi_2 \sin 2k_{1z}z), \quad (2)$$

$$F(z) = F_0 + F_1(z) = E_0(1 + \zeta_1 \cos 2k_{1z}z + \zeta_2 \sin 2k_{1z}z),$$

$$\theta_e(z) = T_e + T_1(z) = T_e(1 + \eta_0 + \eta_1 \cos 2k_{1z}z + \eta_2 \sin 2k_{1z}z),$$

$$\theta_m(z) = T_m + T_2(z) = T_m(1 + \mu_0 + \mu_1 \cos 2k_{1z}z + \mu_2 \sin 2k_{1z}z)$$

The temperatures T_e, T_m in the field E_0 are determined by a familiar technique [7] and will be further regarded as known quantities. The amplitudes ξ_i, ζ_i, η_i, μ_i depend on A_1, A_2, E_0, and FMSC parameters; the method of their calculation is given in [1] in a general form. We present here only the expression for amplitudes ξ_1 and ξ_2 since, as will be seen from subsequent calculations, there are just those which define the processes of wave diffraction and scattering in FMSC with a surface superlattice. Neglecting small terms of the order of $(T_e/\hbar\omega)^{1/2}$ or $\beta^2(T_e/\hbar\omega)^{1/2}$, we obtain for ξ_1 and ξ_2 the following expression

$$\xi_1 = \frac{1}{(\alpha+1)^2 + \beta^2}\left\{\frac{\beta^2-\alpha-1}{2}\eta_1 + \beta(\alpha+1)\eta_2 + 2\beta^2\mu_1 + 2\beta(\alpha+1)\mu_2 + \frac{\beta^2 B}{2}\left[\frac{1}{3}(\pi T_e/\hbar\omega)^{1/2} - \frac{\alpha+1}{\beta}\right]\right\},$$

$$\xi_2 = \frac{1}{(\alpha+1)^2 + \beta^2}\left\{-\frac{\beta(2\alpha+1)}{2}\eta_1 + \frac{\alpha+1-\beta^2}{2}\eta_2 - 2\beta(\alpha+1)\mu_1 - 2\beta(\alpha+1)\mu_1 + 2\beta^2\mu_2 - \frac{\beta^2 B}{2}\left[\frac{\alpha+1}{3}(\pi T_e/\hbar\omega)^{1/2} - 1\right]\right\}, \qquad (3)$$

where

$$\alpha = \frac{\pi e^2 n_0}{\varepsilon_0 k_{1z}^2 T_e}, \quad \beta = \frac{eE_0}{2k_{1z}T_e}, \quad B = \frac{4eA_1A_2}{3\beta mc^2 T_e},$$

ε_0 is the permittivity of FMSC, m is the electron effective mass.

Let us suppose, as in [1,2], the following inequalities take place:

1) $eA_j << c(\hbar\omega m)^{1/2}$, $j = 1,2$; 2) the recipropal wave vector k_{1z}^{-1} exceeds considerably the value of de Broglie wavelength of electrons, remaining at the same time significantly less than the linear dimension of FMSC, $\lambda_D << k_{1z}^{-1} << L$.

Fulfilment of these inequalitities enables us to take into account the effect of HF-field of CLBs in terms of the perturbation theory and to consider the values n_1, T_1, T_2, F_1 as small additions to n_0, T_e, T_m, E_0. We consider "classical" superlattices assuming that the electron dispersion law $\varepsilon(p)$ and electron momentum relaxation time $\tau_p^{em}(\varepsilon)$ are the same as those of homogeneous FMSC.

3. Light scattering in FMSC with a surface superlattice

Now, let a trial wave comes from vacuum to the FMSC surface $x = 0$. Its electric field can be described as

$$E = E(x, z)\exp(-i\omega t). \qquad (4)$$

Then we shall search a solution of (6) in the following form

$$E(x, z) = \Phi(z)\exp(-ik_x x), \qquad (5)$$

where $\Phi(z)$ is determined from the equation

$$\frac{d^2\Phi}{dz^2} + S_z^2\Phi = \alpha_1(\xi^*\exp(2ik_{1z}z) + \xi\exp(-2ik_{1z}z))\Phi. \qquad (6)$$

Since, as we supposed above, $|\xi| << 1$, then, to obtain a solution of (6), one can use the usual perturbation theory. Although for the Bragg resonance region,

when $S_z = k_{1z} + \Delta_k (|\Delta_k| \to 0)$, which we are now interested in, this theory is unacceptible. To solve this problem we use the theory developed in [8–10]. For this purpose, let us present $\Phi(z)$ as the sum

$$\Phi(z) = \sum_l \left\{ A_l \exp\left\{ i\,[(2l+1)\,k_{1z} + \delta] \right\} + \right. \\ \left. + B_l \exp\left\{ -i\,[(2l+1)\,k_{1z} - \delta] \right\} \right\}, \quad (7)$$

where $\delta \to 0$ is the small parameter to be determined. If, as we assumed above, the inequality $(\alpha_1/k_{1z}) << 1$ is fulfilled, then one can put in (7) only the terms with $l = 0$, i.e. use two-wave approximation, as it was done in [8–10]. In this way we obtain for $\Phi(z)$ the expression

$$\Phi(z) = A_0 \exp[i(k_{1z} + \delta)z] + B_0 \exp[-i(k_{1z} - \delta)z]. \quad (8)$$

Substituting (8) into (6) and equating coefficients for similar exponential functions, we obtain the following set of two homogeneous equations in the amplitudes A_0 and B_0

$$\left[-(k_{1z}+\delta)^2 + (k_{1z}+\Delta_k)^2\right] A_0 - \alpha_1(\xi_1 - i\xi_2)\, B_0 = 0$$
$$\left[-(k_{1z}+\delta)^2 + (k_{1z}+\Delta_k)^2\right] B_0 - \alpha_1(\xi_1 - i\xi_2)\, A_0 = 0. \quad (9)$$

Equating the determinant of this set to zero, we obtain that

$$\delta = \pm((\Delta_k)^2 - \alpha_1^2(\xi_1^2 + \xi_2^2)/4k_{1z}^2)^{1/2}, \quad (10)$$

and the amplitude ratio B_0/A_0 being equal to

$$\frac{B_0}{A_0} = R_s = \frac{\alpha_1(\xi_1 + i\xi_2)}{2k_{1z}(\Delta_k + \delta)} = \frac{2k_{1z}(\Delta_k - \delta)}{\alpha_1(\xi_1 - i\xi_2)}. \quad (11)$$

It should be noted that the sign in (10) is determined by natural conditions of an energy flow direction and finiteness of the solution at $z \to 0$.

Thus, for example, if $(\Delta_k)^2 < \alpha_1^2(\xi_1 + \xi_2)/4k_{1z}^2$, then the finiteness of the solution unambigously demand $\delta > 0$. As follows from (10) and (11), $R_s = 1$, and the waves propagating have equal amplitudes both in positive and negative directions. For real δ we have always $|R_s| < 1$.

Now, let us consider calculations of a light reflection coefficient on the surface $z = 0$ of FMSC with a superlattice. Making use of (10) and (11) and keeping in mind that we treat resonant situation by taking into account the reflected wave, we can determine the electric field for the incident wave in vacuum as

$$E(r, t) = E^{(0)}\left[\exp\left\{ i\,(k_x x + u_z z) \right\} + \right. \\ \left. + R_0 \exp\left\{ i\,(k_x x - u_z z) \right\}\right] \exp(-i\Omega t), \quad (12)$$

where $u_z^2 = (\omega_p^2/c^2) + \varepsilon_0^{-1}\left[k_x^2 - (\varepsilon_0 - 1)S_z^2\right]$,
$\Omega^2 = c^2(k_x^2 + u_z^2)$, $S_z = k_{1z} + \Delta_k$. (13)

The light reflection coefficient $|R_0|^2$, from the FMSC outer surface, $z = 0$, and direct wave amplitude A_0 are determined by the boundary conditions for this surface. The calculation gives the following expression for the reflection coefficient

$$|R_0|^2 = \quad (14)$$
$$= \frac{(k_{1z} - u_z)^2 + (k_{1z} + u_z)^2|R_s|^2 - (k_{1z}^2 - u_z^2)(R_s + R_s^*)}{(k_{1z} + u_z)^2 + (k_{1z} - u_z)^2|R_s|^2 - (k_{1z}^2 - u_z^2)(R_s + R_s^*)}$$

$$A_0 = \frac{2S_z}{S_z + k_{1z} + (S_z - k_{1z})R_s} E^{(0)}. \quad (15)$$

Now, let us analyse the result obtained above. As it follows from (11)–(13) the reflection coefficient magnitude $|R_0|^2$ depends substantially on the Δ_k and δ values. For example, if, at given Δ_k, the parameter δ becomes purely imaginary, then, according to (11), $|R_s| = 1$ and, as follows from (14), $|R_0| = 1$. Thus, near to the Bragg resonance, where δ becomes purely imaginary, we have in fact a total reflection and electromagnetic waves does not penetrate into FMSC. When deviating from resonance (for example, with increasing Δ_k or, at fixed Δ_k, with decreasing $(\xi_1^2 + \xi_2^2)$), the magnitude of δ may pass through $\delta = 0$ becoming real. For this case it is convenient to rewrite (14) as

$$|R_0|^2 = \quad (16)$$
$$= \frac{2k_{1z}(u_z^2 + k_{1z}^2)\Delta_k - 4k_{1z}^2\delta u_z - \alpha_1(k_{1z}^2 - u_z^2)\xi_1}{2k_{1z}(u_z^2 + k_{1z}^2)\Delta_k + 4k_{1z}^2\delta u_z - \alpha_1(k_{1z}^2 - u_z^2)\xi_1}.$$

It follows from (16) that, with increasing Δ_k (or decreasing $|\xi_1|$ with increasing E_0), the reflection coefficient tends to $|R_0|_0^2 = ((k_{1z} - u_z)/(k_{1z} + u_z))^2$ which is the value for homogeneous (not irradiated by CLBs (FMSC. Hence, since ξ_1, ξ_2, δ depend on E_0, by varying E_0 at fixed Δ_k one may vary $|R_0|^2$ from 1 to the limiting value $|R_0|_0^2$. It should be noted that the value of $|R_0|^2$ depends not only on E_0 and the magnitude of Δ_k, but also on the sign of Δ_k. If Δ_k and ξ_1 have the same signs, $|R_0|^2$ reaches its minimum at

$$\Delta_k = \frac{\alpha_1}{2} \cdot \frac{k_{1z}^2 + u_z^2}{k_{1z}^2 - u_z^2} \cdot \frac{\xi_1^2 + \xi_2^2}{\xi_1}. \quad (17)$$

At such value of Δ_k, electromagnetic waves penetrate best into FMSC. The presence of a car-

rier density superlattice makes FMSC, in this case, as it were, "antirefractive", while, as we could see above, in another limiting case it may lead to almost total reflection of incident waves. The same effects can be obtained by varying amplitudes of CLBs. The effects described above may be used to obtain information on the FMSC parameters. Since, as follows from (14) and (16), $|R_0|^2$ depends also on the wave angle of incidence (13) at the fixed frequency Ω, for which the conditions of Bragg resonance are accomplished, by varying the incidence angle for the wave (12) one can change the reflection coefficient.

Conclusion

Thus, the coefficient of light reflection obtained in this work for the surface $z = 0$ of FMSC under conditions of Bragg resonance depends indirectly on the values of heating field E_0, angle of incidence of waves and parameters of FMSC. Varying those and the value of E_0, one can decrease the reflection coefficient, i.e. make FMSC "antirefractive", as well as increase it, reaching the case of almost total reflection of light from a surface of FMSC.

In contrast with usual (nonferromagnetic) semiconductors, the effects described above depend indirectly and substantially on the state of a magnetic subsystem of FMSC. As is seen from (3) and (4), the amplitudes of electron density modulation ξ_1 and ξ_2 depend on the magnon temperature T_m through the parameters μ_0, μ_1 and μ_2. Therefore, one can govern the effect described above by varying the amplitude of magnon temperature modulation.

Now, let us make some numerical evaluations. So, for example, assuming that $n_0=10^{15}$ to 10^{16} cm^{-3}, $\omega=5\cdot10^{14}$ s^{-1}, $T=0.5\cdot10^{-21}$ J and the electric field strength being of the order of 10^3 V/cm with the values of FMSC parameters chosen from [11], we obtain that the maximum reflection takes place at $\Delta_k>0.001653$. For homogeneous (not irradiated by CLB) FMSC $|R_0|_0^2 = 0.4026$, that is slightly more than for usual (nonferromagnetic) semiconductors [8]. Thus, the effect described may be observed under the conditions easily reached in experiments.

Finally, the author wish to thank Prof. P.M.Tomchuk for his interest in the work, discussion of results and many helpful conversations.

References

1. A.Yu.Semchuk, A.E.Levshin, P.M.Tomchuk, *Sov.Phys. Solid State*, **28**, 229 (1986).
2. A.Yu.Semchuk, L.G.Grechko, V.M.Ogenko, *Phys.stat.sol.(b)*, **157**, 451 (1990).
3. A.Yu.Semchuk, L.G.Grechko, V.M.Ogenko, *Phys.stat.sol.(b)*, **162**, 539 (1990).
4. A.Yu.Semchuk, L.G.Grechko, V.M.Ogenko, *Physica B*, **176**, 153 (1992).
5. A.Yu.Semchuk, L.G.Grechko, V.M.Ogenko, *Ukr.Fiz.Zhurn.*, **35**, 746 (1990).
6. A.Yu.Semchuk, L.G.Grechko, V.M.Ogenko, *Ukr.Fiz.Zhurn.*, **34**, 1692 (1989).
7. I.Ya.Korenblit, B.G.Tankhilevich, *Sov.Phys. Solid State*, **18**, 34 (1976).
8. I.M.Dykman, P.M.Tomchuk, *Ukr.Fiz.Zhurn.*, **31**, 841 (1989).
9. I.M.Dykman, P.M.Tomchuk, *Fiz.Tekhn.Poluprov.*, **12**, 592 (1978).
10. I.M.Dykman, P.M.Tomchuk, *Phys.stat.sol.(b)*, **86**, 773 (1978).
11. L.Nagaev, Magnetic Semiconductors [in Russian], Moscow (1979), p.350.

Светорассеяние на поверхностных сверхрешетках в ферромагнитных сверхпроводниках, создаваемых воздействием когерентных световых пучков

А.Ю.Семчук

Исследовано влияние поверхностной сверхрешетки электронной плотности на распространение света в ферромагнитных сверхпроводниках (ФМСП). Рассмотрен широкощелевой ФМСП в постоянном электрическом поле и в температурном диапазоне спиновой волны. Неравновесное состояние в ФМСП создается внешним полем. Термостатом служат фононы. В этих условиях воздействие когерентных световых пучков вызывает образование в ФМСП поверхностных сверхрешеток с определенной концентрацией электронов, напряженностью электрического поля, электронной и магнонной температурами. Определен коэффициент отражения света для ФМСП с поверхностными сверхрешетками. Показано также, что, изменяя напряженность внешнего электрического поля, можно уменьшить этот коэффициент, т.е. превратить ФМСП в "неотражающий", а также увеличить его вплоть до случая полного отражения.

Functional Materials 2, No.2 (1995)

Simulation of the cratered destruction of a surface and accompanying processes

A.D.Suprun and S.Ya.Shevchenko

T.Shevchenko Kiev University, 64 Vladimirskaya St., 252601 Kiev, Ukraine

In consequence of our investigations, the effect of powerful electromagnetic pulse (in particular, laser one) upon a material surface, the process of crater formation and accompanying processes were managed to formulate adequately enough and relatively simple mathematical algorithm of such processes as burning of plasma plume, interaction of radiation with plume, which influences both the process of crater formation and the dynamics of plume itself, excitation of intensive shock wave of elastic nature in the bulk material, which can stimulate the destructions in the material volume and, in turn, influences on the quality of the crater formed. These algorithms were also performed partly by numerical and analytical methods. An unexpected result was obtained. It was appeared that the interaction *always* essentially influences on the development of both the plasma plume and the corrosive crater and it should not be neglect even in the case of extra short pulses, when the pulse was believed to have no time to interact with radiation.

В результаті наших досліджень вдалось сформулювати достатньо адекватний реальності і відносно простий математичний алгоритм таких процесів як дія потужного електромагнітного імпульсу (зокрема лазерного) на поверхню матеріалу, процес лазерного формування кратера і супутні цьому процеси: горіння плазменно-корозійного факела, взаємодія випромінювання з факелом, яка впливає як на процес формування кратера, так і на динаміку самого факела, збудження інтенсивної ударної хвилі пружної природи в об'ємі матеріалу, яке може стимулювати об'ємні руйнування і, в свою чергу, впливати на якість утвореного кратера. Вдалось також і частково реалізувати їх чисельно-аналітичними методами. При цьому одразу було одержано непередбачений результат. Виявилось, що взаємодія *завжди* суттєво впливає на розвиток плазменного факела і корозійоного кратера і знехтувати нею не можна навіть у випадку екзотично коротких імпульсів, коли, як вважалось, імпульс просто не встигає провзаємодіяти з випромінюванням.

The cratered destruction of a surface is always a result of heavy and/or local attack on it. This attack may be of different nature including a mechanical impact. The attack of powerful electromagnetic laser pulse on a material surface is the most interesting for numerous practical purposes. It might be well to point out that not only the crater formation with the use of laser radiation but the accompanying processes are very interesting as well. Among these processes are the plasma-corrosion plume and its application for the material spraying in deposition technology; the radiation interaction with the plume which has an influence upon the crater formation as well as on plume dynamics; and at last the generation of an elastic shock wave in the bulk material which can stimulate the volume destruction and, as a result, produces a certain effect on the crater quality.

It is important to realize that taking into account the mutual influence of all these factors is impossible by use only experimental means. Numerical and analytical simulation of the processes which attend the cratered destruction of a surface is necessary to tackle all these problems. Such simulation, especially numerical one, enables to solve such problems as prediction of the surface alteration by powerful pulse action and even optimizing of these processes. High technologies based on the destructive surface treatment have need for such simulation which is cheaper than a real experimental investigation.

Relying on our investigations we succeeded in developing sufficiently faithful and comparatively simple algorithm of all these processes and in carrying out their simulation.

This algorithm involves:

1. A dynamic equation for pressure (all functions and variables are dimensionless here)

$$\frac{\partial P}{\partial t} + \Gamma\kappa\beta P^{\sigma}\ \frac{\partial P}{\partial \Gamma} + \kappa\beta P^{\sigma}\ \frac{\partial P}{\partial z} = \tag{1}$$

$$= F(r)\, g(P)\, E(P)\, P^{\eta+\beta}\ \theta(\tau - t)\, \theta(tP^{\sigma} - z),$$

where P is pressure; t is time; r, z are cylindrical space variables; Γ, κ, β, σ, η are known parameters; $F(r)$, $g(P)$, $E(P)$ are known functions; $\theta(x) = 1$, if $x \geq 0$, $\theta(x) = 0$, if $x < 0$; τ is the pulse duration.

This equation governs real spatial and time dynamics of the plasma-corrosion plume in such its features as pressure, density and convection velocity. The density and convection velocity are determined by:

$$\rho = P^{\eta}; \quad \vec{v} = \vec{\Gamma} P^{\sigma};$$

where $\vec{\Gamma} = \vec{e}_{\perp}\Gamma + \vec{e}_z$; $\vec{e}_{\perp}$, $\vec{e}_z$ are unit vectors of basic cylindrical coordinate system.

2. Three further equations describe the processes at the condensate-plasma interface

$$\frac{\partial P_S}{\partial t} + \kappa\beta\left[\Gamma - \frac{\partial S}{\partial r}\right] P_S^{\sigma}\ \frac{\partial P_S}{\partial r} =$$

$$= \left[\kappa\beta\left(\Gamma\frac{\partial S}{\partial r} + 1\right)\theta(t_p - t) + \right.$$

$$\left. + F(r)\, g(P_S)\, E(P_S)\, \theta(\tau - t)\right] P_S^{\eta+\beta} - \tag{2}$$

$$-\kappa\beta\left(\Gamma\frac{\partial S}{\partial r} + 1\right) P_S^{\beta+1} +$$

$$+ \kappa\beta\, F(r)\, E(P_S)\, P_S^{\eta}\, \theta(\tau - t)\, \theta[q_R(P_S) - 1];$$

where P_s is near-surface pressure; S is crater form function ($z_s = -S$: z_s is coordinate of crater surface); t_p is the post-duration time; $q_R(P_S)$ is a known function (part of radiation flow entered into solid);

$$\frac{\partial S}{\partial t} - \Gamma A\, P_S^{\beta}\ \frac{\partial S}{\partial t} = A\, P_S^{\beta}; \tag{3}$$

where A is a known parameter;

$$P_{ii}^{<o>}\, n_i\, \vec{e}_i = [P_S - (\vec{n}\,\vec{q}_S)]\,\vec{n} - \rho_S\,(\vec{n}\vec{v}_S)\,(\vec{v}_S - \vec{u}); \tag{4}$$

where $P_{ii}^{<o>}$ is the surface value of the elastic stress tensor; $\vec{n}$ is a normal-to-surface vector, n_i are its components; $\vec{e}_i = (\vec{e}_x, \vec{e}_y, \vec{e}_z)$ are unit vectors of basic coordinate system; $\vec{q}_S$ is the value of radiation flow near the surface which is a known function of pressure P_S; $\vec{q}_S = -\vec{e}_z\, q_S$; $\vec{u}$ is the speed of plasma-solid boundary moving, $\vec{u} = -\vec{e}_z\, \frac{\partial S}{\partial t}$.

2.1. Equations (2) and (3) are related and a general solution can be obtained only simultaneously. These two equations are central for the problem. Their simultaneous solution gives the boundary conditions for all other processes, in particular for (1). By convention, (2) may be denoted the equation of surface firing, and (3) the equation of crater formation dynamics. In some approximations, when these equations are independent of each other, they represent the functions consistent with their names.

2.2 Eq. (4) or, in components,

$$P_{xx}^{<o>} = P_{yy}^{<o>} = \left[P_S + \frac{q_S}{|\vec{N}|}\right] -$$

$$-\Gamma\left(\Gamma\frac{\partial S}{\partial r} + 1\right) P_S \left(\frac{\partial S}{\partial r}\right)^{-1}; \tag{4.1}$$

$$P_{zz}^{<o>} = \left[P_S + \frac{q_S}{|\vec{N}|}\right] -$$

$$-\left(\Gamma\frac{\partial S}{\partial r} + 1\right) P_S^{\beta}\left(P_S^{\sigma} + \frac{\partial S}{\partial t}\right)^{-1}; \tag{4.2}$$

where

$$|\vec{N}| = \sqrt{1 + (\partial S/\partial r)^2},$$

are the boundary conditions for the typical transport equation of the elastic medium. A solution of this equation under conditions (4.1), (4.2) may describe the elastic shock wave. If the amplitude of this wave exceeds material strength limit then crack-like damages will arise under the crater in the bulk material.

3. The solution of further problem (all functions and variables are in real dimensions here) containing differential equation:

$$\rho c\,\frac{\partial T}{\partial t} = \mathrm{div}[\lambda\,\mathrm{grad}(T)] +$$

$$+ q_S\, k\, \exp(-kz)\, \theta(\tau - t); \tag{5.1}$$

and initial and boundary conditions:

$$T(0, r, z) = T_0; \tag{5.2}$$

$$T(t, r, \infty) = T_0; \quad \lambda\,\frac{\partial T}{\partial z}(t, r, z_S) = 0, \tag{5.3}$$

where ρ is density of material; c is its specific heat capacity; λ is its heat conductivity; k is absorption coefficient, allows to obtain assessments of the threshold value of the radiation flow and the

post-effect time. The destruction threshold defines the radiation flow value over which the destruction occurs. The post-effect time is the time after pulse termination in which the material destruction is as active as during the pulse.

There is no need, to say that presented algorithms can be realized only numerically. However, for one-dimensional approximation and with neglecting the interaction of radiation with plume, the problem under consideration have series of useful analytical solutions. In this approximation eqs. (2) and (3) become independent. Eq.(3) turns into a simple equality. After its integration, a satisfactory assessment of the crater depth can be gained [1]. The analytical solution of eq.(2) can be found under certain conditions [2]. In this approximation, the time-space dynamics of a plasma-corrosion plume can be analyzed [1] relying on solution of eq.(1). And finally, this approximation gives the possibility to find, by solving eqs. (5.1-3), a sufficiently simple expression for the destruction threshold:

$$q_S^m = \frac{(pirh\ c\lambda)^{1/2}}{2\,\tau^{1/2}}\left(T_k - T_0\right),$$

where T_k is a critical temperature, and for the post-effect time:

$$t_p = \tau\left[\frac{(T_k - T_0)^2}{4\,(T_\pi - T_0)^2} + \frac{1}{2} + \frac{(T_\pi - T_0)^2}{4\,(T_k - T_0)^2}\right],$$

where T_π is the fusion temperature.

At the present time, our main goal is to build the overall numerical model of processes mentioned above. In this way, the program simulating eq.(2) was realized. Whilst one-dimensional problem is solved, it nevertheless accounts for radiation-plasma interaction. As this takes place, an unexpected result was obtained. It turns out that radiation- plume interaction affects the plasma plume (look the figure) and corrosion crater development. Thus, this interaction can not be neglected even for very short pulses.

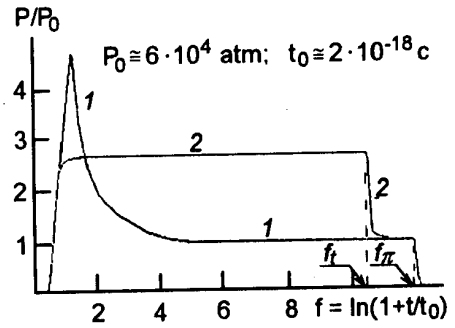

Fig.1. For Al, flow intensity $Q = 10^{11}$ W/cm^2 and pulse duration $\tau = 10^{-13}$s: 1 – behavior of near-surface pressure with interaction taken into consideration; 2 – the same but without interaction. $f_T = \ln(1 + \tau/t_0)$; $f\Pi = \ln(1 + t_\Pi/t_0)$.

References

1. A.D.Suprun, R.M.Chernigha, *Poverkhnost'. Fiz., Khim., Mekh.*, No.12, 37 (1992).
2. P.V.Gerasimenko, A.D.Suprun, L.V.Shmeleva, *Poverkhnost'. Fiz., Khim., Mekh.*, No.7, 71 (1989).

Fig.1. For Al, flow intensity $Q = 10^{11}$ W/cm^2 and pulse duration $\tau = 10^{-13}$s: 1 – behavior of near-surface pressure with interaction taken into consideration; 2 – the same but without interaction. $f_T = \ln(1 + \tau/t_0)$; $f\Pi = \ln(1 + t_\Pi/t_0)$.

Моделирование кратерообразного разрушения поверхности и сопровождающих процессов

А.Д.Супрун, С.Я.Шевченко

В результате наших исследований удалось сформулировать достаточно адекватный реальности и относительно простой математический алгоритм таких процессов как воздействие мощного электромагнитного импульса (в частности лазерного) на поверхность материала, процесс лазерного формирования кратера и сопутствующие этому процессы: горение плазменно-коррозионного факела, взаимодействие излучения с факелом, которое влияет как на процесс формирования кратера, так и на динамику самого факела, возбуждение интенсивной ударной волны упругой природы в объеме материала, которое может стимулировать объемные разрушения и, в свою очередь, влиять на качество образовавшегося кратера. Удалось также и частично реализовать их численно-аналитическими методами. При этом сразу был получен неожиданный результат. Оказалось, что взаимодействие *всегда* существенно влияет на развитие плазменного факела и коррозионного кратера и пренебрегать им нельзя даже в случае экзотически коротких импульсов, когда, как считалось, импульс просто не успевает провзаимодействовать с излучением.

Functional Materials 2, No.2 (1995)

Absorption of the electromagnetic radiation by the surface modes in heterogeneous media

L.G.Grechko, V.G.Levandovskii, V.V.Motrich and V.Yu.Reshetnyak

Institute for Surface Chemistry, National Academy of Sciences of Ukraine,
31 Nauki Ave., 252022 Kiev, Ukraine

The results of studies of the interaction between electromagnetic radiation and heterogeneous systems (HS) are generalized. The calculation schemes of the effective dielectric permeability $\tilde{\varepsilon}$ for two types of HS, namely statistical mixtures and matrix disperse systems (MDS), are presented. The results obtained have been used for the investigation of mechanisms of the electromagnetic radiation absorption caused by surface modes in a MDS with spherical or ellipsoid-shaped metallic conclusions. It is shown that the resonance absorption of electromagnetic radiation is observed at the frequencies of the surface modes. The spectral characteristics of $\tilde{\varepsilon}(\omega)$ as a function of MDS parameters is considered.

В роботі узагальнено результати досліджень взаємодії електромагнітного випромінювання (ЕМВ) з широким спектром гетерогенних систем (ГС). Приведені схеми розрахунку ефективної діелектричної проникності ($\tilde{\varepsilon}$) ГС двох типів: статистичні суміші та матричні дисперсні системи (МДС). Одержані результати використані для дослідження механізмів поглинання ЕМВ в МДС з металевими включеннями сферичної та еліпсоїдальної форми, обумовленого наявністю поверхневих мод. Досліджено спектральний характер $\tilde{\varepsilon}(\omega)$ в залежності від параметрів МДС.

Dielectric permittivity of heterogeneous systems

When analyzing the interaction of the electromagnetic radiation with heterogeneous systems, the main problem is to understand the correlation between the electrodynamic properties of the composite material and its physico-chemical structure. The term "composite material" implies HS of two or more homogeneous phases. Depending on the character of the components' distribution in such materials, the latter are classified into lamellar materials (regular or irregular), matrix and statistic mixtures. The composite in a matrix mixture form is assumed to be a matrix that forms a continuous medium in which distributed are not contacting mutually microscopic inclusions, these phases (matrix and inclusions) being inequitable. From here on, we shall call such systems "matrix disperse systems" (MDS). Statistic mixtures are characterized by an unordered distribution of phases. Here, both phases are equitable. The form and nature of the filler particles in MDS and particles of phases in the statistic mixture may be absolutely different.

To establish a correlation between electrodynamic parameters of HS and the structure of these systems, two methods are mainly used: the effective medium method [1–12] and that of the radiation transfer equations [13–14]. The first was used in this paper: the inhomogeneous medium with spatially varying electrodynamic parameters was substituted by a homogeneous one with the corresponding effective values of electrodynamic parameters (dielectric permittivity $\tilde{\varepsilon}$, magnetic permeability $\tilde{\mu}$, conductivity $\tilde{\sigma}$). The establishment of the correlation between $\tilde{\varepsilon}$, $\tilde{\mu}$ and $\tilde{\sigma}$ and properties of the inhomogeneous medium is associated with the calculation of mean intensities values in different parts of such a medium. Usually, for solving these problems, various approximations are used (long-wave, electrostatic, etc.) [1–12]. We believe that the most efficient approach to solving the problems of the $\tilde{\varepsilon}$, $\tilde{\mu}$, $\tilde{\sigma}$ determination for HS is a set of integral equations of electrodynamics [15]. The idea of the method

consists of the following. Let, in an unlimited space characterized by dielectric ε_m and magnetic μ_m permeabilities, be the given system of currents and charges which initiates primary dropping electric $\vec{E}_0(\vec{r})$ and magnetic $\vec{H}_0(\vec{r})$ fields (time dependence $e^{-i\omega t}$) and N of electrically neutral material bodies of an arbitrary shape and nature with tensors of dielectric $\hat{\varepsilon}_i$ and magnetic μ_i permeabilities. Then, it follows from the Maxwell equations with account for boundary conditions and superposition principle [15] that the electromagnetic field in an arbitrary point of space $\vec{r}$ will be defined by the equations:

$$\vec{E}(\vec{r}) = \vec{E}(\vec{r}) + \sum_{i=1}^{N} \left\{ (\mathrm{grad}\cdot \mathrm{div} + k_1^2)\Pi_i^E(\vec{r}) + ik_1\sqrt{\frac{\mu_m}{\varepsilon_m}}\,\mathrm{rot}\vec{\Pi}_i^M(\vec{r}) \right\}, \quad (1)$$

$$\vec{H}(\vec{r}) = \vec{H}(\vec{r}) + \sum_{i=1}^{N} \left\{ (\mathrm{grad}\cdot \mathrm{div} + k_1^2)\Pi_i^E(\vec{r}) - ik_1\sqrt{\frac{\mu_m}{\varepsilon_m}}\,\mathrm{rot}\vec{\Pi}_i^M(\vec{r}) \right\}, \quad (2)$$

where $k_1 = \frac{\omega}{c}\sqrt{\varepsilon_m \mu_m}$, $\vec{\Pi}_i^E$ and $\vec{\Pi}_i^M$ are the electric and magnetic Herz potentials fully defined provided known are the internal fields in each of the scattering bodies individually:

$$\vec{\Pi}_i^E(\vec{r}) = \frac{1}{4\pi}\int_{V_{(i)}} \left(\frac{\hat{\varepsilon}_{(i)}}{\varepsilon_m} - \hat{I} \right) \vec{E}(\vec{r}_i) f(|\vec{r} - \vec{r}_i|)\, d\vec{r}_i \quad (3)$$

$$\vec{\Pi}_i^M(\vec{r}) = \frac{1}{4\pi}\int_{V_i} \left(\frac{\hat{\varepsilon}_i}{\varepsilon_m} - \hat{I} \right) \vec{E}(\vec{r}_i) f(|\vec{r} - \vec{r}_i|)\, d\vec{r}_i \quad (4)$$

Here $$f(|\vec{r} - \vec{r}'|) = \frac{e^{-ik_1|\vec{r} - \vec{r}'|}}{|\vec{r} - \vec{r}'|} \quad (5)$$

is the Green function satisfying the scalar equation

$$\Delta f + k_1^2 f = -4\pi\delta(\vec{r} - \vec{r}') \quad (6)$$

To determine the internal field in the volume V_i one should consider (and solve) $2N$ integral equations (1) and (2) for the points inside the volume V_i. It is common solution of these equations that determines the internal field in all bodies, consequently, according to (1) and (2), a full field in all points of the space.

The use of the set of electrodynamics integral equations allowed to consider from one viewpoint the problem on $\tilde{\varepsilon}$ and $\tilde{\mu}$ of statistic mixtures and MDS types HS [16–18]. In these papers, general expressions for the calculation of $\tilde{\varepsilon}_{ij}$ were obtained in the form of series by the correlation functions of a random value $\varepsilon_{ij}(\vec{r})$ (statistic mixtures) and by the concentrations of inclusions (MDS). Let us note that, in this case, at each k stage of the ε_{ij} calculation it is necessary either to know the correlation function of the k-th order for

Table 1.

Types of inclusions	Low concentration approximation	Self-consistent approximation	
1. Spheres	$\tilde{\varepsilon} = \varepsilon_m + \frac{3f\varepsilon_m(\varepsilon - \varepsilon_m)}{(2\varepsilon_m + \varepsilon) + f(\varepsilon - \varepsilon_m)}$	$\tilde{\varepsilon} = \varepsilon_m + \frac{3f\tilde{\varepsilon}(\varepsilon - \varepsilon_m)}{(2\tilde{\varepsilon} + \varepsilon) + f(\varepsilon - \tilde{\varepsilon})}$	(7)
2. Randomly oriented cylinders	$\tilde{\varepsilon} = \varepsilon_m + \frac{f(5\varepsilon_m + \varepsilon)(\varepsilon - \varepsilon_m)}{3(\varepsilon_m + \varepsilon) - 2f(\varepsilon - \varepsilon_m)}$	$\tilde{\varepsilon} = \varepsilon_m + \frac{f(5\tilde{\varepsilon} + \varepsilon)(\varepsilon - \varepsilon_m)}{3(\tilde{\varepsilon} + \varepsilon) - 2f(\varepsilon - \tilde{\varepsilon})}$	(8)
3. All the cylinders are in the plane OXY and randomly oriented	$\tilde{\varepsilon} = \varepsilon_m + \frac{2f\varepsilon_m(\varepsilon - \varepsilon_m)}{(\varepsilon_m + \varepsilon) + f(\varepsilon - \varepsilon_m)}$ $\tilde{\varepsilon}_{xx} = \tilde{\varepsilon}_{xy} = \varepsilon_m + \frac{2f(\varepsilon - \varepsilon_m)(\varepsilon + 3\varepsilon_m)}{(\varepsilon_m + \varepsilon) - f(\varepsilon - \varepsilon_m)}$	$\tilde{\varepsilon}_{xz} = \varepsilon_m + \frac{2f(\varepsilon - \varepsilon_m)\tilde{\varepsilon}_{xz}}{(\tilde{\varepsilon}_m + \varepsilon) + f(\varepsilon - \tilde{\varepsilon}_m)}$ $\tilde{\varepsilon}_{xx} = \tilde{\varepsilon}_{xy} = \varepsilon_m + \frac{2f(\varepsilon - \varepsilon_m)(\varepsilon + 3\tilde{\varepsilon}_{xx})}{(\varepsilon + \tilde{\varepsilon}_{xx}) - f(\varepsilon - \tilde{\varepsilon}_{xx})}$	(9)
4. Cylinders are parallel to the axis OZ	$\tilde{\varepsilon}_m = \varepsilon_m + (\varepsilon - \varepsilon_m)f$ $\tilde{\varepsilon}_{xx} = \tilde{\varepsilon}_{yy} = \varepsilon_m + \frac{2f\varepsilon_m(\varepsilon - \varepsilon_m)}{(\varepsilon_m + \varepsilon) - f(\varepsilon - \varepsilon_m)}$	$\tilde{\varepsilon}_m = \varepsilon_m + (\varepsilon - \tilde{\varepsilon}_m)f$ $\tilde{\varepsilon}_{xx} = \tilde{\varepsilon}_{yy} = \varepsilon_m + \frac{2f\varepsilon_{xx}(\varepsilon - \varepsilon_m)}{(\varepsilon + \tilde{\varepsilon}_{xx}) - f(\varepsilon - \tilde{\varepsilon}_{xx})}$	(10)
5. Randomly oriented disks	$\tilde{\varepsilon} = \varepsilon_m + \frac{2f(2\varepsilon + \varepsilon_m)(\varepsilon - \varepsilon_m)}{3\varepsilon - f(\varepsilon - \varepsilon_m)}$	$\tilde{\varepsilon} = \varepsilon_m + \frac{f(2\varepsilon + \tilde{\varepsilon})(\varepsilon - \varepsilon_m)}{3\varepsilon - f(\varepsilon - \tilde{\varepsilon})}$	(11)

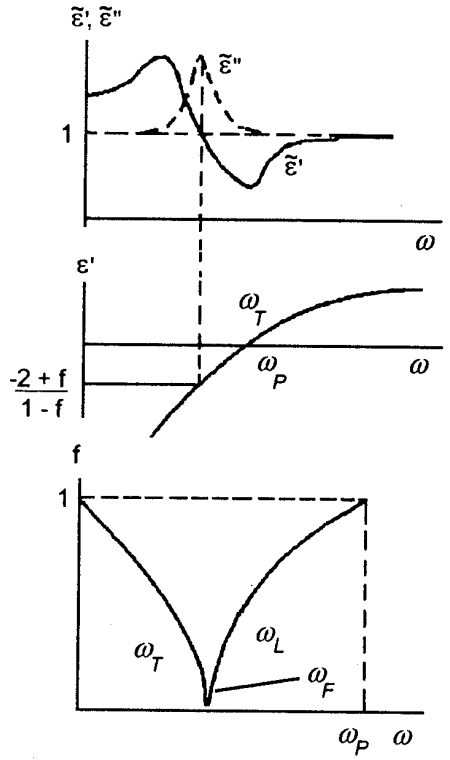

Fig.1. Surface plasmons of spherical metallic particles of dispersively inhomogeneous systems.

$\varepsilon_{ij}(\vec{r})$ or to solve the problem of a common behaviour of k particles in the electromagnetic field. The results of the first approximation both for the case of low concentrations (Maxwell-Garnett [1,2] approximation) and for that of the mean field (Brugerman approximation) [1,3] are summarized for different forms of inclusions in Table 1.

Absorption of electromagnetic radiation by surface modes in MDS

It is known [1] that at the interaction of EMR with separate particles the size of which is significantly smaller than the wavelength of the incident radiation, its absorption by the surface modes (plasmons, polaritons, excitons) of these particles takes place. Given below is a theoretical consideration of the absorption in a MDS with the fillers of spheric and ellipsoidal forms. For obtaining MDS dependences on $\tilde{\varepsilon}'$ and $\tilde{\varepsilon}''$, the relation (7) was used; here the dielectric permittivity of inclusions was expressed in the following form [1]:

$$\varepsilon(\omega) = \varepsilon_\infty \left[1 + \sum_{i=1}^{n} \frac{\omega_{pi}^2}{\omega_{0i}^2 - \omega^2 - i\omega\nu_{0i}} \right] \qquad (12)$$

where $\omega_{pi} = \dfrac{4\pi N_i e^2}{m^*\varepsilon_\infty}$, $N_i = f_i N$ is the concentration of electrons participating in the i-th transition, f_i of the oscillator strength for this transition, ω_{oi} is the intrinsic frequency of this transition, ν_{oi} is the frequency of their relaxation. From (7) and (12) we find for a sphere:

$$\mathrm{Re}\tilde{\varepsilon}(\omega) = \tilde{\varepsilon}_\infty \left[1 + \frac{a\left(\sum_{i=1}^{n}\Omega_i^2\alpha_i a_i\right) + \sum_{i=1}^{n}\Omega_i^2\alpha_i a_i \sum_{i=1}^{n}\omega_{Ti}^2\alpha_i a_i}{\left(a + \sum_{i=1}^{n}\omega_{Ti}^2\alpha_i a_i\right)^2 + \left(\sum_{i=1}^{n}\omega_{Ti}^2\gamma_i a_i\right)^2} + \right.$$

$$\left. + \frac{\sum_{i=1}^{n}\Omega_i^2\gamma_i a_i \sum_{i=1}^{n}\omega_{Ti}^2\alpha_i\gamma_i}{\left(a + \sum_{i=1}^{n}\omega_{Ti}^2\alpha_i a_i\right)^2 + \left(\sum_{i=1}^{n}\omega_{Ti}^2\gamma_i a_i\right)^2} \right]$$

$$\mathrm{Im}\tilde{\varepsilon}(\omega) = \tilde{\varepsilon}(\infty)\frac{a\sum_{i=1}^{n}\Omega_i^2\gamma_i a_i}{\left(a + \sum_{i=1}^{n}\omega_{Ti}^2\gamma_i a_i\right)^2 + \left(\sum_{i=1}^{n}\omega_{Ti}^2\gamma_i a_i\right)^2}; \qquad (13)$$

$$a = \left[\left(\omega_{01}^2 - \omega^2\right)^2 + \omega^2\nu_{01}^2\right] \cdots \left[\left(\omega_{0n}^2 - \omega^2\right)^2 + \omega^2\nu_{0n}^2\right]$$

$$a_i = \frac{a}{\left(\omega_{01}^2 - \omega^2\right)^2 + \omega^2\nu_{01}^2}, \quad \alpha_i = \omega_{01}^2 - \omega^2, \quad \gamma_i = \omega\nu_{0i},$$

$$\Omega_i^2 = \omega_{Li}^2 - \omega_{Ti}^2, \quad \tilde{\varepsilon}(\omega \to \infty) = \varepsilon_m\frac{(1-A) + A\varepsilon_m}{(1-B) + B\varepsilon_\infty},$$

$$\omega_{Li}^2 = \frac{A\varepsilon_m\omega_{pi}^2}{(1-A)\varepsilon_m + A\varepsilon_\infty}, \quad \omega_{Ti}^2 = \frac{B\varepsilon_\infty\omega_{pi}^2}{(1-B)\varepsilon_m + B\varepsilon_\infty}$$

where $B = (1-f)/3$, $A = B + f$, ε_m is the dielectric permittivity of the matrix. The frequency of the surface modes is found from the relation (denominator is in the expression for $\mathrm{Im}\tilde{\varepsilon}(\omega) = 0$):

$$1 + \sum_{i=1}^{n}\frac{\omega_{pi}^2\left(\omega_{0i}^2 - \omega^2\right)}{\left(\omega_{0i}^2 - \omega^2\right)^2 + \omega^2\nu_{i0}^2} = -\frac{1-B}{B}\cdot\frac{\varepsilon_m}{\varepsilon_\infty}. \qquad (14)$$

The formulas (13) and (14) solve in principle the problem of EMR absorption in MDS with the spheric inclusions at a most general character of the frequency dependence $\varepsilon(\omega)$ (13).

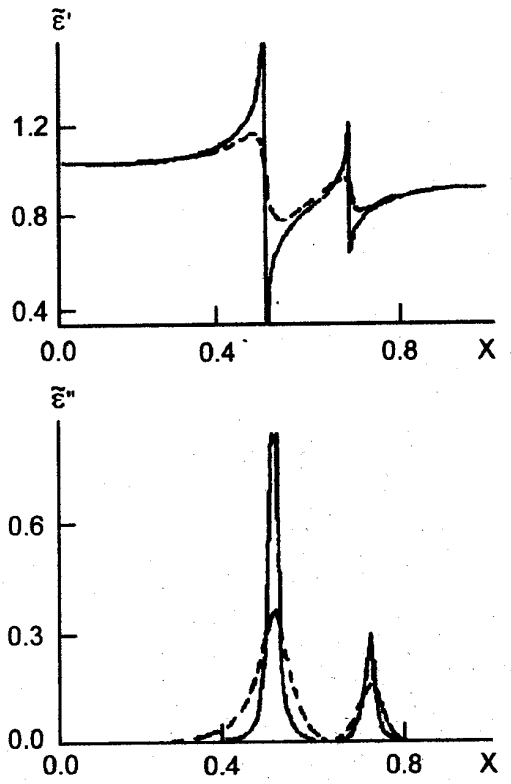

Fig.2. Dependences of the real ($\tilde{\varepsilon}'$) and imaginary ($\tilde{\varepsilon}''$) parts of effective dielectric permittivity on frequency $x = \omega/\omega_p$ at $\varepsilon_m = \varepsilon_\infty = 1$; $f = 0.01$; $L_1 = L_2 = 1/4$; $L_3 = 1/2$; for $\nu/\omega_p = 0.008$ (———); and $\nu/\omega_p = 0.004$ (– · – · –).

In the case of free carriers, at $\varepsilon_m = \varepsilon_\infty = 1$

$$\varepsilon(\omega) = 1 - \frac{\omega_p}{\omega(\omega + i\nu)} \tag{15}$$

$$\tilde{\varepsilon}(\omega) = 1 + \frac{\omega_L^2 - \omega_T^2}{\omega_T^2 - \omega^2 - i\omega\nu} \tag{16}$$

where [19,20]

$$\omega_L^2 = \frac{1+2f}{3}\omega_p^2,\ \omega_T^2 = \frac{1-f}{3}\omega_p^2 \tag{17}$$

Thus, the absorption at a frequency of the surface plasmon ω_T (Frelich mode) has a resonance character and, depending on f, may differ essentially from ω_p. In the case of randomly oriented ellipsoidal particles with the depolarization coefficients [1] $L_1 = L_2 \neq L_3$ and $\varepsilon_{(\omega)}$ according to (15), the analogous calculations [18] give ($\varepsilon_m = \varepsilon_\infty = 1$):

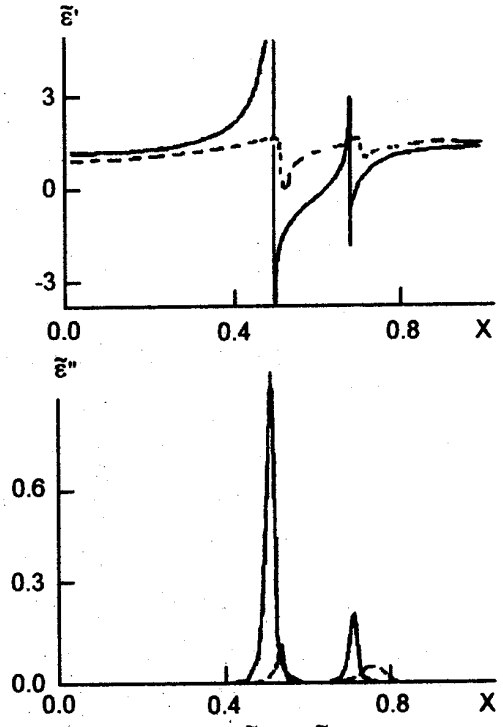

Fig.3. Dependences of $\tilde{\varepsilon}'$ and $\tilde{\varepsilon}''$ on frequency x at $\varepsilon_m = \varepsilon_\infty = 1$; $\nu/\omega_p = 0.008$; $L_1 = L_2 = 1/4$; $L_3 = 1/2$ for $f = 0.1$ (———) and $f = 0.01$ (– · – · –).

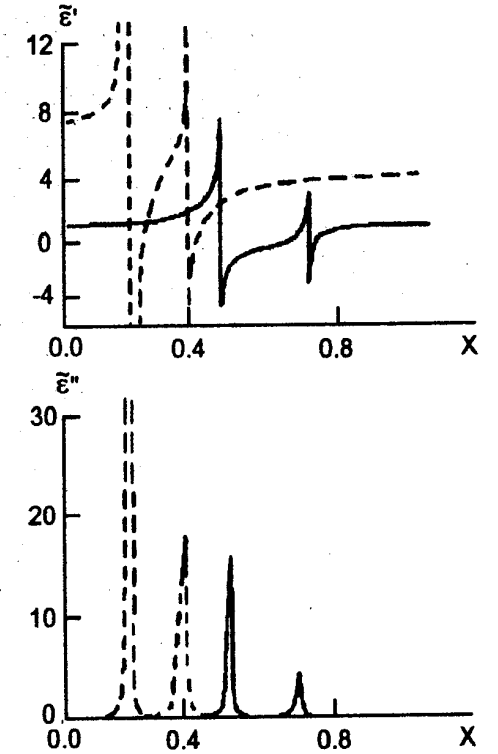

Fig.4. Dependences of $\tilde{\varepsilon}'$ and $\tilde{\varepsilon}''$ on x at $\varepsilon_\infty = 1$; $\nu/\omega_p = 0.008$; $f = 0.1$ for $L_1 = L_2 = 1/4$; $L_3 = 1/2$ for $\varepsilon_m = 1$ (———); $\varepsilon_m = 5$ (– · – · –).

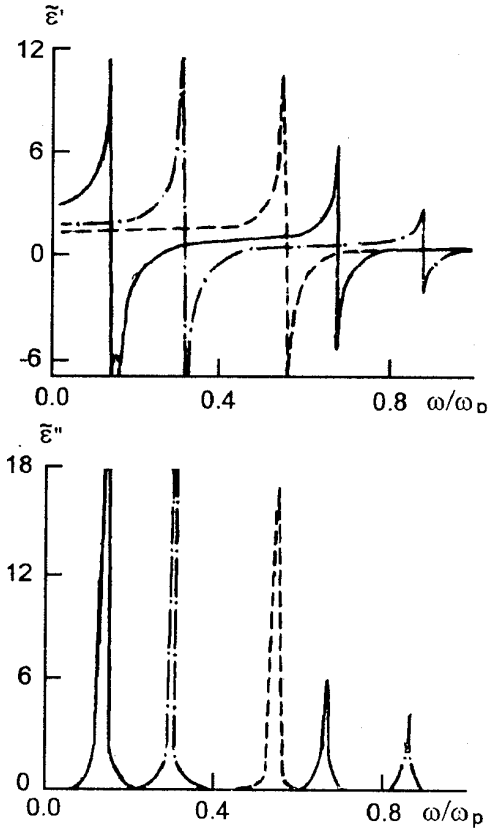

Fig.5. Dependences of $\tilde{\varepsilon}'$ and $\tilde{\varepsilon}''$ on x at $\varepsilon_m = \varepsilon_\infty = 1$; $\nu/\omega_p = 0.008$; $f = 0.1$ for $L_1 = L_2 = 0.49$, $L_3 = 0.02$ (———); $L_1 = L_2 = 0.01$, $L_3 = 0.98$ (– · – · –); $L_1 = L_2 = L_3 = 1/3$ (-----).

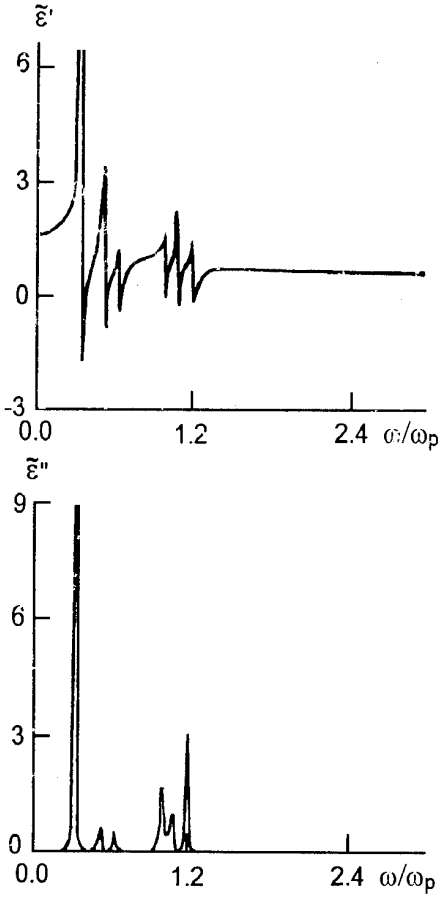

Fig.6. Dependences of $\tilde{\varepsilon}'$ and $\tilde{\varepsilon}''$ on x at $\varepsilon_m = \varepsilon_\infty = 1$; $f = 0.1$; $L_1 = 0.1$, $L_2 = 0.3$, $L_3 = 0.6$.

$$\tilde{\varepsilon}(\omega) = 1 + \frac{f\omega_p^2\gamma_1}{\Omega_{T1}^2 - \Omega^2} + \frac{f\omega_p^2\gamma_2}{\Omega_{T2}^2 - \Omega^2} \qquad (18)$$

where

$$\gamma_1 = \frac{1}{6\gamma}(1 - f - 3a + 3\gamma),\ \gamma_1 + \gamma_2 = 1,\ \Omega^2 = \omega(\omega + i\nu),$$

$$a = (2L_3 + L_1)/3,\ 1/3 \le a \le 2/3,$$

$$\gamma_1 = 1/3\ [(1 - f - 3a)^2 - 4\,(1 - f)\,(2 - 3a)(6a - 1)]^{1/2},$$

and

$$\Omega_{T1,T2}^2 = \frac{\omega_p^2}{2}\,[(1 - L_1 - f/3) \pm$$

$$\pm\,((1 - L_1 - f/3)^2 - 4(1 - f)\,(1 - 2L_1)L_1)^{1/2}]$$

are the frequencies of the surface modes.

Again, we came to the resonance character of EMR absorption in MDS at frequencies Ω_{T1} and Ω_{T2} which is absent in the bulk sample with the dispersion law (15). As it is seen from (18), the absorption spectrum is characterized in this case by two distinguished peaks of about equal width (the peak widths are defined by the attenuation ν) the position and height of which depend essentially on the form of the particle L_1 and dispersion of MDS f.

Presented in Fig.1–6 are the dependences $\tilde{\varepsilon}'(\omega)$ and $\tilde{\varepsilon}''(\omega)$ for some frequency cases. Note that the analysis [18] of the expressions (13) showed that at a decrease of ν and increase of f, the intensity of the peaks on the curve $\tilde{\varepsilon}''(0)$ rises dramatically with their position almost unchanged. The form of particles which is included in (18) via the factor L_1 [1] that may vary from 0 to 1/2 produces a very significant effect on the spectrum of the surface plasmons in MDS.

Thus, in MDS with metallic inclusions, a transformation of the frequency dependence (15) occurs into $\tilde{\varepsilon}(\omega)$ one of the oscillator type with the resonance frequencies corresponding to those of surface modes.

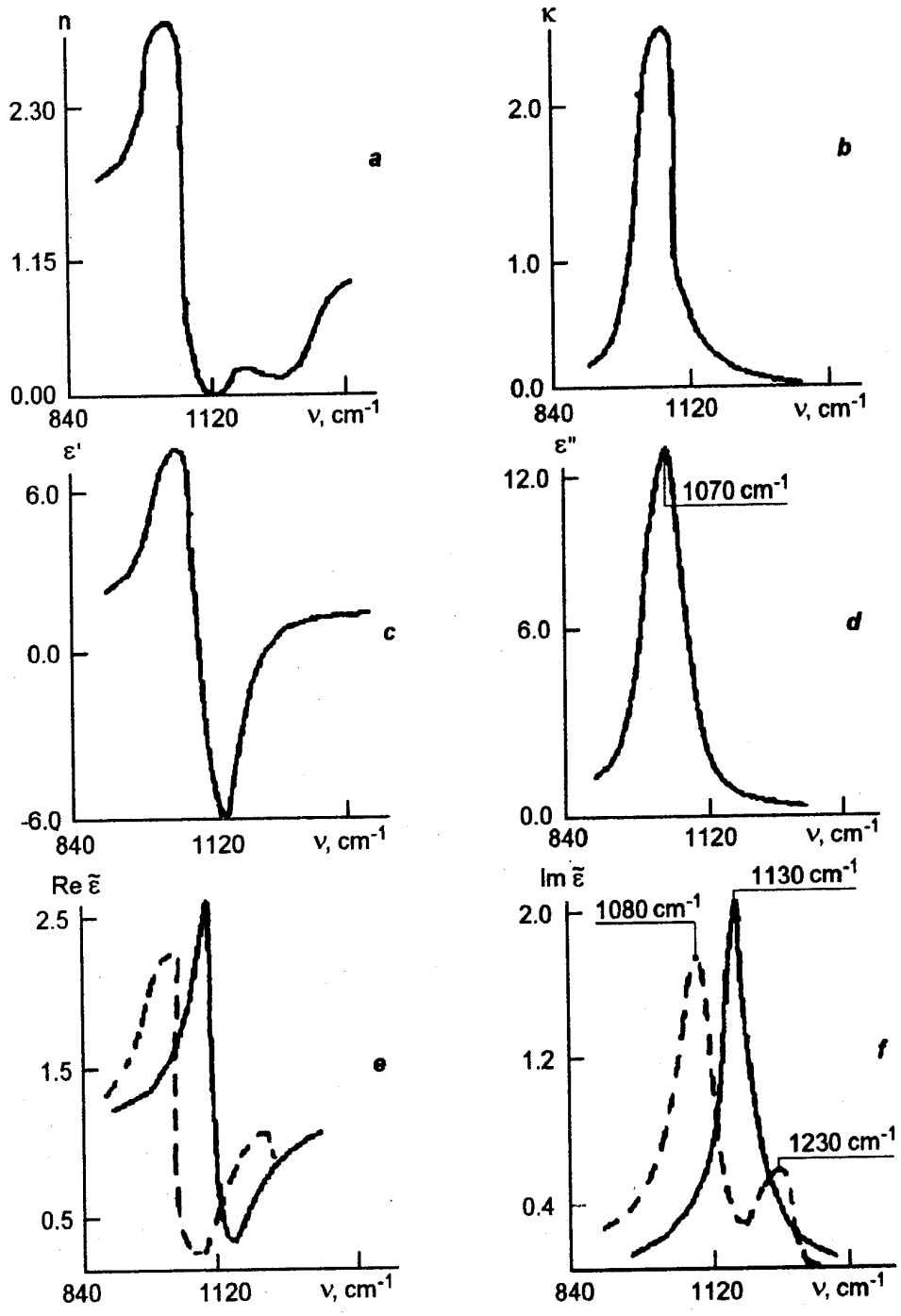

Fig.7. Dielectric properties of the disperse SiO_2 at $f = 0.2$; $L_1 = L_2 = L_3 = 1/3$ (———); $L_1 = L_2 = 0.01$, $L_3 = 0.98$ (– · – · –).

For many substances encountered in practice, the dispersion law $\varepsilon(\omega)$ is determined experimentally and it is difficult to be interpolated in a wide frequency range by some dependence of the type (12). Therefore, in this case, to find the dependence it is necessary to make first of all numeric calculation of $\tilde{\varepsilon}(\omega)$ using the relations from Table 1 or refined relations in the approximation of a multiple scattering [17], using therewith the experimental curves of the $\varepsilon(\omega)$ dependence.

Such a calculation was made for a disperse silicon dioxide (SiO_2) consisting of the particles $\cong$ 10 nm in size in the region of stretching vibration of the bonding Si–O (1070 cm^{-1}). Shown in Fig.7a and Fig.7b are the experimental dependences [21] for the real (n) and imaginary (k) parts of refraction index of a solid sample SiO_2 as well as the dependences $\mathrm{Re}\tilde{\varepsilon}(\omega)$ and $\mathrm{Im}\tilde{\varepsilon}(\omega)$, (Fig.7d and 7e) calculated according to (7) with account for the experimental dependences $n(\omega)$ and $k(\omega)$, for a sphere and compressed ellipsoid (L_1=L_2=0.01, L_3=0.98). The obtained value of the absorption maximum frequency (ω_r) for spheres $\cong$ 1130 cm^{-1} is in a good agreement with the experimental value $\cong$ 1111 cm^{-1} [1].

It follows from the results obtained that using the spectroscopy of the surface modes of small particles in MDS one may in principle determine many parameters of small systems: the degree of filling f (by the height of the peak $\tilde{\varepsilon}''(\omega)$), ellipsoidality of the inclusion particles (by the shift of the peak position and its height), dielectric permittivity of the matrix (also by the shift and height of the peak), etc.

The authors are very grateful to Dr.A.Ya.Blank for useful discussions on the problem of electromagnetic radiation absorption by surface plasmons in disperse media [22].

References

1. C.F.Bohren, D.R.Huffman, Absorption and Scattering of Light by Small Particles, John Wiley and Sons, NY (1983).
2. J.C.Maxwell-Garnett, *Philos.Trans.Roy.Soc.*, **203**, 385 (1904); **205**, 238 (1906).
3. D.A.G.Bruggeman, *Ann.Phys.*, **24**, 636 (1935).
4. L.K.H.Van Beek, *Progress in Dielectrics*, **7**, 69 (1967).
5. V.M.Finkelberg, *Zh.Tekh.Fiz*, **34**, 509 (1964).
6. D.K.Hole, *J.Mater.Sci.*, **11**, 2105 (1976).
7. C.F.Bohren, N.C.Wickramasinphe, *Astrophys.Space Sci.*, **50**, 461 (1977).
8. S.Berthier, *Ann.Phys.*, **13**, 503 (1988).
9. G.A.Nuklasson, C.G.Grangvist, O.Hunderi, *Appl.Opt.*, **20**, 26 (1981).
10. P.O.Neill, A.I.Ignatiev, *Phys.Rev.*, **18**, 6540 (1978).
11. D.-S.Wand, H.C.H.Chen, P.W.Barber, P.J.Wyatt, *Appl.Opt.*, **18**, 2672 (1979).
12. P.Sheng, *Phys.Rev.*, **28**, 6367 (1980).
13. S.Chandrasekhar, Radiative Transfer, Oxford Univ. Press, London (1950), (reprinted by Dover, NY, 1960).
14. A.Ishimaru, Wave Propagation and Scattering in Random Media, Academic Press, NY (1978).
15. N.A.Khiznyak, The Integral Equations of the Macroscopic Electrodynamics [in Russian], Naukova dumka, Kiev (1986).
16. L.G.Grechko, V.V.Motrich, V.M.Ogenko, *Khim.,Fiz.,Tekhnol.Poverkhnosty*, **1**, 17 (1993).
17. L.G.Grechko, V.V.Motrich, V.M.Ogenko, Reprint 90-73P, ITP , Kiev, (1990).
18. L.G.Grechko, V.V.Motrich, V.M.Ogenko, et al., Reprint 90-36P, ITP, Kiev (1973).
19. L.Genzel, T.P.Martin, *Phys.Status Solidi.(b)*, **51**, 91 (1972).
20. L.Genzel, T.P.Martin, *Surf.Sci.*, **34**, 33 (1973).
21. V.M.Zolotarev, *Optika Spektr.*, **29**, 66 (1970).
22. A.Ya.Blank, F.K.Kasumov, A.Ya.Sharshanov, *Fiz. Nizk. Temp.*, **18**, 1048 (1992).

Поглощение электромагнитного излучения поверхностными модами в гетерогенной среде

Л.Г.Гречко, В.Г.Левандовский, В.В.Мотрич, В.Ю.Решетняк

В работе обобщены результаты исследований по взаимодействию электромагнитного излучения (ЭМИ) с широким спектром гетерогенных систем (ГС). Приведены схемы расчета эффективной диэлектрической проницаемости ($\tilde{\varepsilon}$) ГС двух типов: статистических смесей и матричных дисперсных систем (МДС). Полученные результаты использованы для изучения механизмов поглощения ЭМИ в МДС с металлическими включениями сферической и эллипсоидальной формы, обусловленный наличием поверхностных мод. Показано, что в таких системах наблюдается резонансное поглощение ЭМИ на частотах, равных частотам поверхностных мод. Исследован спектральный характер $\tilde{\varepsilon}(\omega)$ в зависимости от параметров МДС.

Functional Materials 2, No.2 (1995)

The role of adsorption phenomena in processes of the metal electrodeposition

Yu.M.Loshkarev

Dnepropetrovsk State University, 72 Gagarin Ave.,
320625 Dnepropetrovsk, Ukraine

The surface-active substances (SAS) influence on different stages of metal electrodeposition processes has been considered. The role of chemical interaction of metal ions with SAS in the kinetics and mechanism of electrode reactions has been investigated systematically. The fundamental mechanisms of SAS influence on initial stages of crystallization and growth of multilayer metal deposits have been established. The SAS action as inhibitors of hydrogen absorption by steel under metal electrodeposition is discussed. The general principles for the choice of SAS, ligands and inorganic compositions of electrolytes for the galvanic technique have been formulated. The main characteristics of new zinc and copper plating processes with optimum combination of technological and ecological features have been shown.

Розглянуто вплив поверхнево-активних речовин (ПАР) на різні стадії процесів електроосадження металів. Систематично досліджена роль хімічної взаємодії іонів металів з ПАР в кінетиці та механізмі електродних реакцій. Встановлені фундаментальні механізми впливу ПАР на початкові стадії кристалізації та ріст полішарових осадів металів. Обговорюється дія ПАР як інгібіторів наводнювання сталі при електроосадженні металів. Сформульовані загальні принципи вибору ПАР, лігандів і неорганічного складу електролітів для нанесення гальванічних покриттів. Приведені основні характеристики нових процесів цинкування та міднення з оптимальним поєднанням технологічних та екологічних показників.

The decisive role of adsorption phenomena of surface-active substances (SAS) in the kinetics and mechanism of the metal electrodeposition is established by many investigations. SAS, being adsorbed on the metal-solution interface, change the conditions of this complex multistage process. Small organic SAS admixtures (from thousandth parts to few grams per liter) to electrolytes are widely used in practice to enhance the structure and working properties of galvanic coatings as well as the electrolysis technologic features (the deposition rate, dissipating ability, etc.).

The theory of the SAS action was developed traditionally as the ever more comprehensive study of their influence on the proper electrochemical discharge act. Therewith, the importance of chemical and crystallization stages was underestimated or ignored at all, though their role in the overall electrode process is also significant. The consideration of the SAS action on several electrodeposition stages under discrimination of corresponding overvoltage components allows to obtain a more comprehensive and impartial picture of the metals cathodic release and to formulate, on that basis, some general principles of technologic control of the galvanic coatings deposition.

Discharge and penetration stages

Most investigation dealing with the SAS influence on the discharge-ionization rate have been performed using the mercury electrode what restricts the possibility of their results application to electrodeposition processes. General statements concerning the inhibiting action dependence on the surface filling degree by SAS, the charge sign of adsorbed and reacting particles, the role of the stage of penetration of metal ions through adsorbed SAS layers [1–3] etc. hold their

validity, however, also for actual conditions of the cathodic metal release.

Main relationships determining the influence of pH, temperature, background anions nature and concentration, and other factors, on the SAS action effectivity at the metal electrodeposition are considered in publications [4–7]. From the viewpoint of the galvanic technique, following results are of most importance.

1. The temperature influence on the admixtures action has been quantitatively studied and critical temperature values corresponding to the disappearance of the additional energetic barrier have been determined. Most of SAS lose their effectivity already at 30–40 °C due to adsorption reduction with temperature increasing. Yet, some organic admixtures have been found to retain their adsorption ability and inhibiting effect at elevated temperatures (polymeric tetraalkyl ammonium salts for the zinc deposition from basic solutions, etc.). Such SAS are of interest not only for the usual galvanic technique but also at the coatings obtaining from low-temperature melts.

2. The dependence of the SAS inhibiting effect on the hydration energy (HE) value of surface-inactive or weakly adsorbing anions (SO_4^{2-}, F^-, ClO_4^-, BF_4^-, etc.) has been established. The SAS inhibiting action on the cadmium, tin, and other metals in the area of the positive surface charge has been shown to be increased sharply with the transition from sulphate solutions to fluoborate, chlorate, and other ones based on anions having small HE values. Admixtures which are ineffective in sulphate-based electrolytes can be used successfully in the cadmium and tin deposition from fluoborate solutions.

3. Surface-active anions of halogens, rhodanide ion, thiourea, and some other thiocompounds have been found to weaken the organic inhibitors effect on the metal cations discharge and enhance the retardation effect if metal ions are bonded into complexes charged negatively.

4. The inhibiting action of SAS forming no complexes with metal cations becomes weaker, as a rule, with the increase of solution pH. When surface complexes of reacting ions with SAS are formed, the retardation increases with the pH increase and becomes particularly significant at pH exceeding pK of the proton addition to a surface-active ligand molecule. The effect of SAS unable to protons addition or splitting out is retained over a wide pH range.

5. The effect of SAS orientation on the kinetics of the metal ions electroreduction has been established and explained. So, the retarding action of alpha napthol in the bismuth ions electroreduction process increases significantly at the transition from horizontal to vertical (or inclined) disposition of adsorbate molecules. The fundamental difference in the effect of thiourea and that of its derivatives (phenyl thiourea, diphenyl thiourea) on the cadmium electrodeposition is due to differences in adsorbed molecules orientation, too.

6. It has been shown that the most strong inhibiting action is exhibited by SAS having great attraction constant a values ($a > 2$) in the Frumkin adsorption isotherm equation or by SAS compositions characterized by strong associative interactions between components (e.g. mixtures of amines with phenols or napthols).

Chemical stages

We have supposed a general approach to consider the inhibiting and accelerating SAS effect taking into account the role of the chemical interaction between metal ions and adsorbed admixtures [8,9]. As a result of such an interaction, the nature of adsorbed particles is changed, and if the complexes being formed are electrically active, the nature of ions being reduced on the cathode undergoes a change, too.

The adsorption of complexes can be inferred by a variation of the double layer differential capacity (C) at the metal ions introduction into indifferent electrolytes containing SAS. So, the adsorption of zinc ion complexes with polyethylene polyamine (PEPA) is manifested by a significant C drop after Zn^{2+} addition to a solution containing PEPA. It is of importance from the viewpoint of the galvanic technique that, at the transition from neutral PEPA particles to its positively-charged complex with Zn^{2+} ions, the adsorption range becomes enlarged towards negative potentials at which the zinc electrodeposition takes place. It is just this circumstance which allows to use polyethylene polyamine successively as the admixture to basic zincing electrolytes.

Surface concentrations (g) of Cd^{2+} and Cu^{2+} complexes with several inorganic and organic ligands have been measured using chronocoulometry, cathodic and anodic chronopotentiometry. The found g values were consistent with those observed usually at the monolayer adsorption.

If reacting ions interact with a SAS under formation of electro-active complexes (EAC), then the electron transfer stage must be preceded by the corresponding chemical reaction. It has been

found, by the chronopotentiometry, that these reactions occur not in a bulk reaction layer, but immediately on the electrode surface involving adsorbed SAS; the rate constants for those reactions have been determined.

The adsorbed EAC formation can result in a acceleration as well in a retardation of discharge, depending on the SAS nature, presence of bridge atoms or groups in their molecules and orientation of those molecules on the surface; in both cases, a surface chemical reaction of metal ions interaction with adsorbed SAS occurs preceding the electron transfer.

If the discharge is hindered due to the surface EAC formation including the reacting ions and SAS, then, the electroreduction can occur also on the outer side of the adsorption layer [10]. It is obviously that this mechanism of the electrode process inhibition may be realized only when the surface is completely filled by surface-active ligands. It is perhaps just such an effect which benzotriazol, fixer DCU and some other SAS have on the copper electrodeposition from sulphate solution.

The metal ions discharge retardation is observed also at the electrically inactive complexes formation with adsorbed SAS; in such systems, precedent chemical reactions take no place (e.g., copper electrodeposition in the presence of sodium diethanol dithiocarbamate).

Thus, basing on the notions about the reacting ions complexing with adsorbed SAS, the accelerating as well as the retarding effect of admixtures on the metal ions discharge can be explained.

Crystallization stages

SAS influence significantly the nucleation process on a foreign surface (initial stages of crystallization) as well as the ensuing growth of polyatomic metal layers [11]. There are only few findings about the SAS effect on the kinetics of initial crystallization stages [11,12].

The interpretation of experimental data concerning the nucleation on foreign electrodes can be based on the nucleation model developed by Markov [13]. The nucleation rate, at a steady distribution of pre-nucleus aggregates in a system, is determined by the simultaneous influence of two factors: the active centers (AC) number limited for a specified oversaturation and the formation of so-called "excluded nucleation " zones (ENZ) around growing nuclei; yet unoccupied active centers are absorbed an eliminated by these expanding zones. After a certain time interval, either the AC depletion or ENZ overlap occurs, both resulting in the attainment of the limiting nuclei number.

We had analysed the cases when admixtures influence preferably only one of the factors mentioned, and two fundamental mechanisms are suggested for the SAS action on the phase formation kinetics [14, 15].

1. The admixture used is not adsorbed essentially on the foreign surface (pyrographite) but is adsorbed strongly on the metal being deposited. Being adsorbed on metal nuclei of a certain size, it inhibits their growth and slows down the development of ENZ forming around growing crystals. Therewith, the number of active AC increases and, ultimately, so does the nuclei number, too. It is polyacryl amide which influences just so the initial stages of copper electrocrystallization from sulphate solutions.

2. The admixture is adsorbed on AC of a foreign surface, thus eliminating them out of the process. So, in the presence of acrylic acid, the AC number of a pyrographite electrode becomes so small that the controlling nucleation stage undergoes a change. The decisive role in the pure concentrated copper sulphate solution belongs to ENZ, while in the electrolyte containing acrylic acid, to AC. At high admixture concentrations AC become completely blocked and the nucleation stops.

The retardation of metal nucleation on foreign electrodes by SAS admixtures manifests itself usually as an increase of the crystallization overvoltage, η_k. Therewith, no correlation exists between η_k and nucleation work, A. So, acrylonitrile (AN) changes η_k insignificantly but causes the triple A increase for the zinc nucleation on pyrographite, while the acrylamide-AN mixture, causing an essential increase of the crystallization overvoltage, leaves A value practically unchanged. The consideration of these experimental data using the equation linking A values with surface tensions on electrode/solution, nucleus/solution, and electrode/nucleus interfaces allows to estimate the SAS adsorption effect on the nucleation work at various interphase boundaries [16].

The SAS influence on crystallization stages at the multilayer metal electrodeposition remains still not adequately investigated, and mechanism of their effect on the electrocrystallization process is yet under discussion. So, the pyrophosphate and selenate anions influence on the copper deposition was explained by an additional retardation of the surface diffusion stage of adatoms preceding their incorporation into growth sites [17]. At the same time, the retardation of the surface dif-

fusion due to the SAS adsorption should cause the electrocrystallization progression according to the mechanism of the direct discharge into incorporation sites. In fact, at the silver electrodeposition under rhodanide anions adsorption, the contribution of the adatoms surface diffusion can be neglected, and it is just the incorporation which becomes the slowed stage [18].

In the course of investigation of the SAS effect on multilayer electrodeposition processes, a combined approach is useful consisting in the study of thin structure and physico-mechanical properties of coatings along with polarization characteristics. The influence of admixtures on proper crystallization stages is most clearly manifested when the discharge and other possible stages (chemical ones, penetration, etc.) are essentially not retarded. The cathodic zinc deposition from the sulphate solution under presence of a mixture of acrylamide (AA) and acrylonitrile is a characteristic example. The SAS mixture causes only slight polarization increase (by 50 mV) while the deposit morphology undergoes radical alteration: mirror-like, bright coatings are deposited in a broad range of current density values (from 30 to 200 A/dm^2). The AA-AN mixture adsorption results in disruption of texture series characteristic for the admixture-free electrolyte: only two growth directions become prevailing over the whole current density range investigated [18]. These effects are due to the admixtures action mainly on the zinc nucleation not involving the retardation of other electrode process stages. Caprolactam, polyacryl amide and its mixture with acrylic acid exhibit a similar effect on the copper electrodeposition from sulphate solutions.

Unusual SAS effects

The polymeric tetraalkylammonium salt (PTAS) differs fundamentally from other SAS in character of its influence on the zinc electrodeposition from an alkaline electrolyte [9].

First, its adsorption and the inhibiting effect on the zinc ions discharge are retained up to strong negative potentials (–2.8 V) which were not attained earlier at all in the water solutions electrolysis.

At such negative E values, the electrochemical insertion of sodium into zinc becomes possible. The hydrogen emission in that potential range is perhaps a result of the destruction of intermetallide formed by water as evidenced by a sharp difference in the admixture action on the hydrogen emission kinetics from the indifferent electrolyte and under electrodeposition conditions.

The possibility of realization of strong negative potentials enables the electrochemical alloying of zinc by electronegative metals and/or by their lower oxides.

Another specific feature is the favourable PTAS influence on the crystallization stages of electrodeposition in the range of the limiting diffusion current (i_{lim}) which allows not only to enhance the coatings quality but also to increase significantly the dissipation characteristic of the electrolyte.

SAS as steel hydrogen absorption inhibitors

The zinc, cadmium, chromium, and some other metals electrodeposition is accompanied by the emission of hydrogen which, in part, is absorbed by the steel support and causes a deterioration of physico-mechanical properties of articles. Some organic brighteners favour to the support hydrogen attack and, what is of specific importance, hinder the hydrogen removal even at a prolonged heat treatment of finished articles. The latter circumstance makes impossible their use in the high-strength steels zincing [20].

At the same time, the properly chosed organic and some inorganic admixtures can assure a significant drop (by 8–10 times and more) of hydrogen content in steel while retaining the high level of its strength and plasticity characteristics. We have showed [21] that hydridization inhibitors must assure the effective hydrogen removal from the surface and, by such a manner, prevent its penetration into the support. In this connection, of special interest are admixtures which are able either to adsorb on a steel surface and to interact chemically with atomic hydrogen (e.g. thiourea derivatives in cadmium deposition, some aldehydes at zincing, high-dispersed metal oxides suspensions in chrome plating) or to accelerate catalytically the recombination of hydrogen (heterocyclic complexes of cobalt, molybdenum, titanium oxides at zincing).

Such mechanism of the hydrogen attack inhibitors action is supported by quantitative analysis of admixtures and their destruction products (thiourea derivatives in the cadmium electrolytes) as well as by thermodynamic (metal oxides in chrome plating) and quantum-mechanical calculations. A good correlation is observed between the lowering of the hydrogen content in steels (ΔH) and parameters characterizing the admixtures ability to interaction with atomic hydrogen, i.e. the electron density on atoms and the chemical bond order (metal oxides, thiourea de-

rivatives) as well as between ΔH and the free valence index characterizing adsorption and catalytic properties (heterocyclic complexes, thiourea derivatives). This allows to choice appropriately the effective hydridization inhibitors using the calculation results only. The possibilities for investigation of hydrogen absorption under electrolysis can be extended substantially by the use of a new method proposed by us to determine separately different hydrogen forms by spectral means [22]. It has been shown for a number of chemical and electrochemical processes (steel dissolution in acid, cathodic hydrogen emission, metal electrodeposition) that the physico-mechanical properties of steel are depended not only on the total hydrogen content, but also on the ratio of its relatively mobile diffusional form (D) and strongly bounded collected (C) one. The latter exerts a decicive effect on the lowering of steel strength characteristics and is therefore the most dangerous, while the plastic properies are better correlated with the total hydrogen content (H_{tot}).

SAS influence not only H_{tot} but, in certain cases, cause a dramatic change of the ratio between D and C hydrogen forms. The compounds allowing to lower "the specific gravity" of the collected form are particularly effective. A polymeric tetraalkyl ammonium salt admixture for the alkaline zincing electrolyte synthetized in our laboratory can be a characteristic example. At relatively high hydrogen content in a steel, the C form amount has been proved to be substantially less than under use of known SAS or their compositions (Limeda NBc, DCTI-150, and others) [23]. It is just this feature which determines the possibility of the deep dehydrogenation of steel articles and regeneration of their physico-mechanical properties.

The control of technological processes of metal electrodeposition

On the basis of concepts described above, the following general principles for the control of galvanic coatings deposition processes have been established [24].

1. In most processes of the metal electrodeposition, efforts should be made not for the maximum retardation of the discharge stage, but for achieving a certain optimum of polarization due to the SAS inhibiting action on several stages of the electrode process. This allows to assure the desired functional properties of coatings in combination with their regular distribution over surface and a sufficiently high deposition rate. The combined use of discharge-inhibiting and discharge-accelerating SAS is an effective way to control the polarization degree.

2. It is advisable to use such SAS mixtures in which some components mainly inhibit the discharge while others influence primary the crystallization stages not changing essentially the polarization degree.

3. The admixtures influencing mainly the crystllization stages are appropriate for use in the hydroelectrometallurgy and in some processes of functional galvanic techniques when the dissipative ability of electrolytes is not a critical requirement (e.g. in tubes, wires, sheets coating under intensive electrolysis modes).

4. In many cases, solutions containing surface-active ligands combine favourably the advantages of simple and comlexing electrolytes, e.g. high deposition rates and dissipative ability values, the fine-crystallic coatings structure, etc., with the absence of electrode passivation in both cathodic and anodic processes.

5. The use of sufficiently high kinetic or diffusion limiting currents in the galvanic techniques is a promising way. The application of agmixtures allowing for the high-quality coatings deposition in the area of limiting currents assures a dissipative ability close to the ideal one and excludes all the limitations concerning the working current density range.

6. As the hydrogen attack inhibitors, substances interacting chemically with the atomic hydrogen or accelerating catalytically its recombination are to be used; therewith, along with reactivity of those admixtures, their adsorption properties must be taken into consideration. It is advisable to use SAS lowering selectively the collected hydrogen content in steels.

We have used these principles in the development, during 1985–94, of a new generation of zincing and coppering electrolytes with the optimum combination of technological and ecological characteristics.

The zincing processes from the alkaline electrolytes have found the widest industrial use. The zincing electrolyte containing the polymeric tetraalkyl ammonium salt admixture called LV 4584 designated for coating of complex-profile articles assures the deposition of high-quality, middle-bright zinc coatings over a very wide current density range (0.1–50 A/dm^2) with exceedingly high dissipative ability values (75–95 % as measured by Mohler method). The LV 4584 admixture is absolutely stable in alkaline medium, electrochemically inert, non-toxic (hazard class III); its industrial production has been mastered.

The electrolyte is used in many Ukrainian enterprises.

The use of a new modification of that admixture, LV 8490, assures an additional lowering of the support hydrogen attack (by several times) and so the retainment of initial physico-mechanical steel characteristics what is of specific importance in the zincing of special articles for aviation and some other areas of use. The ecological characteristics are also enhanced, the LV 8490 admixture has the hazard class IV.

It has been shown that the corrosion resistance and other functional characteristics of zinc coatings can be enhanced substantially by the electrochemical alloying [25] with iron, nickel, cobalt, lead, or lower molybdenum oxides (see Table). The zinc coatings doped by aluminium are

Table.

Alloy	Gain in coating functional properties
Zn–Mo (0.05–0.6 % Mo)	Lowering of steel hydrogen absorption level at the zincing
Zn–Mo (0.2–0.6 % Mo)	Enhanced corrosion resistance
Zn–Fe (10–17 % Fe) Zn–Ni (9–10 % Ni) Zn–Co (0.83–3.8 % Co) Zn–Al (0.06–0.09 % Al)	Enhanced corrosion resistance in neutral media
Zn–Pb (0.8–1.5 % Pb)	Lowering of the coating self-dissolution in the acid medium (0.01 M HCl) by 10–20 times

first deposited from aqueous solutions.

Therewith, the primary advantages of basic zincate solutions containing LV 4584 and LV 8490 are retained, i.e. the high dissipative ability, wide working current density and temperature ranges, low organic admixtures consumption rates, etc. In the Zn–Fe, Zn–Ni, Zn–Co, and Zn–Pb coatings deposition, both the basic and alloying metals are released under limiting current conditions what assures the alloys composition constancy over a wide range of i values (2–15 A/dm^2).

In 20 Ukrainian enterprises, the sulphate electrolytes containing admixtures of "Midel" series are in use; these compositions are designated for the multilayer and double-side printed circuits coppering and for the bright underlayer deposition onto chemical copper or nickel before the subsequent chroming, nickeling, or silvering. The coatings toning for simulation of brass, gold, or old bronze is possible. In the use of those electrolytes for the printed circuits production, the high level of physico-mechanical coating properties is guaranted (relative elongation, tensile strength limit, ductility) competitive with that of foreign analogues. The high resistance of copper deposits against cyclic thermal shocks is the specific feature of the process. Admixture "Midel GS-1" and "Midel GS-2" can be used for the bright decorative coppering instead of foreign composition BS-1, Limeda L-2a, etc. The admixtures are nontoxic (hazard class IV); the use of diluted (in relation to copper ions) electrolytes is possible. The industrial production of brightening admixtures for coppering electrolytes has been pioneered in Ukraine.

References

1. M.A.Loshkarev, *Dokl. AN SSSR*, **72**, 724 (1950).
2. A.N.Frumkin, *Dokl. AN SSSR*, **85** 373 (1952).
3. Electrode Processes in Organic Compounds Solution [in Russian], B.B.Damaskin, Editor, Moscow Univ. Publ., Moscow (1985).
4. Yu.M.Loshkarev, *Zashchita metallov*, **8**, 163 (1972)
5. Yu.M.Loshkarev, *Elektrokhimia*, **13**, 1020 (1977).
6. M.A.Loshkaryov, Yu.M.Loshkaryov, *Surface technology*, **6**, 397 (1978).
7. Yu.M.Loshkarev, *Galvanotekhnika i obrabotka poverkhnosti*, **1**, No.5–6, 7 (1992).
8. Yu.M.Loshkarev, V.F.Vargalyuk, in: Modern Aspects of the Electrochemical Kinetics [in Russian], (Tbilisi, 1980), Mitsneereba Publ., Tbilisi (1980), p.123.
9. Yu.M.Loshkarev, V.F.Vargalyuk, A.Yu.Pikelny, in: Double Layer and Adsorption on Solid Electrodes [in Russian], Tartu (1981), p.225.
10. E.Muller, H.Emous, H.Dorfler et al., *J.Electroanalyt.Chem.*, **142**, 39 (1982).
11. V.V.Trofimenko, Yu.M.Loshkarev. *Elektrokhimia*, **30**, 150 (1994).
12. Yu.M.Polukarov, Adv. in Sci. and Techn., Electrochem. Ser. [in Russian], VINITI Publ., Moscow (1979), No.15, p.3.
13. J.Markov, *Thin Solid Films*, **35**, 11 (1976).
14. V.V.Trofimenko, V.P.Zhitnik, Yu.M.Loshkarev, T.G.Aleksandrova, *Elektrokhimia*, **16**, 1139 (1980).
15. V.V.Trofimenko, V.P.Zhitnik, Yu.M.Loshkarev, T.G.Aleksandrova, *Elektrokhimia*, **17**, 1644 (1981).
16. V.V.Trofimenko, V.S.Kovalenko, G.P.Litovka. Yu.M.Loshkarev, *Elektrokhimia*, **15**, 1644 (1979).
17. E.E.Yuzyalunas, I.Yu.Kamuntavichene, V.AKatkute, R.P.Slizhis, *Tr. AN LitSSR, Ser.B*, **2(153)**, 26 (1986).
18. V.V.Trofimenko, G.P.Litovka, Yu.M.Loshkarev, *Ukr. khim. zhurn.*, **44**, 592 (1978).
19. Yu.M.Loshkaryov, V.M.Blinov, L.Yu.Gnedenkov, V.V.Trofimenko, in 31th Intern. Congress of Pure and Applied Chemistry, Bulgaria, Sofia (1987), **3**, p.770.

20. V.N.Kudryavtsev, *Zhurn. Vsesoyuzn. khim. Obshch. im.D.I.Mendeleeva*, **33**, No.3, 289 (1988).
21. A.N.Baturin, Yu.M.Loshkarev, in: Proc. of 37th Conf. of Intern. Electrochem. Soc. [in Russian], Vilnius (1981), **2**, p.25.
22. A.N.Baturin, Yu.M.Loshkarev, *Fiz.-khim. mekhanika materialov*, No.2, 47 (1991).
23. A.N.Baturin, Yu.M.Loshkarev, Metal Corrosion under Voltage and Protection Methods [in Russian], Lvov (1989), p.288.
24. Yu.M.Loshkarev, *Galvanotekhnika i obrabotka poverkhnosti*, **2**, 36 (1993).
25. Yu.M.Loshkarev, V.I.Korobov, V.V.Trofimenko, F.A.Chmilenko, *Zashchita metallov*, **30**, 79 (1994).

Роль адсорбционных явлений в процессах электроосаждения металлов

Ю.М.Лошкарев

Рассмотрено влияние поверхностно-активных веществ (ПАВ) на различные стадии процессов электроосаждения металлов. Систематически исследована роль химического взаимодействия ионов металлов с ПАВ в кинетике и механизме электродных реакций. Установлены фундаментальные механизмы влияния ПАВ на начальные стадии кристаллизации и рост полислойных осадков металлов. Обсуждается действие ПАВ как ингибиторов наводороживания стали при электроосаждении металлов. Сформулированы общие принципы выбора ПАВ, лигандов и неорганического состава электролитов для нанесения гальванических покрытий. Приведены основные характеристики новых процессов цинкования и меднения с оптимальным сочетанием технологических и экологических показателей.

Functional Materials **2**, No.2 (1995)

Galvanomagnetic and magneto-optical properties of Tb/Fe multilayers

E.Shipil', A.Pogorily, L.Uba* and S.Uba*

Institute of Metal Physics, National Academy of Sciences of Ukraine, 36 Vernadsky St., 252142 Kiev, Ukraine

*Institute of Physics, Warsaw University Branch in Bialystok, 41 Lipova, 15-424 Bialystok, Poland

Transverse Kerr-, Faraday- and spontaneous Hall-effects have been investigated for sets of Tb–Fe samples: amorphous Tb_xFe_{1-x} ($0<x<1$) films and three series of Tb/Fe multilayers. Using comparative analysis of these effects, magnetic properties of Tb/Fe interface are studied. It is shown that spontaneous Hall coefficient attributed to spin-orbital interaction has its maximum value $2.4 \cdot 10^{-4}$ μΩ·cm/Gs in the interface with effective composition near to room temperature compensation composition. This value is approximately one order lower than the same coefficient in amorphous set.

Вимірювались екваторіальний ефект Керра, ефект Фарадея та аномальний ефект Холла у чотирьох серіях зразків: серії аморфних плівок Tb_xFe_{1-x} ($0<x<1$) та трьох серіях багатошарових плівок Tb/Fe. Використовуючи порівняльний аналіз результатів вимірювань ефектів, вивчалися магнітні властивості міжшарової межі. Показано, що коефіцієнт аномального ефекту Холла, обумовлений спін-орбітальною взаємодією, проявляє своє максимальне значення $2.4 \cdot 10^{-4}$ мкОм·см/Гс у міжшаровій межі з ефективним складом, близьким до складу компенсації при кімнатній температурі. Це значення приблизно на порядок величини нижче значення для того ж коефіцієнту в аморфній серії.

Introduction

Existence of relationship between Faraday rotation and Hall effect in amorphous rare-ears-transition metal alloy was shown [1–3]. The spin-orbit interaction of the polarized conduction electrons gives rise to a Hall current perpendicular to the magnetization. Many studies have been devoted in the last years to artificially layered materials. They are interesting both for applications and for possibility to realize structures with different physical interactions. Recently, the possibility was shown [4] to separate contributions of the main films and interfaces of multilayers (MLs) in their magneto-optic dependencies. In this report, we present the study of MLs magnetic properties by comparative analysis of magneto-optical effects (MOE) and spontaneous Hall effect (SHE), taking advantage of the fact that the last one has some features strongly dependent on the magnetic state of the interface. We try here tocompare galvanomagnetic properties of the interface to the properties of amorphous series.

Experiment

The set of amorphous films Tb_xFe_{1-x} ($0<x<1$) (AF) and three series of Tb/Fe MLs with the three fixed thicknesses of Fe layer (one for each series) d_{Fe}= 25, 15 and 8 Å, and the same thicknesses of Tb layers, d_{Tb}= 5, 10, 16, 23, 31, 40 Å for all series were prepared. All samples were electron-beam evaporated from two independent sources in vacuum conditions without oil at a pressure no more than 10^{-7} Torr at room temperature onto glass and quartz for magnetooptical measurements and through the special mask onto ceramics for Hall effect ones, respectively. The instantaneous rates were controlled independently for Tb and Fe with quadruple mass-spectrometer and with two quartz crystal

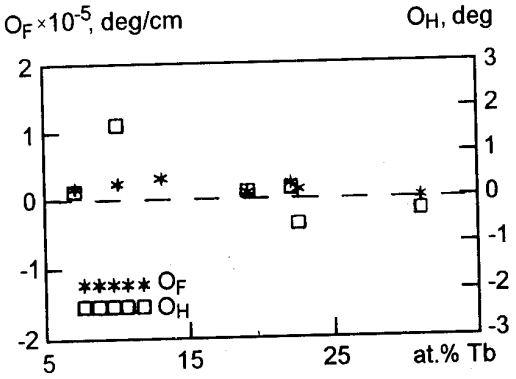

Fig.1. The Faraday rotation and Hall angle on concentration of Tb for Tb_xFe_{1-x} series.

monitors during evaporation. The total thickness of the films in amorphous set was 120 nm, of MLs, 80–90 nm.

The crystallographic structure of the films was examined by the standard diffraction and that of the layered structures by small-angle X-ray diffraction, respectively. All measurements were done at 300 K. Magnetization was measured by vibrating sample magnetometer. Magnetooptical measurements were performed in the reflection (Transverse Kerr effect, TKE) and transmission (Faraday effect) regimes. Magnetooptical loops were measured in the magnetic field up to 22 kOe at the He–Ne laser wavelength ($\lambda = 0.63\mu$). Magnitudes of TKE effect were measured as a function of $H_{||}$ up to 10 kOe. Substrata contribution to the Kerr and Faraday rotation was subtracted. SHE and resistivity were measured using the 4-contact technique by the dc-method in the fields up to 10 kOe.

Experimental results

A characteristic amorphous X-ray diffraction pattern with no crystalline reflections could be observed for sample compositions $0<x<0.50$ of I series. The layers thicknesses in MLs were chosen in such a way all of them to be amorphous [5] and it was confirmed by X-ray analysis. For the three series of MLs, small-angle X-ray diffraction patterns show that films have periodic structure.

The Faraday rotation and Hall angle for Tb_xFe_{1-x} are plotted in Fig.1. Both data being quite correlated slowly decrease with Tb concentration. Nevertheless, some difference can be noticed — the Faraday rotation has only positive sign in the whole range of concentrations while Hall angle changes the sign exactly at the room temperature compensation composition (rtcc).

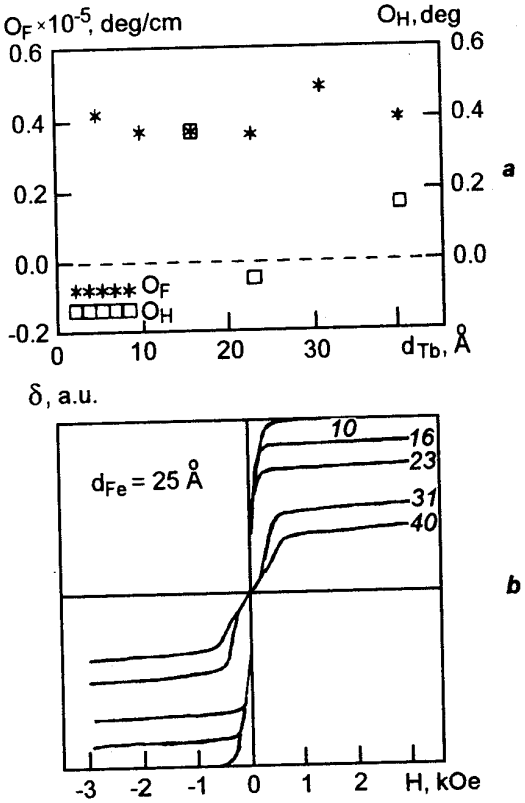

Fig.2. The Faraday rotation and Hall angle for Tb/Fe MLs with $d_{Fe} = 8$ Å (a) and magnitudes of TKE effect, δ, as a function of in-plane field, $H_{||}$, for the same set (b). Dependences δ–$H_{||}$ in Fig.2b, 3b, 4b are mirror-reflected in the negative region for convenience.

Strong correlation between the Faraday effect and the SHE had been observed in [1] and the model had been presented where the Faraday rotation in amorphous alloys was attributed to an interaction of polarized light with the Hall-effect conduction electrons. We shall not analyze here this model in details, but only use it to study interface in MLs.

The dependences of Faraday rotation and Hall angle on d_{Tb} for Tb/Fe MLs with $d_{Fe} = 25$ Å are plotted in Fig.2a. Magnitudes of TKE-effect, δ, as a function of in-plane field, $H_{||}$, for the same set are shown in Fig.2b. Here, $\delta = \Delta I/I$, where I is intensity of the incident light; ΔI is the change of the p-plane polarized reflected light intensity due to the magnetizing of film. The character of these dependences is generally determined by the strong background of Fe-region though interface begins to reveal itself, too. So, increases of d_{Tb} from 10 to 23 Å decreases the change of the TKE inten-

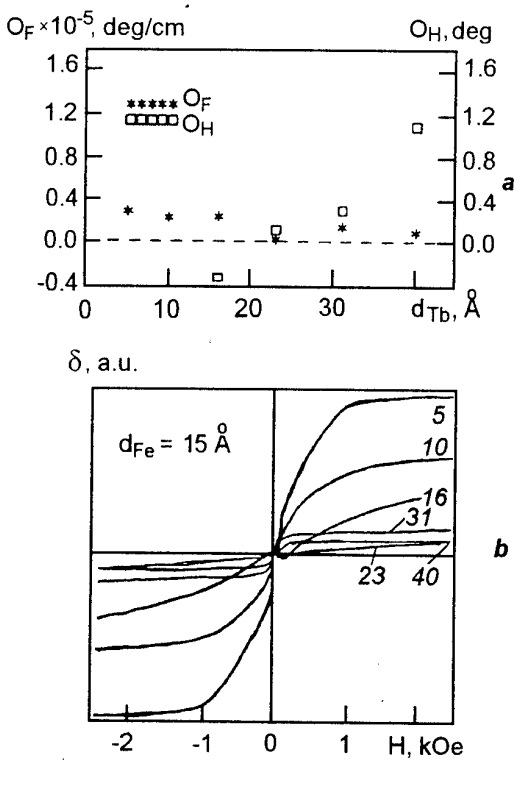

Fig.3. The Faraday rotation and Hall angle for Tb/Fe MLs with d_{Fe} = 15 Å (a) and magnitudes of TKE effect, δ, as a function of in-plane field, $H_{\|}$, for the same set (b)

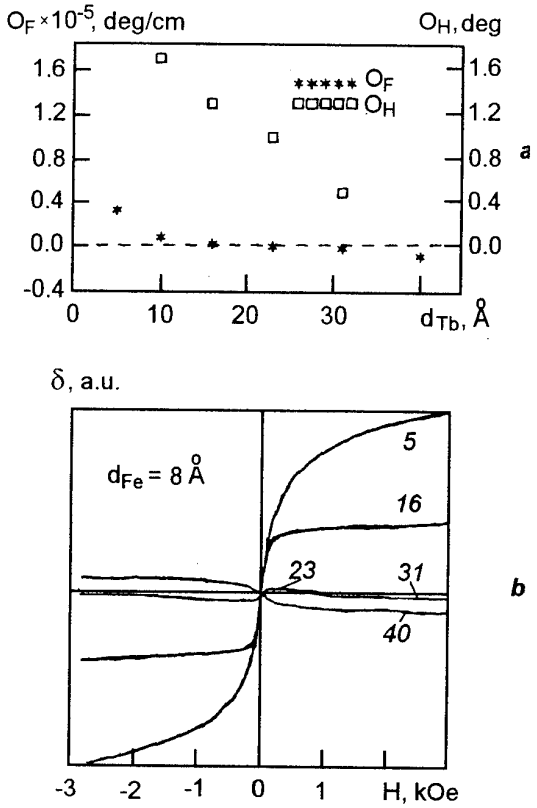

Fig.4. The Faraday rotation and Hall angle for Tb/Fe MLs with d_{Fe} = 8 Å (a) and magnitudes of TKE effect, δ, as a function of in-plane field, $H_{\|}$, for the same set (b)

sity. Meanwhile, the character of the Fe-dependence remains. Increase of d_{Tb} to 31 and 40 Å changes significantly the form of TKE dependence at low fields what can be supposed as the manifestation of the interface effect. Then we can assume that the character of the Hall-dependence at d_{Tb} > 20 Å is determined by interface.

A similar data set for MLs with d_{Fe} = 15 Å is shown in Fig.3a and Fig.3b. TKE dependences show that interface contribution increases. Starting with the film where d_{Tb} = 5 Å, the interface effect reveals itself in the form of 'break' at low fields in the films with d_{Tb} = 5 and 10 Å. In the film with d_{Tb} = 16 Å, one can clearly see the δ–$H_{\|}$ dependences separately in the Fe layer at the fields higher than 1 kOe and in the interface at low fields. In the first case, the intensity variation is significantly decreased by Tb-layer influence. In the second case, the effect has negative sign. Hall angle in this film has negative sign, too (Fig.5a). At the further increasing of d_{Tb}, the difference between effect of Fe-layer and interface on δ–$H_{\|}$ dependences disappears and at last, in the films with d_{Tb} = 31 and 40 Å, the interface influence reveals itself independently. So, we can conclude that the character of the Hall-dependence in Fig.3a is determined by interface.

Data for MLs of the last set (d_{Fe} = 8 Å) confirm that it is just the interface which makes the main contribution into the general picture of magnetization (Fig.4a,b). Already in the film with d_{Tb} = 16 Å, one can notice saturation in δ–$H_{\|}$ dependences at low fields. The further increasing of d_{Tb} causes the strong decrease of the change in transverse Kerr effect intensity. In the films with d_{Tb} = 31 and 40 Å, one can even observe the change of the effect sign, too.The negative sign of Faraday effect in these films supports conclusion concerning the main contribution of the interface in these set of MLs. So, the character of the Hall-dependence in Fig.4a is also determined by interface.

In Fig.5, the SHE loops are shown for two MLs: for 15Fe/16Tb (a) and for 8Fe/10Tb (b). It

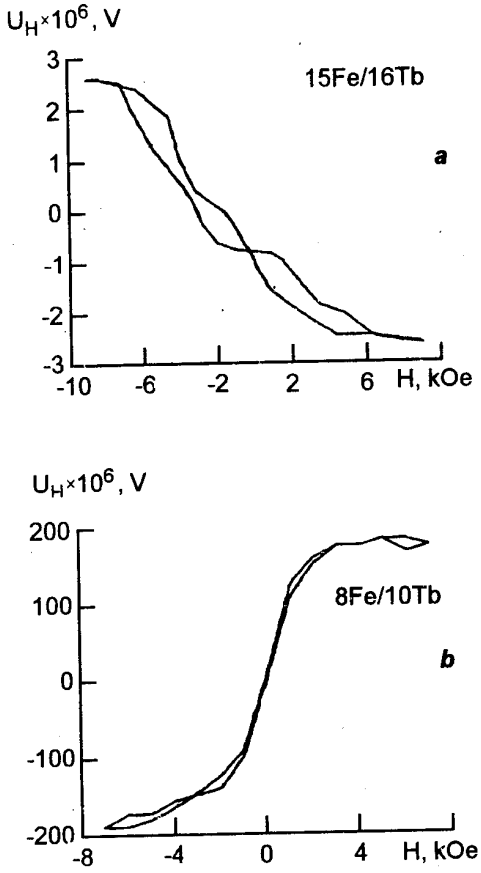

Fig.5. SHE-loops for two MLs: 15Fe/16Tb (a) and 8Fe/10Tb (b)

can be affirmed that there are the loops of interfaces. The complex loop in Fig.5a is the result of the summation of different interfaces in this ML, which are not almost the same and have slightly different individual loops [6]. The SHE loop for 8Fe/10Tb ML (Fig.5b) is less complex, since interfaces in this ML are almost the same. It must be emphasized that Fe atoms are dominant in these interfaces, since the sign of Hall voltage, U_H, is positive contrarily to the interfaces in 15Fe/16Tb ML where SHE is determined by Tb atoms [7].

Discussion

Let us consider Fig.2, 3 and 4 and analyze the SHE dependences in interfaces of MLs. One can see that, at decreasing of d_{Fe} and increasing of d_{Tb}, Hall-angle, Θ_H, increases up to a certain point $\Theta_H \cong 1.7$ deg. and then begins to drop.

Fig.6 and Fig.7 show dependences of resistivity, ρ, and Hall resistivity, ρ_H, respectively, at interface building in the cases of Fe excess

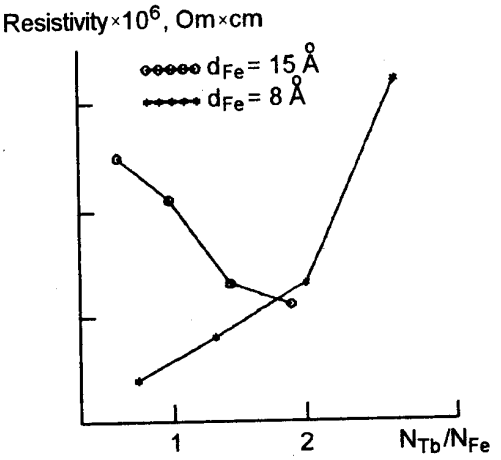

Fig.6. Dependences of resistivity, ρ, on N_{Tb}/N_{Fe} — the ratio of Tb- and Fe-monolayers, participating in interface in the cases of Fe excess (d_{Fe} = 15 Å) and Tb excess (d_{Fe} = 8 Å).

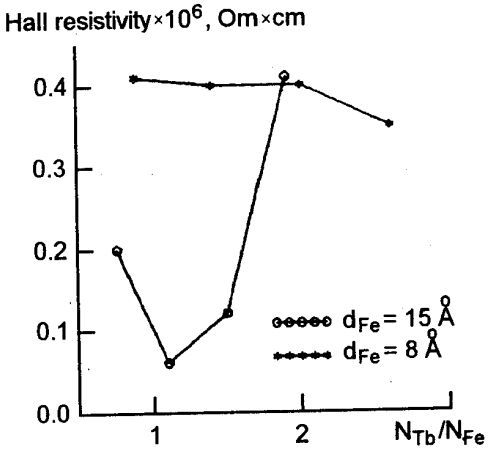

Fig.7. Dependences of Hall resistivity, ρ_H, on N_{Tb}/N_{Fe}

(d_{Fe} = 15 Å) and Tb excess (d_{Fe} = 8 Å). It can be seen that, during the interface building, the values of ρ and the character of $\rho(N_{Tb}/N_{Fe})$ dependences for these series are different, but when the building of interface is finished, data of ρ for both series (d_{Fe} = 15 and 8 Å) are quite close (Fig.6). The same can be said as to ρ_H (Fig.7). The magnitude of resistivity is determined by the quantity of Tb atoms, meanwhile, the Hall-scattering is determined by Fe atoms.

The main data on interfaces are shown in the Table 1. The data for amorphous series are also shown there for comparison. The maximum value of spontaneous Hall coefficient, R_s, is obtained in ML 8Fe/23Tb, in which interface is

Table 1.

Data on Tb–Fe amorphous films

Tb, at. %	M_s, Gs	$\rho_{H/\rho}$, %	Θ_H, deg	R_s, μΩ · cm/Gs
7	1600	0.36	0.20	$7.9 \cdot 10^{-5}$
10	830	2.90	1.67	$3.3 \cdot 10^{-4}$
13	100	-	-	$3.8 \cdot 10^{-3}$
19	50	0.31	0.18	$1.5 \cdot 10^{-3}$
22	30	0.43	0.25	$3.2 \cdot 10^{-3}$
22.5	70	–0.98	–0.55	$3.4 \cdot 10^{-3}$
31	80	–0.25	–0.25	$6.0 \cdot 10^{-4}$

Data on Tb/Fe multilayers

Fe/Tb, Å /Å	M_s, Gs	$\rho_{H/\rho}$, %	Θ_H, deg	R_s, μΩ · cm/Gs	N_{Tb}/N_{Fe}
15/16	150	–0.57	–0.33	$1.1 \cdot 10^{-4}$	0.76
15/23	210	0.19	0.12	$2.3 \cdot 10^{-5}$	1.10
15/31	240	0.52	0.30	$4.0 \cdot 10^{-5}$	1.48
15/40	220	1.95	1.10	$1.5 \cdot 10^{-4}$	1.90
8/10	430	2.93	1.70	$7.6 \cdot 10^{-5}$	0.88
8/16	180	2.22	1.30	$1.8 \cdot 10^{-4}$	1.40
8/23	130	1.74	1.00	$2.4 \cdot 10^{-4}$	2.00
8/31	180	0.83	0.48	$1.5 \cdot 10^{-4}$	2.63

already built, $R_s = 2.4 \cdot 10^{-4}$ μΩ cm/Gs. This value is approximately one order lower than the same coefficient in AF. The values of tan $\Theta_H = \rho_H/\rho$ for amorphous films and for the interface of MLs can be compared to that value for pure iron, tan $\Theta_H = \rho_H/\rho = 1.4 \cdot 10^{-2}$ [8]. For the interface in ML 8Fe/23Tb this value is quite close, $\rho_H/\rho = 1.74 \cdot 10^{-2}$, while in amorphous series the nearest value corresponds to composition 10 at%Tb. It means that when the interface is essentially built, mainly Fe atoms determine the scattering in magnetic field.

It is known [8] that R_s can be expressed as

$$R_s = a\rho + A\rho^2$$

where a and A are the constants of proportionality, which characterize asymmetric scattering and side jump mechanism of scattering, respectively.

In Fig.8, we plot R_s/ρ against ρ for amorphous series (Fig.8a) and for MLs with $d_{Fe} = 8$ Å (Fig.8b). One can see that, in both cases, experimental points does not lay on the straight line, but their distributions are almost the same. It can

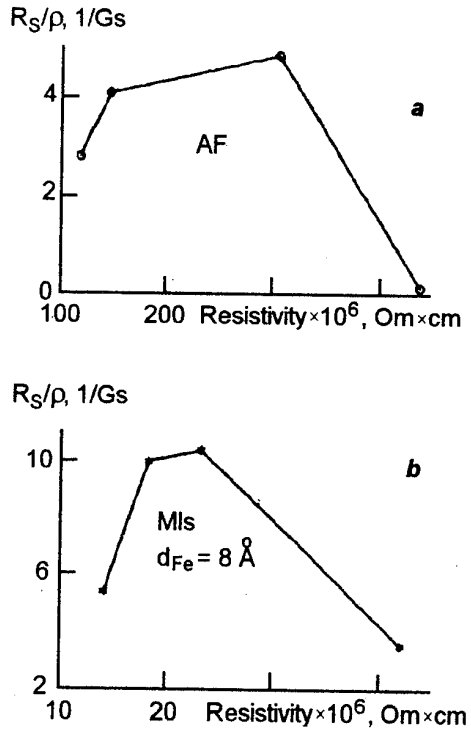

Fig.8. R_s/ρ is plotted vs ρ for amorphous series (a) and for MLs with $d_{Fe} = 8$ Å (b)

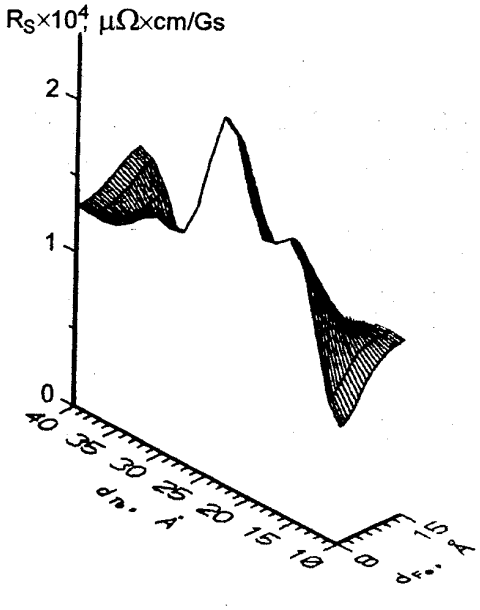

Fig.9. Distribution of SHE coefficient in Tb/Fe interface.

be concluded that neither a nor A are nonzero, that means the presence of asymmetric scattering and side jump mechanism of scattering in amorphous films and in the interface of MLs as well. Unfortunately, these experimental data does not permit to evaluate coefficients a and A neither for amorphous films nor for the interface of MLs.

On the other hand, experimental data obtained in this study permit to draw distribution of SHE coefficient in Tb/Fe interface, which is seen to have wave-interference nature and is shown in Fig.9.

Conclusions

Analysis of three sets of TKE data for MLs permits to separate the contribution of the interface on the background of the whole signal. Comparative analysis of Faraday- and SHE-data for these MLs permits to conclude: I) Spontaneous Hall coefficient which comes from an asymmetric scattering and side jump mechanism of the carriers scattering by the magnetic atoms and attributed to spin-orbital interaction has wave-interference nature of distribution in Tb/Fe interface with its maximum value $2.4 \cdot 10^{-4}$ μΩ cm/Gs in the interface with $N_{Tb}/N_{Fe} = 0.3–0.5$, where N_{Tb}/N_{Fe} is the ratio of Fe and Tb monolayers participated in Tb–Fe interaction; II) The effective composition of such an interface is near to room temperature compensation composition for AF; III) This value of R_s is approximately one order lower than the same coefficient in AF.

Acknowledgment

We are grateful to O.Kuz'mak for experimental assistance.

References

1. M.Hartman, T.R.McGuire, *Phys.Rev.Let.*, **51**, 1194 (1983).
2. T.R.McGuire, R.J.Gambino, A.E.Bell and G.J.Sprokel, *JMMM*,**54-57**, 1387 (1986).
3. R.J.Gambino, T.R.McGuire, *JMMM*, **54-57**, 1365 (1986).
4. E.Shipil', A.Pogorily, L.Uba, S.Uba, *Ukr.J.Phys.*, **39**, 34 (1994).
5. O.M.Kuz'mak, E.V.Shipil', V.I.Shevchenko and S.Ya.Kharitonski, *Ukr.J.Phys.*, **36**, 584 (1991).
6. G.Peral, J.M.B.Ndjaka, D.Givord and J.L.Vicent, *JMMM*, **10-107**, 1755 (1992).
7. T.R.McGuire, R.J.Gambino and R.S.Taylor, *IEEE Trans.Mag.*, **MAG-13**, 1598 (1977).
8. A.K.Majumdar and L.Berger, *Phys.Rev.B.*, **7**, 4209 (1973).
9. A.Ogawa, T.Katayama, M.Hirano and T.Tsushima, *Jap.J.Phys.*, **15**, 575 (1976).

Гальваномагнитные и магнито-оптические свойства многослойных пленок Tb/Fe

Е.В.Шипиль, А.Н.Погорелый, Л.Уба, С.Уба

Измерены экваториальный эффект Керра, эффект Фарадея и аномальный эффект Холла в четырех сериях образцов: серии аморфных пленок Tb_xFe_{1-x} ($0<x<1$) и трех сериях многослойных пленок Tb/Fe. Используя сравнительный анализ измеренных эффектов, изучались магнитные свойства межслойной границы. Показано, что коэффициент аномального эффекта Холла, связанный со спин-орбитальным взаимодействием, проявляет свое максимальное значение $2.4 \cdot 10^{-4}$ мкОм·см/Гс в межслойной границе с эффективным составом вблизи состава компенсации при комнатной температуре. Это значение примерно на порядок ниже значения для того же коэффициента в аморфной серии.

Functional Materials **2**, No.2 (1995)

Surface treatment effect on electromigration stability of oxide high-T_c superconductors

M.A.Tanatar, V.S.Yefanov, A.I.Akimov* and A.P.Chernyakova*

Institute for Surface Chemistry, National Academy of Sciences of Ukraine, 31 Nauki Ave., 252650 Kiev, Ukraine

*Institute of Solid State and Semiconductor Physics, Belorussian Academy of Sciences, 17 P.Brovki St., 220726 Minsk, Belorus

Electromigration stability of $Tl_2Ba_2CuO_{6+x}$ ceramics was shown to decrease notably when the material is treated in water vapor atmosphere. It has been shown that the T_c decrease in these samples is accompanied by the resistance increase, while Seebeck coefficient S remains unchanged. This allowed us to conclude that the main effect comes from grain boundary degradation under the current action. For the initial samples, the electromigration stability depends strongly on the sample doping level and is increased for the materials with higher oxygen content. The effect is supposed to be due to the filling of interstitials in Tl–O layers by oxygen atoms.

Показано, що стабільність кераміки $Tl_2Ba_2CuO_{6+x}$ у процессі електроміграції суттєво зменшується, якщо матеріал витримати в атмосфері водяних парів. Для таких зразків характерно зменшення T_c та збільшення електричного опору, при цьому коефіцієнт термо-е.р.с. S залишається незмінним. Зроблено висновок, що головною підставою для цього є деградація границь зерен під дією електричного струму. Для вихідних зразків електроміграційна стабільність значною мірою залежить від рівня легування і зростає в матеріалах з більш високим вмістом кисню. Припускається, що цей ефект пов'язаний із заповненням вакансій у Tl–O шарах атомами кисню.

Introduction

Oxide high-T_c superconductors are known to be metastable compounds and to degrade quickly under the influence of the ambient factors, mainly water vapor and carbon dioxide, different chemical reagents and thermal cycling [1,2]. Rajan et al. [3] have shown that the compounds may degrade under the long-term high density current flow as well, and the General Physics Institute group have shown that the phenomenon of the electromigration proceeds even under superconducting current [4]. Recently, Mitin et al. [5] have shown that by the electromigration treatment at the liquid nitrogen temperature it is possible to increase essentially T_c for $Tl_2Ba_2CuO_{6+x}$ compound.

It is known that at low temperatures ($T < 0.5T_m$, T_m is melting point for material) the main path for ion movement in metals is formed by the grain boundaries [6]. That is why it may be of interest to study grain boundary treatments effect on electromigration process in the oxide high-T_c superconductors.

In this article we report the electromigration studies in $Tl_2Ba_2CuO_{6+x}$ compound at room temperature. The reasons to choose the compound were (*i*) very high sensitivity of its T_c and normal state properties to oxygen stoichiometry [7,8], (*ii*) the possibility to obtain overdoped materials with bipolar conductivity and thus to study electron wind effects, and (*iii*) the lack of the stoichiometric vacancies in the Tl–O layers, contrary to the $YBa_2Cu_3O_{7-x}$, able to promote accelerated ion movement.

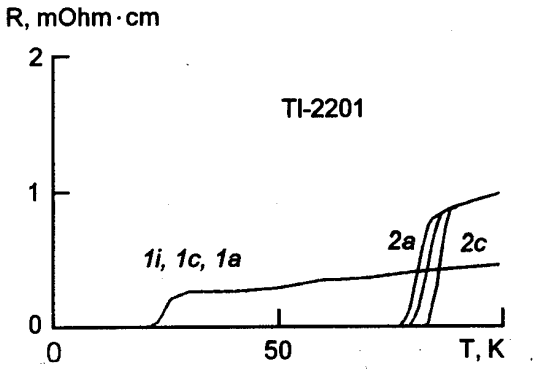

Fig. 1. Resistance vs temperature curves for $Tl_2Ba_2CuO_{6+x}$ samples: (1) as obtained and (2) heat treated in argon at 670 K. The notations *i,c* and *a* refer to initial sample and cathode and anode regions of current-treated sample, respectively.

Experimental

High density ceramics obtained by two-stage solid state reaction was used in the studies. The samples were obtained by mixing $BaCuO_3$ and CuO in 1:1 molar ratio and sintering the mixture at 1123 K for 2 hours. The product was grinded, mixed with Tl_2O_3 in 1.4:1 molar ratio, pressed into the pellets 16 to 20 mm in diameter and sintered at 1123 K for 8 hours in the oxygen flow [9]. Sample bars with typical $10\times0.3\times0.1$ mm^3 dimensions were cut from the pellets and used in the studies. Samples as obtained (1*i*, hereafter) had superconducting transition temperature T_c 20±0.5 K. To obtain higher T_c the samples were annealed at 620–670 K for 6 to 12 hours in the argon atmosphere. Samples so treated (2*i*, hereafter) had T_c of 82±0.5 K (see Fig. 1). Resistivity ρ for the both samples was in the range 1 to 3 mOhm·cm. Some of the 1*i* and 2*i* samples were exposed in saturated water vapor at room temperature for 48 hours. Before this treatment, the vessel with the sample was pumped to exclude carbon dioxide effect, after the removal from the vessel the sample was dried by heating to 373 K in vacuum for 15 minutes. The samples obtained (hereafter H1*i* and H2*i* for 1*i* and 2*i*, respectively) had the same T_c as initial ones, but their resistivity increased typically by 5 to 10 percent. 8 Ohmic indium contacts were alloyed by ultrasonic soldering procedure along the sample length, contact resistances were typically below 0.1 Ohm. DC current of 0.2 to 2 A was passed through the sample, the voltage drop at the inner contacts was controlled and the current had been regulated in such a way that the sample temperature increase, determined from the resistance change, was always below 10 K. Periodically, $R(T)$ curves were measured on different parts of the sample (probe current for resistance measurements was 1 mA).

Table 1.

sample type	No.	j, kA·cm^{-2}	Q, MC·cm^{-2}	ρ, mΩ·cm	T_c, K	S, μV/K
1*i*		-	-	1.2	20.2	–2.2
1*c*	1	1.2	1	1.2	20.2	–2.2
1*c*	2	1.2	10	1.1	20.2	–2.2
1*c*	3	2	10	1.1	20.4	–2.3
1*a*	1	1.2	1	1.2	20.2	–2.2
1*a*	2	1.2	10	1.1	20.2	–2.2
1*a*	3	2	10	1.1	20.1	–2.1
2*i*		-	-	2.5	83.5	+2.7
2*c*	1	1.5	1	2.5	84.5	+2.9
2*c*	2	1.5	3	2.6	85.2	+3.2
2*c*	3	1.5	10	2.6	86.0	+3.5
2*a*	1	1.5	1	2.5	83.0	+2.5
2*a*	2	1.5	3	2.5	82.5	+2.4
2*a*	3	1.5	10	2.4	82.0	+2.3
H1*i*		-	-	1.3	20.2	–2.2
H1*c*	1	1.4	1	1.5	19.0	–2.2
H1*c*	2	1.4	10	2.1	17.0	–2.2
H1*a*	1	1.4	1	1.7	18.7	–2.2
H1*a*	2	1.4	10	2.0	17.4	–2.2
H2*i*		-	-	2.7	83.4	+2.5
H2*c*	1	2.2	1	3.5	82.2	+2.5
H2*c*	2	2.2	10	5.1	78.0	+2.5
H2*a*	1	2.2	1	3.7	81.7	+2.5
H2*a*	2	2.2	10	5.0	77.4	+2.5

Seebeck effect S studies were performed by alternating gradient technique [10] on the initial samples and on the parts of the samples cut after the electromigration treatment from the sample bar.

Electron probe microanalyzis (EPMA) of the samples was performed with the JCXA-733 analyzer at the probe voltage 15 kV.

Results and discussion

The electrical current flow (current density j below 3 kA·cm^{-2}) leads to substantial sample properties changes (Table 1). The most interesting effect is the T_c increase up to 2.5 K at the cathode (2*c*, Fig. 1) and its decrease by nearly the same amount near

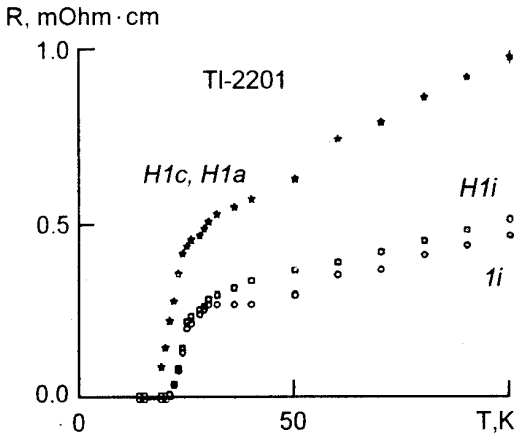

Fig. 2. Resistance vs temperature curves for $Tl_2Ba_2CuO_{6+x}$ sample 1: as obtained (1*i*), after water vapor treatment (H1*i*) and after current treatment (H1*c* and H1*a*).

anode (2*a*, Fig. 1) after passing electrical charge Q of $10{\cdot}10^6$ C·cm^{-2} through the sample 2*i*, analoguosly to Mitin et al. results. For the sample H2*i*, the resistivity increases homogeneously along the sample length at a rate of 10^{-10} Ohm·C^{-1}·cm and the T_c decreases by 2–2.4 K after passage of 10^6C·cm^{-2} (Fig. 2, curves H2*a*, H2*c*) and by almost 6 K for $10{\cdot}10^6$ C·cm^{-2}.At the same time, changes of T_c for the sample 1*i* after passage of $10{\cdot}10^6$ C·cm^{-2} charge never exceeded 0.5 K, and for the water vapor treated sample H1*i*, monotonous T_c decrease and resistivity increase was also typical. Reference samples of 1*i*, 2*i*, H1*i* and H2*i* type showed neither the resistivity nor the T_c changes when stored for the time of electromigration treatment. This allows us to ignore degradation of the samples due to the ambient effect.

To study the origin for T_c changes, chemical composition along the samples length was studied by means of the EPMA technique. The results have shown that concentrations of both heavy atoms (Tl, Ba, Cu) and oxygen remain unchanged, within experimental uncertainty, for all the four sample types. As the oxygen content is rather hard to determine with the sufficiently high accuracy in this experiment, it was estimated qualitatively by using the room-temperature Seebeck coefficient S value. It was shown that the S value in the cathode region increases from +2.7 to 3.5 μV/K. This increase is typical for the decreased doping level in the materials due to smaller oxygen content [8]. In the anode region of the sample, S decreased to 2.3 μV/K, evidencing increased doping level. For the other samples, S value was usually unchanged.

The results obtained have shown that, for the water vapor treated samples, the T_c decrease and the resistance increase are typical, though S remains unchanged. This behavior may be related with the degradation of the sample grain boundaries, not the grains by theirselves. Increased resistance of the samples after vapor treatment is the strong evidence that some perturbations of the grains take place, and probably they promote further sample degradation at the grain boundaries.

As to the untreated samples, we can conclude that, as a result of the current treatment, oxygen atoms migrate from the cathode towards the anode, quite in the accordance with the oxygen anion negative charge and contrary to the hole flow direction in the material. This may evidence that either electronic wind phenomenon is not of the prime importance for such layered compounds with separated rather far hole-conducting Cu–O layer and oxygen conducting Tl–O layers, or in the materials are in fact electronic conductors as it should be according to the band structure calculations, and all anomalous transport phenomena are due to strong carrier coupling with some exitations in the lattice. However, a strong dependence of the migration velocity on the material doping level, namely, its essential decrease for the stronger doped materials, allows us to conclude that this is not an effect of the wind but rather that of the oxygen interstitials filling in the stronger doped materials. This allows us to conclude that the main driving force for the ion migration in the materials is the direct electrostatic force acting on the oxygen atoms in the Tl–O layers which are the most free to move. However, a strong dependence of the effect on the grain boundary treatments allows us to conclude that the essential role may be played by the local overheating in the weak intergranular links and/or creation of the nucleation centers for new phase formation by the adsorbed water molecules. The same may be evidenced by the much larger effects observed in the $Tl_2Ba_2CuO_{6+x}$ compound cooled to the liquid nitrogen temperature [5], since much higher current densities are used in those experiments.

Acknowledgement

The authors acknowledge the support of Ukrainian Scientific Council, Project "Veter".

References

1. A.Ono, S.Takenouchi, Y.Ishizawa, *Jap. J. Appl. Phys.*, **30**, L464 (1991).
2. K.D.Vernon-Parry, L.T.Romano, J.S.Lees, C.R.M.Grovenor, *Physica, C*, **170**, 388 (1990).

3. K.C.Rajan, P.Parameswaran, Jambunatan Janaki, G.V.N.Rao, T.S.Radhakrishna, *Bull. Electrochem.*, **5**, 761 (1989).
4. A.M.Prochorov, Yu.M.Gufan, A.Ye.Krapivka et al., *JETP Lett.*, **51**, 132 (1990).
5. A.V.Mitin, N.E.Alekseevski, E.P.Khlybov, *Physica, C*, **199**, 351 (1992).
6. P.S.Ho, T.Kwok, *Rep. Progr. Physics*, **52**, 301 (1989).
7. J.B.Parise, C.C.Torardi, M.A.Subramanian et al., *Physica, C*, **159**, 239 (1989).
8. M.A.Tanatar, V.V.Dyakin, V.S.Yefanov, A.I.Akimov, A.P.Chernyakova, *Physica, C*, **185-189**, 1247 (1991).
9. A.I.Akimov, B.B.Boiko, V.I.Gatalskaya et al., *Sverkhprovodimost': Fiz., Khim., Tekhn.*, **2**, 41 (1989).
10. P.M.Chaikin, J.F.Kwak, *Rev. of Scie. Instr.*, **46**, 218 (1975).

Влияние обработки поверхности на стабильность оксидных высокотемпературных сверхпроводников в процессе электромиграции

М.А.Танатар, В.С.Ефанов, А.И.Акимов, А.П.Чернякова

Показано, что стабильность керамики $Tl_2Ba_2CuO_{6+x}$ в процессе электромиграции существенно уменьшается, если материал выдержать в атмосфере паров воды. Для таких образцов характерно уменьшение T_c и увеличение сопротивления, при этом коэффициент термо-э.д.с. S остается неизменным. Сделано заключение, что основной причиной этого явления является деградация границ зерен под действием электрического тока. Для исходных образцов стабильность в процессе электромиграции сильно зависит от уровня легирования и возрастает в материалах с более высоким содержанием кислорода. Предполагается, что эффект связан с заполнением вакансий в Tl–O слоях атомами кислорода.

Functional Materials **2**, No.2 (1995)

Positron spectroscopy of $YBa_2Cu_3O_7$ with physically and chemically adsorbed molecules of water

V.T.Adonkin, B.M.Gorelov and V.M.Ogenko

Institute for Surface Chemistry, National Academy of Sciences of Ukraine,
31 Nauki Ave., 252650 Kiev, Ukraine

The effect of physical and chemical adsorption of water molecules on the defect spectrum and electron density of $YBa_2Cu_3O_7$ high-T_c superconductor was investigated by method of lifetime positron spectroscopy and X-ray diffraction analysis. $YBa_2Cu_3O_7$ ceramic samples were investigated after exposure during different time in saturated water vapour at 21 °C. The physical and chemical adsorption were separated by variation of exposure time. At the adsorbate mass $0 < m \leq 1.2$ % physically sorbed water multilayer, decreases the annihilation rate (λ_f) from 5.5 to 4.75 ns^{-1} and affects non-monotonously the capture rate (ν). At the absorbate mass is $m \leq 0.6$ %, ν is decreased from 0.71 to 0.99 ns^{-1}, and with m rise, ν is decreased to initial value at $m \approx 1$ %. In addition, the action of physically sorbed water multilayer reduces the c parameter of crystal lattice, whereas a parameter remains unchanged. The action of chemically sorbed water multilayer does not change the annihilation and crystal lattice parameters in the range $1.2 < m < 5$ %. At $m > 5$ %, λ_f and ν are abruptly decreased. The effect of physically sorbed water molecules is ascribed to redistribution of Ba and Cu ions between the bulk and surface layer of $YBa_2Cu_3O_7$ stimulated by electric field of water dipoles. The effect of chemical adsorption is caused by formation of the new phases in $YBa_2Cu_3O_7$ crystal lattice.

Показано, що фізично сорбований полішар води, коли маса адсорбату $0 < m \leq 1.2$ %, зменшує швидкість анігіляції (λ_f) з 5.5 до 4.75 $нс^{-1}$ і немонотонно змінює швидкість захоплення позитронів (ν). Коли маса адсорбату $m \leq 0.6$ %, ν збільшується з 0.71 до 0.99 $нс^{-1}$ та з ростом m швидкість захоплення зменшується до значення, характерного для $m \approx 1$ %. Вплив фізично сорбованого полішару води змінює параметр c кристалічної гратки, залишаючи незмінним параметр a. Хімічно сорбована вода не змінює параметри анігіляції та кристалічної гратки аж до значень $1.2 < m < 5$ %. Коли $m > 5$ %, λ_f та ν різко зменшуються. Ефект фізично сорбованої води пояснюється перерозподілом іонів барія та міді між об'ємом та поверхневим шаром, стимульованим електричним полем диполів води. Ефект хімічної адсорбції обумовлений утворенням нових фаз в кристалічній гратці $YBa_2Cu_3O_7$.

Introduction

In the degradation process of $YBa_2Cu_3O_{7-\delta}$ high temperature superconductors in water vapour, two stages can be recognized [1,2]. In the first stage, the layer of physically sorbed water molecules is formed on the superconductor surface. With the rise of exposure time the layer thickness is increased, and when that thickness attains approximately 200–500 Å, the chemisorption processes begins. During chemisorption, the bound states of hydroxyl groups are formed and their quantity is increased with the rise of the adsorption time. Besides, the part of water and hydroxyl groups diffuses in the bulk of crystal lattice. These two processes of chemical adsorption give rise to loss of superconductivity. The effect of physical adsorption is usually weaker than that of the chemisorption. However, if the electrical field of adsorbed water dipoles is strong enough for stimulation of diffusion in the bulk adsorbent [3], the redistribution of defect spectrum may be observed. In $YBa_2Cu_3O_{7-\delta}$, the enrichment of surface layer in barium ions and depletion in copper ions under action of physically sorbed water multilayer was observed [2,4].

It can be supposed that the change of surface elemental composition is caused by ion exchange between bulk crystal and surface layer. If this is true, the ion exchange and formation of Ba and Cu vacancies may be manifested in the lifetime spectra of positron annihilation.

In this paper the effect, of physically and chemically sorbed water molecules on the electron density of copper-oxygen bonds and the defect spectrum was investigated in $YBa_2Cu_3O_{7-\delta}$ high temperature superconductor.

Samples and experimental details

The ceramic samples of $YBa_2Cu_3O_{7-\delta}$ with $0 \le \delta < 0.07$ were studied. The samples had density 5.5 g/cm^{-3}, average grain size 10–30 μm, the critical temperature and transition width were ≈91 K and 1.5 K, respectively.

The adsorption of water molecules was realized at ~19 Torr pressure and 21 °C on samples preannealed in 10^{-3} Torr vacuum and 150–180 °C temperatures for ~2 hours. The physical and chemical adsorption were separated varying the exposure time. At short exposure times ($t \le 120$ min) and adsorbate mass $m \le 1.2$ %, the effect of physically sorbed water multilayer dominates. At $t > 120$ min, $m > 1.2$ %, the formation of chemisorbed states and diffusion of water molecules in the bulk crystal are observed. After completing the exposure time, the water multilayer was removed from HTSC surface to conserve of adsorption effect. Before lifetime and X-ray measurements the samples are conserved in ambient conditions. The storage in such conditions does not influence on the adsorption effect. Every sample was undergone singly to adsorbate action.

The positron lifetime measurements were performed at room temperature using "Ortec" spectrometer with FHWM resolution of 220 ps. The lifetime spectra were characterized by two components τ_1, τ_2 – the annihilation times of free positrons and positrons captured by traps, respectively, with intensities of I_1, I_2. From the data obtained, the annihilation rate (λ_f) and capture one (ν) were calculated.

Results and discussion

The experimental data are summarized in Table. Analysis of adsorption effect may be performed using the λ_f and ν dependences on adsorbed water quantity which are shown in Fig.1 and 2. In figures, the various point symbols correspond to three types of $YBa_2Cu_3O_7$ samples

Table. Annihilation lifetimes for $YBa_2Cu_3O_7$ before and after water absorption.

m, %	τ_1, ps	I_1, %	τ, ps	I_2, %
0°	149±13	61.5±5	248±25	38.5±5
0	170±5	83.8±5	331±37	16.2±5
0*	162±6	71.6±5	301±15	28.4±5
0.15*	168±6	74.8±4	318±19	25.2±5
0.56*	159±10	63.5±9	281±18	36.5±8
0.62	188±5	80.2±4	394±28	19.8±4
0.82*	173±7	65.8±6	312±14	34.2±6
1.1*	184±6	73.6±4	351±17	25.4±4
1.14	180±9	69.1±9	321±28	30.9±9
1.50*	205±5	9.2±4	380±23	20.8±4
2.91	180±7	59.9±6	347±26	40.1±6
3.29°	184±10	73.3±5	332±30	29.7±5
4.88	182±9	67.8±7	336±21	32.2±7
5.0°	188±1	71.1±7	347±21	28.9±8
5.12°	198±8	76.7±6	361±24	23.3±6
5.25	201±7	79.5±5	370±25	20.5±5

Upper symbols denote three types of $YBa_2Cu_3O_7$ samples.

prepared from different ceramics blocks. Three regions of different behavior of $\lambda_f(m)$ and $\nu(m)$ dependences can be distinguished. In the first region, where $0 \le m \le 1.2$ %, the effect of physically sorbed water multilayer takes place. This region is characterized by smooth λ_f decrease and unmonotonous ν behavior. In the second region, when $1.2 \le m \le 5$ %, and third one, $m > 5$ %, the effect of chemisorption occurs. However, at $1.2 \le m \le 5$ %, the annihilation parameters are unchanged whereas at $m > 5$ %, the λ_f and ν are abruptly decreased. It should be noted that, at $0 \le m \le 1.2$ %, the parameter c of the crystal lattice is reduced from 11.670 Å to 11.658 Å while a parameter is unchanged. In the range $1.2 \le m \le 5$ %, c and a parameters are constant and at $m > 5$ %, the parameter a increases from 3.837 Å to 3.831 Å whereas c is reduced to 11.653 Å.

Thus, the effect of physically sorbed water multilayer gives rise to the λ_f decrease and unmonotonous ν behavior. The behavior of annihilation parameters points to the lowering of electron density of Cu1 oxygen bonds and un-

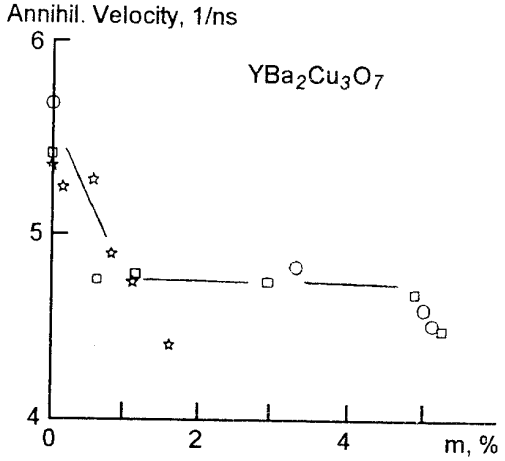

Fig.1. Water adsorption effect on annihilation rate.

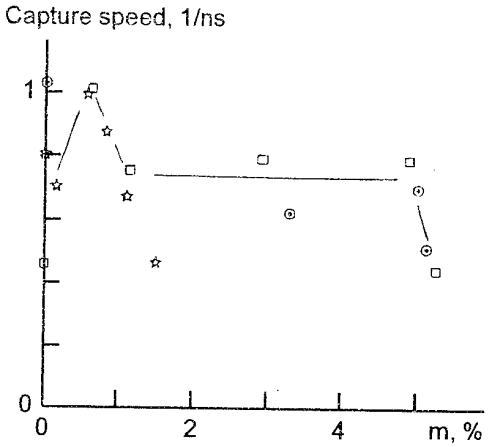

Fig.2. Water adsorption effect on capture rate.

monotonous changes of defects concentration in the crystal lattice. This effect can be expalined by ion exchange between the bulk and surface layer of $YBa_2Cu_3O_7$ crystallites. In the electric field of sorbed water dipoles, Ba ions diffuse to the surface forming the vacancies in the crystal lattice. This process causes an increases of the ν. In the surface layer, the excessive Ba ions force out Cu1 ions from lattice sites which migrate in the bulk crystal compensating the charge of Ba ions. In the process of ion exchange, the part of Cu1 ions probably occupies the Ba positions and vice versa. Such substitution decreases the defect concentration but puts O4–Cu1–O1 bonds in disorder. Both processes, namely, the formation of vacancies and disordering of copper-oxygen bonds, result in the decrease of electron density of O4–Cu1–O1 bonds. Besides, the formation of cation vacancies gives also rise to the reduction of c parameter of the crystal lattice. It should be noted that the layer where the ion exchange takes place probably is the intermediate one between the surface and bulk crystal which is not undergone the action of physically sorbed water molecules.

The formation of chemisorption states and the diffusion of water molecules in the crystal bulk at $1.2 < m < 5$ % does not affect the defect concentration and electron density of O4–Cu1–O1 bonds. The absence of effect can be ascribed to the localization of water molecules in the lattice places which are inaccessible or insensitive for positrons and to the chemisorbed states formation without changes of electron density of copper-oxygen bonds.

The essential changes of λ_f and ν at $m > 5$ %. point to the abrupt decrease of electron density of copper-oxygen bonds and defect concentration. These processes are accompanied by a rise of a parameter and reduction of c parameter of crystal lattice. Such behavior of annihilation and crystal lattice parameters may be caused by the formation of new phases in $YBa_2Cu_3O_7$ crystal lattice. This may be the compounds of metal ions with hydroxyl groups defects. The formation of inhomogeneous regions results in the disordering, lengthening of copper-oxygen bonds and decrease of their electron density, and healing of crystal lattice defects.

Conclusion

Thus, the effect of physically sorbed water molecules gives rise to the decrease of electron density of O4–Cu1–O1 bonds and unmonotonous change of defect concentration. The effect chemically sorbed water has a jump-like character. At the adsorbate mass $m < 5$ %, the electron density and defect concentration are unchanged. At $m > 5$ %, the electron density and concentration defects are abruptly decreased.

We are grateful to Dr. V.S.Melnikov for X-ray measurements and to Dr. V.V.Dyakin for discussions.

References

1. V.T.Adonkin, B.M.Gorelov et al., *React.Kinet.Catal.Lett.*, **50**, 235 (1993).
2. B.M.Gorelov, V.V.Dyakin et al., *Fiz.Tv.Tela*, **35**, 3222 (1993).
3. A.S.Davydov, B.Ya.Antonchenko, V.V.Il'in, Principles of Water Physics [in Russian], Naukova Dumka, Kiev (1991).
4. B.M.Gorelov, V.V.Dyakin et al., *J.El.Spectroscopy and Rel.Phen.*, to be published.

Позитронная спектроскопия $YBa_2Cu_3O_7$ с физически и химически адсорбированными молекулами воды

В.Т.Адонкин, Б.М.Горелов, В.М.Огенко

Показано, что физически сорбированный полислой воды, когда масса адсорбата $0 < m \leq 1.2$ %, уменьшает скорость аннигиляции (λ_f) с 5.5 до 4.75 нс$^{-1}$ и немонотонно изменяет скорость захвата позитронов (ν). Когда масса адсорбата $m \leq 0.6$ %, ν увеличивается с 0.71 до 0.99 нс$^{-1}$ и с ростом m скорость захвата уменьшается до величины, характерной для $m \approx 1$ %. Воздействие физически сорбированного полислоя воды изменяет параметр c кристаллической решетки, оставляя неизменным параметр a. Химически сорбированная вода не изменяет параметры аннигиляции и кристаллической решетки вплоть до значений $1.2 < m < 5$ %. Когда $m > 5$ %, λ_f и ν резко уменьшаются. Эффект физически сорбированной воды объясняется перераспределением ионов бария и меди между объемом и поверхностным слоем, стимулированным электрическим полем диполей воды. Эффект химической адсорбции обусловлен образованием новых фаз в кристаллической решетке $YBa_2Cu_3O_7$.

Functional Materials 2, No.2 (1995)

Influence of atomic arrangement correlation on percolation properties of three-dimensional condensates

A.S.Bakay, V.Yu.Gonchar, S.V.Krikun and G.Ya.Lubarsky

National Scientific Center «Kharkov Physico-Technical Institute»,
1 Akademicheskaya St., 310108 Kharkov, Ukraine

Possibilities to control the structural properties of heterophase carbon condensates are discussed. The process of heterophase condensates growth is simulated by numerical methods taking into account correlations of atoms arrangements, and percolation characteristics of model condensates are studied in relationship with the correlation degree of the atomic arrangement with different local ordering types. The percolation thresholds and critical indices for the conductivity and cluster size distribution are found. It is established that the threshold concentration is very sensitive to correlation changes while critical indices are essentially independent of them. An euristic criterion is proposed to find the threshold concentrations in the presence of correlations which is applicable to any lattice type.

Обговорюються можливості управління структурними властивостями вуглецевих гетерофазних конденсатів. Чисельними методами змодельовано процес росту гетерофазних конденсатів з урахуванням кореляцій у взаємному розташуванні атомів і вивчені перколяційні характеристики модельних конденсатів у залежності від ступеня кореляції взаємного розташування атомів з різними типами локального порядку. Знайдено пороги протікання та критичні індекси для провідності і розподілу кластерів за розмірами. Установлено, що порогова концентрація дуже чутлива до зміни кореляцій, тоді як критичні індекси від них практично не залежать. Запропоновано евристичний критерій для знаходження порогових концентрацій при наявності кореляцій, що застосовується незалежно від типу решітки.

Introduction

In the process of the carbon plasma deposition, condensates containing binarily, ternarily, or quaternarily coordinated carbon atoms with *sp*-, sp^2-, or sp^3-hybridized electronic bonds are forming over a wide range of the support temperature and average ion energy(see reviews [1–7] and also [8–13]). Condensate in which sp^2-bonds are prevailing is similar to graphite, while with prevailing sp^3-bonds, it is a diamond-like one. These condensates are, as a rule, amorphous and show no obvious evidences of long-range ordering, local ordering types being randomly alternated. Such heterostructural (or heterophase) solids, in which the local topological order (determined by the type of the atomic coordination polyhedron) is inhomogeneous and varies from one atom to another even in single-component condensates, are forming under strong thermodynamic non-equilibrium conditions (e.g. at supercooled melts solidification, deposition of atomic or plasma streams onto cold supports, etc.)

For simplicity, let us designate areas filled with atoms having a common type of local order as single-phase ones, the phase being implied to be crystalline or non-crystalline structure with the same local order. If phases possess significantly different electrical, mechanical, and other properties, the macroscopic condensate characteristics depend on the linking of areas of the same phase. So, e.g., the conductivity of a heterostructural carbon condensate depends substantially on the linking of graphite-like areas having a relatively high electrical conductance. In the same time, mechanical properties (strength, microhardness, wear-resistance) are determined by the linking of diamond-like areas having a high local microhardness and great value of the shear module.

In the course of plasma streams with low energy of ions ($\leq 10^2$ eV) deposition onto cold sup-

ports, the growth of heterostructural condensates occurs as a rule if, under thermodynamic equilibrium conditions, one or more metastable phases exist along with the stable one. Under phenomenological approach, the kinetics of heterostructural condensates formation can be described in terms of the chemical kinetics approximation [14]. In that approach, equations for volume parts of phases variation in thickness in the course of growth have been obtained. Therewith, the formation probabilities for a given type of the local ordering as functions of ordering character of the area onto which the ion being deposited falls, are considered as phenomenological coefficients which are to be determined by the correlation with experimental data. Such an approach allows to describe averaged (hydrodynamic) quantities, but structural details, linking, size distribution of areas, interphase boundaries branching remain out of the scope of description. In this connection, of importance is the question about a more comprehensive study of statistic properties of heterostructural condensates forming at the high-energy ions deposition. Such a study can be performed by simulation of the growth process of a condensate and subsequent investigation of structural and physical properties thereof.

As in [14], there are the formation probabilities for a given type of the local ordering at ion deposition which determine the growth process. Let the surface layer be characterized by an initial distribution of atoms with several local ordering types. Then, each freshly deposited ion enters the environment of atoms having several local order types and, depending on its nearest vicinity, acquires a specific bond type, one or another local ordering. The problem is (a) to choose a realistic field of probabilities for the formation, by the ion being deposited, of each local order type, taking into account the structural state of the deposition site; (b) to simulate subsequently the condensate growth process at the probabilities field chosen and (c) to consider and evaluate the structural and physical properties of condensate formed.

In this work, the above scheme is realized using a rather general, three-parameter expression for the formation probabilities of several local order type, and properties of model condensates obtained are studied as functions of one parameter responsive for the degree of the spatial correlation of atoms with a given local order type. Possibilities of an experimental verification of results obtained are also discussed for the case of carbon condensates obtainable by plasma stream deposition.

Probabilities field choice

Let the amorphous structure of an actual condensate be substituted by a regular cubical mesh, with blocks of the initial structure having dimension ξ^3 being corresponding to points of the mesh. Let us to choose $\xi \ll \upsilon$, where υ is the least of averaged dimensions of single-phase areas, so those blocks can be considered as homogeneous ones consisting of one phase only. The building-in of a separate atom being deposited is, as indicated above, a substantially non-equilibrium process during which the energy of that atom as well as those of its surrounding atoms undergo variations.

Spatial and temporal fluctuations of the energy of atoms are, especially on the first stage (the collision one), great in relation to thermal fluctuations determined by the average condensate temperature; nevertheless, it is quite natural to choose, as the distribution of the formation probabilities of several configurations, the Gibbs distribution with a certain effective temperature, T_{ef}, depending on the support temperature, T_s, and energy, E, of atoms in the beam:

$$w_i \sim \exp\left[-E_i/kT_{ef}(T_s, E)\right] \qquad (1)$$

where E_i is the energy of interaction of an atom in i-th phase state with its local surrounding; k, Boltzmann constant. At the transition to blocks, let us believe that the probabilities distribution for the formation of the block in i-th phase state (designated as «the i-th type block») will not change, it is only the explicit form of function $T_{ef}(T_s, E)$ which shall be changed as well as the sense of quantity E_i which will mean now the effective interaction energy of a given i-th type block with its neighbours. In the case where only two phases can occur,

$$E_i = \varepsilon_{i1}n_1 + \varepsilon_{i2}n_2 + \varepsilon_{i0}\cdot(z - n_1 - n_2), \quad (i = 1, 2) \qquad (2)$$

where ε_{ik} are effective binding energies between i type blocks and k type ones (i,k = 1,2); ε_{i0}, effective energy of broken bond of i type block; z, coordination number; n_k, the number of k type neighbours (k = 1,2) for a given block. Taking into account that $w_1+w_2 = 1$ and $\varepsilon_{12} = \varepsilon_{21}$, we obtain from (1) and (2)

$$w_1 = \left[1 + g\cdot\exp(\delta N)\cdot\exp(\lambda n_1)\right]^{-1}, \qquad (3)$$

where $N = n_1 + n_2$, and

$$g = \exp\left[-z(\varepsilon_{20} - \varepsilon_{10})/kT_{ef}(T_s, E)\right]$$
$$\delta = -(\varepsilon_{22} - \varepsilon_{12} - \varepsilon_{20} + \varepsilon_{10})/kT_{ef}(T_s, E) \quad (4)$$
$$\alpha = -(2\varepsilon_{12} - \varepsilon_{11} - \varepsilon_{22})/kT_{ef}(T_s, E)$$

As it follows from (3), the parameter λ determines how strongly w_1 depends on the number of type 1 blocks in nearest lattice points. It is just the value of that parameter on which the degree of lattice correlation primarily depends. At $\lambda < 0$, we have obviously positive correlations, i.e. the probability that a block of 1 type is located side by side with a given 1 type block exceeds the concentration of those blocks (if such a probability is less than the concentration mentioned, we will speak about negative correlations); at $\lambda > 0$, the correlations are negative, and at $\lambda = 0$, there are no correlation. The parameter δ determines the degree of dependence of the probability w_1 on the total number, N, of blocks in nearest lattice points. The parameter g, at specified λ and δ, is responsive primarily for the balance between w_1 and w_2, i.e. for concentration of blocks of a given type in a specimen. In this work, we have studied the dependence of properties of model condensates on the parameter λ determining the correlation degree of a lattice; parameter δ, for simplicity, has been set to zero while parameter g was used to vary concentrations of type 1 and type 2 blocks.

Condensate growth simulation

The simulation process was at follows. The growth starts on a support constituting a quadratic lattice; all point thereof are occupied, with probability g, by type 1 blocks and with probability $p = 1 - g$, by type 2 blocks. Then, a point of this lattice is arbitrarily chosen, and in point positioned over it, a block of 1 or 2 type is positioned with probabilities w_1 and w_2, respectively, defined by (3). The process is repeated until a previously specified space L is filled with blocks, so none vacant place remains therein.

Properties of model condensates

As indicated above, properties of heterophase condensates depend significantly on the linking of areas occupied by the same phase. It is known from the percolation theory [15] that the linking of blocks of a given type occurs first at a certain threshold concentration of those blocks, P_c, which depends on the lattice type and dimensionality as well as on correlations in the blocks arrangement [16,17]. If blocks linked are electrically conductive, the conductivity, σ, of the whole specimen, at concentrations of those blocks close to threshold one, is obeyed to law [16]

$$\sigma \sim (p - P_c)^t \quad (5)$$

where t is so-called critical index for the conductivity.

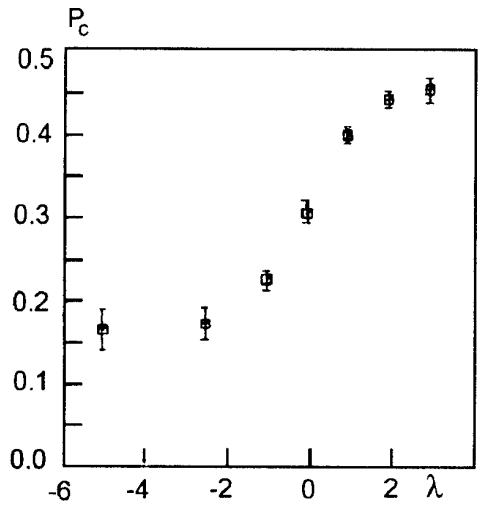

Fig.1. Dependence of percolation thresholds P_c on the parameter λ.

The percolation threshold, P_c, was determined along with the critical index t by the fitting of electroconductivity values near the threshold to linear plot constructed in the dual logarithmic scale, as described, e.g., in [17]. Each σ value was obtained by averaging of the conductivity values for 40 lattices of 30^3 dimension. The conductivity of linkages between type 2 blocks was assumed to be equal to 1, that of all other linkages, to 0. The procedure used for simultaneous evaluation of threshold concentration and critical index gives, in the case of correlations absence ($\lambda = 0$) $P_c = 0.305 \pm 0.010$ and $t = 1.9 \pm 0.35$ what is in good agreement with known [18] values $P_c = 0.3117$ and $t = 2.0$.

The P_c dependence on λ parameter is shown on Fig.1. The threshold concentration is seen to vary in a wide range to both sides. The date show that, from $\lambda \sim -2.5$ on, the threshold concentration decreases asymptotically approaching to value $P_c \approx 0.15$ ($P_c = 0.165 \pm 0.025$ at $\lambda = -5$) what is about half as many as threshold concentration in absence of correlations. The progress into range of $\lambda < -5$ is hindered by a sharp drop of accuracy of t and P_c evaluation. The threshold concentration rises with the increase of λ. So, at uppermost value studied, $\lambda = 3$, $P_c = 0.45 \pm 0.015$

what exceeds significantly the value for uncorrelated lattice.

Conductivity index values, t, at several λ are represented on Fig.2; it follows therefrom that, within the accuracy of the numerical experiment, t can be considered as independent on spatial correlations. Thus, the conductivity variation rate in the neighbourhood of the threshold concentration of conductive blocks does not depend essentially on correlations in their arrangement or, by other words, on the interaction parameters of atoms in the course of deposition. Such a pattern is in agreement with accurate results obtained for Bete lattice with the account for correlations [19].

At $p = P_c$, the average number, n_s, of clusters having dimension s in uncorrelated lattices is defined as [20]

$$n_s \sim s^{-\tau} \quad (\text{at } s \to \infty) \tag{6}$$

where τ is the factor (index) of the cluster size distribution. In the absence of correlations, $\tau = 2.2$ [20].

We had found τ values separately for each of simulated lattices of 30^3 size and then had averaged these values obtaied for 40 lattice realizations at $p = P_c$. Fig.3 shows τ values for different λ ones. Vertical lines show the τ values dispersion for 40 lattice realizations and squares correspond to average τ values. Similar to t, τ is seen to depend only weakly on the atomic interaction parameters decreasing slightly at positive correlations.

It is convenient to characterize the degree of lattice correlation by quantity G, which is the ratio of the average number, Z_{22}^0, of type 2 neighbours of a type 2 block in an uncorrelated lattice to the same number (Z_{22}) in a correlated lattice. It is obvious that, for the cubic lattice, $Z_{22}^0 = 6p$, thus

$$G = 6p/Z_{22}. \tag{7}$$

By definition, $G = 1$ for a lattice in which correlations of the blocks arrangement are absent; it is easy seen that, in the case of positive correlations $G < 1$, and for negative ones, $G > 1$. Fig.4 shows the dependence of G on the λ parameter at concentrations $p = P_c$.

On Fig.5, the P_c dependence on G is presented. It is seen that the points fall good on a some straigth line $P_c = a + b \cdot G$; the fitting by least squares method gives for the parameters values $a = 0.08475$, $b = 0.2094$. Using (7), after simple transformations we obtain that, at $p = P_c$,

$$P_c = Z_{22}(P_c) \cdot a/(Z_{22}(P_c) - 6b).$$

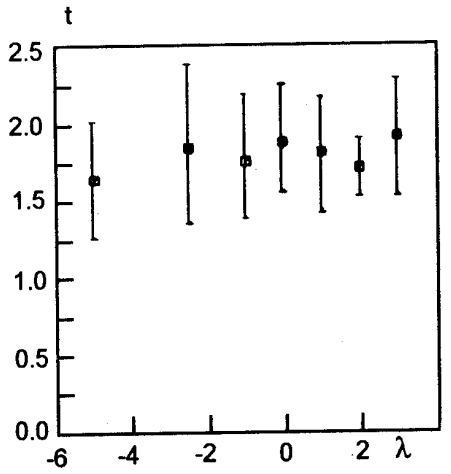

Fig.2. Dependence of the conductivity index σ on λ.

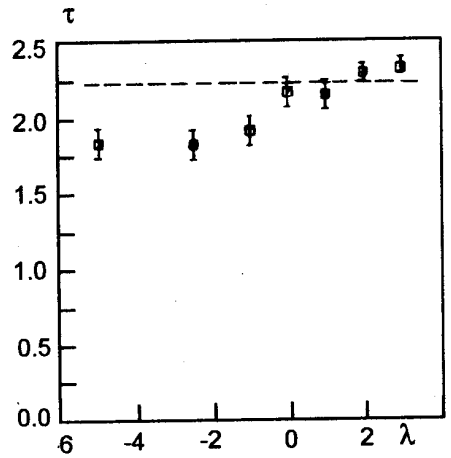

Fig.3. Dependence of the cluster size distribution index τ on λ. The broken line shows τ value for the case of none correlations (λ=0) τ=2.2.

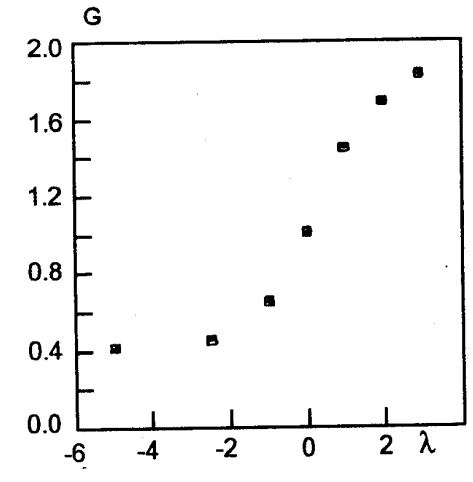

Fig.4. Dependence of the quantity G characterizing the degree of lattice correlation (definition in text) on λ.

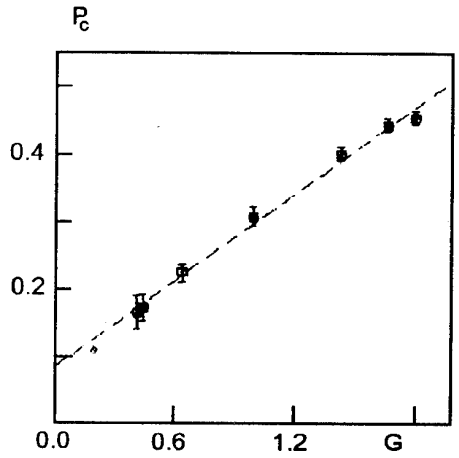

Fig.5. Dependence of percolation thresholds P_c on G. Broken line shows the fitting of experimental points by the least squares method.

Let us introduce the function $F(p) = p - Z_{22}(p) \cdot a/(Z_{22}(p) - 6b)$; then, it is seen that P_c is the root of equation

$$F(p) = 0 \qquad (8)$$

an the percolation criterion can be presented as follows: $p \geq P_c$, where P_c is a roof of (8). An additional study shows that, for uncorrelated lattices as well as for correlations of the type considered by us, the function $F(p)$ has the sole root on the intercept $p \in [0,1]$.

Thus, we propose the following method for the finding of percolation thresholds for blocks in correlated lattices: the percolation threshold P_c is the value of concentration of type Z blocks (i.e. conducting ones) which is the root of $F(p)$ function. An euristic percolation criterion is in essence proposed here with universal values of a and b coefficients in the function $F(p)$. It should be noted that the quantity Z_{22} involved in F can be always determined experimentally without difficulties and, in some cases, it can be found also analytically as a function of the concentration p. The case when the $F(p)$ function has multiple roots on the intercept [0,1] requires a special consideration.

Since uncorrelated lattice is a specific case of correlated one, it is of interest to verity the validity of the criterion formulated for several uncorrelated three-dimensional lattices: diamond (coordination number $z = 4$), volume-centered cubic (VCC) ($z = 8$), and face-centered cubic (FCC) ($z = 12$). For uncorrelated lattices, $Z_{22} = zp$ and the root of F function is easy to find as

$$P_c = a + 6b/z.$$

Introducing in to this expression $z = 4,8,12$ we obtain: $P_c^{diam} = 0.3989$ (0.428); $P_c^{bcc} = 0.2418$ (0.245); $P_c^{fcc} = 0.1895$ (0.198); in brackets, the values known from literature [18] are given. The agreement is seen to be good enough what gives evidence for that the criterion proposed can be applicated for various lattice types, including probably also amorphous structures to which actual heterophase condensates belong.

Discussion

We have seen that the structure and physical properties of heterophase films depend significantly on interatomic bonds correlations which, in turn, are determined by bonding energies ε_{ik} and explicit form of function $T_{ef}(T_s, E)$ and vary at changes of the support temperature and deposited atoms energy. The establishing, empirically or by means of numerical experiments (as is [21]), of a dependence of twin bonding correlations on deposition conditions opens up the possibilities for controlling the percolation threshold of each phase. It should be noted that just the percolation thresholds depend strongly on the deposition conditions; but critical indices and, consequently, near-to-threshold variations of properties are not influenced essentially by the degree of bonds correlation.

The above-mentioned carbon condensates obtained under conditions far from equilibrium, e.g. at the deposition of plasma or ionic streams, are interesting objects for the comparison of theoretic prediction with experimental data. As is shown in [22] (see also [21]), when the average energy of ions being deposited changes approximately by a factor of two, the carbon film density changes also by the same factor, from graphite density to diamond one.

It means that, with the variation of ions energy, the concentration of sp^2 bonds (graphite-like) varies from 1 to 0 (while the concentration of diamond-like sp^3 bonds varies from 0 to 1). In the course of this process, the percolation thresholds for both graphite-like and diamond-like clusters are obviously attained. Near the percolation threshold of graphite-like clusters, at $p = P_c$ (sp^2), a critical conductivity behaviour must be observable because graphite-like clusters are conductors, $\sigma \sim [P(sp^2) - P_c(sp^2)]^t$. In the same time, the percolation threshold of diamond-like clusters can be revealed by an anomaly in microhardness and shear module behaviour, $\mu \sim [P(s\,\hat{p}) - P_c(s\,\hat{p})]^t$. Unfortunately, the experimental date available (see [3]) are too scarce and dispersion thereof is

too great for the theoretical results can be compared with them; but no principial difficulties exist to establish the dependence of bonding correlations and percolation thresholds for both phases in carbon condensates on the deposition conditions (support temperature, energy of ions being deposited). The knowledge of those relationships would open the possibility to control the combination of electric and mechanic properties of condensates by means of deposition conditions variation. For example, if sp^3 bonds are correlated highly, the film can possess the desired resistance, density close to that of graphite and, in the same time, a high microhardness. Our calculations have shown that, at $\lambda \leq -2.5$, the percolation threshold for diamond-like clusters would be as low as $P_c \approx 0.15$.

This work was sponsored by part by the Fundamental Investigations Foundation at the State Committee for Science and Technology of Ukraine.

References

1. G.Gautherin, C.Weissmantel, *Thin Solid Films.*, **50**, 135 (1978).
2. A.V.Balakov, A.E.Konshina, *Optiko-Mekhan. Prom.*, No.9, 52 (1982).
3. A.S.Bakay, V.E.Strelnitsky, Srtuctural and Physical Properties of Carbon Condensates Obtained by the High-Speed Particles Streams Deposition:A review [in Russian], CNIIAtominform, Moscow, (1984).
4. R.C.De Vries, *Annu.Rev.Mater.Sci.*, **17**, Palo Alto, Calif., 161 (1987).
5. R.Messier, A.R.Badzian, T.Badzian et al., *Thin Solid Films*, **153**, 1 (1987).
6. John C.Angus, C.Cliff, *Hayman.Science*, **241**, 913 (1988).
7. John C.Angus, Wang Yaxin, Sunkara Mahendra, *Annu.Rev.Mater.Sci.*, **21**, Palo Alto, Calif., 221 (1991).
8. J.Kakinoki, *Acta Cryst.*, **18**, 578 (1965).
9. S.Aisenberg, R.W.Chabot, *J.Appl.Phys.*, **42**, 2953 (1973).
10. L.P.Anderson, S.Berg, H.Norstron at al., *Thin Solid films.*, **63**, 155 (1979).
11. S.Berg, L.P.Anderson, *Thin solid films*, **58**, 117 (1979).
12. E.I.Zorin, V.V.Sukhorukov, D.I.Tetelbaum, *Zh.Tekhn.Fiz.*, **50**, 175 (1980).
13. D.V.Fedoseev, B.V.Deryagin, I.G.Varshvskaya et al., *Zh. Experim.Teor.Fiz.*, **80**, 413 (1981).
14. A.S.Bakay, V.E.Strelnitsky, *Zh.Tekhn.Fiz.*, **51**, 2414 (1981).
15. J.W.Essam, *Rep.Prog.Phys.*, **43**, 833 (1980).
16. S.Kirkpatrick, *Rev.Modern.Phys.*, **45**, 574 (1973).
17. I.Webman, J.Jortner, M.N.Cohen, *Phys.Rev.*, **14**, 4737 (1976).
18. D.Stauffer, Introduction to Percolation Theory, Taylor & Francis Ltd. (1985), p.124.
19. G.R.Reich, P.L.Leath, *J.Stat.Phys.*, **19**, 611 (1978).
20. D.Stauffer, *Phys.Rep.*, **54**, 1 (1979).
21. H.P.Kaukonen, R.M.Nieminen, *Phys.Rev.Lett.*, **68**, 620 (1992).
22. V.E.Strelnitsky, V.G.Padalka, S.I.Vakula, *Zh.Tekhn.Fiz.*, **48**, 377 (1978)

Влияние корреляций в расположении атомов на перколяционные свойства трехмерных гетерофазных конденсатов

А.С.Бакай, В.Ю.Гончар, С.В.Крикун, Г.Я.Любарский

Обсуждаются возможности управления структурными свойствами углеродных гетерофазных конденсатов. Численными методами смоделирован процесс роста гетерофазных конденсатов с учетом корреляций во взаимном расположении атомов и изучены перколяционные характеристики модельных конденсатов в зависимости от степени скоррелированности взаимного расположения атомов с различными типами локального порядка. Найдены пороги протекания и критические индексы проводимости и распределения кластеров по размерам. Установлено, что пороговая концентрация весьма чувствительна к изменениям корреляций, тогда как критические индексы от них практически не зависят. Предложен эвристический критерий для нахождения пороговых концентраций при наличии корреляций, применимый независимо от типа решетки.

Functional Materials **2**, No.2 (1995)

Self-regulation processes of structural and functional state of biological body surface

J.P.Goudzenko

Institute for Sorption and Endoecology Problems, National Academy of Sciences of Ukraine, 32/34 Palladin Ave., 252142 Kiev, Ukraine

The aim of this work was to study the structural and functional state of biological body surface by electron microscopy both before and in dynamics of proposed actions directed on structural ensurement of regulative reconstruction processes. As consequence of material basis optimization for self-regulation by means of adequate structural ensurement, the effect of structural and functional ordering of the elements of surface system of biological body has been obtained.

Метою роботи є вивчення структурно-функціонального стану поверхні біологічних тіл до та в динаміці здійснюваних заходів, спрямованих на структурне забезпечення реконструктивних регуляторних процесів. Використовувався метод електронної мікроскопії. Завдяки оптималізації матеріальної бази механізму саморегуляції шляхом досягнення адекватного структурного забезпечення був отриманий ефект структурного та функціонального упорядкування елементів системи поверхні біологічного тіла.

In current conditions of growing exoecologic crisis and damaging environmental effects, the interpretation of the self-regulation processes and their role in the structural and functional reconstruction of biological body surface becomes particularly actual.

The purpose of this work was to study, by electron microscopy methods, the structural and functional state of biological bodies surfaces both before and during measures directed toward the structural ensuring of their regulative reconstruction processes. The bioptates of skin, i.e. human biological body surface, were investigated by means of an electron microscope.

A biological system, which the human organism is, develops on its intrinsic elements; their interaction provides the system unity on several structural and functional organization levels – molecular, cellular, tissues, organes, systems, and the whole organism ones [1,2]. This is an open self-organizing system having different levels of ordering dynamic integration: it can be represented as a spatial hierarchy on which qualitative biologic characteristics are imposed.

The essence of a biological system function and biological processes self-movement reduces itself to that such a system, being a genetically self-reproducing one, possesses the ability to preserve its morphofunctional structure and to adapt to an environmental medium by means of self-regulation mechanisms. The basis for the self-regulation is the functional system which is a combination of interacting elements unified in a totality by a useful, for the system, result which it creates in the course of function of its different sections [3]. It is just the useful result obtainable by common function of the system individual parts which is the only factor determining the selective consolidation of different sections (elements) into a common system. There is a large number of functional systems according to the variety of useful results.

The self-regulation is a determinated dynamic process, since self-regulation mechanisms are realized in determinated conditions. Their "starting" occurs as a result of some specified factors action and they are directed, respectively, to the achieving of the useful result required. Thereat, the self-regulation processes occur in a certain regime induced by various environmental influences. It is reasonable that the activity of the self-regulation mechanism sections is adequate to

corresponding variations of the strength and frequency of action of those environmental factors.

A substantial feature of the functional system consists in its ability to the fast reconstruction which becomes necessary when a defect arises in anyone of its sections hindering the useful result achieving. As a result, an adaptive useful result is ensured by such a reconstruction of system.

From the viewpoint of the concept of block organization of biologic system structures and functions [4–8], the self-regulation mechanisms are realized on the basis of the recombination and transposition of universal functional blocks consisting in their redistribution which required the adequate material provision.

The surface of biological bodies, especially that of the human organism, is represented by the skin which, being a complex organ (section, subsystem), consists, in turn, skin coats system. The latter includes two layers of distinct origin, connected firmly together, and appendices, viz. hair follicules, nails, sweat and sedaceous glands, etc.

The human organism skin as the surface of biological body system and as one of its sections (subsystems) is connected tightly to all inner organs and systems of the organism. The skin coat plays an important role in the homoeokinesis ad the homoeostasis performing the protective barrier and thermal regulation functions, participating in the immunological reactions, production of biologically active substances, etc. [9].

The surface of a biological body-human organism represented by the skin coats system is characterized by the system ordering and the dynamic integration of functions on the basis of its subsystems intercommunication. This fact determines a certain influence of the integral functional system of the biological body on its surface reconstruction an, on the other hand, ensures that the biological body surface is a sensitive indicator for the function level of the biological body as a whole. It should be noted that, when a reconstruction becomes necessary, the biological body surface, similar to other organs (sections, subsystems), can use not only its intrinsic possibilities, but also the resources of the whole biological system.

Environmental changes cause deviation of some parameters in the morphofunctional structure of the biological body surface, which are compensated by the self-regulation processes, provided that the skin resistance and adaptivity threshold is not exceeded. Otherwise, a localized or generalised damage of the skin coat occurs, whereat various disturbations of exchange reactions and disintegration of functional elements are observed. Since, in normal conditions, the self-regulation of a biological system is intended to ensure optimal condition of its function, the self-conservation and self-rehabilitation of regulative mechanism must be attained if the morphofunctional structure of the biological body surface has undergone a damage [1].

In connection with the foregoing, the optimization of self-regulation mechanisms in biological bodies becomes necessary under pathologic conditions. It means, first of all, the optimum structural provision of the regulative reconstruction processes in the functioning biological system subunits, viz. its organs (sections, elements) [10–13]. It is just the equivalency of the structural provision which determines the reliability of the system as a whole under regulative processes reconstruction.

At an unsufficient structural provision of the human organism surface, structural and functional changes occur in the skin coat system elements. viz. in the melanocyte cells, as a result thereof, those elements loose their specific function to synthetize melanin; visually, this phenomenon manifests itself as the skin discoloration and the appearance of white spots on it (vitiligo).

As a result of measures directed to the substrate deficit elimination, promoting the regulative reconstruction processes and the self-regulation mechanism self-restoration, the structural and functional self-ordering according to genetically conditioned specialization occur in afunctional melanocytes and epitelial cells. The energy exchange improves, i.e. the glycogene synthesis in the cells becomes activated from the initial process stage on to the abundant energy accumulation accompanied by large glycogene congestions in the cell cytoplasm (Fig.1). The number of active mitochondria increases (Fig.2); on the background of those, the albumen synthesis processes become activated, which cause the restoration of intracellular structures, viz. premelanosomes (Fig.3) and melanosomes (Fig.4). Along with these, on the background of active mitochondria and of great number of ribosomes not connected to the diaphragm, the melanosomes of increased size are observed containing lots of meanin grains (Fig.5). As a result of the melanogenesis process activation, the ripe melanin granules are formed (Fig.6). In parallel with these processes, the skin coats colour restoration is observed, determinable visually and by means of photoelectrical dermochromography [14]. The dynamics of intensity variations of the light reflected by skin as measured by the photo-

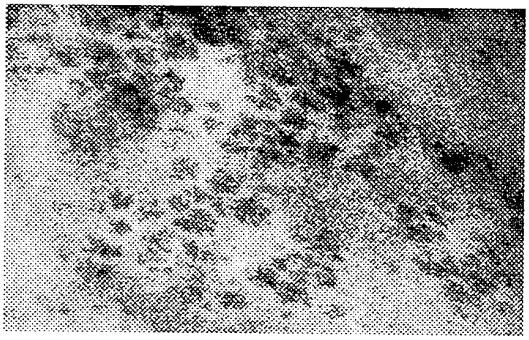

Fig.1. Melanocyte fragment containing a large glycogene congestion (GL) indicating the intercell metabolism change toward the increased energy formation. × 105,000

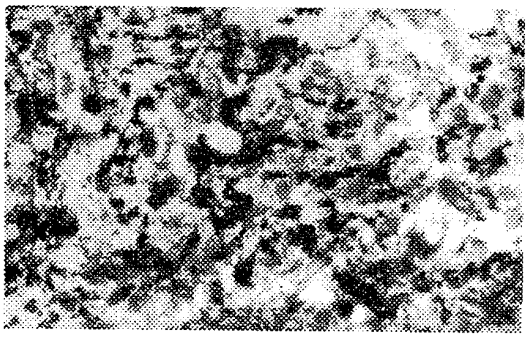

Fig.2. Epithelium cell cytoplasm of spinous layer contains a lot of mitochondria (M). The cells are rich in cytoskeleton elements (CS). The initial phase of keratohyalin (KH) synthesis. The intercell contacts are represented by desmosomes. × 10,000

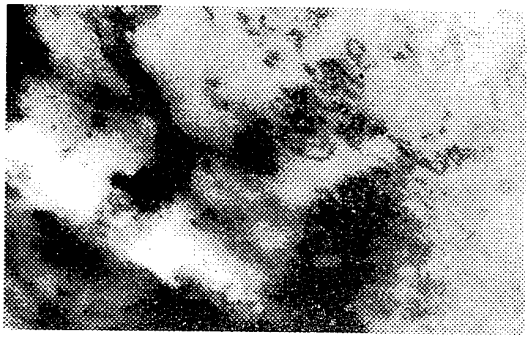

Fig.3. Melanocyte cytoplasm fragment containing vesicula, premelanosomes (PMS) and newly formed melanosomes with single melanin grains. × 35,000

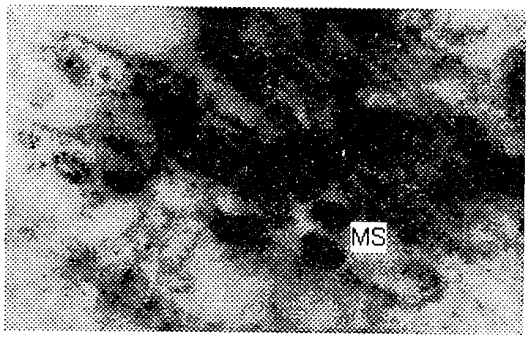

Fig.4. Melanocyte fragment with melanosomes (MS) containing small melanin grains. In comparison with the previous figure (Fig.3), the melanosomes number on the cytoplasm area unit is increased. × 35,000

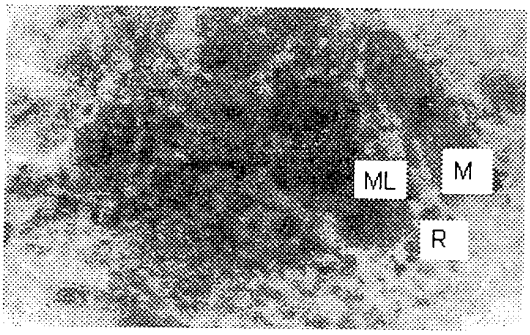

Fig.5. A big active melanocyte cytoplasm fragment containing melanosomes increased in size, of irregular form, with a lot of pigment grains (ML) as well as a great number of ribosomes (R) not connected with the diaphragm and actively functioning mitochondria (V). × 21,000

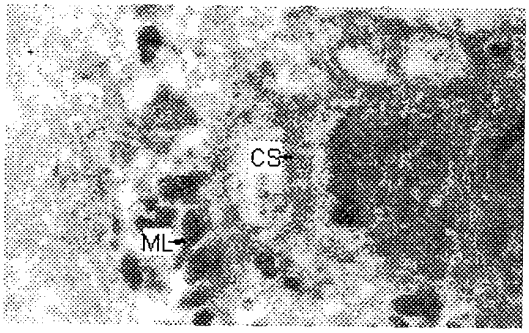

Fig.6. Melanocyte fragment on final stage of melanin synthesis; in the cytoplasm, there are many pigment granules (ML) surrounded by monostratal envelope. The granules are dense, their envelopes are connected with cytoskeleton fascicles (CS). The latter points to the possibility of granule displacement and therefore proves a great extent of melanocyte ripeness and its specific functon perfection. × 38,000

electric method shows that the skin repigmentation process follows the exponential relationship.

Thus, due to an adequate elimination of the substrate deficit, the proper material provision of the regulative processes and the restoration of those is achieved, what is accompanied immediately by the system morpho-functional reconstruction of the biological body surface elements.

Conclusions

1. In the conditions of growing frequency of exoecological damaging effects, the realization of self-regulation mechanisms is associated with the intensification of physiological processes which are the basis of those mechanisms, and with additional material expenditures.

2. Processes of regulative reconstruction of the biological body surface require the adequate structural provision.

3. The optimization of the material basis of self-regulation mechanism is accompanied by the self-ordering of structural and functional elements on the biological body surface.

References

1. V.P.Petlenko, V.F.Serzhantov, Problem of Man in the Medical Theory [in Russian], Zdorovya, Kiev (1984).
2. Yu.A.Ershov, N.N.Mushkambarov, Kinetics and Thermodynamics of Biochemical and Physiological Processes [in Russian], Medicina, Moscow (1979).
3. P.K.Anokhin, Selected Works [in Russian], Medicina, Moscow (1979).
4. A.M.Ugolev, *Klinicheskaya Medicina*, No.6, 15 (1986).
5. A.M.Ugolev, *Zh.Evoluc.Biokhimii i Fiziologii*, **26**, 441 (1990).
6. A.M.Ugolev, Theory of the Adequate Alimentation and the Trophology [in Russian], Nauka, Leningrad (1991).
7. V.T.Ivashkin, V.Yu.Vasil'ev, E.S.Severin, Regulation Levels of Functional Activity of Organs and Tissues [in Russian], Nauka, Leningrad (1987).
8. V.T.Ivashkin, G.A.Minasyan, A.M.Ugolev, Functional Blocks Theory and Clinical Medicine Problems [in Russian], Nauka, Leningrad (1990).
9. Skin (Structure, Functions, General Pathology and Therapy) [in Russian], ed. by A.M.Chernukh and E.P.Frolov, Medicina, Moscow (1982).
10. Zh.P.Gudzenko, in: Digestion and Absorption Physiology [in Russian], Krasnodar (1990).
11. Zh.P.Gudzenko, in :Children Pancreas Diseases [in Russian], Medicina, Tashkent (1990).
12. Zh.P.Gudzenko, Yu.D.Usenko, E.V.Korotkaya et al., in:Proc. IV All-Union Gastroenterologic Congress [in Russian], v.II, 395, Moscow-Leningrad (1990).
13. Zh.P.Gudzenko, T.V.Shatilo, E.V.Korotkaya, in: European Region Clinical Section Congress, 237, Florence, Italy (1994).
14. Yu.A.Myagchenko, L.V.Poperenko, Pat.USSR No.1809373

Процессы саморегуляции структурно-функционального состояния поверхности биологических тел

Ж.П.Гудзенко

Целью настоящей работы явилось изучение структурно-функционального состояния поверхности биологических тел посредством электронно-микроскопических исследо ваний до и в динамике проводимых мероприятий, направленных на структурное обеспечение процессов регуляторной перестройки. В результате оптимизации материальной основы механизма саморегуляции путем достижения адекватного структурного обеспечения был получен эффект структурного и функционального упорядочения элементов системы поверхности биологического тела.

Functional Materials 2, No.2 (1995)

Surface influence on the decay process and evolution of the mechanical properties of the amorphous metallic alloys of metal-metalloid type

S.G.Zaichenko and V.M.Kachalov

Institute for Metals Science and Metals Physics,
9/23 2nd Baumanskaya St., Moscow, Russian Federation

Decay of amorphous alloys (AMA) of metall-metalloid type from the initial state up to the first state of crystallization owing to thermal action has been studied. It is shown that mechanical properties of AMA reflect main stages of the decay process, namely, the material transformations from plastic to embrittled state and then from the latter to crystalline one. Embrittlement is described as two-stage process. Correlation between AMA mechanical properties changing and evolution of heat emisssion of relaxation spectrum has been obtained experimentally for the first time. The degree of AMA decay may be established from the parameters of heat emission of relaxation spectrum. The surface of AMA strip acts as a sink for metalloid atoms heading to the beginning of embrittlement and crystallization process. Microscopic mechanism for every stage of AMA decay is proposed.

Проведено дослідження розпаду аморфних металічних сплавів типу метал-металоїд під впливом термічних дій вихідного стану до початкових стадій кристалізації. Установлено, що механічні характеристики АМС відображають основні стадії цього процесу, тобто спостерігається перехід матеріалу із пластичного стану в крихкий, причому цей процес носить двостадійний характер. Вперше виявлено тісну кореляцію між зміною механічних характеристик АМС та еволюцією тепловиділення релаксаційного спектра, кількісні параметри якого дозволяють визначити стан матеріалу АМС на різних стадіях розпаду. Зміна концентрації металоїдів в приповерхневих областях обумовлює зародження кластерів нової аморфної фази, відповідальних за крихкування, а також протікання поверхневої кристалізації за рахунок селективного окислення металоїдів. Коротко розглянуто практичне застосування отриманих результатів.

From the viewpoint of deformable solid mechanics, amorphous metallic alloys (AMAs) of metal-metalloid type can be considered as a medium with an almost ideal combination of elastic and plastic properties.Especially, in the initial (freshly chilled) state, AMAs have combined, in a unique manner, the high strength which is close to theoretical one for a number of compositions, with the plastic formability. In AMAs, the plastic deformation is realized in the form of shift bands and surfaces of destructed specimens show the vein-like pattern characteristic for the viscous failure [1–5].

The high sensitivity of mechanical properties to minor structure changes is one of specific AMAs features. In other words, mechanical properties can be a peculiar indicator of an AMA structure state variations. And, since those variations begin, as a rule, in skin surface areas, the mechanical characteristics of AMA response to them beginning from the surface [5–7].

It is known that amorphous alloys are in a metastable equilibrium state. Therefore, under influence of destabilizing factors, mainly that of temperature, time, irradiation with several particles, they lose their initial plasticity and convert to the embrittled state and then from the latter to crystalline one [6–10]. In this paper, temperature T and time t will be primarily considered as the destabilizing effects.

Thus, the main purposes of this work, along with the study of the surface influence on the amorphous state decay process, are:

– the determination of temperature-time intervals during which the mechanical characteristics of metal-metalloid type AMAs remain unchanged. The relative deformation at failure, ε_f, was chosed as the main characteristic of the specimen state;
– the development of microscale AMA models for several stages of their decay.

Experimental

Specimens of AMAs of three different compositions:
$Fe_{90.3}Ni_{1.5}Si_{5.2}B_3$ (a), $Fe_{69.5}Co_{24.4}Si_{2.9}B_{3.2}$ (b) and $Fe_{5.7}Co_{72}Ni_{12.2}Si_{6.5}B_{3.6}$ (c) obtained by spinning method, 20 mm wide and 20 to 25 μm thick, were subjected to isochronic annealings (τ = 10 min) in the temperature range from 250 °C to the point of crystallization beginning, with the 20 °C steps. To obtain each point on the $\varepsilon_f - T_0$ plot, where ε_f is the relative deformation at failure (RDF), and T_0 is the annealing temperature, 30 specimens were mechanically tested, what assures the 95 % confidence level. The relative deformation at failure was calculated as $\varepsilon_f = d/(D - d)$ where d is the strip thickness, D is the distance between micrometer plates at the instant of failure of the half-loop of the bent strip specimen. For freshly-chilled specimens or those which have retained their plasticity, ε_f was arbitrarily believed to be equal to 1. Fig.1 shows the ε_f dependence on T_0 for the (b) alloy. For (a) and (c) alloys, similar relationships were obtained. It is clearly demonstrated by Fig.1 that the AMA embrittlement process is a two-stage one, the beginning of each stage being indicated by a bend on the $\varepsilon_f(T_0)$ curve. For the (b) alloy, a shoulder on $\varepsilon_f(T_0)$ plot beginning at T_0 = 350 °C and ending at 2nd bend at T_0 = 475 °C is related to the first embrittlement stage. The temperature range 280–350 °C is respective to a "half-embrittled" AMA state where some part of the specimens group (30 pieces) is failed while other remain plastic. This phenomenon is explained, first of all, by variations in the strip thickness amounting up to 10 % of the average value. The second embrittlement stage begins immediately before the 2nd bend of $\varepsilon_f(T_0)$ relationship and ends at the instant when the crystalline phase arises at the surface crystallization ($T_0 \approx$ 510–520 °C).

It should be noted that, on the 1st embrittlement stage (the shoulder, see Fig.1), ε_f decreases slightly when T_0 raises. This is explained by the increase of thickness of surface strip layers losing the plasticity. This thickness is, as we have shown earlier [6,7], a function of the alloy composition,

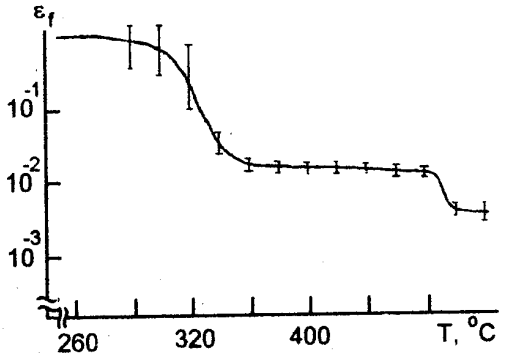

Fig.1. Dependence of the relative deformation at failure (ε_f) on the isochronic annealing temperature (T_0) for AMA (b).

annealing temperature and time; the removal of those layers by any means (etching, electropolishing, machining) results in the complete restoring of the initial plasticity (equal to that of freshly chilled strip) [2].

The evolution of the relaxation spectrum heat emission (RSHE) at the increasing temperature of isochronic annealings was studied on specimens of alloys mentioned immediately after mechanical tests. The measurements were performed by the differential scanning calorimetry (DSC) using Du Pont thermoanalyzer. The results obtained for (b) alloy are shown on Fig.2 where the spectral heat emission $h(T_0, T, \tau)$ is plotted as a function of the annealing temperature, T, and its duration, τ. Fig.2 illustrates clearly the evolution of RSHE with the increase of T_0. Specific features of the $h(T_0, T, \tau)$ evolution are:
– a rapid disappearance of the low-temperature (under 365–375 °C) relaxation spectrum (RS) area while the high- temperature one (from 360–375 to 400–430 °C) remains essentially unchanged under low-temperature annealings;
– a progressive disappearance of the high-temperature RS area with increasing T_0;
– the initiation of areas where the sign of heat evolution is reversed both in low-temperature and high-temperature RS ranges;
– the complete disappearance of the whole RS at annealing temperatures 480–530 °C before the surface crystallization begins.

These regularities are characteristic for all AMA investigated.

In Fig.3, the variation of the low-temperature part, Q_n, of RS as a T_0 function is shown for alloys (a–c). The figure illustrates clearly that the Q_n dependence on T_0 is essentially linear. The point of Q_n intersection with the temperature axis corresponds to the complete disappearance of

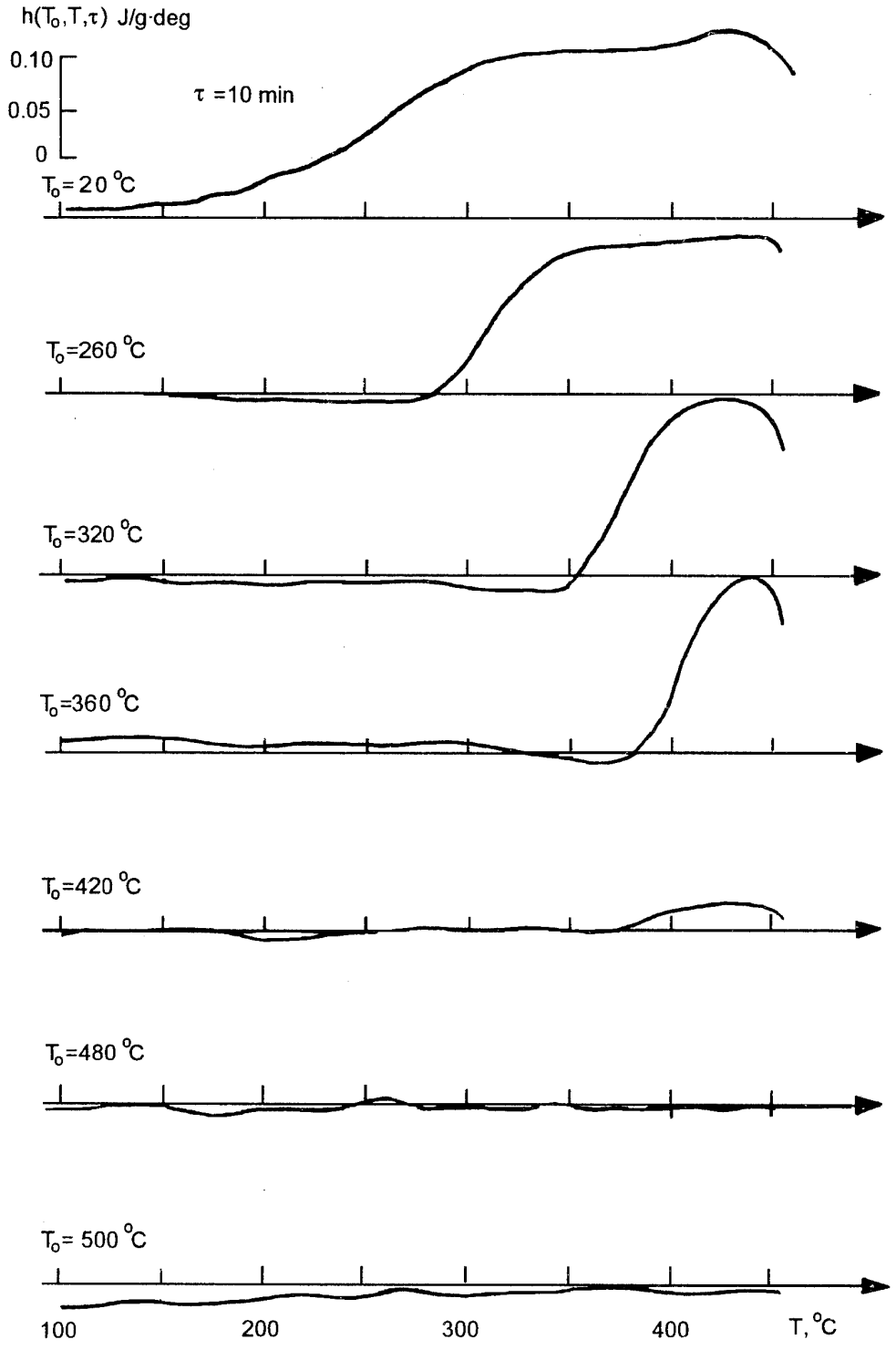

Fig.2. Dependence of the spectral density of heat emission $\mathbf{h}(T_0, T, \tau)$ on the isochronic annealing temperature (T_0) for AMA (b) at τ = 10 min.

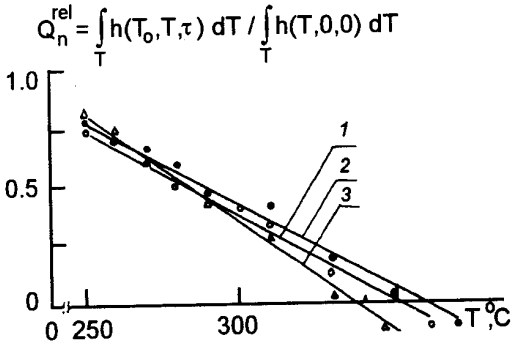

Fig.3. Dependence of the relative heat emission, Q_n, of the relaxation spectrum low-temperature part on the isochronic annealing temperature for AMAs: 1— (a), 2 — (b), 3 — (c), solid lines are approximations of experimental points by the least square method.

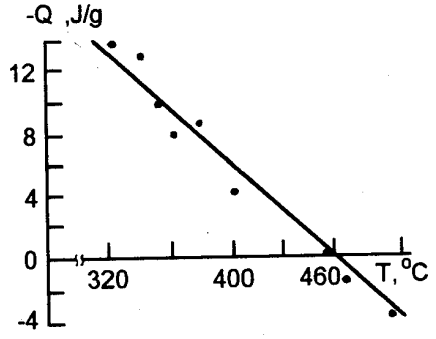

Fig.4. Dependence of heat emission (Q) of the RS high-temperature part on the isochronic annealing temperature for AMA (b). The solid line is obtained by the least square method.

heat evolution of the low-temperature RS range. Correlating the temperature corresponding to the equality $Q_n = 0$ with the mechanical tests results of the (b) alloy (see Fig.1) we obtain that it is equal to ~350 °C (within the limits of experimental error). This value coincides with the temperature of the 1st embrittlement stage onset for the amorphous alloy mentioned. For two other AMAs, (a) and (b), the temperature determined by the $Q_n = 0$ condition, was found, too, to be corresponding with the onset of the 1st embrittlement stage. Thus, the zero heat evolution value of the low-temperature part of the relaxation spectrum is the criterion of the 1st embrittlement stage commencement.

Physically, this evidences the transition of an AMA from the plastic state to embrittled one. Expressed mathematically, the criterion mentioned has a form

$$Q_n = \int_{T_n}^{T^*} h(T_0, T, \tau)\,dT = 0 \qquad (1)$$

where the lower and upper integration limits correspond to temperature of the heat emission onset (T_n) and to that of the upper limit of the low-temperature RS area (T^*).

Fig.4 shows the dependences of the heat emission variations on isochronic annealing temperatures, T_0, for the high-temperature part of the relaxation spectrum. For all the AMAs studied, intersection points of $Q(T_0)$ plot with the temperature axis, $Q(T_0)= 0$, are positioned immediately ahead of 2nd bend of the $\varepsilon_f(T_0)$ relationship (see Fig.1, alloy (b)). Therefore, the zero heat emission Q of the whole RS is the criterium of the completion of 1st embrittlement stage and onset of 2nd one; mathematically, this criterion is expressed as

$$Q_n = \int_{T_n}^{T_v} h(T_0, T, \tau)\,dT = 0 \qquad (2)$$

where the upper integration limit is the temperature of the RS upper boundary.

Thus, by measuring the heat emission of the relaxation spectrum, the onset, completion, and duration of 1st and 2nd stages of the AMA embrittlement can be determined. It should be noted that the duration of 2nd embrittlement stage corresponds physically to the incubative period of the surface crystallization, and the completion of the latter is evidenced by the crystallization phase occurrence.

According to modern concepts, for the vast majority of AMAs of metal-metalloid type, the bulk crystallization is preceded by the surface one (SC) [13]. The SC differs from bulk one, first of all, by the composition of crystallizing phases. For Fe-based AMAs, the SC proceeds according to so-called primary mechanism. It consists in the formation of α-Fe crystallites in the surface-near areas of the strip having thickness of 0.5–2 μm. The boron and carbon atoms play a leading part in the change of the crystallization character [14,15]. The selective oxidation of B atoms which were bonded with Fe atoms in the freshly chilled state causes the α-Fe crystallization, since the chemical composition of the surface-near areas comes out of amorphization range due to carbonization [6,7,14]. This explanation is supported by the analysis of surface-near layers of the freshly chilled and annealed AMA (a) performed by the Auger spectroscopy. Since concentrations of elements under analysis are proportional to the

corresponding Auger peaks amplitudes [16], concentration profiles in depth of strip specimens were constructed in the scale of relative amplitudes of Auger peaks which were calculated as

$$A_{rel} = \frac{A_{(i)}}{\sum_i A_{(i)}} \quad (3)$$

where $A(i)$ is the Auger peak amplitude corresponding to the element analyzed; $\sum_i A_{(i)}$, the sum of Auger peaks amplitudes for all elements.

Correlation of the concentration profiles for strip specimens of AMAs (a,b,c) in freshly chilled and annealed states leads to following conclusions:

- boron atoms diffuse toward the surface where they undergo the selective oxidation;
- a surface layer forms, depleted in boron;
- the annealing effect causes the diffusion of atmospheric oxygen atoms and carbonization of surface layers.

To describe the SC kinetics, the Mehl-Jones-Avraami law is conventionally used [17]:

$$\chi(t) = 1 - \exp[-b \cdot (t - t_0)^n] \quad (4)$$

where $\chi(t)$ is the crystalline phase concentration; t_0 is the incubative period duration; $b = b_0 \cdot \exp(-U/RT)$, b_0 is a constant; U is the SC activation energy; R is the gas constant; T is the temperature (K).

Thickness of layers containing the crystalline phase was studied experimentally as a function of the annealing temperature and duration. Strip AMA specimens after the thermo-magnetic treatment (TMT) are three-layer plates consisting of partially crystallized layers adjacent both to the contact and free surfaces and separated by an amorphous core [18,19]. Specimens after TMT had a straight form which indicated to the equal thickness, d, and properties of layers mentioned. The layer containing the crystalline phase was etched on one side of the strip specimen. Beginning from a certain thickness of the removed layer depending on the annealing duration (T_0= 480 °C, τ = 45, 60, 75, 90, and 115 min), the curvature radius of specimens remained constant. The technique of the crystallized surface layer thickness determination is described in detail in [18]. Table 1 shows the experimental results of d values determinations for the AMA(a). It is seen from those data that the SC, on its initial stages, is characterized by following features:

Table 1. Thickness of the crystallized layer, d, and stable curvature radius for AMA (a) as functions of the isothermal annealing duration, τ, at T = 480 °C.

Annealing time, min	45	60	75	90	115
Layer thickness, d, μm	0.2	0.39	0.47	0.67	0.92
Stationary curvature radius, R, mm	239.5	194	96	78	67.2

- the linear relationship between the thickness of layer containing crystalline phase and the high-temperature annealing duration;
- the incubative period duration (t_0) is close to 25 min at T_0 = 480 °C.

To describe the movement of the surface crystallization front, let assume that the incubative period duration, t_0, for a layer having thickness dz and positioned at distance z from the strip surface, is a function of boron atoms concentration. The latter is, as it follows from the boron atoms concentration profile in depth, the linear function of z, i.e.

$$\frac{dt_0(z)}{dz} = k \cdot C_b, \quad k = \text{const} \quad (5)$$

By integrating of Eq.(5) with regard for boundary conditions

$$t_0(z)\big|_{z=0} = t_0, \quad t_0(z)\big|_{z=D} = \frac{D}{V} + t_0 \quad (6)$$

where D is the maximum thickness of layer crystallized from the surface on and containing α-Fe; V is the SC front velocity, we obtain

$$t_0(z, t) = \frac{z}{V} + t_0, \quad k \cdot C_b = V \quad (7)$$

Inserting $t_0(z,t)$ into Eq.(4), we have as an ultimate result

$$\chi(t, z) = 1 - \exp\left[-b\left(t - \left[t_0 + \frac{z}{V}\right]\right)^n\right] \quad (8)$$

Unknown parameters U and n involved in Eq.(8) were evaluated by independent experiments. The SC activation energy, U, was determined using Kissinger method [6,19,20] from the temperature-caused displacement of the crystallization peak at varying heat rates (dT/dt = 2; 5; 10; 20 deg/min). The value of parameter n was obtained from experimental relationships

$$n = \frac{\ln\left(\ln\left[1 - \chi(t_i, z_i)/\ln[1 - \chi(t_j, z_j)]\right]\right)}{\ln(t_i - t_0)/\ln(t_j - t_0)} \quad (9)$$

where i, j are ordinal numbers corresponding to annealing durations τ = 45, 60, 75, 90, 115 min ($i \neq j$); $\chi(t_i, z_i)$ is the α-Fe concentration on the crystallization front, whose value, according to structural investigations, does not exceed 1–5 %. As is shown in [13–15], the $\chi(t)$ value on the SC front depends only slightly on the time t at initial stages. Besides, it follows from [16] that, in the primary crystallization case (i.e. in that just under consideration), n = 1. The n value averaged over the entire experimental data set (9) amounted, in fact, to n = 1.0635 for AMA (a) and n = 1.0314 for (c). Numerical values of SC activation energy were U = 90 kJ/mol for the (a) AMA and U = 68 kJ/mol for (c).

Furthermore, the direct experimental study was performed to confirm the above criterion (Eq.(1)) of the 1st embrittlement stage onset. The (b) AMA specimens were subjected to annealing at T = 300 °C (Fig.5). From some specimens, embrittled layers were removed by etching, electropolishing or machining methods. Thereafter, relative heat emissions in the low-temperature RS range were correlated expressed by ratios

$$\frac{\int_T h(T_0, T, \tau)\, dT}{\int_T h(T, T = 20\ ^\circ C, \tau = 0)\, dT} \qquad (10)$$

where numerator is the heat evolution of specimens with and without embrittled layers, denominator is that of the freshly chilled ctrip (see Fig.5). For specimens with embrittled layers. this ratio had always a negative value, while for those from which embrittled layers were removed, a positive one. Mechanical tests have shown that specimens devoid of embrittled layers demonstrated the plasticity in full measure (as much as the freshly chilled strip) what was evidenced by the occurrence of a residual unbending angle after the testing of free bending by 180 degrees [21].

Discussion

The performed study of the viscous-to-brittle transition (1st embrittlement stage) of amorphous metal-metalloid type alloys allow to conclude that:

– the embrittlement of AMAs is a process developping in time; the overlap of the whole transversal section of a strip by embrittled layers indicates to the completion of the 1st embrittlement stage and onset of 2nd one;

– this process commences from the strip surface; the thickness of layers having losen the plasticity is a function of the intensity and duration of destabilizing effects, especially, at annealing, a function of its temperature, T_0, and duration, τ;

– embrittled layers are in an amorphous state, what is evidenced by the structure investigation results using X-ray analysis [22], Moessbauer spectroscopy [9,23], differential scanning calorimetry [6,7], electron microscopy [10], spectral ellipsometry [24].

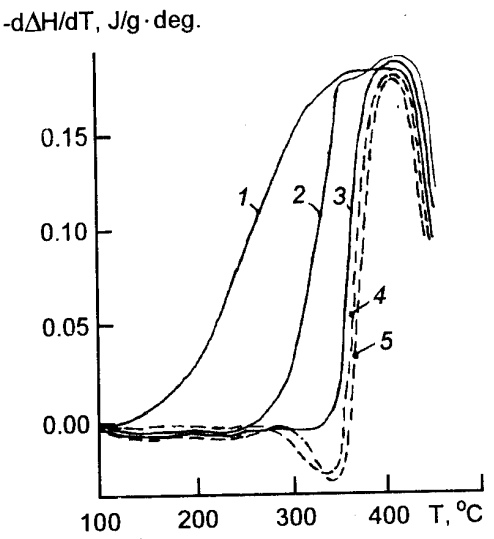

Fig.5. Variation of the RSHE for AMA(b) at isothermal annealings, T_0 = 300 °C: for freshly chilled specimen, (1), annealed for τ = 10 min, (2), τ = 40 min, (3), τ = 90 min, (4), and τ = 180 min, (5); specimens 4 and 5 are embrittled.

The amorphous state of those deplasticized surface layers differs, however, both from initial one and from that of the amorphous core. The above-mentioned experimental results of mechanical tests and variations of the RSHE associated strongly with those results give the most compelling evidence for this statement. Moreover, the difference between of Young module values for embrittled layers and for the plastic core is shown to amount up to 15 % [25].

There is a number of indirect evidences supporting the above interpretation of mechanical test results and calorimetric measurements. Especially, the occurrence of second Curie temperature, T_c, was found for AMA $Fe_{40}Ni_{40}P_{20}$ after annealing resulting in emhbrittlement. Spectro-ellipsometric measurements performed on an AMA of Fe–Ni–Si–B system have shown the occurrence of a doublet structure in the IR range of the optical conductivity spectrum after annealings [24]. This anomaly indicates that, in surface-near areas, structural inhomogeneities are appeared having dimensions of several hundreds of Angstrom units. The doublet structure occurrence is

explained by collisions of conductivity electrons with those inhomogeneities.

The sound emission study performed on freshly chilled and embrittled AMAs specimens of several compositions including alloys (a), (b), and (c), under uniaxial tension and bending test conditions, demonstrated substantial changes of the acoustic emission spectrum characteristics after a thermal treatment. These changes involve a new pattern of distribution of shift pulses, a reduction of their number and transformation of form, as well as the occurrence for embrittled specimens, of several powerful pulses which correspond to the formation and growth of embrittlement fractures [26].

Experimental data relating to the X-ray small-angle dissipation showed the dissipation intensity increasing by 3–4 times for embrittled specimens as compared with freshly chilled ones [27].

Thus, it is believed that, in embrittled layers, some structural changes take place not removing the material from the amorphous state but resulting in the formation of a new amorphous phase. That is supported by the Auger spectroscopy data [28,29] which evidence a change of the chemical composition of surface layers in AMAs strip specimens after annealing. That change consists in the increase of metalloid atoms concentration by 3–4 times in comparison with the initial state due to transition of those atoms into surface-near areas. We have found the inhomogeneity of the metalloid atoms distribution not only in depth but also in planes parallel to strip specimen surface. The measurements were performed using X-ray microprobe [30]. It follows from this fact that metalloid atoms are gathered together forming clusters having transversal dimensions of several hundreds of Å and consisting, in our opinion, a new amorphous phase.

The first reversible embrittlement stage terminates when deplasticized layers overlap the whole section of amorphous strip. From this instant on, the second irreversible AMA embrittlement stage begins. On this stage, the mechanical behaviour of an AMA of metal-metalloid type is characterized by a sharp ε_f drop from values of $\sim 10^{-1}$ to those of $\leq 10^{-2}$ (see Fig.1). This fact is associated with precrystallization processes: the crystallization centers formation and pre-critical growth of crystalline phase nuclei. These latter are, on the one hand, concentration sites for external stresses and, on the other hand, the source of internal ones. In [18], a mechanism is supposed for the occurrence of a stressed state in partially crystallized (from the surface on) AMAs, and the main contribution is shown to be due not to "phase" stresses [14, 15] but to those occurring as a result of the difference between thermal expansion coefficients of the crystalline phase and amorphous matrix. Processes resulting in the increase of internal stresses and concentration of external ones cause a sharp drop of the relative deformation at failure, ε_f, to $\leq 10^{-2}$ values.

The result obtained can be used to resolve some practical problems: prediction of thermal stability of AMAs mechanical characteristics at any temperature [6]; evaluation of allowable temperature-and-time working ranges for AMAs used as construction materials; calculations of the guaranteed service life for cores made of AMAs in medium- and high-power transformers; regulation of hysteresis loop characteristics (the rectangularity coefficient and slope) by means of stressed state variation in partially crystallized strips of magnetic circuits [10].

Conclusions

1. The decay process of amorphous alloys of the metal-metalloid type is accompanied by the degradation of mechanical properties and is characterized by a transition from plastic state to embrittled one and from the latter to the crystalline. The AMA embrittlement is the two-stage process. On the first reversible stage, it is associated with the formation of deplasticized layers growing from the surface on. The second stage is the incubative period of the surface crystallization.

2. A close correlation between the heat emission of the relaxation spectrum and embrittlement kinetics is first revealed for AMAs of the type mentioned. The entire disappearance of the heat emission of the relaxation spectrum low-temperature part dropping, at a fixed temperature, proportionally to logarithm of the thermal action duration, corresponds to the onset of 1st embrittlement stage, i.e. to AMA transition from the plastic state to the embrittled one. The onset of the second embrittlement stage is determined by zero heat emission of the relaxation spectrum.

3. It is found that the free surface plays a leading part in the process of amorphous state decay. Both embrittlement and crystallization begin from amorphous strip surface. In the first case, that is associated with the transition of metalloid atoms into surface-near areas and formation of a new amorphous phase clusters, while, in another, with selective oxidation of those atoms removing the composition of surface layers from the amorphization area and causing the surface crystallization.

The results obtained allowed to develop procedures for the determination of thermal stability of AMA mechanical characteristics, as well as to evaluate the time of transition from the plastic state to embrittled one and the duration of the surface crystallization incubative period for any temperatures.

References

1. D.G.Ast, D.J.Krenitsky, *Mater.Sci.and Eng.*, **43**, 241 (1980).
2. A.M.Glezer, B.V.Molotilov, Structure and Mechanical Properties of Amorphous Alloys [in Russian], Metallurgia, Moscow (1992).
3. V.P.Alyokhin, V.A.Khonik, Structure and Physical Regularities of Amorphous Alloys [in Russian], Metallurgia, Moscow (1992).
4. K.Suzuki, H.Fujimori, K.Hashimoto, Amorphous Metals [in Russian], Metallugria, Moscow (1987).
5. J.J.Gilman, *Appl.Phys.*, **46**, 1625 (1975).
6. S.G.Zaichenko, V.M.Kachalov, V.T.Borisov, *Izv.RAN, Metally*, **4**, 165 (1992).
7. S.G.Zaichenko, V.M.Kachalov, *Metally*, **3**, 132 (1994).
8. R.Gerling, F.P.Schimansky, R.Wagner, *Acta Metall.*, **36**, 575 (1988).
9. B.George, *Ann.Chim.*, **10**, 725 (1985).
10. V.A.Makarov, S.G.Zaichenko, A.I.Zaitsev et al, *Magn. and Magn.Mater.*, **133**, 351 (1994).
11. H.S.Chen, E.K.Koleman, *Appl.Phys.Lett.*, **29**, 245 (1976).
12. S.G.Zaichenko, V.V.Minin, V.M.Kachalov, Abstr. of 3rd All-Union Conf. on the Struct.Investig. of Amorphous Metallic Alloys [in Russian], (Moscow, 1988), Metallurgia, Moscow , Part 2, p.305.
13. U.Koster, *Mater.Sci. and Eng.*, **97**, 233 (1988).
14. G.Herzer, H.R.Hilzinger, *Magn. and Magn.Mater*, **62**, 143 (1986).
15. H.N.Ok, A.H.Morrish, *Appl.Phys.*, **52**, 1885 (1981.
16. A.I.Kovalev, G.V.Shcherbedinsky, Modern Methods of Metals and Alloys Surface Investigation [in Russian], Metallurgia, Moscow (1989).
17. F.Varret, M.Bourrous, *Solid State Comm.*, **63**, 683 (1987).
18. S.G.Zaichenko, V.M.Kachalov, *Poverkhnost. Fizika, khimia, mekhanika*, **3**, 119 (1994).
19. H.F.Kissinger, *Anal.Chem.*, **29**, 1702 (1957).
20. T.Ozawa, *Therm.Analys.*, **2**, 301 (1970).
21. S.G.Zaichenko, V.T.Borisov, V.V.Minin et al., *Zav.labor.*, **5**, 76 (1989).
22. A.M.Glezer, B.V.Molotilov, O.L.Utevskaya, *FMM*, **58**, 991 (1984).
23. V.K.Sethy, R.Gibala, A.H.Heyer, *Scr.Metall.*, **12**, 207 (1978).
24. S.G.Zaichenko, T.N.Krasnozhen, L.V.Poperenko et al., Abstr. of 4th All-Union Conf. on the Struct.Investig. of Amorphous Materials [in Russian], (Izhevsk 1992), Udmurt GU Publ. (Izhevsk) p. 59.
25. S.G.Zaichenko, V.V.Minin, in 9th Inter-High-School Collect. of Works on the Metal Amorphous Materials [in Russian], Udmurt GU Publ., Izhevsk (1988), p.46.
26. S.G.Zaichenko, V.V.Braginsky, *Metallofizika*, **12**, 15 (1990).
27. E.M.Vlasova, B.V.Molotilov, M.A.Arcishevsky, *FMM*, **63**, 490 (1987).
28. J.L.Walter, F.Becon, F.E.Luborsky, *Mater.Sci. and Eng.*, **24**, 239 (1976).
29. F.Okuyama, N.Fujimori, S.Sobue et. al., *Appl.Phys.*, **60**, 2618 (1986).
30. S.G.Zaichenko, V.T.Borisov, V.V.Minin, in Abstr. of 10th All-Union Seminar on Metallic and Non-metallic Glasses Structure and Nature [in Russian], (Izhevsk 1989), Udmurt GU Publ., Izhevsk, 1989, p.154.

Влияние поверхности на процесс распада и эволюцию механических свойств аморфных металлических сплавов типа металл-металлоид

С.Г.Зайченко, В.М.Качалов

Проведено исследование аморфных металлических сплавов типа металл-металлоид под влиянием термических воздействий от исходного состояния до начальных стадий кристаллизации. Установлено, что механические характеристики АМС отражают основные стадии этого процесса, то есть наблюдается переход материала из пластичного состояния в охрупченное. Впервые обнаружена тесная корреляция между изменениями механических характеристик АМС и эволюцией тепловыделения релаксационного спектра, количественные параметры которого позволяют определять состояние материала АМС на различных стадиях распада. Изменение концентрации последних в приповерхностных областях обусловливает зарождение ответственных за охрупчивание кластеров новой аморфной фазы и протекание поверхностной кристаллизации за счет селективного окисления металлоидов. Кратко рассмотрены практические приложения полученных результатов.

Functional Materials **2**, No.2 (1995)

Distortions induced by surfacelike elastic constants in NLC confined to cylindrical cavity

A.D.Kiselev and V.Yu.Reshetnyak*

Chernigov Technological Institute, 95 Shevchenko St.,
250027 Chernigov, Ukraine

*Institute for Surface Chemistry, National Academy of Sciences of Ukraine,
31 Nauki Ave., 252028 Kiev, Ukraine

In this paper we consider NLC confined in a cylindrical cavity under the anchoring conditions of various types. The influence of the saddle-splay and splay-bend terms (the K_{24}-term and the K_{13}-term) on the axial director configuration stability is investigated. By using the Fourier expansion of director fluctuations over azimuth angle our analytical method of attack enables the stability conditions to be found in terms of the stability with respect to each fluctuation mode. Two ways to stabilize the structure are explored: the stabilization by magnetic field and by the action of the boundary conditions. We get the restrictions imposed on the values of the constants to make the stabilization possible. The dependence of the resultant stability threshold on the surfacelike elastic constant values is calculated. We discuss in detail experimentally detectable effects due to the presence of the K_{19}-term. It is shown that the escaped-radial director structure exhibits some special features induced by the K_{13}-term.

В статті розглянуто нематичний рідкий кристал, замкнутий у циліндричній порожнині, при різних умовах зчеплення. Досліджено вплив членів K_{24} і K_{13}, що описують комбіновані деформації (скошену сідловидність та косий вигин), на стійкість аксіальної конфігурації директора. Аналітичний підхід авторів із використанням розкладу флуктуацій директора в ряд Фур'є, дозволяє визначити умови стійкості по відношенню до кожної моди флуктуацій. Досліджено два способи стабілізації структури: з допомогою магнітного поля та впливу крайових умов. Знайдено обмеження значень констант, що забезпечують можливість стабілізації. Розраховано залежність результуючого порогу стійкості від значень поверхнево-подібних констант пружності. Докладно розглянуто експериментально виявлені ефекти, обумовлені наявністю члена K_{19}. Показано, що радіальна структура директора має деякі специфічні особливості, обумовлені членом K_{13}.

I. Introduction

As it have been shown in the papers [1–3], in addition to the usual Frank terms (splay plus twist plus bend) the nematic free energy contains so-called surfacelike elastic terms, that is, two terms of divergence form, saddle-splay and splay-bend ones which can be transformed into integrals over the boundary surface and are proportional to the surface elastic constants being referred as K_{24} and K_{13}, respectively. They may be taken in the following forms:

$$F_{24} = -\frac{K_{24}}{2}\int_v dv\ \mathrm{div}\,[\underline{\mathbf{n}}\,\mathrm{div}\,\underline{\mathbf{n}} + [\underline{\mathbf{n}}\,\mathrm{curl}\,\underline{\mathbf{n}}]] \tag{1}$$

$$F_{13} = -\frac{K_{13}}{2}\int_v dv\ \mathrm{div}\,[\underline{\mathbf{n}}\,\mathrm{div}\,\underline{\mathbf{n}}] \tag{2}$$

where $\underline{\mathbf{n}}$ is the nematic director field.

The surface terms are irrelevant if we are interested in the bulk properties of NLC, but they are of considerable importance in the understanding of the physical properties of NLC confined in geometries more restrictive than bulk.

Taking up first the K_{24}-problem, the case when the K_{13}-term is disregarded, notice that the problem of minimizing the free energy with the K_{24}-term was shown to be always well-posed because this term does not contain the director derivatives along the directions normal to the boundary surface [4,5]. Hence, the K_{24}-term only affects the standard boundary conditions. Recently, physical effects whose very occurrence critically depends on the value of K_{24} has been shown to exist [5-7], and even estimates of the constant has been made [8.9].

In contrary to the K_{24} problem, the issue concerning K_{13}-term is much more questionable. In the strict sense, the free energy functional with the K_{13}-term is unbounded from below and that is the reason why strong spontaneous substrate director deformations were found to be possible [10]. One way to avoid such an unphysical effect, proposed in [11,12], is to search the director distribution minimizing the free energy functional among the solutions of the Euler-Lagrange equations. To examine the validity of this approach we study in this paper how the surfacelike terms affect the stability threshold of axial director configuration for NLC confined in a cylindrical cavity in the presence of stabilizing magnetic field under the anchoring conditions of different kind.

In Sec.II, the stability analysis is given in the one-constant approximation. But using the Fourier expansion of director fluctuation over azimuth angle we derive inequalities which give the stability condition for axial structure with respect to each fluctuation harmonics. We explore two ways to stabilize the structure in question: by the magnetic field and by the action of boundary conditions. In both cases we have had the restrictions imposed on the values of K_{13} and K_{24} if one takes the assumption that the configuration can be stabilized. Namely, the stabilization is appeared to be possible provided that the quantity $K_{13}/4K$ takes the values lying between $q_{24} - (q_{24})^{1/2}$ and $q_{24} + (q_{24})^{1/2}$, where the notation q_{24} denotes $K_{24}/2K$. We also discuss whether the number of fluctuation harmonics, which determines the resultant stability threshold, could be changed by the magnetic field or by the anchoring energy at the given values of K_{24} and K_{13}. The results of numerical calculations are presented.

The escaped-radial director configuration is investigated in Sec.III. The stability threshold with respect to zero fluctuation harmonics is shown to describe the transition between the axial structure and the escape-radial one. A comparison of the energies reveals that there are the values of K_{13} at which the stability condition does not provide the global stability of the axial pattern. The K_{13}-term is found may produce an additional degree of the energy degeneracy and that, in its turn, would result in the appearance of disclination circle a the surface.

II. Stability of axial director configuration

Let us consider a NLC confined in a the cylindrical cavity of radius R in the presence of magnetic field applied along the cavity axis, $\underline{\mathbf{H}} = H\,\underline{\mathbf{e}}_z$. The NLC free energy may be taken in its standard form:

$$F = \frac{K}{2}\int_v dv\left[(\mathrm{div}\,\underline{\mathbf{n}})^2 + (\mathrm{curl}\,\underline{\mathbf{n}})^2 - q^2 n_z^2\right] + F_{24} + F_{13} - \frac{W_h}{2}\int_s ds\,(\underline{\mathbf{n}}, \underline{\mathbf{e}}_R)^2 - \frac{W_p}{2}\int_s ds\,(\underline{\mathbf{n}}, \underline{\mathbf{e}}_z)^2 \qquad (3)$$

where the one-constant approximation is used and $q^2 = \chi_a H/K$ (q^{-1} is the magnetic coherent length, χ_a is the anisotropic part of magnetic susceptibility, which is assumed to be positive). In Eq.(3), the energy of the interaction between the NLC and the cavity wall is presented as a sum of two addens written in the Rapini-Papoular form [13]. The first one is the anchoring energy under the homeotropic boundary conditions (the vector of easy orientation is normal to the confining surface) and the last term represents the energy of planar director anchoring to the wall (the vector of easy orientation is directed along the cavity axis). To begin with the stability analysis it is convenient to write the director in the cylindrical coordinate system (0Z axis is parallel to the cavity axis) as follows:

$$\underline{\mathbf{n}} = \cos\Theta\cos\Phi\,\underline{\mathbf{e}}_z + \cos\Theta\cos\Phi\,\underline{\mathbf{e}}_R + \sin\Theta\,\underline{\mathbf{e}}_\varphi \qquad (4)$$

where $\Theta = \Theta(r,\varphi)$ and $\Phi = \Phi(r,\varphi)$. Evidently, the axial director distribution ($\underline{\mathbf{n}}_0 = \underline{\mathbf{e}}_Z$) can be obtained from Eq.(4) on putting $\Theta = \Phi = 0$. Hereinafter, we shall use the notations θ and ϕ for small deviations of the angles Θ and Φ from zero.

To study the axial configuration stability one has to substitute the director field given by Eq.(4) into the expression for the NLC free energy Eq.(3) and derive the second-order variation of the free energy functional as a second-order part of the energy in the angle fluctuations θ and ϕ. For short, we omit the expression for the second-order variation from which one can obtain the Euler-Lagrange equations:

$$\begin{bmatrix} \Delta - 1 - q^2 r^2 & 2\dfrac{\partial}{\partial\varphi} \\ -2\dfrac{\partial}{\partial\varphi} & \Delta - 1 - q^2 r^2 \end{bmatrix} \begin{bmatrix} \theta \\ \phi \end{bmatrix} = 0 \tag{5}$$

where

$$\Delta = \left(r\frac{\partial}{\partial r}\right)^2 + \left(\frac{\partial}{\partial\varphi}\right)^2.$$

Since the angle fluctuations are 2π-periodic functions of the azimuth angle, they can be expanded in the Fourier series over φ.

$$\theta = (2\pi)^{-1/2} \sum_{m=-\infty}^{\infty} \theta_m(r) \exp(im\varphi) \tag{6a}$$

$$\phi = (2\pi)^{-1/2} \sum_{m=-\infty}^{\infty} \phi_m(r) \exp(im\varphi) \tag{6b}$$

To solve the Euler-Lagrange equations let us introduce new Fourier amplitudes in the following way:

$$\phi_m^1(r) = (\phi(r) + i\theta_m(r)/2 \tag{7a}$$

$$\theta_m^1(r) = (\phi(r) + i\theta_m(r)/2 \tag{7b}$$

The solutions are expressed in terms of modified Bessel functions [14]:

$$\theta_m^1(r) = C_m^1 I_{|m-1|}(q\,r);\ \phi_m^1(r) = C_m^2 I_{m+1}(q\,r), \tag{8}$$

where C_m^j are the complex coefficients (Re $C_m^j = A_m^j$ and Im $C_m^j = B_m^j$, j = 1, 2), $I_m(x)$ is the modified Bessel function of order m.

After inserting Eqs.(6–8) into the expression for the second-order variation of the free energy we have the one as a sum of quadratic forms in A_j and B_j.

$$\delta^2 F = \sum_{m=0}^{\infty} \left[\delta^2 F_m(A) + \delta^2 F_m(B)\right] \tag{9}$$

For the axial configuration to be stable all the quadratic forms $\delta^2 F_m(A)$ should be positive definitely, so that the condition of the axial structure stability is given by a set of inequalities descriptive of the stability with respect to each fluctuation harmonics specified by number m. Standard algebraic analysis provides the conditions for $\delta^2 F_m(A)$ to be definitely positive which are taken in the form suitable for subsequent discussion.

$m = 0$:

$$\begin{cases} w_h < (1 + 2q_{13})\,\gamma_{+1}(x) - q_{24} + w_p = T_0(x) \\ 0 < \gamma_{+1}(x) - q_{24} + w_p = p_0(x) \end{cases} \tag{10a}$$

$m > 0$:

$$\begin{cases} w_h < T_m(x) = t_m(x)/(2p_m(x)) \\ 0 < p_m(x) = \alpha_m(x) + \beta_m(x) - 2q_{24} + 2w_p \end{cases} \tag{10b}$$

where

$$\gamma_{m+1}(x) = \frac{xI_m(x)}{2(m+1)I_{m+1}(x)} = \frac{\beta_m(x)}{m+1} \tag{11a}$$

$$\gamma_{m-1}(x) = \frac{2mI_m(x)}{xI_{m-1}(x)} = 4m\alpha_m(x)x^{-2} \tag{11b}$$

$$\begin{aligned} t_m(x) = {} & -q_{13}^2\left(\alpha_m(x) - \beta_m(x)\right)^2 + \\ & + 4q_{13}\left(\alpha_m(x)[2\beta_m(x) - (m+1)q_{24}] + \right. \\ & \left. + q_{24}(m-1)\beta_m(x) + w_p(\alpha_m(x) + \beta_m(x))\right) + \\ & + 4\left(\alpha_m(x) + (m-1)q_{24} + w_p\right) \times \\ & \times \left(\beta_m(x) - (m+1)q_{24} + w_p\right). \end{aligned} \tag{12}$$

The following designations for four dimensionless parameters were used: $w_h = W_h R/2K$, $w_p = W_p R/2K$, $q_{24} = K_{24}/2K$ and $q_{13} = K_{13}/2K$.

Since parameter w_h is nonnegative, we can determine the resultant stability threshold as a greatest lower bound of the quantities which determine the stability for each fluctuation mode:

$$W_c(x) = \inf_m \left\{TR_m(x)\right\} \tag{13}$$

$$TR_m = \begin{cases} T_m(x), & \text{if } T_m(x) > 0 \text{ and } p_m(x) > 0 \\ 0, & \text{otherwise} \end{cases} \tag{14}$$

Then the stability condition becomes

$$w_h < W_c(x). \tag{15}$$

In what follows we consider the possibility for the axial director pattern to be stabilized either by applying the magnetic field or by increasing the anchoring energy W_p. Mathematically, if $W_c(x) = 0$ at $w_p = 0$ for all $x > 0$ one can say that the magnetic field fails to stabilize the axial configuration under the homeotropic anchoring conditions. In other case, of $W_c(x) = 0$ at $x = 0$ for all $w_p > 0$ we have the configuration to be unstable, even though the boundary conditions make the molecules of NLC orient along the cavity axis.

K_{24}-term influence on the stability threshold

In this subsection, we deal with the case of $K_{13} = 0$. There is no need to make numerical calculation to arrive at the conclusion that the axial

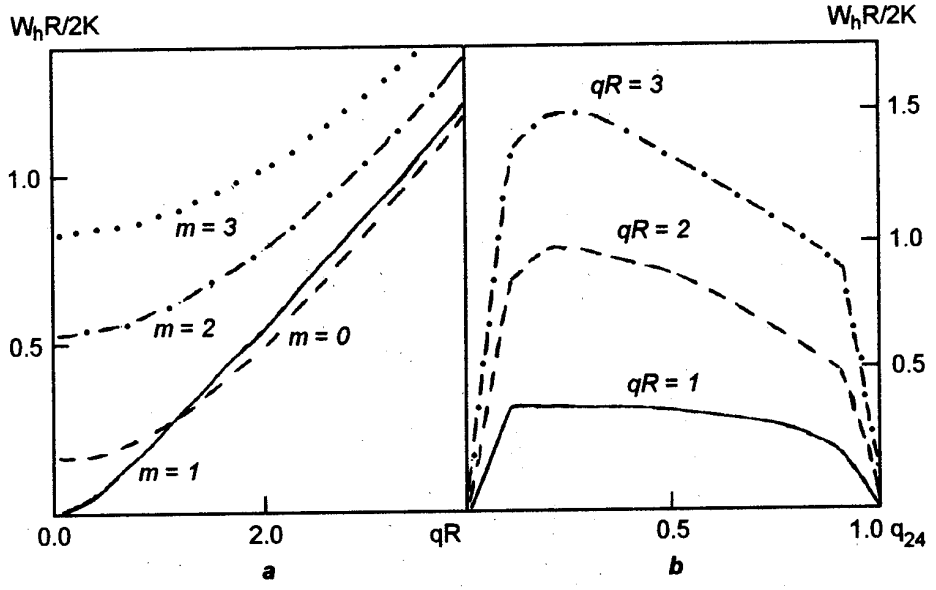

Fig.1. *a*.The plots of TR_m versus qR for $m = 0 - 3$ at $q_{24} = 0.8$. *b*.The stability diagram in $w_h - q_{24}$ plane at $qR = 1 - 3$. In both figures the stability region is arranged below the curves.

structure cannot be stabilized by the magnetic field if the value of q_{24} does not lie within the interval (0,1). In other words, it means that, for a given value of x, it is possible to find a number m such that either $P_{m(x)<0}$ or $T_m(x) < 0$ if q_{24} takes the value which is outside the interval (0,1). To prove our contention let q_{24} initially be negative, so that $P_m(x) > 0$ for any m. The expression for $t_m(x)$ can be derived from Eq.(12) on putting $w_p = q_{13} = 0$.

$$t_m(x) = 4\,(m+1)\left[\alpha_m + (m-1)\,q_{24}\right] \times \times \left[\gamma_{m+1} - q_{24}\right] \qquad (16)$$

Obviously, the sign of $t_m(x)$ is determined by the first factor enclosed in square brackets and it remains to see that the factor goes negative if m is a sufficiently large number, since $\alpha_m(x)$ goes to zero as $m \to \infty$ (see Eq.(11b)). If q_{24} is greater than unity it will suffice to note that $\gamma_{m+1}(x)$ is monotonically decreasing function of m, which tends to unity as $m \to \infty$, and therefore, the second factor of Eq.(16) enclosed in square brackets will be negative, beginning with sufficiently large number m, while the first one is positive.

In the case of the stabilization by the action of boundary conditions ($x = 0$ and $w_p > 0$), we come readily to the similar conclusion. As $\alpha_m(0) = 0$ and $\beta_m(0) = m+1$, from Eq.(12) one can obtain

$$t_m(0) = 4\,(m+1)\left[w_p + (m-1)\,q_{24}\right] \times \times \left[1 - q_{24} + w_p/(m+1)\right] \qquad (17)$$

It is clear that $t_m(0)$ goes negative for sufficiently large number m under q_{24} being out of the interval [0,1].

The plots of TR_m in relation to $x = qR$ are presented in Fig.1a at $q_{24} = 0.8$ and $m = 0 - 3$. As illustrated, the first fluctuation harmonics ($m = 1$) defines the stability threshold in the case of small magnetic field strength ($TR_1(0) = 0$), but the number of the mode, governing the threshold, changes to zero as the field strength increases. The harmonics which contribute to the resultant stability threshold, $W_c(x)$, are increasing in number with the quantity q_{24} approaching zero or unity. Interestingly, $TR_m(x)$ are not equal to zero for all m, if q_{24} takes a critical value (0 or 1) and $x \neq 0$, but $\lim TR_m = 0$ as $m \to \infty$ and, as a consequence, $W_c(x) = 0$ for any x. Hence, high order harmonics play an important part in the vicinity of critical values of K_{24} causing the axial structure to be destabilized. The effect of the destabilization is illustrated in Fig.1b, where the plots of W_c as a function of q_{24} are shown at $qR = 1,2,3$.

When we alter the anchoring energy W_p to gain the stabilization of the axial director structure, the situation we encounter is rather different. Simple analysis reveals the fluctuation mode with $m = 1$ alone to determine the stability threshold $W_c(0)$:

$$W_c = \frac{w_p(2 - 2q_{24} + w_p)}{1 - q_{24} + w_p} \qquad (18)$$

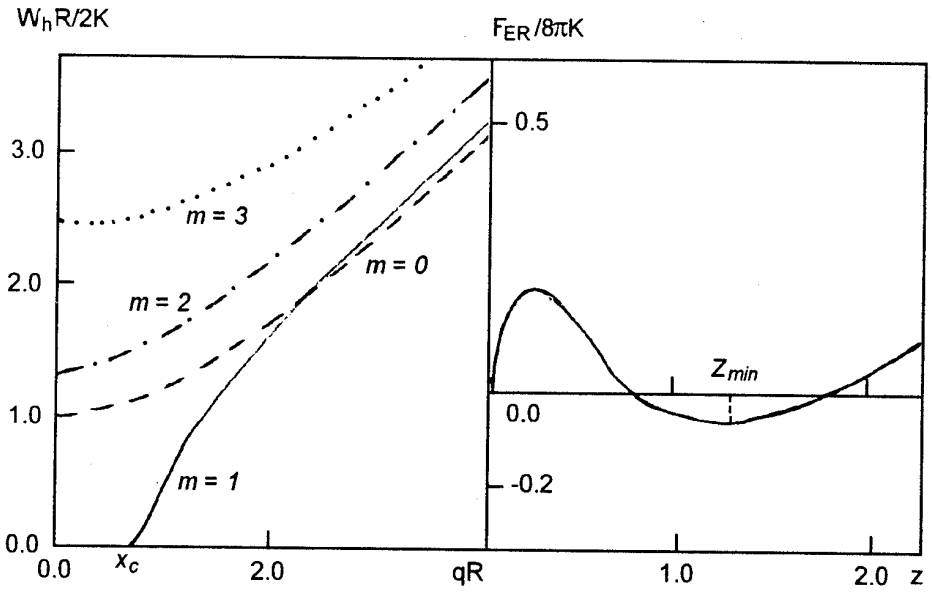

Fig.2. ***a***.The qR-dependence of TR_m for $m = 0 - 3$ at $q_{24} = 0.8$ and $q_{13} = 0.5$. ***b***.The energy of the escaped-radial configuration as a function of parameter z at $q_{24} = 2.0$, $q_{13} = 1.2$, $w_h = 0.75$ and $w_p = 0$.

so that it is impossible to change the number of fluctuation mode contributing to the threshold. At last there is nothing to forbid the value of q_{24} be equal to zero or unity.

K_{13}-term influence on the stability threshold

Here we find out how the surface elastic constant K_{13} affects the axial pattern stability. As can be seen from Eqs.(11a–11b), the quantities $P_m(x)$ do not depend on K_{13} and, even if $q_{24} > 1$, it is possible to meet the condition $P_m(x) > 0$ by choosing an appropriate magnitude of the field strength, that is x, or the anchoring energy, W_p. Because of this, one has to analyze the expression for $t_m(x)$ as it has been done above. Let us first have the case of $x = 0$ and $w_p > 0$. From Eq.(12) we have:

$$t_m(0) = Am^2 + 2\,(-q_{13}^2 + 2q_{13}w_p + 2w_p)\,m - \\ - q_{13}^2 + 4\,q_{13}\left(w_p - q_{24}\right) + \\ + 4\left(w_p - q_{24}\right)\left(w_p - q_{24} + 1\right) \qquad (19)$$

where

$$A = -q_{13}^2 + 4\,q_{13}\,q_{24} + 4\,q_{24}\,(1 - q_{24}) \qquad (20)$$

The requirement $A > 0$ places the restrictions on q_{13} and q_{24}:

$$2\left[q_{24} - (q_{24})^{1/2}\right] < q_{13} < 2\left[q_{24} + (q_{24})^{1/2}\right], \\ q_{24} > 0$$

or (21)

$$1 + q_{13} - [1 + q_{13}]^{1/2} < 2\,q_{24} < 1 + q_{13} + [1 + 2q_{13}]^{1/2} \\ q_{13} > -1/2$$

From the inequality $P_1(0) > 0$ we have the threshold for w_p:

$$w_p > q_{24} - q_{13} - 1 + [(q_{24} - q_{13} - 1)^2 + q_{13}^2]^{1/2} \qquad (22)$$

Bearing in mind Eqs.(21,22), the function $TR_m(0)$ can be proved to be an increasing function of m for $m \geq 1$. Thus we arrive at the conclusion that $W_c = TR_1(0)$:

$$W_c = \frac{-q_{13}^2 + w_p\,(w_p + 2 + 2\,q_{13} - 2\,q_{24})}{1 + w_p - q_{24}} \qquad (23)$$

Notice that the result of the previous subsection $0 < q_{24} < 1$ is a direct consequence of Eq.(21) and from Eq.(22) we get $w_p > 0$. The latter implies no threshold for w_p at $q_{13} = 0$.

Coming back to the stabilization by the action of magnetic field under the homeotropic anchoring conditions, $w_p = 0$, one can see the restriction given by Eq.(21) remains unchanged since the coefficient A of the quadratic polynomial in m of Eq.(19) differs from one in the case of nonzero magnetic field by quantities which tend to zero as $m \to \infty$. Interestingly, there are no restrictions on q_{24} value from above and q_{24} just must be positive. Referring to Fig.2a, it can be seen that, even if $w_h = 0$, the axial pattern is unstable until the strength of magnetic field reaches its critical

value, $x = x_c$, which depends strongly on q_{24} and q_{13}. Indeed, from Eq.(17) we find out that $t_1(0) < 0$ at $w_p = 0$. Therefore, it is necessary to apply the magnetic field of finite amplitude to make $t_1(0)$ positive. So in the presence of K_{13}-term both the magnetic field ($w_h \geq 0$, $w_p = 0$) and the anchoring energy $W_h(x = w_h = 0)$ must exceed their threshold values to make the axial structure stable. Here we have the effect to be detected experimentally.

III. The escaped-radial structure in the presence of K_{13}- term

To clarify the role of that term we study here how the surfacelike elastic constants affect the escaped-radial director structure [15]. The configuration had been explored in [9,16] with K_{24}-term alone, but some new effects are appeared to be induced by the K_{13}-term. The director field and the free energy for the structure under investigation are given by

$$\underline{\mathbf{n}} = \sin\chi(r)\,\underline{\mathbf{e}}_z + \cos\chi(r)\,\underline{\mathbf{e}}_R \tag{24}$$

$$\sin\chi(r) = \frac{\rho^2 - r^2}{\rho^2 + r^2} \tag{25}$$

where ρ is the integration constant.

$$F_{\mathbf{ER}}(z)/(2\pi K) = 2\,z\,(1+z)^{-3} \times \times\Big[z^2 + (3 - 2\,q_{24} + 2w_p - 2\,w_h)\,z + + 2\,(1 - q_{24} + w_p - w_h + 2\,q_{13})\Big] - w_p \tag{26}$$

where $z = (R/\rho)^2$. It is easy to see that Eqs.(25,26) lead us to the axial structure, provided that $z = 0$, and $F_A = 2\pi K w_p$. Therefore, the stability of the structure is governed by the sign of the term in square brackets of Eq.(26). We have the axial configuration favourable in energy over the escaped-radial on under the term being positive for all $z > 0$. Interestingly, the stability condition $w_h < T_0(0)$ yields the increasing of $F_{\mathbf{ER}}(z)$ at $z = 0$, that is to say it means the local stability of the axial configuration. In the event when $K_{13} = 0$, the condition is sufficient, but as evident from Fig.2b, in the presence of the K_{13}-term, the local stability does not imply the global one. Thus, we encounter here the effect which looks like as bistable and caused by the K_{13}-term. For sake of definiteness, one has to point out the fact that Eq.(22) supplies more rigid requirement for the axial configuration to be stable which makes the difference $F_{\mathbf{ER}} - F_{\mathbf{A}}$ positive under the planar anchoring conditions, so that there is nothing to contradict our stability analysis and the effect may be attributed to the existence of the threshold for w_p.

Another effect which we are able to discuss is connected with the escaped-radial configuration degeneracy in energy. The structure is known to be doubly degenerate due to the mirror symmetry $\chi \to -\chi$, that is the reason for the point defects to appear along the cavity axis [9]. The K_{13}-term may result in an increase in the degree of the degeneracy in the event when the energy $F_{\mathbf{ER}}(z)$ reaches its minimum at $z = z_{\min} > 1$ (see Fig.2b). If so, a new configuration of the same energy can be defined in the following way:

$$\sin\chi(r) = \begin{cases} \sin\chi(r), & r < \rho_{\min} \\ -\sin\chi(r), & \rho_{\min} \leq r \leq R \end{cases} \tag{27}$$

where $\sin\chi(r)$ is given by Eq.(25) with $\rho = \rho_{\min} = R/z_{\min}^{1/2}$. In the same manner as it had been shown for the mirror symmetry one can expect such kind of degeneracy to produce circles of the disclinations at the surface. It must be emphasized that the K_{13}-term do not necessary make the value of $z_{\min}$ greater than unity, but we always have $z_{\min}$ less than unity provided the term being neglected.

Acknowledgment

Authors acknowledge gratefully the financial support of the International Science Foundation under the Grant No. U58000.

References

1. C.W.Oseen, *Trans.Faraday Soc.*, **29**, 883 (1933).
2. F.C.Frank, *Discuss.Faraday Soc.*, **25**, 19 (1958).
3. J.Nehring, A.Saupe, *J.Chem.Phys.*, **54**, 337 (1971).
4. V.M.Pergamenshchik, *Ukr.Phys.Zh.*, **35**, 1352 (1990).
5. G.Barbero, S.Sparavigna, A.Strigazzi. *Nuovo Cimento*, **12**, 1259 (1990).
6. O.D.Lavrentovich, *Mol.Cryst.Liq.Cryst.*, **179**, 125 (1990).
7. V.M.Pergamenshchik, *Phys.Rev.E.*, **47**, 1881 (1993).
8. O.D.Lavrentovich, *Phys.Scr.*, **39**, 349 (1991).
9. G.P.Crawford, D.W.Allender, J.W.Doane, *Phys.Rev.A*, **45** (1992).
10. G.Barbero, C.Oldano, *Mol.Cryst.Liq.Cryst.*, **170**, 99 (1989).
11. H.P.Hinov, *Mol.Cryst.Liq.Cryst.*, **148**, 197 (1987).
12. V.M.Pergamenshchik, *Phys.Rev.E.*, **48**, 1254 (1993).
13. A.Rapini, M.J.Papoular, *J.de Phys.(Paris) Colloq.*, **30**, C4 (1969).
14. Handbook of Mathematical Functions, Ed.by M.Abramowitz, I.A.Stegun, National Bureau of Standards (1964).
15. P.E.Cladis, M.Cleman, *J.Phys.(Paris)*, **33**, 591 (1972).
16. A.D.Kiselev, V.Yu.Reshetnyak, In: Proc.SPIE, **1815**, 206 (1992).

Возмущения в НЖК, заключенном в цилиндрической полости, под влиянием поверхностно-подобных констант упругости

А.Д.Киселев, В.Ю.Решетняк

В статье рассмотрен нематический жидкий кристалл, заключенный в цилиндрическую полость, при различных условиях сцепления. Исследовано влияние членов K_{24} и K_{13}, описывающих комбинированные деформации (скошенную седловидность и косой изгиб), на устойчивость аксиальной конфигурации директора. Аналитический подход авторов с использованием разложения флуктуаций директора в ряд Фурье, позволяет определить условия устойчивости по отношению к каждой моде флуктуаций. Использованы два способа стабилизации структуры: с помощью магнитного поля и воздействия краевых условий. Найдены ограничения значений констант, обеспечивающие возможность стабилизации. Рассчитана зависимость результирующего порога устойчивости от значений поверхностно-подобных констант упругости. Подробно рассмотрены экспериментально обнаруживаемые эффекты, обусловленные наличием члена K_{13}. Показано, что радиальная структура директора обладает некоторыми специфическими особенностями, обусловленными членом K_{13}.

Functional Materials 2, No.2 (1995)

Interaction with surface and the director field structure in the plane-parallel cell of liquid crystal with Grandjean-Cano type disclinations

M.F.Ledney and I.P.Pinkevich

T.Shevchenko Kiev University, 64 Vladimirskaya St., 252017 Kiev, Ukraine

The cholesteric liquid crystal with monotonous change of twisting power along the plane-parallel cell resulting in the appearance of Grandjean-Cano type disclinations is considered. It is shown that the ingomogeneity of the cholesteric twisting power and the finite value of the director adherence energy with the cell bounding surfaces influence considerably the director field structure near the disclination. The director field in the neighbourhood of disclination is found for the case of the limited longitudinal dimension ($d \neq \infty$) of disclination structure. It is shown that its dependence on the value d is significant if d has the order of the cell thickness or less.

Розглянуто холестеричний рідкий кристал, закручуюча здатність якого монотонно змінюється по довжині плоскопаралельної комірки, що приводить до появи дисклінацій типу Гранжана-Кано. Показано, що неоднорідність закручуючої здатності холестерина і кінцева величина енергії зчеплення директора з обмежуючими поверхнями комірки суттєво впливають на структуру поля директора поблизу дисклінації. Знайдено поле директора в околі дисклінації при обмеженому повздовжньому розмірі ($d \neq \infty$) дисклінаційної структури. Показано, що його залежність від величини d стає значною, якщо d має порядок товщини комірки або менший.

1. Introduction

Unique physical properties of liquid crystals (LC) depend on the director field spatial structure which, in its turn, is determined by the director interaction with external fields and the cell surface. This interaction, in some cases, causes discontinuities in the director variation, i.e. so-called disclinations.

The Grandjean-Cano disclinations are known [1] to arise in wedge-shaped cells of cholesteric liquid crystals (CLC) when a jump-like director change by one-half revolution of the cholesteric spiral occurs. Expressions for the director field distribution near a Grandjean-Cano disclination were derived earlier [2] in form of infinite series, while in [3] a solution by means of elementar functions was found, though neglecting the cell wedge-like shape. In both works mentioned, infinitely rigid boundary conditions were supposed for the CLC director on the cell surface. Actually, the director interaction with the cell surface is of course not infinitely strong, and, since significant strains take place near to a disclination due to the director jump-like change, an essential change of the CLC director field structure in the vicinity of a disclination are to be expected already at relatively small diminishing of the boundary conditions rigidity.

In a plane-parallel CLC cell with planar boundary conditions, disclinations can be obtained if use is made of the molecular photo conversion phenomenon. In fact, molecules of some LC are able, as a result of the incident light absorption, to change its conformation transforming into relatively long-lived photo-converted states [4]. Parameters of such photo-converted molecules (PCM) differ from those of LC molecules in the ground state. In the case of CLC, this fact can result in a dependence of the twisting power (the spiral pitch) on the PCM concentration.

Then, if the PCM concentration varies monotonically along the planar cell length, whole numbers of cholesteric spiral half-waves will fit in the cell thickness in its certain areas. In the case of

rigid boundary conditions, the half-waves number will change jump-like at the transition from such an area to a neighbouring one, and Grandjean-Cano type disclinations will occur. The director field structure nearby such a disclination will discussed below for the case when the boundary conditions on the cell surface are not absolutely rigid. The influence of finite longitudinal dimension of the area where the disclination is located on this structure will also be considered.

2.Basic equations

Picture a CLC plane-parallel cell of $2L$ thickness with planar boundary conditions. Let 0Z axis of a Cartesian coordinate system be directed normal to the cell planes, the coordinates origin being placed in the cell center. Assume that the cell is infinite in the 0X and 0Y directions. Let us imagine, further, that, by means of an incident light field, in the CLC cell, a stable, inhomogeneous along the cell, distribution of PCM is maintained, whose chirality differs from that of ground CLC molecules, so the cholesteric twisting power depends monotonically on the x coordinate: $t = t(x)$. Assume, however, this dependence to be small, so the $t(x)$ function change on the characteristic length of director change in the CLC cell (having order of the twist pitch) can be neglected.

Then, the CLC cell free energy can be written [5] as

$$F = F_v + F_s,$$

$$F_v = \frac{1}{2}\int dV\{K_{11}(\mathrm{div}\,)^2 + K_{22}[\vec{n}\cdot \mathrm{rot}\,\vec{n} + t(x)]^2 + K_{33}[\vec{n}\times \mathrm{rot}\,\vec{n}]^2\}, \quad (1)$$

$$F_s = -\frac{W}{2}\int dS\,(\vec{n}\cdot\vec{e})^2, \quad w > 0.$$

where F_v is Frank volume elastic energy; F_s is the surface free energy expressed by Rappini potential [6]; $\vec{n}$ is director; $\vec{e}=\{\cos\varphi_0, \sin\varphi_0, 0\}$, unit vector of easy director orientation on the cell planes. In the expression(1), terms containing the elastic constants K_{13}, K_{24} are absent, since their corresponding integrals over the plane-parallel cell surface with planar director orientation equal to zero. Moreover, since the light field being absorbed with the PCM creation is assumed to be weak, its contribution to the CLC free energy due to the interaction with director will be neglected.

For definiteness sake, let us believe that the axis of the director easy orientation on cell planes is directed along the 0X axis, i.e. assume $\varphi_0 = 0$. Since the boundary conditions are planar, the director spatial distribution in the CLC cell volume can be looked for in form $\vec{n}=\{\cos\varphi(x,z), \sin\varphi(x,z), 0\}$, where $\varphi(x,z)$ is the angle between the director and 0X axis depending also on the x coordinate value because of inhomogeneity of the CLC twisting power.

Minimizing the expression (1) in relation to φ angle, we obtain, in the one-constant approximation ($K_{11} = K_{22} = K_{33} = K$) the following equation:

$$\frac{\partial^2\varphi}{\partial x^2} + \frac{\partial^2\varphi}{\partial z^2} = 0 \quad (2)$$

and the boundary conditions to it

$$\left[\frac{\partial\varphi}{\partial z} - t(x) \pm \frac{\sigma}{2L}\sin 2\varphi\right]_{z=\pm L} = 0 \quad (3)$$

Here, the parameter $\sigma = WL/K$.

3. The director spatial distribution at a finite adherence energy W value

Let a function $t(x)$ be monotonic over the $(-\infty, +\infty)$ range and of such character that, in the case of the infinitely rigid adherence of the director to the cell surface ($\sigma = \infty$), the CLC spiral pitch, at $x \to -\infty$, equals to $P_{-\infty} = \frac{2\pi}{t(-\infty)} = \frac{4L}{n}$, i.e. n halfwaves of a cholesteric spiral fit in the cell thickness, while, at $x \to \infty$, $P_{\infty} = \frac{2\pi}{t(\infty)} = \frac{4L}{n+1}$ and $n+1$ of spiral half-waves fall in the cell thickness. Then, as it is known, a disclination of Grandjean-Cano type arises perpendicular to X0Z plane; let the 0Y axis be directed along that disclination. The development of the director disclinational structure along the 0X axis is quite unlimited and depends only on the type of the disclination itself.

If the parameter $\sigma = \infty$, the problem of the director orientation determination in the volume of a CLC plane-parallel cell with a specified $t(x)$ is similar to that considered in [3] for a flat wedge with CLC having the homogeneous twisting power.

The solution of Eq.(2), in this case, is

$$\varphi_\infty(x,z) = \frac{2n+1}{4L}\pi z + \frac{\pi n}{2} + \varphi'(x,z);$$

$$\varphi'(x,z) = \tfrac{1}{2}\,\mathrm{arctg}\left\{\frac{\mathrm{tg}(\pi z/2L)}{\mathrm{th}(\pi x/2L)}\right\} + \varphi'_0; \quad (4)$$

$$\varphi'_0 = \begin{cases} -\pi/2; & x > 0,\ z > 0 \\ 0; & x < 0 \\ \pi/2 & x > 0,\ z < 0. \end{cases}$$

Generally, for finite σ values, equation (2) and (3) can be solved only numerically. For the most interesting and often practically realizable case $\sigma >> 1$, however, the approximative solution of these equations can be obtained in the analytical form. To this end, let the solution sought be presented as

$$\varphi(x,z) = \varphi_{\infty}(x,z) + \\ + \frac{1}{\sigma}\left\{\left[t(x) - \frac{2n+1}{4L}\cdot\pi\right]z + b(x,z)\right\} \qquad (5)$$

and let believe, because function $t(x)$ varies smoothly, that $L\frac{\partial^2 t}{\partial x^2} << \frac{\partial^2 b}{\partial x^2}$. Then, it follows from (2), (3) that the function $b(x,z)$ satisfies the two-dimensional Laplace equation and the following boundary conditions on the cell surface:

$$b(x,z=\pm L) = \mp\frac{\pi}{4}\,\mathrm{th}\left(\frac{\pi x}{2L}\right) \qquad (6)$$

At the obtaining of Eq.(6), terms of order higher than σ^{-1} were discarded.

At $x \to \pm\infty$, the CLC spiral distortion due to a disclination disappears, and $\varphi(-\infty,z) = \frac{\pi n}{2L}z + C_1$, $\varphi(\infty,z) = \frac{n+1}{2L}\pi z + C_2$. Then, using the expression (5), the following values for $b(x,z)$ function at $x \to \pm\infty$ can be obtained:

$$b(\pm\infty,z) = \mp\frac{\pi z}{4L}. \qquad (7)$$

It follows from the sense of the $\varphi(x,z)$ function definition as the angle between director and 0X axis as well as from the symmetry of the problem, that the $b(x,z)$ function is an odd one of the z coordinate. Thus, the problem of the $\varphi(x,z)$ determination is reduced to the solution of Laplace two-dimensional equation for the $b(x,z)$ function in the range $-\infty < x < \infty$, $0 \le z \le L$ with boundary conditions (6), (7), accounting for $b(x,0) = 0$.

The solution of this boundary problem can be presented [6] in the form

$$b(x,z) = \frac{1}{2\pi}\int b(x',z')\frac{\partial}{\partial N}G(x,z;x',z')\,dS' \qquad (8)$$

where $G(x, z; x', z')$ is the Green function corresponding to the boundary problem; N is the internal normal to the integration contour enclosing the two-dimensional area under consideration.

The function $\dfrac{\exp\left(\frac{\pi S}{L}\right) - \exp\left(\frac{\pi S'}{L}\right)}{\exp\left(\frac{\pi S}{L}\right) - \exp\left(\frac{\pi S'^{*}}{L}\right)}$ can be shown to display conformically an infinite strip $-\infty < x < \infty$, $0 \le z \le L$ of the complex plane $S = x + iz$ onto the internal area of a circle of unit radius. Then, as is known [6], the sought Green function will be determined by the expression

$$G(x,z;x',z') = \frac{1}{2\pi}\ln\left|\frac{e^{\pi/L(x+iz)} - e^{\pi/L(x'+iz')}}{e^{\pi/L(x+iz)} - e^{\pi/L(x'-iz')}}\right|. \qquad (9)$$

Inserting the expression (9) in Eq.(8) and accounting for values (6), (7) being taken by the function $b(x',z')$ on the integration contour, we obtin, after integration:

$$b(x,z) = \frac{\pi}{4L}\,\frac{x\sin\left(\frac{\pi z}{L}\right) - z\,\mathrm{sh}\left(\frac{\pi x}{L}\right)}{\mathrm{ch}\left(\frac{\pi x}{L}\right) - \cos\left(\frac{\pi z}{L}\right)}. \qquad (10)$$

Thus, it follows from Eqs.(5), (4) and (10), that the director spatial distribution in the neighbourhood of a Grandjean-Cano disclination depends on the adherence energy of the director with the cell surface, that energy is characterised by the σ parameter. At a finite value of $\sigma >> 1$, two mechanisms contribute to the change of the disclination structure: the CLC twisting power inhomogeneity which is described by the first braced term of Eq.(5), and the straightening of the disclination structure due to the weakening of the boundary conditions rigidity. The contribution of this mechanism is described by the $b(x,z)$ function and does not depend on the form of the smooth monotonous function $t(x)$.

The function $\left[t(x) - \frac{2n+1}{4L}\cdot\pi\right]z$ accounting, in Eq.(5), the influence of variation of the CLC twisting power from its average value in the $(-\infty, +\infty)$ range on the director distribution, attains its maximum value $\pm\frac{\pi z}{4L}$ at $x \to \pm\infty$.

Fig.1 shows the calculated values of the $b(x,z)$ function for several values of z argument. It is seen that the maximum $b(x,z)$ values do not exceed those of $\left[t(x) - \frac{2n+1}{4L}\cdot\pi\right]z$ function; however, the $b(x,z)$ function achieves these values already in the distance ~ L from the disclination center. Therefore, in the vicinity of a disclination, the director orientation variation at finite values of its adherence energy with the cell surface is associated mainly with the dislocation structure

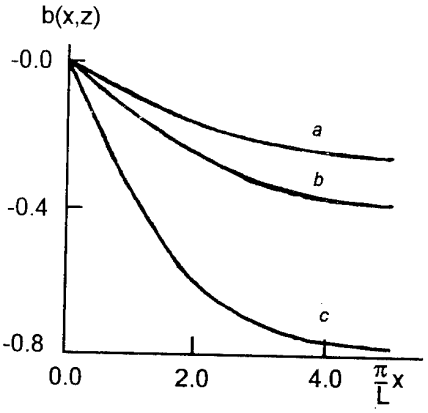

Fig.1. $z = L/3$ – a, $L/2$ – b, L – c.

straightening not depending on the form of $t(x)$ function.

4. Influence of the finite longitudinal dimension of disclination structure

Let now be a smooth function $t(x)$ such that, in the point $x = x_n$, n half-waves of the cholesteric spiral fit in the cell thickness, and in the point $x = x_{n+1}$, $n+1$ the half-waves, i.e. the disclination structure is limited, along the 0X axis, by a finite length $[x_n, x_{n+1}]$. Let assume, for simplicity sake, that a disclination ($x = 0$) is positioned in the center of this length, i.e. $x_n = -d$, $x_{n+1} = d$, and the director adherence with the cell surface is absolutely rigid ($W = \infty$).

It is convenient, in this case, to look for solution of Eq.(2) in the form similar to the solution (4) of the problem involving the infinitely rigid director-to-surface adherence but with an unlimited, along 0X axis, dimension of disclinational structure area:

$$\varphi(x,z) = \frac{2n+1}{4L}\pi z + \frac{\pi n}{2} + \varphi_1(x,z), \qquad (11)$$

where $\varphi_1(x,z)$ satisfies the two-dimensional Laplace equation and the same boundary conditions on the cell surface as $\varphi'(x,z)$. Similar to $\varphi'(x,z)$, the $\varphi_1(x,z)$ function is odd in relation to z coordinate, therefore, it is sufficient to consider it in the area $0 \le z \le L$, $-d \le x \le d$.

The values of $\varphi_1(x,z)$, at $x = \pm d$ can be found taking into account that, in these planes, whole numbers of CLC spiral half-waves are specified to fall in the cell thickness. We obtain

$$\varphi_1(-d,z) = -\frac{\pi z}{4L}, \quad \varphi_1(d,z) = -\frac{\pi z}{4L} - \frac{\pi}{2} \qquad (12)$$

To find $\varphi_1(x,z)$, let consider the plane of complex variable $S = x + iz$ and display conformically the tetragon ($x = -d$, $x = d$, $z = 0$, $z = L$) onto the upper half-plane of the complex variable $w = u + iv$.

Such a displaying is realized by means of the elliptic sine function and has the form [6]

$$w = \mathrm{sn}\left(\frac{k}{d}\cdot s, m\right) \qquad (13)$$

where

$$k \equiv F(1,m) = \int_0^1 \frac{dt}{\sqrt{(1-t^2)(1-m^2t^2)}} \qquad (14)$$

is the full elliptic integral of 1st order; m is the module of elliptic integral.

As a result of displaying (13), the function $\varphi_1(s) \equiv \varphi_1(x,z)$, will transform to the function $\tilde{\varphi}(w)$ and boundary points of the tetragon ($x = \pm d$, $z = 0, L$) will convert to points on the real axis in the plane w; therewith, an equation to determine the module of elliptic integral will also be obtained:

$$\frac{k}{k'} = \frac{d}{L} \qquad (15)$$

where

$$k' \equiv f(1,m'), \qquad (16)$$
$$m' = (1-m^2)^{1/2}.$$

The boundary conditions for the function $\varphi_1(x,z)$ will give, after the conversion (13), the function $\tilde{\varphi}(w)$ values on the real axis.

Thus, for a harmonic function $\tilde{\varphi}(w)$, we have the Dirichle problem for a half-plane. Its solution can be written by means of the Poisson integral [6]:

$$\tilde{\varphi}(w) = \frac{1}{\pi}\int_{-\infty}^{\infty} \tilde{\varphi}(t)\frac{v\,dt}{(t-u)^2+v^2}. \qquad (17)$$

Inserting the $\tilde{\varphi}(w)$ values on the real axis and integrating, we obtain

$$\varphi_1(x,z) = \tilde{\varphi}(w) = \frac{1}{4}\left(1-\frac{z}{L}\right)\mathrm{arctg}\frac{1+mu}{mv} + \frac{1}{4}\left(\frac{z}{L}-1\right)\mathrm{arctg}\frac{1-mu}{mv} - \frac{z}{4L}\mathrm{arctg}\frac{1-u}{v} + \frac{z}{4L}\mathrm{arctg}\frac{1+u}{v} - \frac{1}{2}\mathrm{arctg}\frac{u}{v} - \frac{\pi}{4}, \qquad (18)$$

where

$$u = \frac{1}{A}\,\mathrm{sn}\left(\frac{k}{d}\cdot x, m\right)\mathrm{dn}\left(\frac{k}{d}\cdot x, m'\right),$$
$$v = \frac{1}{A}\,\mathrm{cn}\left(\frac{k}{d}\cdot x, m\right)\mathrm{dn}\left(\frac{k}{d}\cdot x, m\right)\times$$
$$\times\,\mathrm{sn}\left(\frac{k}{d}\cdot z, m'\right)\mathrm{cn}\left(\frac{k}{d}\cdot z, m'\right),$$
$$A = \mathrm{cn}^2\left(\frac{k}{d}\cdot z, m'\right) + \qquad (19)$$
$$+ m^2\,\mathrm{sn}^2\left(\frac{k}{d}\cdot x, m\right)\mathrm{sn}^2\left(\frac{k}{d}\cdot z, m'\right),$$
$$\mathrm{cn}(a,m) = (1 - \mathrm{sn}^2(a,m))^{1/2},$$
$$\mathrm{dn}(a,m) = (1 - m^2\,\mathrm{sn}^2(a,m))^{1/2}$$

The expressions (11), (18), (19) define the sought distribution of the director at a finite longitudinal dimension of a disclination structure.

In a specific case, when $d\to\infty$, we will obtain, from Eqs.(15), (16) for the module of elliptic integral, that $m = 1$, $m' = 0$, $k' = \pi/2$, $k/d = \pi/(2L)$. Then, after simple conversions, it follows from Eqs.(18), (19) that $\varphi_1(x,z) = \varphi'(x,z)$, i.e. we obtain the problem solution for the case of unlimited size of the disclination structure along 0X axis.

Fig.2 shows the calculated dependence of $\varphi_1(x,z)$ function values on the distance to a disclination along 0X axis for several z coordinate values and two longitudinal dimensions of the disclination structure described by the parameter d/L. It is seen that it is in the vicinity of the disclination where, at a change of d/L parameter, the maximum variation of the $\varphi_1(x,z)$ occurs. Therewith, when the z coordinate increases (i.e. as the cell limiting planes are approached), the maximum changes of the $\varphi_1(x,z)$ function are shifted themselves toward larger x values. It should be noted that, as the calculation shows, already at $d/L>2$, the director field of a disclination structure becomes close to that at its unlimited size along 0X axis (i.e. at $d = \infty$). Therefore, the director field structure variations near to a disclination become significant only at $d \le 2L$.

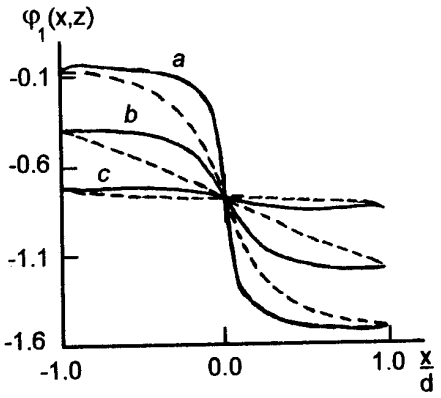

Fig.2. $d/L = 2$ – solid lines, $d/L = 0.5$ – broken lines; $z = 0.1$ – a, 0.5 – b, 0.9 – c.

References

1. R.Cano, *Bull.Soc.Mineral.Cryst.*, **91**, 20 (1968.
2. P.G. de Gennes, *Mol.Cryst.Liq.Cryst.*, **7**, 325 (1969).
3. T.J.Scheffer, *Phys.Rev.*, **A.5**, 1327 (1972).
4. S.G.Odulov,Yu.AReznikov, M.S.Soskin et.al, *Zh.Eksperim.Teor.Fiz.*, **82**, 1475 (1982).
5. I.P.Pinkevich, V.Yu.Reshetnyak, Yu.A.Reznikov, *Mol.Cryst.Liq.Cryst.*, **222**, 269 (1992).
6. P.G.de Gennes, The Physics of Liquid Crystals, Clarendon Press, Oxford (1974).
7. M.A.Lavrent'ev, B.V.Shabat, Methods of Theory of Complex Variable Functions [in Russian], Nauka; Moscow (1965).

Взаимодействие с поверхностью и структура поля директора в плоскопараллельной ячейке жидкого кристалла с дисклинациями типа Гранжана-Кано

М.Ф.Ледней, И.П.Пинкевич

Рассмотрен холестерический жидкий кристалл, закручивающая способность которого монотонно изменяется по длине плоскопараллельной ячейки, что приводит к появлению дисклинаций типа Лагранжа-Кано. Показано, что неоднородность закручивающей способности холестерина и конечность энергии сцепления директора с ограничивающими поверхностями ячейки существенно влияют на структуру поля директора вблизи дисклинации. Найдено поле директора при ограниченном продольном размере ($d \neq \infty$) дисклинационной структуры. Показано, что его зависимость от величины d становится значительной, если d порядка и меньше толщины ячейки.

Functional Materials 2, No.2 (1995)

Influence of aerosil surface on frequency characteristics of filled nematics

G.Ya.Guba**, A.V.Glushchenko*, N.Yu.Lopukhovich**, V.V.Ogenko**, Yu.A.Reznikov*, V.Yu.Reshetnyak**, O.V.Yaroshchuk*

*Institute for Physics, National Academy of Sciences of Ukraine, 46 Nauki Ave., 252650 Kiev, Ukraine

**Institute for Surface Chemistry, National Academy of Sciences of Ukraine, 31 Nauki Ave., 252022 Kiev, Ukraine

Influence of the aerosil surface modification on the electrooptical properties of heterogeneous systems aerosil – liquid crystal has been investigated. It is found that aerosil particles can be considered, within systems in question, as macroscopic admixtures. A model is proposed according to which the response frequency limit of the system is associated with the minimum size of the director inhomogeneity regions.

Досліджено вплив модифікації поверхні аеросилу на електрооптичні властивості гетерогенних систем аеросил – рідкий кристал. Показано, що в досліджуваних системах частинки аеросилу можна розглядати як макроскопічні домішки. Запропоновано модель, згідно з якою гранична частота відгуку системи пов'язується з мінімальним розміром областей неоднорідності директора.

1. Intensive investigations of various systems on liquid crystals (LC) basis got recently under way [1–3] what is motivated by the perspective of creation, on that basis, of new information displaying systems as well as by that such systems offer new possibilities to study interactions between a LC and a surface.

Among various geterogeneous LC media are so-called filled nematics, consisting of small-size silica (aerosil) particles suspended in a nematic LC [4,5]. Such systems are characterized by a strong effect of the electrically controlled light dissipation, i.e. an electric field application thereto causes the clearing-up of the medium which was initially opaque [6].

Since any filled LC is a system with largely developed surface, the state of the aerosil–LC interface can influence significantly the macroscopic characteristics of suspension. Influence of the aerosil surface modification on the characteristics of optical response of filled nematics at the electric field application thereto was studied earlier by us. The chemical grafting of various molecular fragments to the aerosil surface makes possible to vary the state of surface endowing it with hydrophilic or hydrophobic properties. The investigations have shown that the electooptical features of filled LC become enhanced when the hydrophobic character of the aerosil surface becomes more pronounced: the working stability and switching contrast increase, the saturation voltage (U_{sat}) of the $T(U)$ dependence decreases (here T is the system light transmission; U, the voltage applied to a sample).

A more comprehensive study of the electrooptical characteristics of filled LC is necessary to understand physical processes occurring therein at the electric field application and to choose a working model for calculations. The purpose of this work was to investigate the dependence of the filled LC light transmission on the applied field frequency and on aerosil surface modification type.

2. The commercially available aerosil A-300 with the grain size 100 Å was used to suspensions preparation. The surfaces of silica particles were hydrophobized to depress the particles aggregation in the suspension. The modification was performed by means of surface fragments deposition from a solution. It is known from literature [7] that organosiloxanes are excellent silica surface hydrophobizing agents widely used in practice. Octamethylcyclotetrasiloxane (OMCTS), methylphenylcyclotrisiloxane (MPhCTS), methylvinylcyclotrisiloxane (MVCTS), aminopropyltriethoxysilane (AGM-9), poly(dimethyl)siloxane (PMS-5), and hexamethyldisilazane (HMDS) were chosen as modifying agents.

The aerosil surface modification was performed both by liquid-phase method and by catalytic method under vacuum [8,9]. Silica was pretreated by heating at 610 K for 2 h (in the case of liquid-phase synthesis) or at 720 K under vacuum.

The chemical modification of the silica surface with OMCTS was performed by vacuum-treatment method at 720 K for 2 h.

The modification with MVCTS was performed at 580 K with consequent vacuum treatment at 620 K for 2 h.

The reaction with MPhCTS was conducted at 430 K in the presence of diethylamine.

The liquid-phase technique was used to modify the aerosil surface with AGM-9, HMDS, and PMS-5. The reaction with AGM-9 was performed in the presence of OMCTS, that with HMDS in the presence of trimethylacetoxysilane over 66 h with subsequent thermal treatment at 350 °C for 1 h in the case of HMDS or at 100 °C for 1 h in that of AGM-9.

The surface modification with PMS-5 was conducted in 5 per cent solution in hexane under the presence of OMCTS with subsequent thermal vacuum treatment at 670 K for 2 h. In the course of the investigation of samples where the silica modified with PMS-5 was used as the filler, the reaction conditions mentioned above were found to be the best ones for the preparation of silicas intended to serve as LC fillers.

The IR spectra consideration had shown that surface hydroxyls are effectively substituted in all silicas modified. Materials modified with MPhCTS were the only exclusion. The cause is perhaps that the phenyl group is more voluminous than vinyl one and thus hinders the reaction between MPhCTS and surface hydroxyls.

In the course of chemisorption of modifying agents mentioned, siloxane complexes become grafted to the aerosil surface (Fig.1,a). In the case

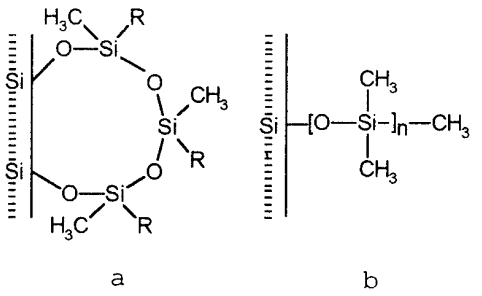

Fig.1. a) Siloxane complexes on the aerosil surface. $R = CH_3$ for OMCTS, C_6H_5 for MPhCTS, $CH_2{=}CH$ for MVCTS, $CH_2CH_2CH_3$ for AGM-9, CH_3 for HMDS. b) Linear siloxane structures on the aerosil surface after its modification with PMS-5; n = 1–4.

of modification by PMS-5, linear siloxane structures are formed on the surface (Fig.1,b).

The nematic ZhKM-1285 (NIOPIK, Russia) having the dielectric constant anisotropy $\Delta\varepsilon = 11.8$ and birefringence $\Delta n = 0.156$ was used as the LC. It is a mixture of cyanobiphenyls and cyclohexancarboxylic acids esters. Suspensions were prepared by blending the components in an ultrasonic mixer. The aerosil concentration in the mixture varied from 2 to 20 %. The suspension layers of 10 μm thickness placed between two glasses with transparent electrodes were investigated. The sample thickness was preset by means of a small amount of spacers added to the mixture under study.

In Fig.2, the device used to measure the dependence of sample light transmission, T, on the frequency, f, of the voltage applied, U, is schematically presented. The light beam of a HeNe laser ($\lambda = 0.63$ μm) goes through the sample under study, dissipating partly therein. The undissipated light as well as that dissipated within a solid angle not exceeding 2 ° is registrated by the photodiode *Phd*1 connected with a digital oscilloscope. The photodiode *Phd*2 is intended to

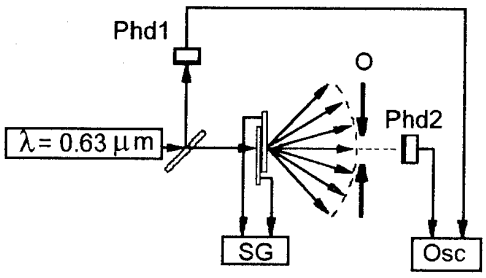

Fig.2. Schematic view of the experimental device used to measure the dependence of samples light transmission, T, on the frequency, f, of the voltage applied, U.

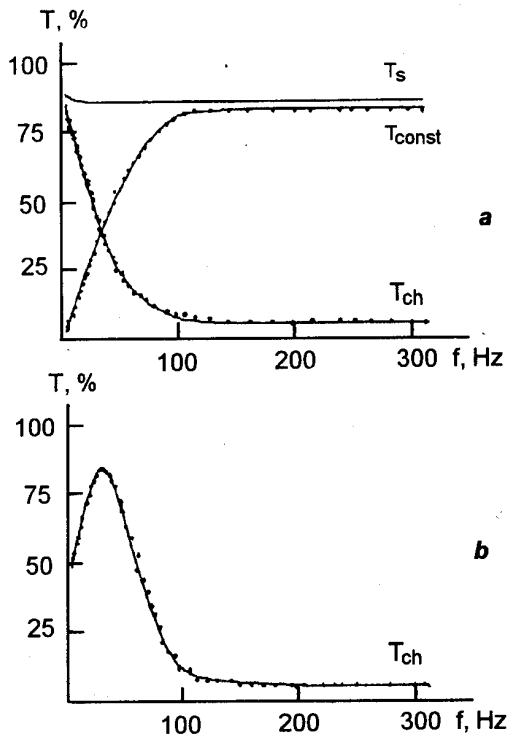

Fig.3. a) Dependence of the light transmission constant component, variable one, and sum thereof on the voltage U for first type samples; b) the variable light transmission component for second type samples.

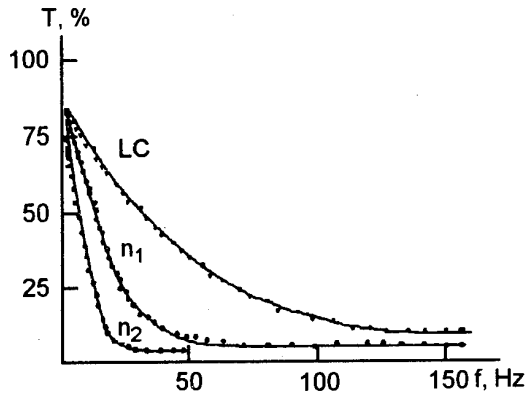

Fig.4. Dependence of the frequency characteristics on the aerosil concentration, C, for first type samples.

Table.

Aerosil No.	Modifying agent type	Frequency characteristic type
1	OMCTS	1
2	MPhCTS	1
3	MVCTS	1
4	AGM-9	1
5	PMS-5	2
6	HMDS	2

control the testing beam intensity. The voltage U is applied to the sample by means of an audio-frequency signal generator *GS* allowing for the frequency variation in the range 0.1 – 20000 Hz. The signal intensity proportional to that of the light incident on the *Phd*1 photodiode was measured as a function of the applied voltage frequency, f, at U = 15 V. The stability of U at frequency variations was controlled by means of a selective voltmeter.

We have noticed that the experimental results reproducibility can be attained, for some filled LC samples, only after several measurements of electrooptical characteristics. Namely, at the first voltage-contrast characteristic measurement, curves obtained under voltage increase and decrease do not coincide with each other, what results in a residual cell clearing. The degree of that residual clearing depends significantly on the surface modification type and diminishes when the aerosil surface becomes more hydrophobic. A constant response to the alternating field applied was established a few minutes after the start of experiment. All the results described below have been obtained for cells preconditioned in an alternating electric field what assured the results repeatability.

At applying of alternating voltage to the sample, a time constant light transmission component ($T_=$) as well as variable one ($T_\sim$) were observed (Fig.3). The frequency of the variable component exceeded twice that of the electric field. As a result, two types of the $T_=$ and $T_\sim$ curves behaviour were revealed. The first type (1) is characterized by monotonic increase of $T_=$ component and monotonic decrease of $T_\sim$ with the applied field frequency (f) rise. Therewith, the total light transmission, $T_= + T_\sim$, depends only slightly on the frequency (Fig.3,a). This fact suggests that the eventual redistribution of the light dissipation intensity between various angles at the field application is small.

For two samples (see Table), another behaviour type of frequency dependencies was observed: those were unmonotonic. The $T_\sim$ dependence characteristic for that type (2) is presented on Fig.3,b.

The frequency characteristics dependence on the aerosil concentration, C, was also studied. Fig.4 shows the $T_\sim$ dependence for the suspension 1, which corresponds to the type 1. In the

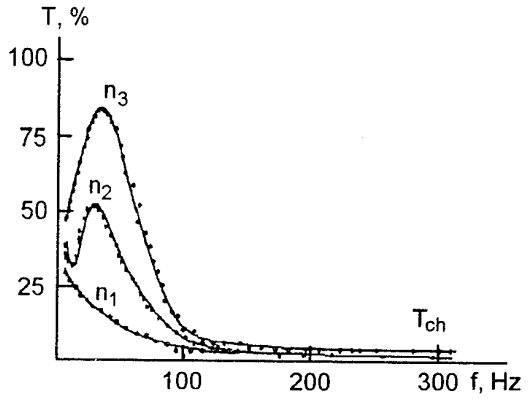

Fig.5. Dependence of the frequency characteristic on the aerosil concentration, C, for second type samples.

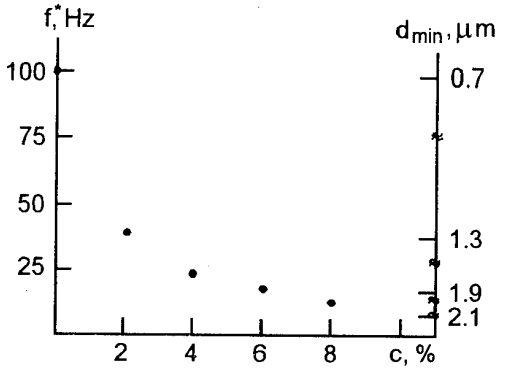

Fig.6. Dependence of the limit response frequency f^* of the system and of d_{min} value on the aerosil concentration.

same figure, the $T_\sim$ dependence is displayed for the pure liquid crystal of 100 μm thickness. As is seen from these data, the frequency characteristic steepness increases at the aerosil admission into suspension and the subsequent increase of its concentration.

In Fig.5, the frequency characteristics are presented for the suspension 5 belonging to second type. It is seen that the curve unmonotony begins to manifest itself only when a certain aerosil concentration (9 %) is achieved. At smaller concentrations, curves show the same appearance and the same dependence on the aerosil concentration as similar relationships for first type samples.

3. The electrically controlled light transmission variation in pure liquid crystal was studied on a non-oriented sample, i.e. on the sample formed by domains having randomly distributed director orientations. The transmission variation of such a system is due, in this case, to the reorientation of individual domains along the electric field direction. In such a geometry, the light dissipation is less effective [10] what result in an observable increase of the system light transmission.

Effectiveness of the domains response to an electric field application is determined by their characteristic times of reorientation in the field and is, to a first approximation, proportional thereto [10]. Since the reorientation time depends on the domain dimensions, the frequency characteristic $T_\sim(f)$ is defined by the domain size distribution.

The reorientation time in an electric field for an individual domain having the characteristic dimension d can be evaluated as

$$\tau \approx \frac{\eta d^2}{\pi K} \qquad (1)$$

where η is the orientational viscosity; K, the Frank constant.

In the case of monodomain sample, the $T_\sim(U)$ value must not depend on frequency at $f \le 1/\tau^* \approx \pi K/\eta L^2$ and drops sharply at the attaining of the limit frequency $f \approx 1/\tau^*$. In a polydomain sample, the $T_\sim(f)$ is influenced by the domain size distribution and has, therefore, a more complex character. The drop of the $T_\sim$ value with the frequency increase is caused by fact that lesser and lesser size domains "leave the field". It is obvious that the limit frequency of system response, f^*, is defined by the reorientation of the least domains, the size of the latter can be evaluated as

$$d_{min} \approx \sqrt{\pi K/f\eta}. \qquad (2)$$

In our case, $f^* \approx 100$ Hz what corresponds to $d_{min} \approx 1$ μm. It should be noted that this value is substantially less than the LC layer thickness (100 μm) and is defined likely by the balance of the free energy of a homogeneously oriented domain system and the disordering effect of heat energy.

The admission of aerosil to LC results in an increase of the $T_\sim(f)$ curve slope and diminishing of the frequency limit value, f^*. In Fig.6, dependences of f^* as well as of d_{min} value on the aerosil concentration, C, are shown. The character of those dependences indicates that the aerosil addition causes an increase of the characteristic region of the director inhomogeneity.

We have found that the aerosil presence does not influence substantially the temperature of the system transition into the isotropic state, T_C (the relative shift $\Delta T_C/T_C < 10^{-2}$). This indicates that aerosil is to be considered not as a molecular admixture, but as a macroscopic particle which is a

source of defects. This, in turn, allows to use the notions of the LC macroscopic theory (director, Frank constants, cohesion energy, etc.) when considering the LC-aerosil system characteristics.

At low concentration of aerosil particles, the d_{min} value must be of the same order of magnitude as the average distance between the aerosil particles, d, when corresponding inhomogeneity regions begin to overlap. If a concentration, C, of 2 % can be considered as a small one, then $d \approx 1.3$ μm. Such a correlation between C and d values points on the aggregation of aerosil particles in the LC. In fact, there are agglomerates consisting of approximately 3,000 microscopic aerosil particles which were estimated to correspond to the d value about 1.3 μm. This estimation supports our conclusion that, in our case, the aerosil particles can be considered as macroscopic admixtures.

The increase of the minimum domain size with the concentration (C) rise can be explained either by the increase of the aggregation effectiveness with growing C, or by the intensifying influence of collective interaction effects between aerosil particles through the LC director field. To elucidate the role of each of these factors, a further study must be performed.

4. Thus, the work results lead to following conclusions:

– In systems under question, the aerosil particles can be considered as macroscopic scale admixtures distorting the director field of the LC matrix and influencing only slightly its average ordering parameter.

– The frequency dependence of system light transmission at the electric field application is defined by the spatial size distribution of aerosil particles at a constant concentration thereof in the system, and the limit response frequency of the system corresponds to the minimum size of the director unhomogeneity region.

– The admission of aerosil to LC results in an increase of the minimum size of the director unhomogeneity region in the system.

References

1. J.W.Doane, N.A.Var, D.G.Wu, *Appl.Phys.Lett.*, **48**, 269 (1989).
2. H.G.Craighead, Yu.Cheng, S.Hackwood, *Ibid.*, **40**, 22 (1982).
3. R.Stannarius, W.H. de Jeu, L.C.Chien, J.W.Doane, *J.Appl.Phys.*, **70**, 135 (1991).
4. R.Eidenschink, W.H. de Jeu, *Electronics Lett.*, **27**, 1195 (1991).
5. M.Kreuzer, T.Tshudi, R.Eidenschink, *Mol.Cryst.Liq.Cryst.*, **223**, 219 (1992).
6. M.Kreuzer, T.Tshudi, W.H. de Jeu, R.Eidenschink, *Appl.Phys.Lett.*, **62**, 1712 (1993).
7. A.A.Chuyko, Yu.I.Gorlov, Silica Surface Chemistry: Surface Structure, Active Sites, Sorption Mechanisms [In Russian], Naukova Dumka, Kiev (1991).
8. A.A.Chuyko, V.A.Tertykh, *Ukr.Khim.Zh.*, **37**, 35 (1971).
9. A.A.Chuyko, G.Ya.Guba, *Zh.Teor.Eksp.Khim.*, **28**, 57 (1992).
10. L.M.Blinov, Electro- and Magnetooptics of Liquid Crystals [In Russian], Nauka, Moscow (1978).

О влиянии поверхности аэросила на частотные характеристики наполненных нематиков

Г.Я.Губа, А.В.Глущенко, Н.Ю.Лопухович, В.В.Огенко, Ю.А.Резников, В.Ю.Решетняк, О.В.Ярощук

Исследовано влияние модификации поверхности аэросила на электрооптические свойства гетерогенных систем аэросил – жидкий кристалл. Показано, что в рассматриваемых системах частицы аэросила можно рассматривать как макроскопические примеси. Предложена модель, согласно которой предельная частота отклика системы связывается с минимальным размером области неоднородности директора.

Functional Materials **2**, No.2 (1995)

Spectroellipsometry of surface layers of deformed strips made of amorphous metal alloys

M.V.Vinnichenko and L.V.Poperenko

T.Shevchenko Kiev University, 6 Acad.Glushkov Ave., 252022 Kiev, Ukraine

The angular and spectral dependences of ellipsometric parameters have been measured for the amorphous metal strips of $Fe_{81}(B,Si,C)_{19}$ with the aim to study the plastic deformation (rolling) influence on the structure and optical properties of their surface layers. It is established that the plastic deformation results not only in changes of ESESD features near the Fermi level, but influences also the mechanisms of current carriers scattering.

Проведено вимірювання кутових та спектральних залежностей еліпсометричних параметрів аморфних металевих стрічок $Fe_{81}(B,Si,C)_{19}$ з метою вивчення впливу пластичної деформації внаслідок прокатки на структуру та оптичні властивості їх приповерхневих прошарків. З'ясовано, що пластична деформація викликає не тільки зміну особливостей ЕСГСЕ поблизу рівня Фермі, а й впливає на механізми розсіювання носіїв струму.

In the modern materials science, one of the most important problems is to determine, reliably and operatively, the atomic and electron structure parameters for disordered systems, especially for amorphous metal alloys (AMA), and the dependences of such parameters on action of various physical factors (e.g. deformation, temperature, etc.) The plastic deformation influence on mechanic [1] and magnetic [2,3] properties of AMA is relatively well studied; but the question about AMA optical characteristics changes after a deformation remains still not clearly investigated [4].

Ellipsometry methods [5] can contribute significantly to the solution of that problem because of their high sensitivity to short-range order changes on the background of the destructed long-range one. Therefore, we have studied the optical properties and structural peculiarities of surface layers of fast-chilled iron-metalloid strips using angular ellipsometry, reflectometry near to normal incidence angle and spectral ellipsometry (Bitty method). Specimens of the amorphous $Fe_{81}(B,Si,C)_{19}$ were studied, made by the melt spinning method, in the forms of strips having approximately 1 cm in width and thickness $d = 16$ μm and $d = 10$ μm; both the contact side (i.e. having contact with cooler during the preparation) and incontact one (remaining free during preparation) are investigated. Before measurements, specimens were polished using the ASM diamond paste with minimum grain size 1/0.

The angular dependences of ellipsometric parameters, such as phase shift Δ between the orthogonal components of polarization vector and azimuth ψ of the restored linear polarization, were studied, for the strips described above, on a LEF-3M-1 ellipsometer with operating wavelength $\lambda = 632.8$ nm. From these dependences, the main angle of incidence $\varphi = \varphi_0$, corresponding to $\Delta = \pi/2$, was determined. The average absolute error of the value obtained did not exceed 0.2 deg and was due to specimens surface quality.

Reflectometric measurements designated to determine the surface state were performed using a reflectometer of normal incidence [6]. By its means, the scattering indicatrices over the polarization azimuth (SIPA) were obtained which provide information on the structural anisotropy of specimens.

Spectroellipsometric investigations of the optical constants, namely, of alloy surface layers refraction index, n, and absorption coefficient, κ, were performed on a universal ellipsometer according to Bitty's method in the range of sounding photons energy $\hbar\omega = 0.5 - 3.82$ eV, at the

angle of incidence $\varphi = 72$ deg. The RMS error of n and κ determination was within 3 percent. A filmless plane surface confining a semi-infinite conducting medium was chosen as the system model; on its basis, the dispersion characteristics were calculated for the optical conductivity, $\sigma(\hbar\omega) = n\kappa\omega/2\pi$, real part of the dielectric constant, $\varepsilon(\hbar\omega) = n^2 - \kappa^2$, and reflection coefficient, $R(\hbar\omega) = [(n-1)^2 + \kappa^2]/[(n-1)^2 + \kappa^2]$.

To characterize the structure anisotropy of $Fe_{81}(B,Si,C)_{19}$ AMA surface layers, the following parameters were proposed: the difference between main angles, $\Delta\varphi_0 = \varphi_{0\parallel} - \varphi_{0\perp}$, at the two mutually perpendicular orientations of the strip longitudinal axis in relation to the incidence plane, and characteristics of SIPA being presented in form of an oval, namely, the ratio ot its axes and slope the long axis to a chosen fixed direction coincident with the strip longitudinal axis.

As the result of investigation of the parameters mentioned in relation to the plastic deformation degree during rolling, a structural anisotropy has been found on the both surfaces of freshly produced amorphous strips; and what is of importance, its characterizing parameter, $\Delta\varphi_0$, is noted to increase after the rolling and to diminish during a further deformation. The previous studies [7] allow to associate the structural anisotropy on the incontact side of the initial specimen with different melt flow velocities in the longitudinal and transversal directions during the specimen preparation; this difference is believed to be responsible for the strength anisotropy (that of breaking stress, σ_f) relative to those directions [8]. This factor is absent on the contact surface of a specimen having $d = 25$ μm, where, however, mechanical stresses may reveal themselves which arose in the strip during its production. The specific behavior of parameters characterizing the structural anisotropy under the influence of two sequential deformations is to be associated, most likely, to the structure changes in the alloy (the crystallization fronts arising after first deformation and additional structure disordering after second one). The reflection from oriented imperfections cannot be used to explain the surface layers structural anisotropy since the latter does not disappear after the mechanical polishing of the surface.

Having revealed the plastic deformation influence on the atomic structure of the alloy, its electron structure changes must be considered. For this purpose, the spectra of $\sigma(\hbar\omega)$, $\varepsilon_1(\hbar\omega)$, $R(\hbar\omega)$ were calculated according to above formulas; these spectra are showed on the Fig.1. The dispersions of $\sigma(\hbar\omega)$ and $R(\hbar\omega)$ (curves 1–4) for the initial specimen show an absorption band at photon energy $\hbar\omega = 1.3$ eV characteristic for iron-metalloid type systems; that band can be assigned to the electron transitions from Fe $3d$ zone levels to Fermi level E_F. In the IR range (1–2.48 μm), the relationships mentioned run like to those described by Drude, which evidences the predominant absorption by free electrons and allows to determine, in terms of Drude model, the dynamic characteristics of the conductivity electrons in the alloy: the relaxation frequency, γ, and plasma one, Ω. To this end, the following function [9] was calculated:

$$F_1(\omega^2) = (1 - \varepsilon_1)^{-1} = \omega^2/\Omega^2 + \gamma^2/\Omega^2$$

which was then linearly approximated using least-squares method. The error of these parameters determination did not exceed 9%. For a freshly produced specimen, the values $\Omega = 6.23 \cdot 10^{15}$ s^{-1}, $\gamma = 0.97 \cdot 10^{15}$ s^{-1}, have been obtained.

It is found that, after a deformation, the absorption band in the $\sigma(\hbar\omega)$ and $R(\hbar\omega)$ spectra becomes broadened and shifts somewhat toward IR range, while the absolute values of σ and R diminish, what was observed already for other AMA [4]. Therewith, according to calculations, a deformation causes also a decrease of Ω to $5.40 \cdot 10^{15}$ s^{-1} and increase of γ to $1.07 \cdot 10^{15}$ s^{-1}. The further rolling results in a fading of absorption band in respective spectra, while Ω and γ estimations show some increase of Ω value at γ remaining unchanged.

Thus, the absorption band broadening in the corresponding relationships indicates the broadening of Fe $3d$ zone due to an additional structure disordering at the rolling, since the deformation is associated intimately with the atomic structure rearrangement, the deciding part is therewith played by the places exchange between the nearest neighboring atoms. The absorption band shift toward long-wave spectral region is explained by the E_F shift to the Fe $3d$ zone, while the intensity drop of $\sigma(\hbar\omega)$ and $R(\hbar\omega)$ spectra is due to decreasing of the d-like peak in the energetic spectrum of the electron states density (ESESD). These conclusions are in agreement with results of study of the disordering influence on the ESESD of amorphous systems [10].

In our opinion, the results obtained allow to state that plastic deformation not only causes changes in the ESESD characteristics near the Fermi level, but also influences on the mechanisms of current carriers scattering (taking into

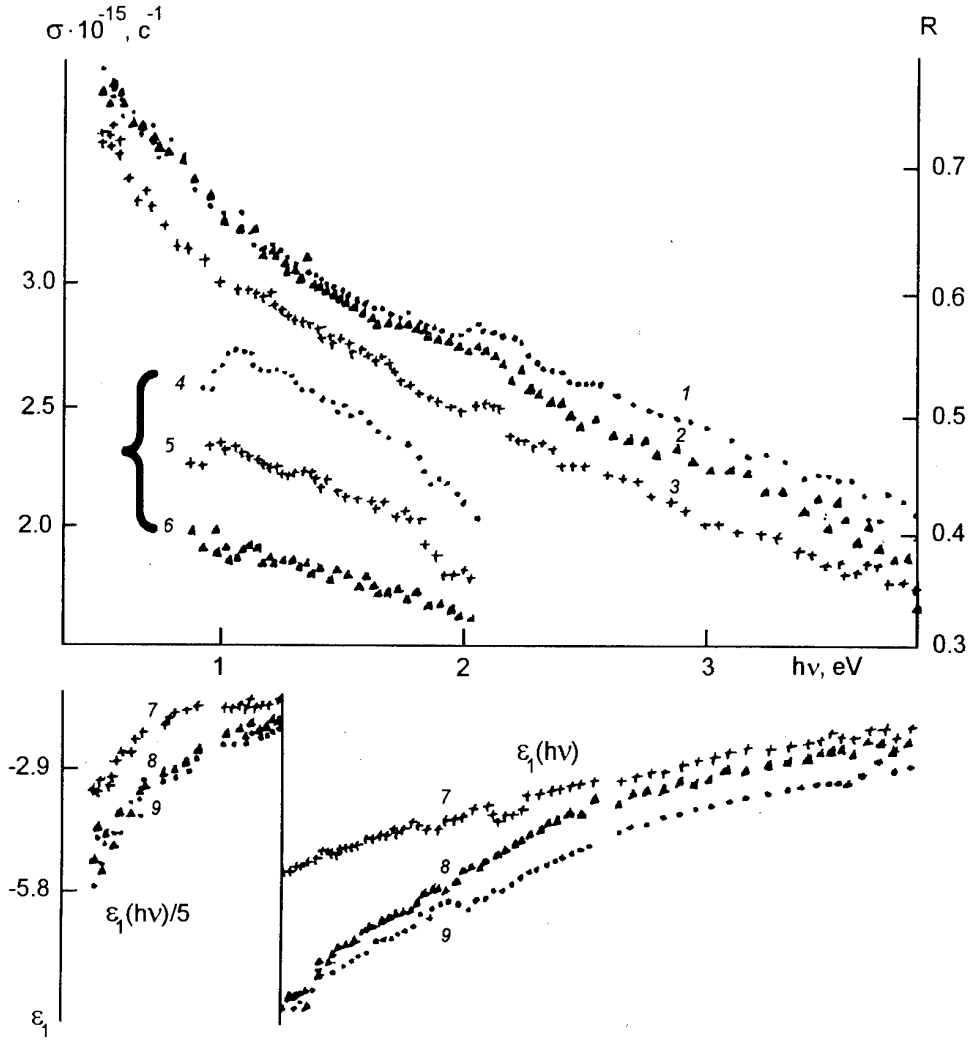

Fig. 1. The reflection coefficient (curves 1–4), optical conductivity (curves 4–6) and dielectric constant (curves 7–9) for a freshly prepared specimen d = 25 μm (1, 4, 9) of amorphous strip of $Fe_{81}(B,Si,C)_{19}$ alloy, and for similar strips rolled one time, d = 16 μm (3, 5, 7) and two times, d = 10 μm (2, 6, 8).

account the $R(\hbar\omega)$ and $\varepsilon_1(\hbar\omega)$ behavior changes in the IR spectral region).

Thus, plastic deformation results in significant changes in the atomic and electronic structures of $Fe_{81}(B,Si,C)_{19}$ amorphous alloy strips, as it is seen from their optical properties analyzes, and that fact allows to suggest the weak resistance of such alloys against the rolling.

References

1. Yu.A.Kunitski, V.N.Korzhik, Yu.S.Borisov, Non-Crystallic Metallic Materials and Coatings in Engineering [in Russian], Tekhnika, Kiev (1988).
2. Kai-Yuan Ho, Joing-Hui Mao, Ouen Wang, Young Shy He, Proc. Int. Symp. Phys. Magnet. Mater., Singapore, 378 (1987)
3. I.B.Kekalo, A.N.Zhdanov, V.Yu.Tsvetkov, Structure, Structural Transformations and Magnetic Properties of Amorphous Metallic Alloys [in Russian], Metallurgia, Moscow (1986).
4. V.D.Karpusha, L.V.Poperenko, S.L.Revo, Atomic Sci. and Techn. Problems, Ser. Nuclear-physical Investigations (Theory and Experiment) [in Russian], Issue 2 (10), 99 (1990).
5. A.V.Rzhanov, I.I.Svitashev, A.I.Semenenko, et. al., Fundamentals of Ellipsometry [in Russian], Nauka, Novosibirsk (1979)
6. V.G.Kravets, N.I.Mishchenko, L.V.Poperenko, I.A.Shaykevich, Thes. of 22-nd Sci. and Techn. Conf. of Young Scientists [in Russian], Kharkov, 51 (1991).

7. I.Lovas, E.J.Kisdi-Kozso, *J. Mater. Sci.*, **22**, 1535 (1987).
8. V.Z.Bengus, E.B.Korol'kova, Thes. All-Union Seminar "Dislocations Structure and Mechan. Properties of Metals and Alloys" [in Russian], Sverdlovsk, 11, (1990).
9. S.V.Sudareva, I.I.Sasovskaya, V.M.Mayevsky, et. al., Ural. Dept. of USSR Acad. Sci., Inst.Phys.Met., Preprint, Sverdlovsk, 12 (1988).
10. K.Sudzuki, X.Fudzimori, K.Xasimoto, Amorphous Metals, Omusija, Japan (1982).

Спектроэлектрометрия приповерхностных слоев аморфных металлических лент

М.В. Винниченко, Л.В. Поперенко

Проведены измерения угловых и спектральных зависимостей эллипсометрических параметров аморфных металлических лент $Fe_{81}(B,Si,C)_{19}$ с целью изучения влияния пластической деформации вследствие прокатки на структуру и оптические свойства их приповерхностных слоев. Установлено, что пластическая деформация приводит не только к изменениям особенностей в ЭСПСЭ вблизи уровня Ферми, но и влияет на механизмы рассеяния носителей тока.

Functional Materials **2**, No.2 (1995)

Magnetism and electronic structure of the Ni–Cr–Si–B amorphous ribbons

N.G. Babich, O.I.Nakonechnaya, L.V. Poperenko,
T.M. Tsvetkova and N.I. Zakharenko

T.Shevchenko Kiev University, 64 Vladimirskaya St., 252017 Kiev, Ukraine

Magnetic susceptibility, optical conductivity spectra and thermo-e.m.f. data were obtained for amorphous Ni–Cr–Si–B ribbons, prepared at different overheating degrees of the melt. The experimental results show that the properties of these alloys are determined by the density of electronic states variation in the vicinity of the Fermi level rather than by the presence of the magnetic inhomogeneities.

Одержано дані про магнітну сприйнятливість, спектри оптичної провідності та термо-е.р.с. аморфних стрічок Ni–Cr–Si–B, виготовлених при різних температурах перегріву розплаву. Експериментальні результати свідчать про те, що властивості цих сплавів визначаються насамперед зміною густини електронних станів поблизу рівня Фермі, а не присутністю магнітних неоднорідностей.

Amorphous alloys of the transition metal-metalloid type (TM–M) with TM = Ni have not been studied in such detail as those with TM = Co, Ni. According to Krishnan et al. [1] and Bakonyi et al. [2], the magnetism of Ni-based metallic glasses reveals an inhomogeneous behavior, e.g. the magnetic moment is attributed to the presence of Ni-rich paramagnetic clusters. However, this situation is still not clear enough.

In order to gain a better understanding of the nature of the magnetism in Ni-based glasses, we investigated the temperature dependences of magnetic susceptibility $\chi(T)$ of $Ni_{62.3}Cr_{17.6}Si_{13.8}B_{6.3}$ ribbons prepared at different overheating degree of the melt ΔT = 250, 300, 350 and 400 K. $\chi(T)$ curves (Fig.1) were obtained by Faraday-type technique. One can see that χ is decreases slowly in the range T < 680 K and then changes abruptly at T = 680–700 K. The latter is associated with crystallization of the samples. Obviously, the crystallization temperature T_x is almost independent of ΔT. The value of $|\partial\chi/\partial T|$ below T_x decreases monotonously as ΔT increases. However, for all investigated alloys it is always higher than for earlier investigated Ni–Si–B alloys [3]. Apparently it is due to the influence of chromium on the electronic structure of alloys. To confirm this assumption we treated our data according to the following equation:

$$\chi(T) = \chi_0 + AT^2 + N\mu^2\mu_B^2/3k(T-\theta) \qquad (1)$$

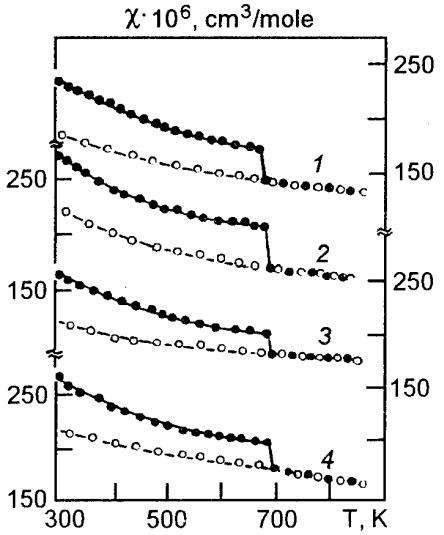

Fig.1 Temperature dependences of magnetic susceptibility for $Ni_{62.3}Cr_{17.6}Si_{13.8}B_{6.3}$ ribbons with ΔT = 250 (1), 300(2), 350(3) and 450 K (4) (• – heating, ° – cooling).

where $\chi_0 + AT^2$ is the temperature independent term, $N\mu^2\mu_B^2/3k(T-\theta)$ is the Curie-Weiss susceptibility χ_{CW}, μ is the magnetic moment and θ is the paramagnetic Curie temperature. The χ_0 values are listed in Table 1. Its main contribution is the Pauli susceptibility due to predominantly *d*-like itinerant electrons [4]. Hence, χ_0 reflects in a way the change of electronic states density at the Fermi level $n(E_F)$ at ΔT increase. One can see that χ_0 values are increased with ΔT indicating Fermi level is shifted to higher $n(E_F)$ values. Furthermore, χ_0 is greater for Ni–Cr–Si–B type amorphous alloys than for Ni–Si–B ones [3], what is probably caused by additional *d*-bonds formation between Ni and Cr atoms and, as a result, due to increasing of itinerant electrons quantity.

To study the role of overheating in the electronic localization effects and to eliminate the influence of composition inhomogeneities on magnetism of Ni-based amorphous alloys let us consider the Curie-Weiss constituent χ_{CW}. This term has been analysed in a routine manner. The θ values (not higher than 60 K) reflect the weak interactions between magnetic moments. For all alloys in amorphous state, the magnetic moment per Ni atom, according to $\mu_{Ni} = \mu\cdot(C_{Ni})^{-1/2}$ ($C_{Ni} = 0.623$), was found to be equal to $(0.37\pm0.10)\ \mu_B$. Such a small μ_{Ni} value can be explained, as in the case of Ni–Si–B ribbons [3], by partial quenching of the Ni spin moment. But μ_{Ni} values for studied ribbons exceed somewhat those found for Ni–Si–B. To our knowledge, this may be due to the presence of Cr atoms which form the additional *d*-bonds with Ni atoms, decreasing the degree of spin moment quenching.

Another conclusion can be drawn from our investigations: the μ_{Ni} values remain almost constant while ΔT increases. Obviously, the larger is ΔT, the more homogeneous is the spatial distribution of component's atoms. If the magnetism of investigated alloys is defined by Ni-rich clusters, as is shown in [2], one would expect a decreasing of μ_{Ni} while ΔT increased. So far, such behavior has not been observed, so one can assert that composition inhomogeneities influence on the magnetic susceptibility of these alloys is negligible.

Additional information on this problem was obtained from optical conductivity spectra $\sigma(\hbar\omega)$ (Fig.2), obtained by the Beattie method. Evidently, $\sigma(\hbar\omega)$ curves demonstrate the presence of the wide maximum with some structure for all ΔT values within the photon energy range 0.5–2.2 eV. On the one hand, the atoms in the samples prepared under lower ΔT are located closer to each other than in samples prepared at higher ΔT. In the latter case, the stronger electron localization effects take place resulting in narrowing of the energy band. On the other hand, in amorphous systems the energy band is broaden because of chaotic deviation of the interatomic distances from the average value, which is greater at higher ΔT. Taking into account this reasoning one can explain the $\sigma(\hbar\omega)$ peculiarities for these ribbons in the visible region [5]. Thus, no essential changes in electronic structure of $Ni_{62.3}Cr_{17.6}Si_{13.8}B_{6.3}$ amorphous ribbons in the vicinity of E_F is found while ΔT increases. Our thermo-e.m.f. measurements also indicate zero values in a couple consisting of the ribbons prepared with different ΔT. This is another confirmation of the above conclusion.

So, all the experimental facts disclosed here permit us to state that it is impossible to assume, at least within the experimental temperature region, the existence of Ni-rich magnetic clusters that might essentially influence the electronic properties of the ribbons studied.

Table 1. The values of χ_0 and T_x for $Ni_{62.3}Cr_{17.6}Si_{13.8}B_{6.3}$ amorphous ribbons with different ΔT.

ΔT, K	$\chi_0 \cdot 10^6$, cm^3/mole	T_x, K
250	250	678
300	263	680
350	260	682
450	265	688

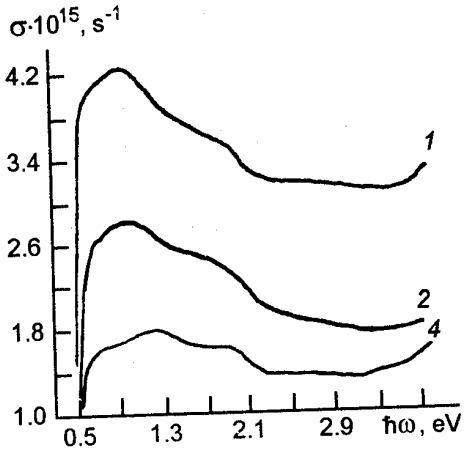

Fig.2 Optical conductivity spectra for $Ni_{62.3}Cr_{17.6}Si_{13.8}B_{6.3}$ amorphous ribbons (curve's numbering scheme corresponds to Fig. 1)

References

1. R.Krishnan, M.Duncigier and P.Rougier, *J. Magn. Magn. Mater.*, 31–34, 1501 (1983).
2. I.Bakonyi, P.Panissod, M.Miljak and E.Babich, *J. Magn. Magn. Mater.*, 58, 97 (1986).
3. N.I.Zakharenko, N.G.Babich, O.I.Nakonechna and S.L.Revo, In: Digests of EMMA'93 Conf., Kosice, Slovacia, A-P-37 (1993).
4. C.Coulson, Valence, 2nd Ed., Oxford Univ.Press (1960).
5. T.M.Krasnozhon and L.V.Poperenko, *Vestn.Kiev. Univ., Fiz.-Mat.*, 7, 82 (1992).

Магнетизм и электронная структура аморфных лент Ni–Cr–Si–B

Н.Г.Бабич, О.И.Наконечная, Л.В.Поперенко, Т.М.Цветкова, Н.И.Захаренко

Получены данные о магнитной восприимчивости, спектрах оптической проводимости и термо-э.д.с. аморфных лент Ni–Cr–Si–B, приготовленных при различных температурах перегрева расплава. Экспериментальные результаты свидетельствуют о том, что свойства этих сплавов определяются прежде всего изменением плотности электронных состояний в окрестности уровня Ферми, а не присутствием магнитных неоднородностей.

Functional Materials 2, No.2 (1995)

Optical properties of metallic surfaces modified by the ion implantation

L.V.Poperenko, O.M.Tolopa and V.D.Karpusha

T.Shevchenko Kiev University, 64 Vladimirskaya St., 252601 Kiev, Ukraine

The results of optical and Auger-electron spectroscopy experiments for surface of Mo specimens modified by high-dose implantation by Cu^+ and mixed beam of Fe^+ and B^+ are analysed. It is shown that the role of the foreign impurity atoms such as carbon in the formation of interatomic binding into the near-surfaces layer is essential.

Проаналізовано результати оптичних та оже-спектроскопічних досліджень модифікованих високодозною імплантацією поверхонь молібденових зразків іонами Cu^+ та змішаним потоком Fe^+ і B^+. Визначено, що у приповерхневому прошарку речовини виникає міжатомний зв'язок такого типу, де роль металоїдних атомів відіграють сторонні домішки вуглецю та інших елементів.

One of the most urgent tasks of modern applied physics is to obtain the scientific data which are used as the basis of new techniques to extend the machines and tools lifetime, to change the surface conductivity and metallization of dielectrics, to create the anti-frictional, corrosion-resistant, erosion-resistant, and other coatings including those made of elements which, in the equilibrium conditions, are mutually insoluble, e.g. Cu–Mo or Cu–W type [1]. Investigation in this area are performed in two directions complementing each other: the creation of large-aperture streams of ions and plasma and the study of properties of coatings obtained by such techniques.

The purpose of this work is to study the optical properties of the coating obtained by high-dose ion implantation (HII) and also to elucidate the elements distribution in depth for specimens treated by HII and by ion-plasma mixing (IPM). As a ions source, the vacuum-arc large-aperture (S = 200 to 400 cm^2) ion injector was used [2]. The accelerating potential was 80 kV, the ion implantation dose $10^{17} - 10^{18}$ cm^{-2}. As the implantation object, a Mo substrate was used in combination with the copper cathode; also, the mixed Fe^+, B^+ stream implantation into molybdenic substrate was performed. For optical studies, a specimen of unimplanted Mo was used, too.

The elements distribution in depth was measured by Auger spectroscopy. The optical properties of coatings were studied by means of Beattie-Cohn spectroellipsometric method in the energy range 0.5 – 4.5 eV. The angle of beam incidence on the specimen was 70 °. From the optical measurements data, the absorption and refraction coefficients were calculated as well as the optical conductivity $\sigma = n\kappa\nu$, where ν is the sounding light frequency, and the real component of the dielectric constant, ε_1. The error of measurement of optical absorption and refraction indices did not exceed 3 %.

It follows from the consideration of concentration profiles for the implanted surfaces (Fig.1) that, in the IPM mode, a significant increase of concentration and of modified layer thickness takes place. The observed distribution of elements in specimen depth cannot, in this case, be predicted on the basis of the equilibrium state diagram for respective systems. Such a situation is possible if either the amorphous state exists, or a phase distribution induced by high-dose implantation with formation of micro-clusters of each element atoms having size of several coordination spheres. The prevailing diffusion of surface atoms having affinity both with implanted

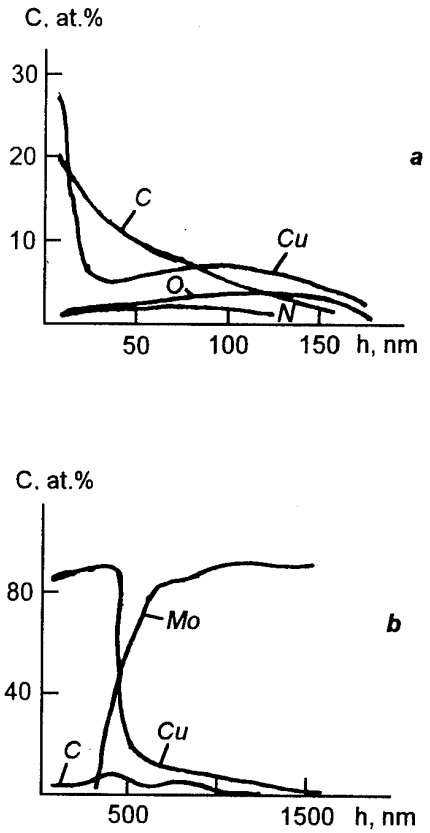

Fig.1. Admixtures concentration profiles for molybdenum coatings implanted with Cu^+ ions by HII (*a*) and IPM (*b*).

atoms and the substrate confirms the hypothesis about the advantage of radiation-atimulated diffusion processes over the ballistic mixing of atoms with neighbouring ones [1]. When, in the HII method, the implantation dose (time) increases up to $D_i > 5 \cdot 10^{17}$ ions/cm^2, the target sputtering and implanted ions penetration processes come to saturation. Thus, in that technique, the concentration of ions implanted into a surface is limited by a value of 20...30 atom.%. The coating thickness can be increased if carbon is present on the target surface due to diminished surface sputtering during the HII process.

Considering the spectral dependence of the optical conductivity, $\sigma(E)$ (Fig.2), one can suppose that, at HII, the optical features of coatings under question undergo an essential change. So, after the Cu^+ ions implantation into Mo, the absorption peak at the impinging photons energy 1.8 eV which is characteristic for Mo vanishes completely. Such a relationship, however, differs also from the optical properties of Cu, what is due to a substantial content of carbon and other

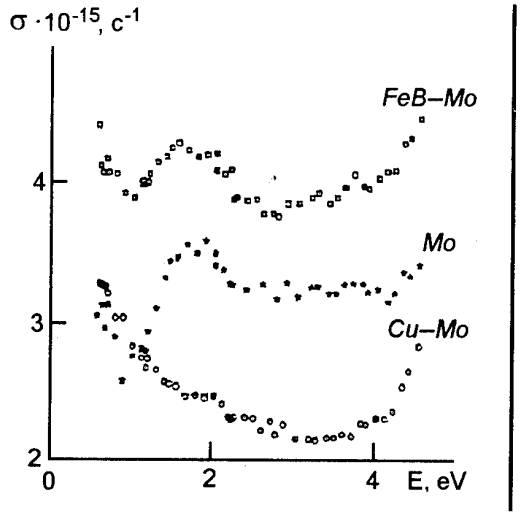

Fig.2. Spectral dependences of the optical conductivity of coatings.

impurities atoms in the surface layers. The implantation of a mixed Fe and B ions stream results in a certain modification of the absorption peak at 1.8 eV energy: the absorption maximum shifts toward the IR spectral range, and an additional singularity at the photons energy 2 eV appears. It is characteristic, too, that, in the case of modification by Cu atoms, some lowering of absolute $\sigma(E)$ values takes place, while the implantation of a mixed Fe^+ and B^+ ionic stream results in their increase.

The correct analysis of the light absorption mechanism for the specimens under study is made difficult by the lack of calculations of the electronic structure for such systems. It can be said with confidence, however, that absorption peaks in the photons energy range 1.5 – 2 eV are associated with interzonal electron transitions from the filled *d*-like electron states in metallic atoms to the empty ones positioned near to Fermi level. This conclusion is confirmed by a considerable body of published data referring to the study of the electronic structure and related optical features of disordered, amorphous, and other alloys containing the transition metals. The significant increase (decrease) of the absolute optical conductivity values reflects the fact that the electron states density near the Fermi level undergoes changes.

Information about the optical properties of a substance is completed essentially by the analysis of the spectral dependences of the dielectric constant real component. It follows from such an analysis that the modification of the molybdenum surface results in the tendency to an anomalous, as compared to metals, $\varepsilon_1(E)$ dependence in the

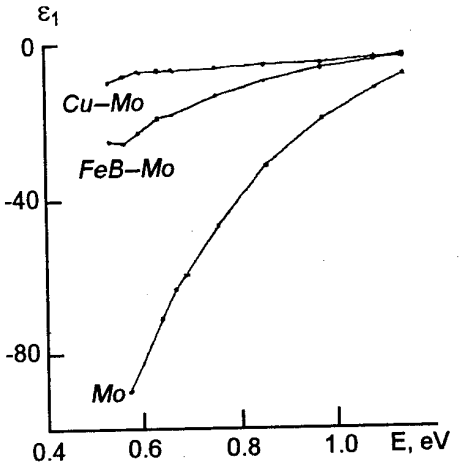

Fig.3. Spectral dependences of the real part of dielectric constant for coatings.

IR spectral region (Fig.3). For metals and their alloys, a Drude-like relationship of the dielectric constant real part is characteristic, which is just observed for unmodified Mo specimens. Yet, the ionic implantation results in a less sharp drop of the value mentioned when the photons energy decreases. As one of the authors had shown earlier [3], such a shape of the $\varepsilon_1(E)$ dependence reflects the electron density localization in the space between the unlike atoms pairs (metal-metalloid), and the diminishing of the generalized electrons fraction in the area of metallic atoms overlap. Such a covalent- and ionic-like bounding of the close-neighbouring atoms in relation to metallic ones, associated with Anderson's localization, results in an incerased stability of the atomic structure formed and, respectively, in an enhance of working characteristics for articles made of such materials. It can be supposed that, at ionic implantation, just the interatomic bonds of such a type arise, where carbon and other elements admixtures act as the metalloid atoms. This results in the possibility of existence of a stable disordered structure characterized by high working characteristics.

Thus, the consideration of results of performed optical and Auger spectroscopic studies shows that the Mo surface implantation by HII method causes substantial shanges in its electronic structure and in optical properties related with it. The formation of stable systems including different groups of atoms is due, in considerable measure, to the arising, during HII, of localized electronic states, what results in an enhance of mechanical working characteristics of such coatings.

References

1. Yu.F.Bykowski, V.N.Nevolin, V.Yu.Fominski, Ionic and Laser Implantation of Metal Materials [in Russian], Energoatomizdat, Moscow (1991).
2. A.L.Aksenov, S.P.Bugayev, A.M.Tolopa, *Pribory i technika eksperimenta*, No.3, 139 (1987).
3. L.V.Poperenko, Optical Properties and Electron Structure of Amorphous Alloys Based on the Iron Group Elements [in Russian], Phys.-Math.Doctoral Thesis, Kiev (1992).

Оптические свойства модифицированных ионной имплантацией металлических поверхностей

Л.А.Поперенко, О.М.Толопа, В.Д.Карпуша

Проанализированы результаты оптических и оже-спектроскопических исследований модифицированных имплантацией поверхностей молибденовых образцов ионами Cu^+ и смешанным потоком Fe^+, B^+ и определено, что в приповерхностном слое вещества возникает межатомная связь такого типа, где роль металлоидных атомов играют внешние примеси углерода и других элементов.

Functional Materials **2**, No.2 (1995)

Photoacoustic and luminescent properties of porous silicon

I.V.Blonsky, M.S.Brodyn, V.A.Tkhorik,
Yu.P.Piryatinsky* and G.Yu.Rudko*

Institute of Physics, National Academy of Sciences of Ukraine,
46 Nauki Ave., 252650 Kiev, Ukraine

*Institute of Semiconductor Physics, National Academy of Sciences of Ukraine, 45 Nauki Ave., 252028 Kiev, Ukraine

Photoacoustic spectra of porous silicon have been first investigated with the signal recording by gas microphone; on the basis of those spectra, the fundamental absorption edge of the material has been reproduced and the temperature conductivity coefficient $D = 0.09$ cm^2/s was determined. The results obtained are correlated with time-resolved photoluminescence spectra obtained by the authors, what allows the conclusion about a «bottle neck» existence in the energy relaxation of electronic excitations of por-Si.

Вперше досліджено фотоакустичні спектри пористого кремнію при газомікрофонній реєстрації сигналу, на основі яких відтворено його фундаментальний край поглинання та визначено коефіцієнт температуропровідності $D = 0{,}09$ см^2/с. Результати досліджень фотоакустичних спектрів співставлені з отриманими авторами спектрами фотолюмінісценції з часовим розвитком, що дозволяє зробити висновок про існування «пляшкового горла» в енергетичній релаксації електронних збуджень por-Si.

Introduction.

The remarkable property of porous silicon (por-Si) is the intense visible photoluminescence at room temperature [1]. The nature of this phenomenon is not clear yet. There are several hypotheses of its origin. The most popular explanations are:

1) the modification of electronic bands structure due to the quantum size effects in silicon quantum wires formed by anodizing [2];
2) formation of certain chemical compounds ($Si_6O_3H_6$, SiH, SiH_2, etc.) which radiate in the wide spectral range 1.6–2.6 eV [3];
3) the existence of amorphous silicon phase of various chemical compositions on the walls of the pores [4].

To prove any of these models, the knowledge of the fundamental adsorption edge of por-Si is very important. The solution of this problem by means of traditional absorption spectroscopy methods is rather complicated due to following reasons:

1) the samples under investigation consist usually of two layers with different properties (thin porous layer covers comparatively thick bulk single crystalline silicon wafer);
2) the porous layer gives the essential contribution to the total extinction of the sample due to the diffuse light scattering.

Experimental

During last years, new methods based on the photoacoustic (PA) effect were elaborated for the investigation of optical and thermoelastic properties of inhomogeneous media (e.g. for layered systems) [5]. The photoacoustic effect is the generation of acoustic waves in the sample itself as well as in the surrounding gas due to the absorption of modulated radiation. To investigate the PA effect a special cell is usually used. It is

closed chamber with optical windows which is filled with a gas. PA signal is detected by microphone built into a wall of the chamber. The variations of gas pressure due to the thermal exchange between the light-heated sample and the gas inside the cell cause the vibrations of the microphone membrane. The measured values are the amplitude U and the phase φ of the signal. Generally, the U value corresponds to the efficiency of transformation of the absorbed light beam energy to the thermal one, while the value φ characterizes the delay of the PA signal which depends on the time of the temperature relaxation, the time of thermal diffusion and the time constant of experimental equipment.

Results and discussion

The present paper deals with the first investigations of PA response of por-Si vs. the light modulation frequency $\omega=2\pi f$ and excitation light wavelength λ. From these dependences, the spectral dependence of absorption coefficient near the high-frequency edge of por-Si luminescence band was deduced. The comparison of por-Si and bulk Si thermal properties is carried out. The proposed method of the fundamental absorption edge determination is based on the fact that amplitude U and phase φ of PA-signal are changed at the transition from the transparency region of por-Si to the high absorbance region due to the transformation of heat-generating zone.

The measurements were carried out at room temperature using specially designed PA specrtrometer based on gas microphone method of signal detection.

Three types of samples with equal thicknesses (500 μm) were investigated. They were the single crystalline silicon wafers and Si wafers with layers of por-Si of 5 μm and 50 μm thickness. The por-Si layers were obtained by anodizing in the ethanolic HF solution at current density 40 mA/cm^2.

Fig.1 shows the frequency dependences of PA signal amplitude U and phase φ for three types of samples measured at λ = 632.8 nm. It is seen that $U(f)$ and $\varphi(f)$ dependences are almost the same for the bulk Si wafer and for the sample with 5mm por-Si layer while the corresponding dependences for the sample with 50 μm por-Si layer are somewhat different. This fact can be explained in the framework of the model for PA response in two-layer system assuming that the absorbance of por-Si layer at λ = 632.8 nm is low. Then it is obvious that, in the bulk Si heat generation takes place in a thin subsurface layer with

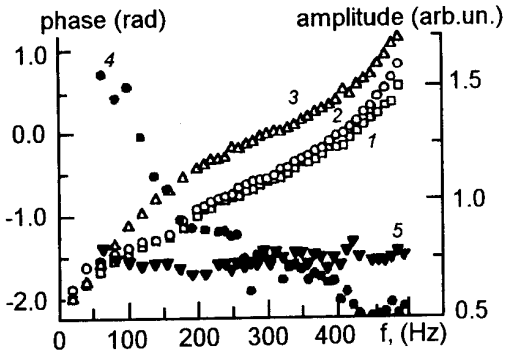

Fig.1. The frequency dependences of the PA signal phase φ for single crystalline Si and for the samples with 5 μm and 50 μm por-Si layers (curves 1–3, respectively) and the frequency dependences (curves 4 and 5) of PA signal amplitude U for the samples with 5 μm and 50 μm por-Si layers, respectively, normalized to the PA signal amplitude for single crystalline Si.

the thickness $L \sim 10^{-8}$ cm which is determined by the absorption coefficient at λ = 632.8 nm. In the sample with por-Si layer the heat source is located on the por-Si/bulk Si interface. The phase shift of PA response depends in this case on the delay of the thermal wave due to the propagation through the por-Si layer.The larger is the thickness h of por-Si layer, the larger would be φ. The latter value is also influenced by the thermal diffusivity coefficient D. In fact, the wavelength of the thermal wave is given by $l = (2D/\omega)^{1/2}$.

The above considerations elucidate the source of the discrepancies in $U(f)$ and $\varphi(f)$ dependencies obtained for the samples with 5 μm and 50 μm por-Si layers, and evidence that, in the chosen range of ω values, the samples with the por-Si thickness $h > 5$ μm should be investigated by PA-spectroscopy methods. Using the phase-frequency dependences (Fig.1) and the conclusions of theory [6], derived for the case of two-layer system, we estimated the thermal diffusivity for the porous layer to be D_{por} = 0.04 cm^2/s. Note that, for the bulk Si, D = 0.9 cm^2/s [7]. However, it should be emphasized that in the case of por-Si, the value of D_{por} depends on porosity and is not the universal parameter of material. The porosity of the samples under investigation was 40 %. The detailed comparison of thermal properties of por-Si and bulk Si is given elsewhere.

Fig.2 shows the spectral dependencies of U and φ of PA signal. It is seen that the spectrum of the sample with thin porous layer is smooth and has no characteristic features. This behavior is obvious because, at f = 120 Hz, the porous layer is thermally

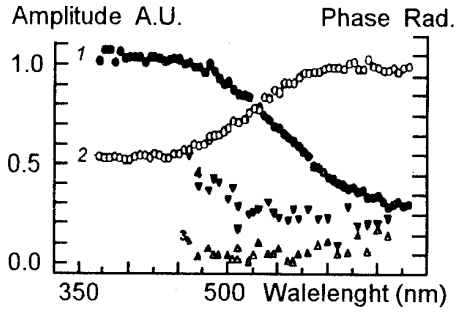

Fig.2. The spectral dependences of the amplitude U (curves 1,4) and of the phase shift φ(2,3) of the PA signal for the samples with 5 μm (curves 3,4) and 50 μm (curves 1,2) por-Si layers.

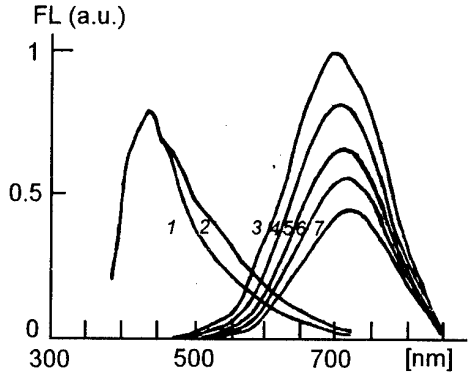

Fig.3. Time resolved fluorescence spectra of por-Si. The delay time, t_3: 1 – 1 ns, 2 – 10 ns, 3 – 1 μs, 5 – 20 μs, 6 – 30 μs, 7 – 40 μs, λ_{ex} = 337.1 nm, T = 300 K.

thin (at f = 120 Hz, l = 103 μm, i.e. $l >> h$). On the other hand, the dependences $U(\lambda)$ and $\varphi(\lambda)$ for the sample with the 50 μm por-Si layer ($l = h$) exhibit the abrupt increase of phase shift and amplitude with the decrease of wavelength starting with λ = 630 nm. Since the dependences $U(\lambda)$ and $\varphi(\lambda)$ were obtained for the fixed modulation frequency value f = 120 Hz, this increase may be caused only by the spatial change of the region where thermal release takes place. With the decrease of exciting wavelength, this region shifts from the por-Si/bulk Si interface towards the surface of the sample. This shift may be caused only by an increase of exciting light absorption in the surface layer. Thus, the results obtained evidence that, in the sample with 50 μm por-Si layer, the increase of $U(\lambda)$ and $\varphi(\lambda)$ corresponds to the absorption edge $\alpha(\lambda)$.

For the advance in the understanding of the nature of visible light radiation in por-Si, the comparison of PA spectra, which give the information about nonradiative energy dissipation, with photoluminescence (PL) spectra is carried out. The latter were measured under the nitrogen laser excitation (λ_{ex} = 337.1 nm, t = 6 ns, p = 5 mW) in the strobe regime. Typical time dependent spectra are shown in Fig.3. The main PL results are:

1) in the spectra measured with the delay time t_3 of about several ns, the wide high frequency PL band with the maximum at 440 nm is observed. This band consists probably of three overlapping bands, and their intensities are saturated under the high exitation laser intensity;

2) With the increase of the delay time, the intensity of 440 nm band decreases and the latter disappears at t_3 = 100 ns while the new band in the spectral range 550–800 nm emerges;

3) with the increase of t_3 from 100 ns to 30 ms, the spectral position of the low frequency band shifts from 680 nm to 720 nm.

The continuous and nonmonotonous character of photoluminescence spectrum transformation with the increase of t_3 leads to the conclusion about the common origin of these bands and the existence of a «bottle neck» (500–600 nm) in the energy relaxation of PL-related electronic excitations. One of the probable sources of «bottle neck» effect may be the mobility edge occurence in the density of states $g(E)$ which is characteristic of the systems with inhomogeneous broadening. In this case, the low frequency PL band which is observed on the final stages of electronic excitations relaxation would correspond to the localized electronic states range, and the spectrum in Fig.2 would reflect $g(E)$ distribution below the mobility edge. The results of our investigations of PL and PA spectra at the excitation of carriers into the nonhomogeneously broadened states as well as the mechanisms of PL will be discussed elsewhere.

References

1. L.T.Cancham, *Appl. Phys. Lett.*, **57**, 16 (1988).
2. A.Lechmann, U. Gosele, *Appl. Phys. Lett.*, **58**, 856 (1991).
3. L.Tsybeskov, P.Fauchet, *Appl. Phys. Lett.*, **64**, 1983 (1994).
4. K.S.Murayama, S.M.Miyazaki, M.Hirose, *Jpn. J.Appl. Phys*, **31**, L1358 (1992).
5. Ju.V.Guljaev, A.K.Arbachov, A.M.Morozov et al., *Doklady AN SSSR*, **302**, 89 (1988).
6. A.Rosenzwaig, A.Gersho, *J.Appl. Phys.*, **47**, 46 (1976).
7. A.A.Blistanov, V.S.Bondarenko, N.V.Perelomova, Acoustic Crystals [in Russian], Nauka, Moscow (1982), p.632.
8. V.S.Bondarenko et al., in: Abstr. of 1 Russian Conf. on Semiconductors Physics [in Russian], Nizhnii Novgorod, (1992), vol.2, p.260.

Фотоакустика и люминесценция пористого кремния

И.В.Блонский, М.С.Бродин, В.А.Тхорик,
Ю.П.Пирятинский, Г.Ю.Рудько

Впервые исследованы фотоакустические спектры пористого кремния при газомикрофонной регистрации сигнала, на основе которых воспроизведен его фундаментальный край поглощения и определен коэффициент температуропроводности $D = 0{,}09$ см^2/с. Результаты исследований фотоакустических спектров сопоставлены с полученными авторами спектрами фотолюминесценции с временным разрешением, что позволяет сделать заключение о существовании «бутылочного горла» в энергетической релаксации электронных возбуждений por-Si.

Functional Materials 2, No.2 (1995)

The study of the substance desorption process using holographic interferometry

Yu.I. Onischenko, L.I.Kostrova, E.P.Udalov, L.I.Robur and G.A.Avtonomov

T.Shevchenko Kiev University, 64 Vladimirskaya St., 252017 Kiev, Ukraine

One of the most important problems in the investigation of the solid and liquid surfaces interaction with gaseous and liquid media is providing the non-destructive and contactless control of surface structure. The holographic interferometry can be succesfully used for this purpose. The principle of the holographic interferogram record consists of the interference of two states of the same surface of the studied object: in initial state and that after being exposed to some changes. The slightest changes of the surface structure that were caused by desorption of the substance lead to the changes of the contrasts in interference pattern. This allows to evaluate the rate and intensity of the substance interaction with surface.

Однією з важливих задач при дослідженні взаємодії твердих та рідких поверхонь з газоподібними і рідкими речовинами є забезпечення безконтактного та неруйнівного контролю структури поверхні. Для цієї мети можна з успіхом застосувати метод голографічної інтерферометрії. Принцип запису голографічних інтерферограм полягає в інтерференції двох станів однієї й тієї ж поверхні досліджуваного об'єкту: в початковому стані та після деякої взаємодії. Найменші зміни структури поверхні, викликані десорбцією речовини, призводять до зміни контрасту інтерференційної картини смуг. Це дозволяє оцінити швидкість та інтенсивність взаємодії речовини з поверхнею.

When creating new composite materials, indicating devices, products and constructions operating in aggressive media, one should have information on the state of the surface and dynamics of its properties variation as a result of the interaction with gaseous and liquid substances. One of the most important problems in the study of the interaction processes of solid and liquid surface with gases and liquids is a provision of a contactless and nondestructive methods for the surface state control.

A holographic interferometry method ensuring a possibility to make contactless measurements on any type surfaces without a preliminary preparation or treatment can be applied for this purpose. The simplicity and high accuracy of this method open wide perspectives for it to be used for the solution of scientific and application problems when studying the processes that occur on the surface of different materials. An approach according to which every point of the iliuminated surface absorbs and reflects the light and thus acts as a source of spheric waves is taken as a basis of the proposed method of holographic interferometry. The complex amplitude of the scattering light in a random point of space is equal to the sum of the amplitudes of the waves scattered by every point of the surface. The height of the surface relief in some point (x,y) is the function $\xi(x,y)$ which is defined as:

$$\xi(x,y) = f(R_a, R_z), \tag{1}$$

where R_a is a mean arithmetical deviation of the profile from the central line within the limits of some length l; R_z is the height of the profile uneventies.

$$R_a = \frac{1}{l}\int_0^1 |y|\,dx \approx \frac{1}{n}\sum_{i=1}^{n} |y_i|;$$
$$R_z = \frac{1}{5}\sum_{i=1}^{5} h_{imax} - \sum_{i=1}^{5} h_{imin} \tag{2}$$

The expression for the complex amplitude of the scattered light in a random point of space P may be written in the form [1]:

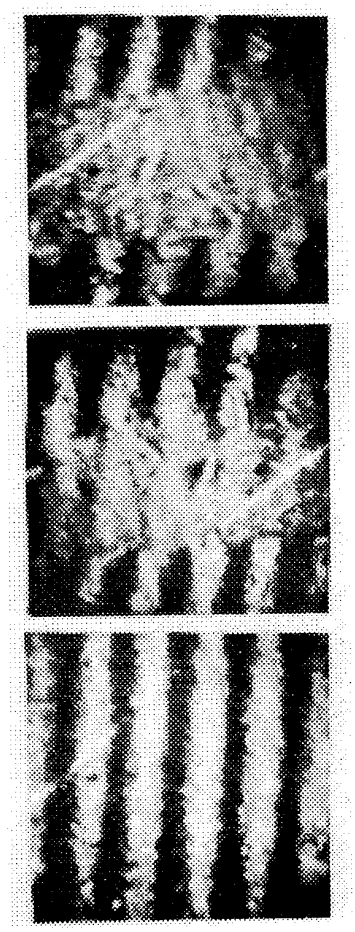

Fig.1. Changes in the contrast of the interference patterns of displacement bands caused by the liquid desorption from a solid surface: a) liquid sorbed by the surface; b) liquid partially desorbed; c) liquid fully desorbed.

$$U(x,y) = k \int_{-\infty}^{\infty} U(x,y) \exp[i2\pi G\xi(x,y)/\lambda]\, dx\, dy \qquad (3)$$

where k is constant; $U(x,y)$ describes the complex amplitude of light incident on the point (x,y); G is geometric factor defined by the directions of the illumination and observation.

Since the parameters characterizing the state of the surface (relief, structure, etc.) vary randomly by the value of the wavelength λ or more, the phase member $G\xi(x,y)$ will vary proportionally to random values. Consequently, a full amplitude at the point P is described by the sum of vectors with random phases; their addition gives a random resulting amplitude. The value of the full amplitude

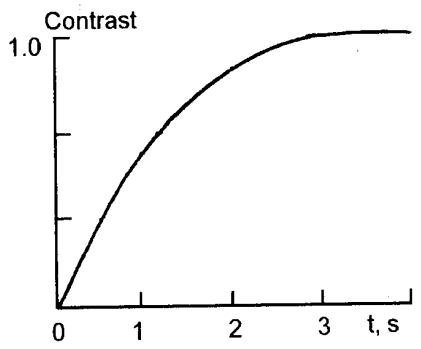

Fig.2. The dynamics of contrast changes of the interference pattern with time in the process of liquid desorption from a solid surface.

varies from 0 to maximum depending on the value of the individual components' phase.

At the change of the characteristic factors of the studied surface, the full amplitude and, consequently, the intensity of the scattered light change as well. This is well visualized by the modification of the interference pattern of the displacement bands formed by this surface.

The experiments on the study of the liquid (alcohol) desorption process from the surface of aluminium plate were carried out. Fig.1 shows the dynamics of the change in the interference pattern in the course of the liquid desorption from the solid surface. It is evident that the slightest changes of the surface state caused by the substance desorption lead to change in the contrast of the bands interference pattern. By the contrast change with time (Fig.2), one may quantitatively estimate the liquid desorption rate from the studied surface.

The presented results give evidence to the possibilities of the holographic interferometry method and to the necessity to elaborate, on its basis, a high accuracy method for the investigation of Langmuir-Blodgett films, adsorption monolayers on liquid and solid surfaces, modified surfaces of adsorbents, etc.

This registration method can be applied in the creation of devices for a nondestructive control of operational characteristics of the working surfaces of constructions and products as well as in ecology for the development of a new generation of sensors for enviromental monitoring.

References

1.R.Jones, K.Wykes, Holographic and Spektral Interferometry [in Russian], Mir, Moscow (1986).

Изучение процесса десорбции веществ с помощью голографической интерферометрии

Ю.И.Онищенко, Л.И.Кострова, Е.П.Удалов,
Л.И.Робур, Г.А.Автономов

Одной из важнейших задач при исследовании взаимодействия твердых и жидких поверхностей с газообразными и жидкими средами является обеспечение бесконтактного и неразрушающего контроля структуры поверхности. Для этой цели может быть успешно применен метод голографической интерферометрии. Принцип записи голографических интерферограмм заключается в использовании интерференции двух состояний одной и той же поверхности исследуемого объекта: в начальном состоянии и после некоторого взаимодействия. Малейшие изменения структуры поверхности, вызванные десорбцией вещества, приводят к изменению контраста интерференционной картины полос. Это позволяет оценить скорость и интенсивность взаимодействия вещества с поверхностью.

Functional Materials 2, No.2 (1995)

Ellipsometric analysis of irradiated copper mirrors

B.V.Grigorenko, R.S.Mikhalchenko and V.S.Voitsenia*

Institute for Low Temperature Physics and Engineering, National Academy of Sciences of Ukraine, 47 Lenin Ave., 310164 Kharkov, Ukraine

*Kharkov Physico-Technical Institute, 1 Akademicheskaya St., 310108 Kharkov, Ukraine

To analyze irradiated mirror surfaces, the ellipsometric method is used as the reflecting surface model, a homogeneous absorbing film on a homogeneous absorbing substrate was used. The principal ellipsometric equation was solved numerically. The optical constants of the substrate and the film, the film thickness, the reflectance and absorptivity of the mirrors as functions of Cu^+ and Ar^+ penetration into copper were calculated. It is shown that the method can be used to study surface roughness prior and subsequent to irradiation. Irradiation of copper mirror surfaces with the Cu^+ ions of 3 MeV or Ar^+ ions of 4 keV increases their reflectivity, the high reflectivity properties are retained for several months.

Для аналізу опроміненої поверхні застосовували еліпсометричний метод. За модель відбиваючої поверхні використовували однорідну поглинаючу плівку на однорідній поглинаючій підкладці. Основне рівняння еліпсометрії розв'язували чисельним методом. В результаті розрахунку знаходили оптичні показники підкладки і плівки, товщину плівки, коефіцієнт відбивання в залежності від глибини проникання іонів Cu^+ та Ar^+ в мідь. В роботі відображена можливість застосування методу для дослідження шорсткості поверхні до і після опромінення. Опромінення мідних дзеркал іонами Cu^+ з енергією 3 МеВ або Ar^+ з енергією 4 кеВ призводить до збільшення коефіцієнту відбивання, причому високі відбиваючі властивості зберігаються протягом кількох місяців.

1. Introduction

Polished copper mirrors noted for their low emissivity factor and high thermal conductivity are widely used in cryogenic engineering. But copper is characterized by a disadvantage, viz. fast oxidation in air. For instance, at 35 °C and the relative humidity of 45 %, the emissivity factor of copper increases by 22 % (from 0.013 to 0.0167) in 50 h. The importance of improvement of the metal corrosion resistance is obvious. The protective SiO coating commonly applied to reflective copper surfaces protects them against oxidation but it increases their emissivity factor by 40 %.

2. Problem

Let us consider another method of corrosion abatement. Extensive studies of the tokamak-based thermonuclear fusion reactor (TFR) (INTOR, ITER projects) have been performed in recent years. To assure a reliable TFR operation, a continuous monitoring of a number of the high-temperature plasma parameters is required. The monitoring devices include mainly the viewing metallic mirrors placed in the immediate vicinity of plasma.Their surfaces are thus exposed to penetrating radiation (neutrons and γ-quanta), to neutral charge exchange atom bombardment and to electromagnetic radiation in a wide range of energies. This irradiation degrades the mirror quality.

The mirror-aided diagnostics of plasma uses electromagnetic waves ranging from ultraviolet to near IR wavelengths. The requirements to the mirror surface quality are most stringent in the short-wave region of spectrum where even slight changes in the surface topography (e.g., the appearance of a microrelief 20 nm = 1/10 λ deep)

would sharply affect the performance characteristics of the mirrors. It seems that the problem can be solved through simulating the penetrating radiation by metal ions. The irradiation of stainless steel mirrors caused radiation damage (RD) of the surface which could be seen quite clearly in the reflected light. The mirror reflectivity was observed to decline and this degradation increased with the radiation dose [1]. However, contrary to these results, irradiation of copper mirrors made their reflectivity increase [2].

The are two promising strategies of using ion implantation to abate corrosion:

i) to use the implantation as a tool for introducing a certain component into the surface layers of the metal to improve its corrosion resistance;

ii) to employ ion irradiation for studying and better understanding the corrosion mechanisms.

Thus, the application of ion implantation to study oxidation is of great practical and scientific value. The mechanism of variations of the corrosion resistance of metals due to ion introduction is not clear yet. At present, there is no general agreement regarding the reason why ion bombardment slows down metal oxidation.

3. Technique and equipment

Along with EPR, electron microscopy, Auger electron spectroscopy, the method of ellipsometry can effectively be used to study the properties of materials with ion-implanted layers because the physico-chemical state of the surface layer in metallic mirrors influences essentially the polarization characteristics of the light reflected from them.

In this communication we report the results of the ellipsometric analysis of the effect produced by neutrons on the reflective properties of oxygen-free pure copper mirrors in the visible part of the spectrum. Neutron irradiation was simulated using Cu^+ bombardment of copper mirror surfaces.

The influence of charge exchange atom flow was imitated using Ar^+ ions. The Cu^+ and Ar^+ irradiation was performed by means of an electrostatic ion accelerator.

The quantitative characterization of radiation damage can be judged from the displacements per atom (DPA). In the above simulation experiment, about 50 % radiation damage occurred under the conditions identical to those of the neutron damage with neutron energies of 14 MeV incident on the first wall.

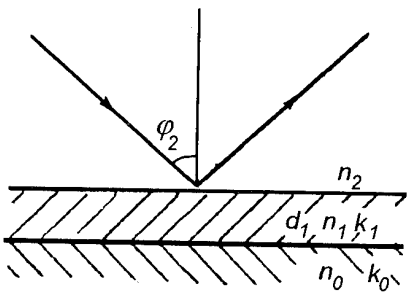

Fig.1. Model of the reflecting copper mirror surface with the ion-implanted layer.

Mechanically polished copper mirrors were irradiated by Cu^+ ions at 3 MeV, dose level up to 10^{17} ion/cm^2 to attain 20 DPA profile. The samples were etched by 4 keV Ar^+ ions. The resulting depths of the etched layers were measured to be 0.1, 0.2, 0.5, 0.75 and 1 μm. For removing the non-metallic impurities from the samples, they were exposed to a chemical treatment by H^+ ions and H^0 atoms, and the ellipsometric data were recorded every 24 hours.

The phase shift Δ and the azimuth of recovered linear polarization ψ have been measured using a laser photoelectric ellipsometer LEF-3M in the polarizer-compensator-sample-analyzer (PCSA) configuration at 632.8 nm wavelength. The rotation angles of the polarizer, compensator and analyzer as well as the angle of light incidence on the sample were measured to within 1′ and the scatter in the polarization angle values was $\delta D = -5'$, $\delta\psi = -1'$, respectively. In our calculations, the values of Δ and ψ have been averaged over two conjugate zones.

At the wavelength of the laser $\lambda = 632.8$ nm, the electromagnetic radiation extended into the surface of the copper mirror to a depth $d = 1/k = \lambda/4\pi k = 16.9$ nm (where k is the natural absorption coefficient) and, hence, the absorptive near-to-surface layer and the absorptive substrate could be considered as being uniform (Fig.1). The complex index of refraction has been calculated for both the film and the substrate, and from the values obtained, the reflection coefficient R for the normal incidence has been determined.

4. Results and discussion

The results of calculation are shown in Fig.2. It can be seen from this figure that the reflectivity of the sample after the Cu^+ ion implantation shows an increase of 5.5 % as compared to the sample before irradiation and increases further in depth under the copper mirror surface. The Cu^+

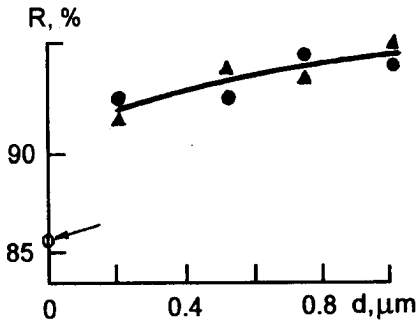

Fig.2. The reflection coefficient versus the depth to which the Cu^+ and Ar^+ ions penetrated into the copper mirror. The arrow indicates the reflection of the unirradiated sample.

ion bombardment will cause the main absorption coefficient of the oxide film CuO to decrease. The irradiated surface has been observed to remain bright during several months unlike the control sample which grows dim at once.

Table. Influence of the ion implantation on optical properties of copper mirrors

Optical parameters	Without implantation	With implantation Cu^+
Complex index of copper refraction, N	0.525–i2.987	0.267–i3.898
Coefficient of reflection, R, %	85.5	91.0
Natural absorption coefficient, K, μ^{-1}	59	77
Depth of the irradiated zone of copper sample, d, nm	16.9	12.9
Optical conductivity, G, s^{-1}	$7.5 \cdot 10^{14}$	$4.9 \cdot 10^{14}$

The ellipsometric data obtained for the copper mirrors with the Cu^+ ions implantation at a depth of 1 μm are tabulated in the Table below.

It is obvious that the ion-radiation damage caused significant changes in Cu lattice which, in turn, tend to increase the natural absorption coefficient (by 30.5 %) and to decrease the depth of the irradiated zone thus resulting in an increasing coefficient of reflection for the irradiated copper mirrors.

The surface roughness can also influence the reflection coefficient. The surface becomes more smooth after irradiation as demonstrated by a twofold reduction in the real part of the complex

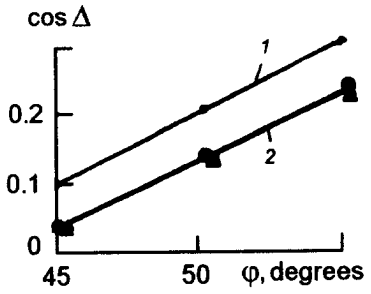

Fig.3. Cos Δ as a function of φ: 1 – before the irradiation; 2 – after Cu^+ and Ar^+ ions implantation.

index of refraction and an increase in its imaginary component as well as by a decrease of the optical conductivity in this region of spectrum in contrast to polished Ni, Pb, Sn samples. So, one can conclude that a decrease in the surface irregularities causes the coefficient of reflection to increase.

The correctness of the calculations performed was confirmed by the results of the ellipsometric angles (Δ and Ψ) measurement which are shown in Fig.3. From this figure, it can be seen that with increasing angle of light incidence on the sample the curve is shifted to the region of greater angles. This fact can be explained as follows: the ion bombardment of the sample tends to smooth out the surface and, as a result, the incidence angle φ will increase.

5. Conclusions

Scanning tunneling microscopy of the samples after irradiation has detected a change in the surface microrelief as compared to unetched samples. The decreased number of the small-scale structure areas of size 300 Å and appearance of the relatively large smooth areas of linear sizes 5000 Å has confirmed the validity of the ellipsometric analysis carried out. Irradiation of the copper mirrors with 3 MeV Cu^+ ions at the dose level 10^{17} ion/cm^2 or with 4 keV Ar^+ causes the reflection coefficient to increase, and the mirrors so treated keep the improved reflectivity for several months.

References

1. Yu.N.Borisenko, V.V.Bryk, V.V.Gann, et al., *Plasma Devices and Operations*, **3**, 157 (1994).
2. Yu.N.Borisenko, V.V.Voevodin, V.S.Vojtsenya, et al., in: Paper Q 011 at 6-th Intern.Conf.on Fusion Reactor Materials, Stresa, Italy (1993).

Эллипсометрический метод анализа облученных медных зеркал

Б.В.Григоренко, Р.С.Михальченко, В.С.Войценя

Для анализа облученных поверхностей применяли эллипсометрический метод. В качестве модели отражающей поверхности использовали однородную поглощающую пленку на однородной поглощающей подложке. Основное уравнение эллипсометрии решали численным методом. В результате расчета находили оптич ческие показатели подложки и пленки, толщину пленки, коэффициенты отражения и поглощения зеркал в зависимости от глубины проникновения ионов Cu^+ и Ar^+ в медь. Показана возможность применения метода для исследования шероховатости поверхности до и после облучения. Облучение медных зеркал ионами Cu^+ с энергией 3 МэВ или Ar^+ с энергией 4 кэВ приводит к увеличению коэффициента отражения, при этом высокие отражательные свойства сохраняются в течение нескольких месяцев.

Functional Materials 2, No.2 (1995)

Electropolishing influence on the optical properties of amorphous metal strips

V.V.Vovochak and L.V.Poperenko

T.Shevchenko Kiev University, 6 Acad. Glushkov Ave., 252022 Kiev, Ukraine

Electropolishing influence on the structure and optical properties of the skin-layers of the amorphous metallic alloys $Fe_{60}Ni_{20}B_{20}$ and $Ni_{78}Si_8B_{14}$ have been studied. It was found that electro polishing does not remove existent structural anisotropy and does not result in the specimen surface enrichment by one of the components.

Вивчено вплив електролітичної поліровки на атомну структуру та оптичні властивості приповерхневих прошарків аморфних металевих сплавів $Fe_{60}Ni_{20}B_{20}$ та $Ni_{78}Si_8B_{14}$. Показано, що електролітична поліровка не знімає існуючої структурної анізотропії і не призводить до збагачення поверхні зразка однією із компонент.

The detailed information about the electronic and atomic structure of amorphous materials is necessary for their use in the creation of technologically new instruments. Taking into account the miniaturization of those instruments, the dependence of the material properties on the specimen thickness is of importance. Some of these properties were determined by X-ray and Auger methods [2]. To more detailed study of the atomic and electronic structure, amorphous alloys must be investigated by optical methods which will allow to elucidate some new features of their electronic properties, especially in the spectral range adjacent to Fermi level.

Thus, the aim of this work is to study, using reflectometry near to the normal incidence angle, spectroellipsometry, and Fourier spectroscopy, the structural and electronic features of amorphous alloys $Fe_{60}Ni_{20}B_{20}$ and $Ni_{78}Si_8B_{14}$ made into strips, in the sounding photons energy ranges $\hbar\omega$ = 0.056–0.01 eV and 0.5–3.7 eV; as well as to clarify the influence of the electropolishing on the optical absorption and reflection spectra for both surfaces of the strip. The reflection spectra of alloys in the far IR range were obtained using Fourier specrometer LAFS-1000 having resolution 0.1–0.05 cm^{-1}. The experiments were performed in the spectral range 80–450cm^{-1}. The relative reflection factor $R_{rel} = R/R_{Al}$, where R_{Al} is the reflection coefficient for aluminium, and optical constants, n (refraction index) and k (absorption coefficient) were determined, and the frequency spectrum of the optical conductivity was calculated using formula $\sigma(\hbar\omega) = nk\omega/2\pi$. The determination error for the optical constants n and k in the visible range was 1 to 3%, while in the IR region, does not exceed 5–6%.

The structural anisotropy of the skin layer of amorphous alloys was studied using the normal incidence reflectometer. In that instrument, the light beam from a source is reflected from the strip surface and, being passed through a polaroid in the direction opposite to that of incident beam, comes to a photoreceiver whose photo current is recorded by a microampermeter. The scattering indicatrices over the polarization azimuth (SIPA) are the results of those measurements [3].

Some information about the surface anisotropy of the alloys being investigated was obtained also using angular ellipsometric measurements, by which, the ellipsometric parameters $\cos\Delta$ and $\mathrm{tg}\psi$ for the amorphous alloys were determined (where Δ is the phase shift between the polarization vector orthogonal components; ψ, the azimuth of the restored linear polarization). The strip longitudinal axis was oriented in two mutually perpendicular directions, one of the which was coincident with the incidence plane of the

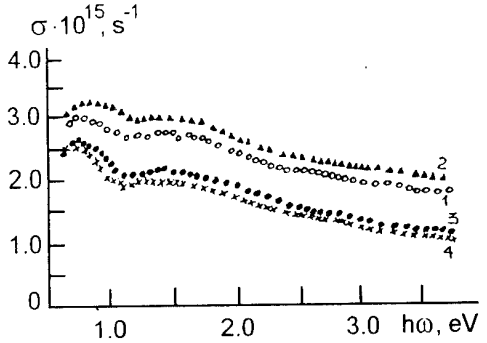

Fig.1. Specrtal dependences of the optical conductivity for initial (1,4) and electropolished (2,3) specimens of the amorphous $Fe_{60}Ni_{20}B_{20}$ alloy strip measured on the incontact (1,3) and contact (2,4) strip sides. The curve 4 is deplaced down by $0.5 \cdot 10^{15}$ s^{-1}.

light beam. Both strip surface were studied: incontact (IS) which is formed freely in course of the strip preparation by the melt spinning, and contact (CS) having contact with the cooled disc. On the basis of the dependences obtained for $\cos\Delta$ and $tg\psi$ vs angle of incidence, φ, the optical polarisation characteristics of the strip were determined for two orientations of its longitudinal axis (parallel, $\varphi_{0\|}$, and perpendicular, $\varphi_{0\perp}$, relatively to *p*-plane). In our experiments, after the system was readjusted, the $\varphi_{0\|}$ and $\varphi_{0\perp}$ scatter about the average value obtained from a series of measurements did not exceed 0.2–0.3%.

Consideration of these measurements results did allow to establish that the maximum $tg\psi$ value in the minimum point of the curve corresponds to minimum roughness. Both specimens are anisotropic on the contact surface as well as on incontact one, the anisotropy parameter $\Delta\varphi_0 = \varphi_{0\|} - \varphi_{0\perp}$ at the main incidence angle and also the ratio of extremal SIPA axes being greater for the incontact surface: both for CS and IS, the SIPA has an oval shape, but, for IS, that oval is of more elongated form, and the difference between main angles $\varphi_{0\|}$ and $\varphi_{0\perp}$ values for CS is less than for IS. Such a structural anisotropy is perhaps due to the uneven melt flowing at its solidification on a moving disc.

Using the reflectometry, the surface roughess level of strips has been also studied. For initial specimens of the $Fe_{60}Ni_{20}B_{20}$ and $Ni_{78}Si_8B_{14}$ alloys, the roughness parameters are higher than for polished ones. This fact reflects itself in that the difference values of the reflection coefficients for both surfaces, are less for electropolished specimens than for unpolished ones.

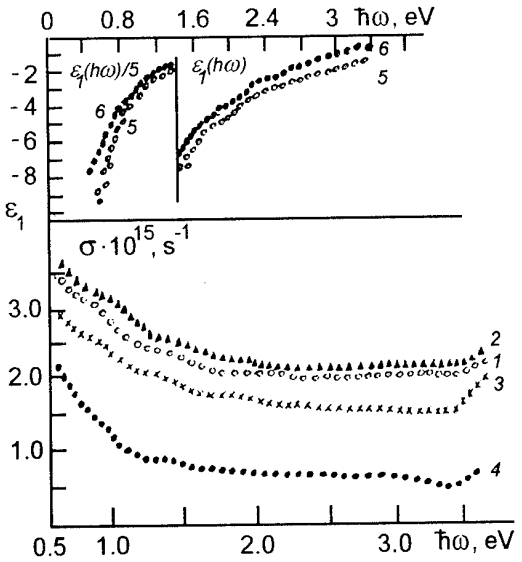

Fig.2. Spectral dependences of the optical conductivity and real component of dielectric constant for initial (1,4,5,6) and electropolished (2,3) specimens of the amorphous $Ni_{78}Si_8B_{14}$ alloy strip measured on the in contact (1,2,5) and contact (3,4,6) strip sides.

The dispersion dependences for Fe–Ni–B and Ni–Si–B alloys have been obtained; they are presented on Figs.1 and 2, respectively. The Fig.1 shows that the optical conductivity curves for the $Fe_{60}Ni_{20}B_{20}$ alloy contain a weak absorption curve in the 1.2–1.5 eV range. That band is perhaps due to electron transitions to the Fermi level from states lying within an accumulation of the energetic spectrum of the electron states density formed near iron *d*-zone bottom by hybridization of metalloid *p*-states with Fe and Ni *d*-states; and also to transitions from Fermi level to energetically higher ones corresponding to hybridized 2*p*-states of the metalloid and *s*-states of the both metals.

The appearance of real dielectric permeability $\varepsilon_1(\hbar\omega)$ and optical conductivity $\sigma(\hbar\omega)$ curves for the Ni–Si–B alloy in the IR range (Fig.2) reveals a typical «metallic» behaviour of those characteristics, what is evidence of prevailing contribution of free charge carriers to the absorption, according to Drude-Zener theory.

Considering the $\sigma(\hbar\omega)$ dependences presented on Figs.1 and 2, one can easily conclude that the spectral shape remains unchanged no matter on contact or incontact side the spectrum was measured. This is explained by the approximately uniform alloy component distribution on both strip sides, thus, the behaviour of a reflected light beam should be essentially the same in both cases.

So, from the spectral viewpoint, the difference between the CS and IS of a strip is smoothed out [1].

As for the electropolishing influence on dispersional relationships, it should be expected that it will result in the enrichment of the alloy surface by at least one of the alloy components. That would change the shape of optical conductivity spectra $\sigma(\hbar\omega)$. According to experimental results, however, the spectrum shape remains unchanged. This means that, up to the depth of the layer being removed during electropolishing (order of 2.5 μm), no fluctuations of components concentrations take place in the amorphous alloy. This suggestion is confirmed by the Auger analysis date [2].

For all the specimens being investigated, the reflection spectra show a characteristic Drude-like feature: values of the surface relative reflection coefficient increase when the sounding photons energy drops. That R_{rel} increase is more sharp for the contact side both before and after strip polishing. Thus, the increased roughness on CS results in the increased energy losses at short wavelengths.

In studies of atomic structure features, the dynamic characteristics of conductivity electrons were evaluated, especially, the relaxation frequency for the initial amorphous $Ni_{78}Si_8B_{14}$ alloy (for both sides). This frequency, γ, as determined by linear approximation of the function $f(\lambda) = \varepsilon_2/(1-\varepsilon_1) = \gamma\lambda/2\pi c$, is equal, for CS, $2.21 \cdot 10^{15}$ s^{-1}, while for IS, $0.76 \cdot 10^{15}$ s^{-1}. The determination error for those values did not exceed 10 per cent. Thus, the CS is characterized by a higher γ value, what is confirmed by the data of [3] related to the surface finish on the CS as compared to that of IS. Conclusively, the atomic structure of contact and incontact sides of an amorphous alloy strip is anisotropic, and the optical parameter of the anisotropy, $\Delta\varphi_0 = \varphi_{0\parallel} - \varphi_{0\perp}$ is higher for the incontact side. The electropolishing does not remove that anisotropy and does not result in the specimen surface enrichment by any of alloy components. The components concentrations on both sides are essentially the same.

References

1. L.V.Poperenko, *Visnyk Kiev. Universytetu, Fiz.-mat. nauky*, **2**, 69 (1992).
2. V.G.Kravets, L.V.Poperenko, O.A.Yakubtson, *Visnyk Kiev. Universytety, Fiz.-mat. nauky*, **1**, 96 (1991).
3. L.Kraus, I.Tomas, E.Kratochvilova, *Phys.Stat Sol. (a)*, **100**, 288 (1987).

Влияние электролитической полировки на оптические свойства аморфных металлических лент

В.В.Вовочак, Л.В.Поперенко

Изучено влияние электролитической полировки на атомную структуру и оптические свойства приповерхностных слоев аморфных металлических сплавов $Fe_{60}Ni_{20}B_{20}$ и $Ni_{78}Si_8B_{14}$. Показано, что электролитическая полировка не снимает существующую структурную анизотропию и не вызывает обогащение поверхности образца одной из компонент.

Functional Materials 2, No.2 (1995)

Investigation of metal—GaAs structures exposed to beam treatments

J.Breza*, K.A.Ismailov**, R.V.Konakova***, J.Liday*,
V.G.Lyapin***, V.V.Milenin***, A.A.Naumovets***,
I.V.Prokopenko***, V.A.Statov** and Yu.A.Tkhorik***

*Slovak Technical University, 3 Ilkovicova, 81219 Bratislava, Slovakia

**Karakalpak University, 1 Universitet koshesi, 742012 Nukus, Uzbekistan

***Institute of Semiconductor Physics, National Academy of Sciences of Ukraine, 45 Nauki Ave., 252650 Kiev, Ukraine

The effect of electron beam and ^{60}Co γ-irradiation on the properties of some metal (Au, Cr, Mo, Pt, Sn, Ti, W) — GaAs Schottky contacts was investigated. Electrophysical characteristics, such as barrier hight φ_B, ideality parameter n, minority carriers effective lifetime τ_p and reverse current I_R, were measured as functions of the adsorbed dose. It was shown that both beam treatments may considerably improve these characteristics. Interdiffusion in contacts and charge in sample deformation under γ-irradiation were studied also.

Досліджено вплив електронно-променевого та ^{60}Co γ-опромінювання на властивості контактів Шотткі метал (Au, Cr, Mo, Pt, Sn, Ti, W) — GaAs. Отримано дозові залежності таких електрофізичних характеристик як висота бар'єру φ_B, параметр ідеальності n, ефективний час життя неосновних носіїв τ_p та зворотний струм I_R. Показано, що обидва типи обробки можуть спричиняти істотне покращення цих характеристик. Досліджено також взаємодифузію у контактах і зміну деформації зразків при γ-опромінюванні.

Introduction

The active elements with Schottky barriers, such as microwave Schottky diodes, a wide range of Schottky-barrier gate field-effect transistors and many others, form the basis for the GaAs microelectronics [1]. That is why studying the properties of Schottky barrier structures is of importance not only for the pure science but also for numerous technical applications. The principal parameters of these structures (barrier hight φ_B, ideality parameter n, avalanche breakdown voltage V_B, minority carriers effective lifetime τ_p, reverse current I_R) may be changed by various treatments, including the beam ones.

It is well known that ionizing radiation is a universal tool to modify physico-chemical state of matter. In spatially nonuniform metal – semiconductor structures, the processes of interaction with ionizing radiation occur more actively near the interfaces. Reconstruction and annihilation of structural defects, mass transport and chemical reactions in heterostructures can be regulated by varying type of radiation, particle energy and adsorbed dose. By this way, one can shape interfaces having specific composition and structure and, consequently, having fixed electrophysical parameters of the interphase boundaries.

Subject of research and experimental procedures

The Me—GaAs heterostructures (metal Me = Au, Cr, Mo, Pt, Sn, Ti, W) were prepared in vacuum (pressure not higher than 10^{-3} Pa) by

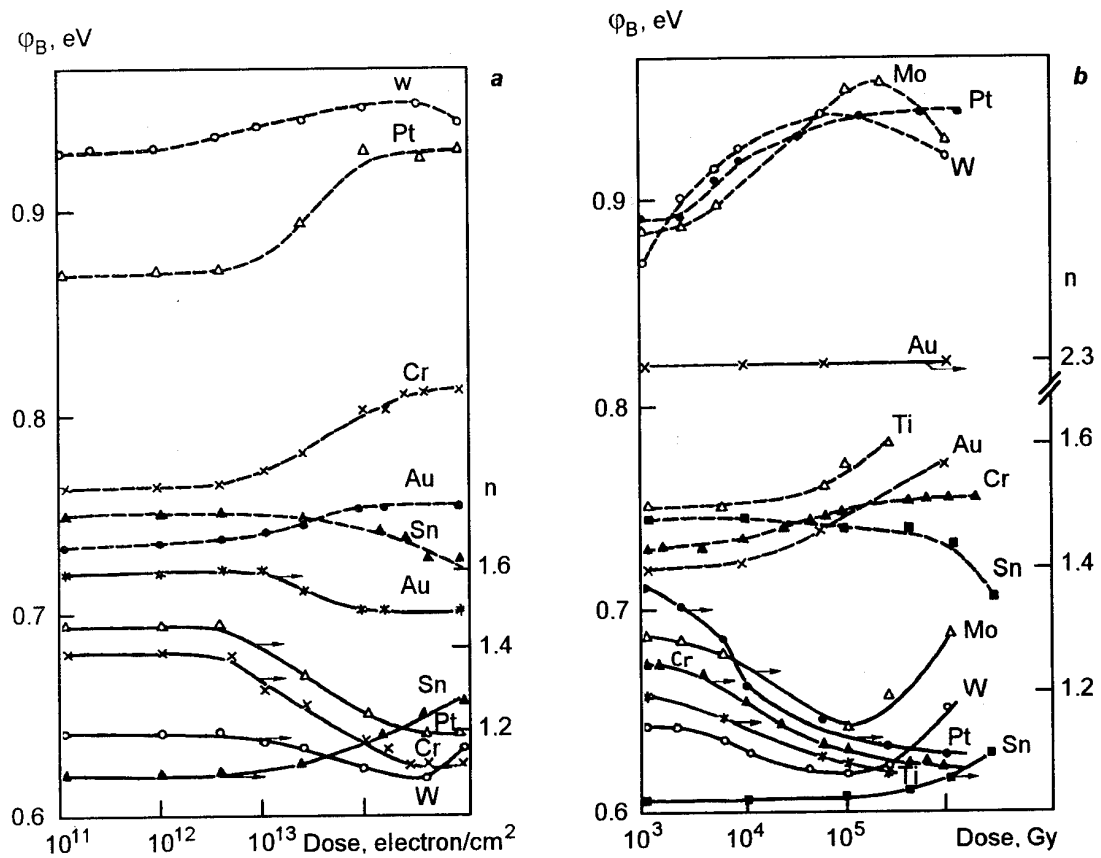

Fig.1. Barrier height φ_B (dashed lines) and ideality parameter n (full lines) as functions of absorbed electron beam (*a*) and γ-irradiation (*b*) dose.

sputtering the electron-beam evaporated metal onto the (100) surface of *n*-GaAs films (the majority varriers concentration $n = 10^{16}$–10^{17} cm^{-3}). The films were grown by vapor-phase epitaxy on a highly-doped *n*-GaAs substrate (n=10^{18} cm^{-3}). Their surface was chemically cleaned by etching during 3 min in 50 % solution of hydrochloric acid. The thickness values of the sputtered polycrystalline metal layers varied from 100 (for the Cr—GaAs contact) to 200 nm (for the Pt—GaAs contact).

The heterostructures obtained were exposed to electron beam (energy E = 2.2 MeV, dose range 10^{11} to 10^{15} electron/cm^2) or to ^{60}Co γ-irradiation (dose range 10^3 to 10^6 Gy, dose rate 3 Gy/s). Electrophysical parameters of both the Me—GaAs interfaces and GaAs near-the-boundary regions were studied by taking I–V and C–V curves and also by measuring short-circuit photocurrent at different reverse biases and electron beam induced currents, thus enabling to estimate the lifetime for non-equilibrium photocarriers [2–4]. Structural and morphological investigations were carried out using transmission electron microscopy, while both X-ray photoelectron (XPS) and Auger electron (AES) spectroscopies were used to analyse elemental and phase composition [5]. Internal static deformations were studied by X-ray diffraction; they were calculated from the structure curvatures, i.e. from angular shifts of the diffraction reflection peaks after translating the samples over the known distances [6,7].

Experimental results and discussion

The barrier height φ_B and the ideality factor n of the Me—GaAs Schottky contacts are given as functions of absorbed irradiation dose in Fig.1. The minority carriers effective lifetime τ_p versus absorbed dose curves are shown in Fig.2. While all these parameters change non-monotonously with the absorbed dose, the τ_p changes are far beyond those of both φ_B and B. (The reverse current I_R, being inversely proportional to τ_p, also changes drastically with the absorbed dose.) Since

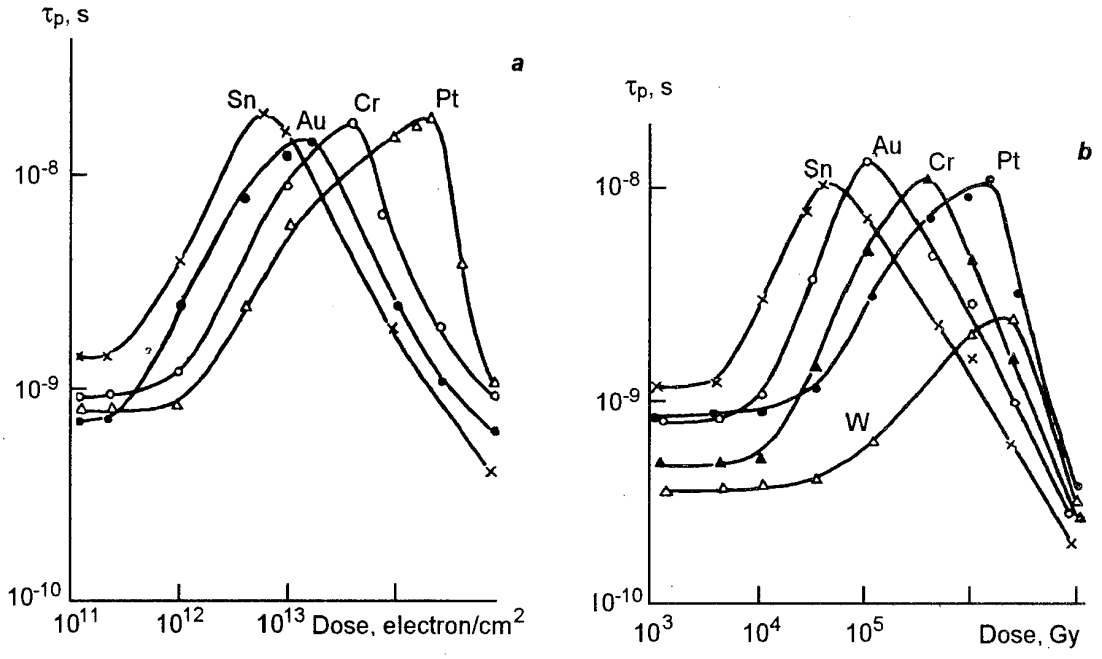

Fig.2. Minority carriers effective lifetime τ_p as a function of absorbed electron beam (*a*) and γ-irradiation (*b*) dose.

these parameters are linked with the physico-chemical structure of the interphase boundaries, one may suppose that radiation processing has changed structure of the interface, or its phase composition, or both of them.

The energy needed for irreversible displacement of an atom from Ga(As) sublattice is 8.8–9.0 eV (9.4–10.1 eV); this value corresponds to the threshold electron energy 228 keV (273 keV) [8]. So, intense defect creation in GaAs results from electron beam as well as from γ-irradiation (in the last case due to Compton electrons), the two types of processing thus being adequate to some extent. In a thin subsurface layer of GaAs, chemical bonding is somewhat weakened due to metal atoms penetration into the host lattice. This makes radiation defects creation much more intense that in semiconductor bulk. Optimum doses of irradiation lead to both predominance of structural defects annihilation and formation of electrically inactive complexes in the GaAs near-contact layer. For Me—GaAs heterostructures, this results in decreasing reverse current I_R and increasing minority carriers effective lifetime τ_p. And v.v., accumulation of radiation defects in the subsurface layer of a semiconductor increases reverse current.

The γ-irradiation led to components redistribution in the transition layers of the Me—GaAs heterostructures studied. This follows from comparing of concentration depth profiles taken before and after irradiation. The transition layer width as a characteristic feature of the interface transformations in the Me—GaAs contact under γ-irradiation is given in Table 1. (The transition layer width, defined from AES or XPS spectra of a given compotent, was taken, by convention, as the difference between the depths at which the signal of that component dropped from 90 to 10 % of its maximum value inside the contact region.) The cor-

Table 1. Transition layer width (nm) for some Schottky contacts before and after γ-irradiation.

Component	Before γ-irradiation	Absorbed dose, Gy	
		10^5	10^8
Mo	30	39	33
Ga	21	39	14
As	21	39	18
Pt	180	115	-
Ga	190	100	-
As	100	100	-
Ti	33	41	-
Ga	87	78	-
As	63	57	-

responding values for the Cr—GaAs heterosystem, along with the components concentration depth profiles, are given in [9].

From these results one may conclude that γ-irradiation substantially affects both stoichiometry of the semiconductor near-contact region and the transition layer width. Changes in the transition layer width range from several tens of per cent (Ti—GaAs contact) to about two times (Cr—GaAs, Mo—GaAs contacts). Such changes are not monotonous with absorbed dose: the initial expanding of the transition layer gives way to its narrowing. It should be noted that transition layer widening may result from an increse in defect concentration as well as from decrease of activation energies for contact components diffusion. Such a decrease may be due either to energy transfer from hot electrons (excited by radiation) to the diffusing atoms or to changing their charge after capturing non-equilibrium carriers [7]. The peculiarities mentioned are responsible for redistribution of both atoms and defects in the Me—GaAs heterostructures. In such a situation, one could expect that only widening of the transition layers must occur under γ-irradiation. Such a concept is in contradiction with experimental facts (non-monotonous changes of transition layer width with absorbed dose, see Table 1). To make an adequate approach to the problem of the spatial distribution of different components near the interface one must take into account also internal stresses and electric fields generated at contact formation. Then the following expression may be used for particle flow density in the heterosystems studied [7]:

$$j = -D\left\{\frac{dN}{dx} + \frac{K\beta\Omega}{k_B T} N \frac{dN}{dx} - N\frac{qE}{k_B T}\right\} \qquad (1)$$

Here D is diffusion coefficient (under irradiation its value may differ condiderebly from that for the ordinary thermal diffusion); N, Ω and q are, respectively, concentration, atomic (ionic) volume and charge of diffusing particles; K is bulk modulus; β is coefficient of the host lattice expansion due to penetration of diffusing particles; E is electric field strenght; T is temperature and k_B is Boltzmann constant. (The x axis is normal to the interface plane.) It can be seen from the expression (1) that (even for $E = 0$) the uphill diffusion (up the gradient of concentration) may occur if $\beta < 0$ and the second term in (1) prevails.

The assumption that internal stresses may be of considerable importance for mass transport in heterostructures is confirmed by our studies of the Me—GaAs contacts using X-ray diffraction. After absorbing sufficiently high γ-irradiation doses, the transition regions became narrower and components concentration depth profiles became more steeply sloping that those for lower doses. Both effects are correlated with changes in sample inverse curvature R and elastic bending deformation ε_R – see Table 2.

Table 2. Inverse curvatures and elastic bending deformations ε_R of the samples before (left subcolumns) and after (right subcolumns) γ-irradiation (absorbed dose 10^5 Gy).

Heterosystem	R, m		$\varepsilon_P \times 10^5$	
Au–Ti–GaAs	11.4	17	3	2.06
Mo–GaAs	10.3	∞	15	0
Pt–GaAs	15.9	25.8	0.95	0.58
W–GaAs	41.4	∞	36	0

A sufficiently fair account of structural relaxation in multilayer systems constitutes a rather complicated problem because there is a lot of contributors of internal stresses in such systems [10]. Some of these contributors may enhance deformations in heterocontacts, while the others may act in the opposite direction.

For some of the contacts studied (e.g., Cr—GaAs [9]) the components concentration depth profiles had no pronounced peculiarities that could be connected with intermetallic phase formation. So in these cases the ordinary equation for a completed chemical reaction

$$(nh + mq)\mathrm{Me} + nq\mathrm{GaAs} \rightarrow$$
$$\rightarrow n\mathrm{Me_hGa_q} + q\mathrm{Me_mAs_n}$$

failed and the irradiation doses used had no pronounced effect on the rate of intermetallic phase formation. In other cases (e.g, Pt—GaAs [11]) the intermetallic phase formation was found. The problem of chemical reactions in the Me—GaAs heterostructures under irradiation seems to need further investigations.

Conclusion

The results obtained indicate that physicochemical processes at the Me—GaAs interfaces are common, to an extent, for both cases of sample processing (electron beam and γ-irradiation). One can substantially improve electrophysical parameters of the Schottky barrier structures by using some optimum doses of irradiation.

Acknowledgment

This work was supported by a Grant from the Ukrainian State Committee for Sciences and Technologies.

References

1. GaAs Microelectronics (VLSI Electronics Microstructure Science, v.11), ed. by N.G.Einspruch and W.R.Wisseman, Academic Press, Inc., Orlando et al. (1985).
2. E.H.Rhoderick, Metal – Semiconductor Contacts, Clarendon Press, Oxford (1978).
3. O.Yu.Borkovskaya, N.L.Dmitruk, M.Dubovinsky, R.V.Konakova, O.N.Mishuk, Yu.A.Tkhorik, P.Kordos, F.Stofanik, *Electrotechn.Casopis*, **40**, 877 (1989).
4. S.G.Konnikov, O.V.Salata, V.A.Soloviev, M.A.Sinitsin, V.A.Umanskii, D.A.Vinokurov, *Fiz. Thekhn. Poluprov.*, **23**, 1416 (1989).
5. L.C.Feldman and J.W.Mayer, Fundamentals of Surfaces and Thin Film Analysis, North – Holland, New-York – Amsterdam – London (1986).
6. I.V.Prokopenko, in Proc. Intern. Conf. on Microelectronics and Computer Science (ICMCS-92), ed. by V.P.Shontya and V.I.Rusanovski, Polytechnic Institute, Kishinev (1992), p.41.
7. S.A.Grusha, R.V.Konakova, V.V.Milenin, A.A.Naumovets, B.A, Nesterenko, I.V.Prokopenko, Yu.A.Tkhorik, L.S.Khazan, *Elektronnaya Tekhnika, Ser.2, Poluprovodnikovye Pribory*, **5(208)**, 68 (1990).
8. R.Baeuerlein, *Z.Physik*, **176**, 498 (1963).
9. J.Breza, R.V.Konakova, V.G.Lyapin, V.V.Milenin, V.A.Statov, Yu.A.Tkhorik, M.Yu.Filatov, *Poverkhnost'*, No.6, 103 (1994).
10. E.F.Venger, M.Hrendel, V.Daniska, R.V.Konakova, I.V.Prokopenko, Yu.A.Tkhorik, L.S.Khazan,
11. O.Yu.Borkovskaya, N.L.Dmitruk, R.V.Konakova, V.V.Milenin, A.A.Naunovets, B.A.Nesterenko, Yu.A.Tkhorik, M.A.Filatov, *Zhurn.Tekhn.Fiz.*, **62**, 88 (1992).

Исследование структур Me—GaAs, подвергнутых лучевым обработкам

Ю.Бреза, К.А.Исмайлов, Р.В.Конакова, Й.Лидаи, В.В.Миленин, А.А.Наумовец, И.В.Прокопенко, В.А.Статов, Ю.А.Тхорик

Исследовано влияние электронно-лучевого и ^{60}Co γ-облучения на свойства контактов Шоттки металл (Au, Cr, Mo, Pt, Sn, Ti, W) — GaAs. Найдены дозовые зависимости таких электрофизических характеристик как высота барьера φ_B, параметр идеальности n, эффективное время жизни неосновных носителей τ_p и обратный ток I_R. Показано, что оба типа обработки могут приводить к существенному улучшению этих характеристик. Исследованы также взаимодиффузия в контактах и изменение деформации образцов при γ-облучении.

Functional Materials **2**, No.2 (1995)

Optical properties of copper and aluminium studied with consideration for a surface layer using ordinary and polariton spectroellipsometry

V.A.Bolottsev, L.Yu.Melnichenko and I.A.Shaikevich

T.Shevchenko Kiev University, 64 Vladimirskaya St., 252017 Kiev, Ukraine

Using both usual and polariton multiangular spectroellipsometry the spectroellipsometric investigations are carried out for the oxidic and ion bombardment surface of Cu and Al. The optical constants of pure metal and transitional surface layers are obtained which allowed to find some features of electronic structure of investigated samples as well as consistence of surface layer. In particular, we found experimentally at first two types of interband transitions near the **W** and **K** points of Brillouin zone for Al.

Проведено спектроеліпсометричне дослідження із застосуванням як звичайної, так і поляритонної багатокутової спектроеліпсометрії окислених та іонно-бомбардованих поверхонь Al і Cu. Одержано оптичні сталі чистого металу та перехідного поверхневого шару, що дозволило виявити ряд особливостей електронної структури досліджених зразків, а також склад поверхневого шару. Вперше вдалося експериментально виявити два типи міжзонних переходів поблизу **W** та **K** точок зони Бріллюена для Al.

Optical properties of metals contain a comprehensive and useful information on their electron structure, in particular on the behaviour of free electrons, electron energy zones etc. Making spectroellipsometric measurements one may obtain spectral dependences of optical conduction and dielectric permeability which are used for the calculation of the parameters of free electrons, energy gap between electron zones, density of electron states, etc. However, both the measured optical constants and calculated electron parameters are distorted to a significant extent by the presence of a surface layer on the metallic mirror under study. This layer consists essentially of an oxide layer and compounds adsorbed on the rough surface of metal distorted by polishing and finishing. Therefore, consideration or removal of the surface oxide layer and adsorbed compounds with a simultaneous smoothing of the surface roughness when measuring optical constants of metals increases essentially the degree of certainty of the results obtained and electron parameters calculated by optical constants.

Both consideration of the effect of the oxide layer and adsorbed compounds on the measured optical constants and removal of this layer by ion bombardment were used in our experiments. The latter allowed to obtain some new results which will be given below. Optical measurements were performed using conventional spectroellipsometry as well as that with the excitation of surface polaritons at different light incidence angles to the studied sample. Taking several incidence angles gave the possibility to solve, on a computer with numerical methods used, the reverse problem of ellipsometry for the case of a uniform layer on the surface of metal and to find five unknown values in case of usual ellipsometry [1], i.e. refraction and absorption indices of metal n and χ, those for the surface layer n_1 and χ_1 and effective thickness of the layer d. The incidence angles in this case were chosen to be near the main angle. In the case of ellipsometry with the excitation of surface polaritons, the Otto method [2] was utilized. The incidence angles were chosen near that of maximum polariton excitation. In this case, one more value was added to the five unknown ones mentioned above, this being the thickness of an air interlayer d_1 between the glass prism and

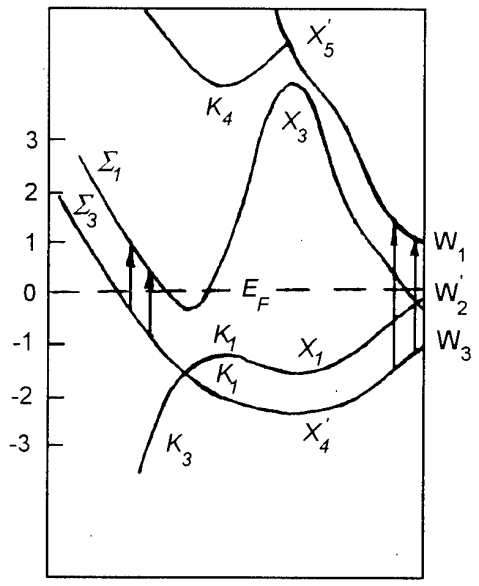

Fig.1.

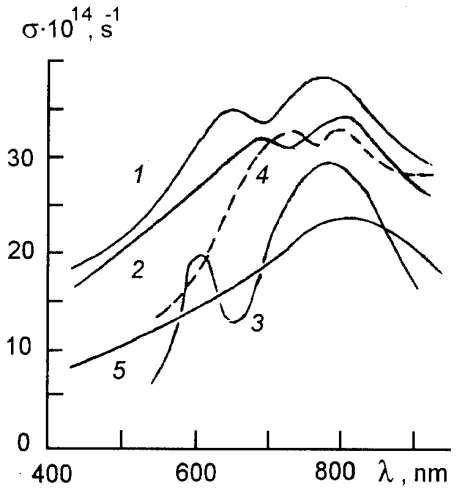

Fig.2.

metallic mirror. In both cases, the measurements of ellipsometric parameters were made by Beattie method using ellipsometer with a continuous variation of the incidence angles [3]. The surface of the investigated samples was subjected to the bombardment with low energy ions in a subnormal discharge to remove the layer of oxide and adsorbed compounds. The bombardment conditions (voltage, current strength, pressure in the chamber) were chosen so that the rate of the mentioned layer removal would exceed that of its formation.

Aluminium. It is known that the layer of an oxide and adsorbed compounds on the metal surface may lead to two effects on the spectral behaviour of metal optical conduction. On the one hand, it masks the fine structure of the optical conduction spectrum (blurs small peaks on it) as it was observed in [4] for nickel, and on the other hand, creates faulse structures belonging to this layer itself as it was observed in [5] for tin. Optical properties of aluminium have been well studied in a big number of papers in a wide range of the spectrum and are presented in a review [6]. In all without exception investigations of different authors a maximum at 1.55 eV is observed on the spectral curve of aluminium optical conduction which is caused by interzone transitions near **K** and **W** points of Brillouin zone [7]. Energy zone structure for aluminium and the corresponding transitions according to [7] are shown by arrows in Fig.1. As it is seen from Fig.1 the transitions in the neigbourhood of **W** point should lie in a higher energy part of the spectrum than those near **K** point. The latter must correspond to two separate absorption bands. However, in all papers dedicated to the study of optical properties of Al, this band was observed as a single one with the maximum at 1.55 eV [6].

Taking into consideration the surface layer of the oxide and adsorbed compounds gave us the possibility to discriminate for the first time the bands on the spectral optical conduction curve; those correspond to the above mentioned interzone transitions. Shown in Fig.2 are the spectral curves of optical conduction σ for two thicknesses of the surface layer d – 5 nm and 4 nm. It should be noted that neither mechanical nor ionic polishing of mirrors removes completely the transitional layer of the oxide and adsorbed compounds as it follows from calculations made using the experimental data. The curves 1 and 2 in Fig.2 correspond to optical conduction of Al measured by the usual ellipsometry for the oxide layer on the sample, 4 nm and 5 nm, respectively, and 3 and 4, for the same layer thicknesses but obtained by the polariton ellipsometry. And, finally, curve 5 corresponds to optical conduction calculated from ellipsometric measurements performed on our sample without consideration for transitional layer on the surface as it was done in the previous works. The curves mentioned show that, with the decrease of the layer thickness, the structure on the optical conduction curve sharpens which is particularly well seen at the polariton spectroellipsometry, the latter being more sensitive to the

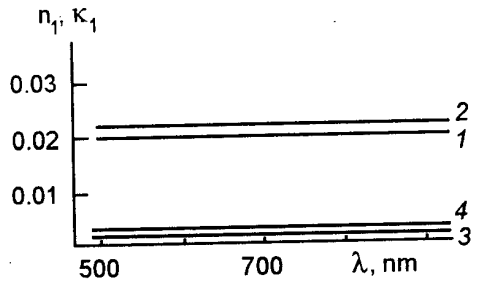

Fig.3.

state of the surface layer than the usual one. On the contrary, no structure is observed on the curve 5 which is in agreement with the results of all previous works by different authors. Thus, our experiments corroborate that two types of interzone transitions really occur in aluminium. A shorter wavelength band should correspond to the transitions at **W** point of Brillouin zone and a longer wavelength one – to those at **K** point. Presented in Fig.3 are the results obtained for the dependences of the refraction n_1 and absorption χ_1 indices on the light wavelength λ for the transitonal surface layer on Al with the thickness d=4 nm. The curves 1 and 3 correspond to ellipsometric measurements, 2 and 4 – to ellipsometry with surface polaritons excitation. A very small value of the refraction index, weak dispersion dependence of n_1 and χ_1 and, finally, absolute value of the refraction index n_1 give evidence to the fact that the transitional layer consists mainly of Al_2O_3 though, due to the surface roughness, there are certainly inclusions of pure Al, this resulting in a somewhat increased absorption coefficient, especially at polaritonic spectroellipsometry.

Copper. Optical properties of copper have been studied also rather in detail by various authors and are presented in the same review [6]. The spectral behaviour of optical conduction of copper in the visible and UV ranges is conditioned by strong interzone transitions near **X** and **L** points of Brilouin zone from the states lying below the Fermi level into those lying above it. In the IR region, the main contribution into optical conduction is made by free electrons. As it was mentioned above for the determinaton of electron parameters, it is necessary to have copper optical constants not distorted by the effect of transitional surface layer. Therefore, when studying copper we used the same method as for aluminium, i.e. removal of the oxide and adsorbed compounds layer by ionic bombardment and consideration of this layer in calculations according to the method [1] from the results of the measure-

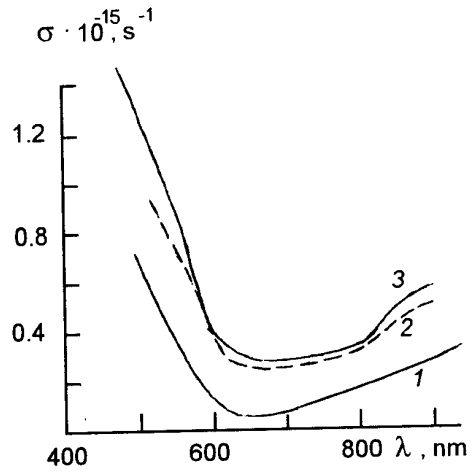

Fig.4.

ments with several incidence angles at both ordinary and polaritonic spectroellipsometry.

Spectral dependences of optical conduction σ on the wavelength λ for copper samples with the thickness of the surface layer 5 nm (curve 2) and 3 nm (curve 3) obtained using polaritonic spectroellipsometry are shown in Fig.4. As in the case of the aluminium sample, the ionic polishing did not remove completely the oxide layer from a copper mirror. The curve 1 in Fig.4 corresponds to optical conduction of the copper sample found by our ellipsometric measurements without consideration for the surface layer as it was usually done in all previous works. It should be noted that the data obtained for optical conduction σ of copper by ordinary ellipsometry practically coincide with the curves 2 and 3. Attracts attention the fact that the spectral curves 2 and 3 little differ from each other. This may testify to the fact that the surface layer on copper is more uniform than on aluminium; this leads to the coincidence of the results at ordinary and polaritonic spectroellipsometries for different thickness of the layer.

Fig.5 shows the dependences on the wavelength λ, of the refraction index n_1 of the surface layer for the thickness 5 nm (curve 1) and 3 nm (curve 2) as well as of the absorption coefficient χ_1 for the same thicknesses (curve 3,4) obtained at polaritonic spectroellipsometry.

Optical, electron diffraction and other, studies of copper films oxidized in oxygen under different conditions were carried out in [8]. It turned out that, depending on the oxidation conditions, copper films transformed into a mixture of Cu_2O, CuO in different concentrations and under some conditions – into that of Cu_2O, CuO and Cu. For

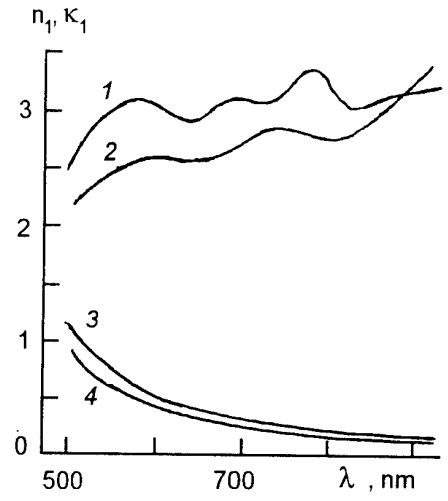

Fig.5.

all cases mentioned, measured were spectral dependences of the refraction n_1 and absorption χ_1 indices. The comparison of the results obtained (see Fig.5) and data from [8] shows that the curve 1 corresponds mainly to the presence of Cu_2O in the surface layer of our sample. The curve 3 confirms this conclusion by the behaviour of the spectral dependence similar to [8]. However, in its absolute value the curve 3 corresponds to the presence of a certain amount of pure copper in the surface layer which is rather logic taking into account the surface roughness. With the decrease of the layer thickness, the Cu_2O concentration becomes lower and that of CuO rises what follows from the comparison of the curve 2 with the analog curve in [8]. At the same time, the decrease in the thickness of the surface layer owing to ionic bombardment results in the lowering of pure copper content what follows from the decrease of the absolute value of the absorption coefficient χ_1 (curve 4). Thus, ionic bombardment leads not only to the decrease in the thickness of the surface layer but also to the variation of its composition, i.e. to the rise of CuO concentration as compared to Cu_2O and lowering of the pure copper concentration in it.

Summarising the results one can say that taking into account the surface layer of the oxide and adsorbed compounds on the metal at spectroellipsometric measurements gives the possibility to obtain more exact results for optical constants of metal and consequently, its electronic parameters what is demonstrated in this paper on the examples of aluminium and copper. Apart from this, a number of conclusions on the nature of the surface layer itself can be made.

References

1. Algorythms and Programs for Numerical Solving of Some Problems of Ellipsometry [in Russian], Ed. by A.V.Rzhanov, Nauka, Novosibirsk (1980).
2. Surface Polaritons. Electromagnetic Waves on Surfaces and Media Interfaces [in Russian], Ed. by V.M.Agranovich and D.L.Mills, Nauka, Moscow (1985).
3. I.A.Shaikevich, P.I.Drozd, L.V.Poperenko, *Zavodskaya Laboratoriya*, **51**, 35 (1985).
4. S.I.Kavun, L.V.Poperenko, I.A.Shailevich, *Fiz.Metalov and Metalovedenie*, **60**, 480 (1985).
5. I.A.Shaikevich, P.I.Drozd, L.V.Poperenko, N.V.Sopinskii, *Opt.Spektrosk.*, **53**, 145 (1982).
6. J.Weaver, C.Krafka, D.W.Lynch, E.E.Koch, in: Optical Properties of Metals, v.I,II Intern.Report D.E.S.J.F.41, Hasylab 81/01, (1981) p.172, p.256.
7. W.Harrison, Solid State Theory [in Russian], Mir, Moscow (1972) (cited by the Russian issue).
8. V.F.Drobny, D.L.Pulfrey, *Thin Solid Films*, **61**, 89 (1979).

Оптические свойства меди и алюминия, полученные с учетом поверхностного слоя методом обычной и поляритонной спектроэллипсометрии

В.А.Болотцев, Л.Ю.Мельниченко, В.Ю.Пасько, И.А.Шайкевич

Проведены спектроэллипсометрические исследования с применением как обычной, так и поляритонной многоугловой спектроэллипсометрии окисленных и ионно-бомбардированных поверхностей Al и Cu. Получены оптические постоянные чистого металла и переходных поверхностных слоев, что позволило выявить ряд особенностей электронной структуры исследуемых образцов, а также состава поверхностного слоя. Впервые экспериментально удалось обнаружить два типа межзонных переходов вблизи точек **W** и **K** зоны Бриллюэна для Al.

Functional Materials 2, No.2 (1995)

Dynamics of the space charge accumulation at the nonpolar liquid dielectric – metal interface

S.Ya.Shevchenko

T.Shevchenko Kiev University, 64 Vladimirskaya St., 252017 Kiev, Ukraine

An experimental measurement method of the space charge density distribution at the interface metal – liquid dielectric is described. The method depends on the transient current measurement just after applying the external transport field. It is suggested that the charge carriers have only one sign and the injection from electrodes is absent. One can succeed in calculation of the space charge dynamics by means of changing the short circuit period before the applying the transport field. The experimental results for the liquid G2 used in electrophotography are obtained. The maximum space charge density is $3 \cdot 10^{-9}$ Q/cm^3 at 0.1 cm distance from electrode. The negative ions mobility is $2 \cdot 10^{-4}$ cm^2/V·sec.

Описано експериментальний метод вимірювання розподілу густини просторового заряду подвійного шару поблизу межі розділу метал – рідкий діелектрик. Метод базується на вимірюванні перехідного струму відразу після прикладення зовнішнього транспортного поля і припускає наявність носіїв одного знаку та відсутність інжекції з електродів. Зміна часу витримки рідкого діелектрика у короткозамкнутому стані перед прикладенням зовнішнього поля дає можливість розрахувати динаміку розподілу просторового заряду. Одержано експериментальні залежності для рідини Ж2, що використовується в електрофотографії. Максимальна густина просторового заряду $3 \cdot 10^{-9}$ Кл/см^3 на відстані 0.1 см від металевого електроду. Рухомість від'ємного іонного заряду складає $2 \cdot 10^{-4}$ см^2/В·с.

Investigation of the space charge processes in the nonpolar liquid dielectrics under low electric field conditions is an important and challenging problem. The well-known experimental procedures which are based, for instance, on the optical beam polarization [1] can be used only at high fields and have insufficient resolution. Moreover, these procedures are appropriate only for optically active liquids. The purpose of this paper was to investigate the initial stages of nonpolar liquid dielectric conductivity caused by the accumulation and relaxation of the volume charge near the dielectric – metal interface.

The investigation of these processes in a commonly used sandwich cell is complicated by the very small value of appropriate current (down to 10^{-15} A and below) and by the superimposing of processes near opposite electrodes. The double layer charge, on the other hand, can be investigated by way of measuring the electrical current in the external circuit after applying the electric field to the dielectric layer. The circuit chart is shown in Fig.1. Before applying the transport field the cell is short circuited. At this stage, the volume charge regions develop near the metal electrodes.

After applying an external field the total current in any point is equal to the sum of conduction and displacement currents:

$$J(x, t) = \mu \cdot \rho(x, t) \cdot E(x, t) - D \cdot \frac{\partial \rho(x, t)}{\partial x} + \varepsilon\varepsilon_0 \cdot \frac{\partial E(x, t)}{\partial t}, \qquad (1)$$

where ε_0 is the electrical constant, ε – permittivity of the liquid, D – diffusion coefficient of the charge carriers, μ – their mobility, $\rho(x,t)$ and $E(x,t)$ are the space charge density and electrical field strength at a distance x from the measuring electrode at the instant t.

Integrating eqn.(1) over the dielectric thickness with regard to the conservation of the total current we obtain the expression for the current in the external circuit:

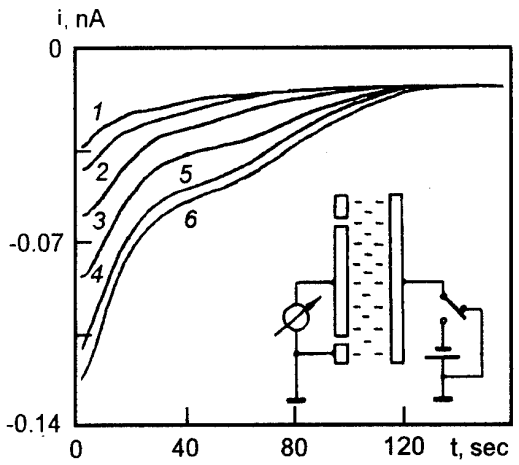

Fig.1. The time dependence of the transient current through the nonpolar dielectric liquid G2 used at present in electrostatic photography. The layer thickness is 0.7 cm, measuring electrode diameter 3.0 cm, external source voltage 350 V. Period of short circuit in minutes: curve 1 – 1, curve 2 – 2, curve 3 – 4, curve 4 – 8, curve 5 – 16, curve 6 – 32.

$$\frac{L}{S}\cdot J(t)=\mu\cdot\int_0^L \rho(x,t)\cdot E(x,t)\cdot dx- \qquad (2)$$

$$-D\cdot\frac{\partial}{\partial x}\int_0^L \rho(x,t)\cdot dx+\varepsilon\varepsilon_0\cdot\frac{\partial}{\partial t}\int_0^L E(x,t)\cdot dx,$$

where S is the measuring electrode area. When the field is greater than 10 V/cm and the mobility is less than 1 $cm^2/V\cdot s$, the diffusion term in eqn.(2) may be neglected.

For a constant applied voltage during the measurement, the third term in the right hand part of eqn.(2) is also equal to zero. This reasoning yields a simple equation:

$$J(t)=\frac{\mu\cdot S}{L}\int_0^L \rho(x,t)\cdot E(x,t)\cdot dx \qquad (3)$$

When the field of volume charge is much less than the external transport field, $E(x,t)$ may be thought of as a constant. Therefore, it may be factored outside the integral. Performing the differentiation of the expression obtained with respect to time, we obtain the equation which relates the volume charge density at the measuring electrode to the current in the external circuit:

$$\frac{d}{dt}J(t)=\frac{S\mu E}{L}\frac{d}{dt}\left(\int_0^L \rho(x,t)\cdot dx\right)=$$

$$=\frac{S\mu E}{L}\rho(L,t)\frac{dx}{dt}. \qquad (4)$$

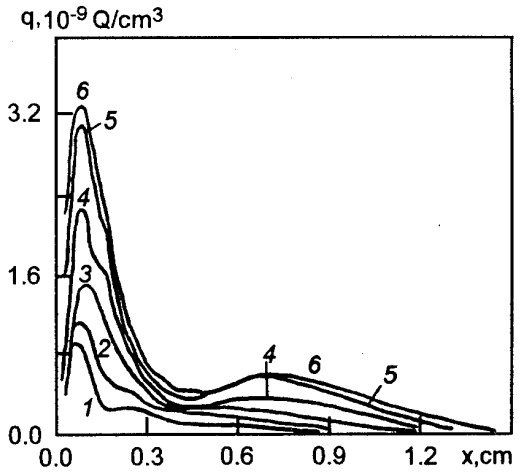

Fig.2. Space charge distribution in the dielectric liquid calculated from the data of Fig.1 with the use of eqn.(5).

$$\rho(L,t)=\frac{L}{S(\mu E)^2}\frac{d}{dt}J(t). \qquad (5)$$

Hence, the time derivative of the measured current defines the volume charge density at its exit to the measuring electrode.

The amount of the space charge near the metallic electrodes tends to grow with the duration of dielectric exposure in a short circuit. The transient current after applying the transient field undergoes corresponding changes (Fig.2). Both the current curve form and space charge distribution become stable for a period of a few hours. The total volume charge can be calculated through integration of the experimental current dependence:

$$Q=-\int_0^\infty J(t)\cdot dt. \qquad (6)$$

On the other hand, in the small signal approximation (external field is well in excess of the space charge field), the initial current is determined by space charge distribution before application of the external field:

$$J(t_0)=\frac{\mu\cdot E}{L}S\int_0^L \rho(x,t_0)\,dx=\frac{\mu\cdot E}{L}Q. \qquad (7)$$

One can calculate from this equation the mobility of ions which form at the charged double layer:

$$\mu=\frac{L\cdot J(t_0)}{E\cdot Q}. \qquad (8)$$

For the dielectric liquid under investigation, the mobility was $1.95\cdot10^{-4}$ $cm^2/V\cdot s$. A knowledge of μ makes it possible to calculate, with the use of

eqn.(5), the distribution of charge density for different durations of stay in the short circuit (Fig.2). The values of distance passed by charge carriers in the period t with the velocity $\mu \cdot E$ are plotted as abscissas (Fig.2) in place of time t. It is reasonable that the conditions of the function $\rho(x,t)$ formation undergo a change at the instant when the field is applied to the dielectric. The longer is the drift of charge carriers, the greater the function $\rho(x,t)$ changes its shape as compared with the initial one. Thus, the space charge arrived from the opposite electrode undergoes more changes.

References

1. U.Gafvert, A.Jaksts, C,Tornkvist, L.Walfridsson, *IEEE Trans.*, **EI–27**, 647 (1992).

Динамика аккумулирования объемного заряда у поверхности раздела жидкий диэлектрик – металл

С.Я.Шевченко

Описан экспериментальный метод измерения распределения плотности пространственного заряда двойного слоя вблизи границы раздела металл – жидкий диэлектрик. Метод основан на измерении переходного тока сразу после приложения внешнего транспортного поля и предполагает наличие носителей одного знака и отсутствие инжекции из электродов. Изменяя время выдержки жидкого диэлектрика в короткозамкнутом состоянии перед приложением внешнего поля,удается рассчитать динамику распределения пространственного заряда. Получены экспериментальные зависимости для жидкости Ж2, применяемой в электрофотографии. Максимальная плотность пространственного заряда $3 \cdot 10^{-9}$ Кл/см^3 на расстоянии 0.1 см от металлического электрода. Подвижность отрицательного ионного заряда составляет $2 \cdot 10^{-4}$ см^2/В·с.

Functional Materials **2**, No.2 (1995)

Simulation of phosphor on the diamond surface and its superfine structure

N.V.Tokii, M.V.Grebenyuk and V.V.Tokii

Donbass State Academy of Architecture and Constructions,
339023 Makeyevka, Ukraine

The molecular-orbital approach is applied for phosphor on the relaxed (1×1) surface (111) of diamond. The wave functions for different values of relaxation were calculated and a comparison with the EMR data was made. The results of this comparison allow to make a conclusion that the paramagnetic phosphor in diamond is the second nearest neighbour of the vacant site of the lattice.

Молекулярно-орбітальний підхід застосовано до фосфору на релаксованій (1×1) поверхні (111) алмазу. Обчислено хвильові функції для різних величин релаксації та проведено порівняння з ЕПР даними. Результати дозволяють зробити висновок, що парамагнітний фосфор у алмазі є другим найближчим сусідом вакантного вузла гратки.

The active electronics requires a semiconducting diamond of the *n*-type. The mechanisms of different defects and their properties formation are unknown so far. Both these aspects of the problem of defects in diamond are mutually connected and the progress in one of them makes possible the progress in the other. Recently, we have studied the hyperfine structure of the paramagnetic nitrogen and phosphor impurities [1–3]. In particular, the EPR spectrum of phosphor looks like a doublet of low intensity but with distinct lines at the edges of the central component of the nitrogen triplet and having the following parameters: g=2.0025±0.0002, A=20.8±0.2 Gs, B=1.2±0.2 Gs. However, the phosphor position in the lattice of diamond has not been established. The present paper is dedicated to a simulation of the phosphor paramagnetic center on the surface of diamond using modern mathematical models [4].

For the calculations we used a group consisting of 21 carbon atoms and one phosphor atom. This group was in the form of a semisphere and included the central phosphor in the site (000). Our consideration was based on the theory of strong bounding and unielectron Shroedinger wave equation. The basis of the system was limited by the sp^3-hybridized orbitals constructed of the 2*s* and 2*p* atomic wave functions of carbon and 3*s* atomic wave functions of phosphor. These orbitals were assumed to be orthogonal in different sites of the lattice. The interaction of the first nearest neighbours was described in the scope of Harrison matrix elements. The intrinsic functions and energy values of the electron system were defined by the Hamiltonian diagonalisation. The calculations were made for an ideal (unshifted) (111) surface of diamond and were repeated for a (111) (1×1) surface relaxed [5] by various values.

The results of the calculations are given in the Table 1.

Table 1. Parameters of a hyperfine structure and coefficients of the wave function of the uncoupled electron on the phosphor nucleus on the (111) (1×1) surface of diamond.

r(pm)	α^2	β^2	$A_{\parallel}$ (Gs)	$A_{\perp}$ (Gs)
0.00	0.018	0.141	93.7	50.1
4.62	0.015	0.138	83.1	40.5
18.52	0.008	0.124	54.7	16.3
Experiment	0.006	0.012	23.2	19.6

where r is the shift of the first surface atom layer in the crystal bulk direction; the ionizing potentials of carbon atoms 19.5 eV and 10.7 eV for the

2*s* and 2*p* orbitals, respectively, were taken from [6]. A part of the unielectron crystal orbital of the uncoupled electron centered on the phosphor atom was chosen in the form:

$$\Phi = \alpha\,\Psi_{3s} + \sum_{k=1}^{3} \beta_k\,\Psi_{3p_k}, \quad \text{and} \quad \beta^2 = \sum_{k=1}^{3} \left(\beta_k\right)^2;$$

The values $A_{\|} = 3846$ Gs and $A_{\perp} = 3537$ Gs for a free phosphor using the Hartry-Fock calculations [7].

Discussion

Comparing the calculations with the experimental data of the Table 1 we see a rather poor agreement between the theory and experiment which is inferior to our recent calculations [8] for phosphor near a vacant site given in the Table 2.

Table 2. Parameters of a superfine structure and coefficients of the wave function of the uncoupled electron on the nucleus of phosphor near the central site of the diamond cluster.

System	Phospor	α^2	β^2	$A_{\|}$ (Gs)	$A_{\perp}$ (Gs)
V+27C+P	(1,1,1)	0.116	0.570	538	362
V+27C+P	(2,2,0)	0.005	0.021	24.2	17.7
V+27C+P	(3,1,1)	0.000	0.014	2.9	−1.5

where, in the calculations, phosphor subsequently substitutes the first nearest neighbour (1,1,1) of the vacant site (0,0,0) of the 28-atomic diamond cluster and then the second (2,2,0) and the third (3,1,1) nearest neighbours.

The analysis of the Table 1 and 2 allow to conclude that the paramagnetic phosphor in diamond is the second nearest neighbour of the vacant site of the lattice.

References

1. N.D.Samsonenko, V.V.Tokiy, S.V.Gorban, V.I.Timchenko, *Surface and Coating Technology*, **47**, 618 (1991).
2. N.D.Samsonenko, V.V.Tokiy, S.V.Gorban, *Sov.Phys. Solid State*, **33**, 1409 (1991).
3. V.Tokiy, N.Samsonenko, S.Gorban, Proc. XIII AIRAPT Int. Conf. on High Science and Technol., Bangalor, A-10 (1991).
4. W.Harrison, Electronic Structure and the Properties of Solids (1980), Freeman, San Francisco, reprinted by Dover, New York (1989).
5. V.V.Tokiy, N.D.Samsonenko, D.L.Savina, Diamond Films-93, 4-th European Conf. on Diam., Diamond-like and Related Mater. Albufeira, Algarve, Portugal 12.019, (1993).
6. A.Levin, Solid State Quantum Chemistry, McGraw-Hill, N.Y. (1974).
7. R.Watson and A.Freeman, *Phys. Rev.*, **123**, 521 (1961).
8. V.V.Tokiy, N.D.Samsonenko, D.L.Savina, S.V.Gorban, Proceedings of 2-nd Int. Conf. on the Applications of Diam. Films and Related Materials, Saitama, Japan, 757 (1993).

Моделирование фосфора на алмазной (111) (1×1) поверхности и его сверхтонкая структура

Н.В.Токий, М.В.Гребенюк, В.В.Токий

Молекулярно-орбитальный подход применяется к фосфору на релаксированной (1×1) поверхности (111) алмаза. Вычислены волновые функции для различных величин релаксации и проведено сравнение с ЭПР данными. Результаты позволяют сделать вывод, что парамагнитный фосфор в алмазе является вторым ближайшим соседом вакантного узла решетки.

Functional Materials **2**, No.2 (1995)

Mechanical stresses and charge stability in non-polar polymeric electrets

V.G.Boitsov, A.A.Rychkov and I.N.Rozhkov

Russian State Pedagogical University, 48 Moika,
St.Petersburg, Russian Federation

A correlation between morphology and charge stability in non-polar polymeric electrets has been studied. Isomeric heating of polymer is shown to cause the changes in the supermolecular structure, particularly in the crystallinity. Measurements on electrets were made using special experimental method based on simultaneous registration of the thermal shrinkage stresses and the surface potential relaxation. It has been found that mechanical stresses in the polymer influence the charge stability significantly. From the results obtained we were able to determine the isometric heating conditions which were useful to improve charge stability of non-polar polymeric electrets.

Вивчено зв'язок між морфологією і стабільністю заряду в неполярних полімерних електретах. Показано, що ізометричне нагрівання приводить до зміни надмолекулярної структури полімера, особливо його кристалічності. При вимірюваннях використовувалась оригінальна методика, що базується на одночасній реєстрації термоусадкових напруг і релаксації поверхневого потенціалу. Результати досліджень дають можливість визначити режими ізометричної термообробки полімерних плівок при промисловому виробництві полімерних плівкових електретів.

Introduction

The membranes made of the polymer electrets are widely used for electret transducers production. The electret membranes production includes the thermal treatment which leads to the shrinkage stresses. The connection between the shrinkage stress and electrophysic parameters of the polymer electrets is still insufficiently studied. The establishment of these connections and ways to manage the mechanical and electrical stability of the electret membranes would allow to formulate the demands to the polymer materials and technology of electrets and to improve the transducers quality.

Experimental results and discussion

Our samples were uniaxially oriented films of PP, PTFE and FEP-Teflon with 10 μm of thickness, metallized on one side with 500 Å vacuum evaporated aluminium. The electrization was carried out by corona triod. The distance between the needle and the grid was 15 mm, that between the grid and the dielectric surface – 3 mm. The sample holder potential was 300 V.

The curves of isometric heating (CIH) and thermally stimulated relaxation of the surface potential (TSRSP) for the PTFE, FEP-Teflon and PP samples are shown on Fig.1, 2 and 3, respectively.

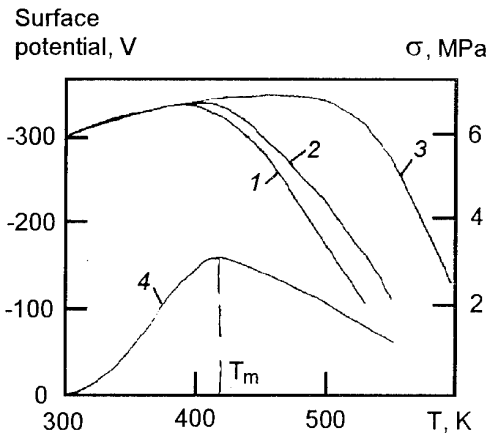

Fig.1. CIH (4) and the TSRSP (1,2,3) curves for uniaxial oriented PTFE films.

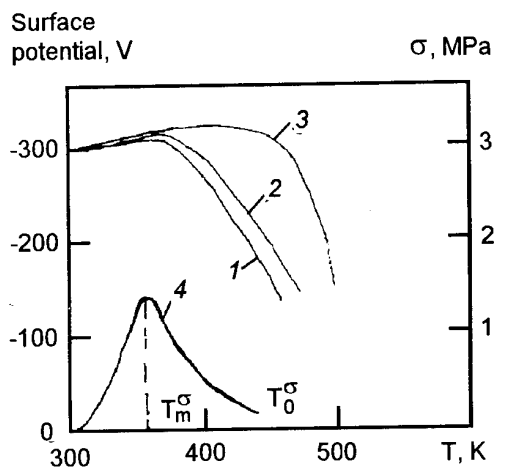

Fig.2. CIH (4) and the TSRSP (1,2,3) curves for uniaxial oriented FEP-Teflon films.

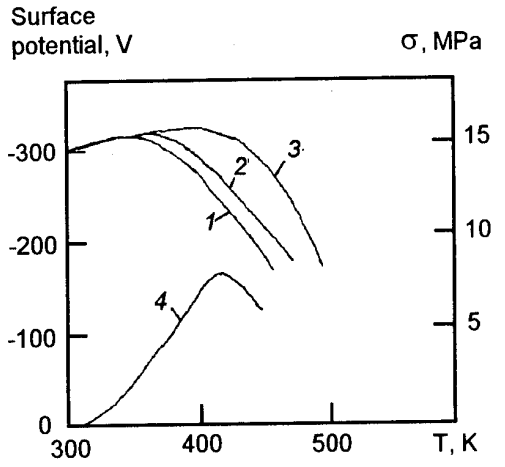

Fig.3. CIH (4) and the TSRSP (1,2,3) curves for uniaxial oriented PP films.

The heating rate of 4.4 K/min was used. The curves of CIH and TSRSP were measured simultaneously. After first cycle TSRSP up to $T < T_m$ (curve 1), there is almost no increase of charge thermostability in the second cycle (curve 2).

If the heating in the first cycle reaches $T > T_m$ (but not melting point) a charge thermostability increase takes place (curve 3).

Thus, the maximum point on the CIH separates the temperature regions where thermal processing of the sample influences or influences not the thermostability of the electrets. It is evident that the growth of charge thermostability in the second TSRSP cycle occurs if the heating brings to temperature at which the shrinkage mechanical stresses in the membranes attain almost the relaxation. If the sample heating almost reaches the melting temperature of crystallites then stability decreases considerably. We established that the increase of thermostability after the thermal processing is observed at fluorine polymers only for negative charge and at PP foil electrets for charge of both signs.

The relaxation of shrinkage stresses reflects the variations in the supermolecular structure of a polymer. According to [1] the relaxation of shrinkage stresses occurs as a result of stretching out the ends of the tied macromolecules in amorphous phase from the crystalline blocks. The growth of the contour length of macromolecules makes the folding of the chain and its crystallization easier.

At the same time, the share of the defect crystalline phase and the density of amorphous regions in the polymer microfibrilles are increased. Such processes stimulate the formation of new structural traps at the amorphous-crystalline phase interface and also limit the conformation set of macromolecules in the amorphous phase. That is why after the second charging of the thermally processed sample the release of the charge carriers captured at the structural traps occurs at higher temperature. Thus, the growth of the electret charge thermostability after thermal processing and relaxation of shrinkage mechanical stresses occurs as a result of crystallization finished relaxation of tied macromolecules. This was confirmed by investigations of nuclear magnetic resonance spectra of the polymer films [2].

References

1. F.Decandia, R.Russo, A.Peterlin, *J.Polym. Sci.: Polum. Phys.Ed.*, **20**, U75 (1982).
2. J.N.Rozhkov, Thesis Pedagogical Univ., Leningrad (1990).

Механические напряжения и стабильность заряда в неполярных полимерных электретах

В.Г.Бойцов, А.А.Рычков, И.Н.Рожков

Изучена связь между морфологией и стабильностью заряда в неполярных полимерных электретах. Показано, что изометрическое нагревание приводит к изменению сверхмолекулярной структуры полимера, в особенности его кристалличности. При измерениях использовалась оригинальная методика, основанная на одновременной регистрации термоусадочных напряжений и релаксации поверхностного потенциала. Результаты исследований дают возможность определить режимы изометрической термообработки полимерных пленок при промышленном производстве полимерных пленочных электретов.

Amcrys-H

Scintillation detectors

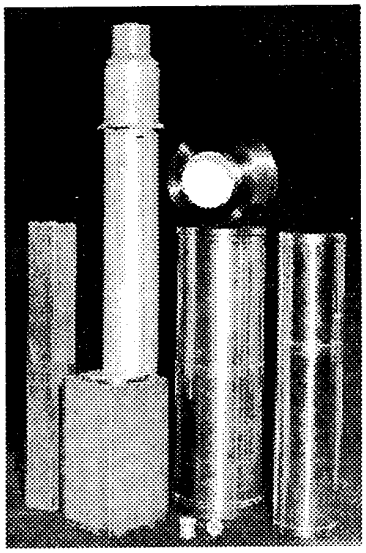

- **Detectors of general purpose** for the registration and spectrometry of gamma radiation.
- **Scintiblocks** - scintillator plus photomultipier with high energy resolution for the registration and spectrometry of gamma radiation of the energy of 50 keV and higher.
- **Phoswiches** - combined detectors for highly sensitiv selective spectro- and radiometry under conditions of natural and increased background.
- **X-ray detectors** converting X-ray and soft gamma radiation into light energy.

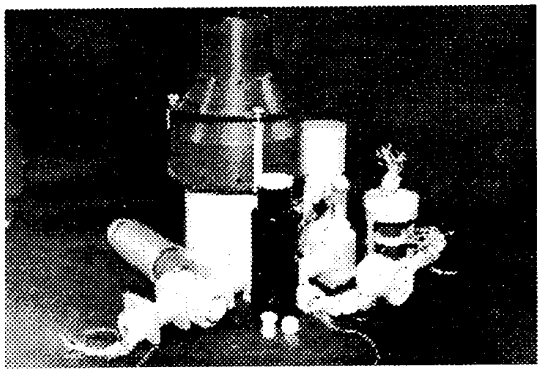

- **Low background detectors** possessing low intrinsic background for the registration and spectrometry of weak flows of gamma radiation.
- **Vibrothermostable detectors,** operating in a wide temperature (–60... + 150 °C) and mechanical load range.

Scintillation materials

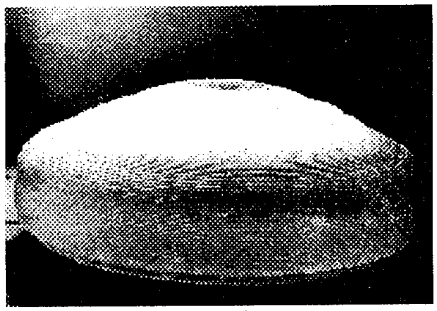

- **Halogenides of alkali metals**
  - sodium iodide doped with thallium;
  - cesium iodide doped with thallium;
  - cesium iodide doped with sodium;
  - combined cesium iodide and cesium bromide single crystals;
  - cesium iodide doped with cesium carbonate;
  - potassium chloride;
  - potassium bromide;
  - combined potassium chloride and bromide single crystals.

Amcrys–H Limited

ALCALI HALIDE CRYSTALS

60 Lenin Ave.,
310001 Kharkov,
Ukraine

Tel.: 380 (572) 307 906
Fax: 380 (572) 320 207
E-mail: amcrys-h@isc.kharkov.ua

Information for Authors

The journal *"Functional Materials"* issued by the National Academy of Sciences of Ukraine publishes papers, short communications, letters to the Editor, and comments comprising results of theoretical and experimental studies, descriptions of preparation methods and practical use of the wide scope of organic and inorganic materials intended for various functional purposes. Special attention is given to works dealing with problems of obtaining new materials having complex schemotechnical functions. The journal publishes also requested reviews on the actual problems corresponding to its subjects as well as current information, e.g. chronicle, personalia, paid advertising communications, etc.

The journal topics include:

- structure, phase transformations and properties of single crystals, ceramics, composites, nanocrystals, amorphous solids, liquid crystals, polymers, thin films, and low-dimensional systems (superlattices, heterostructures, Langmuir-Blodgett films, etc.) as applied to materials science problems;
- ways to creating new functional materials with preset properties;
- modern methods of materials research;
- problems and methods of functional materials use in modern technologies.

Communications submitted to Editorial board must be stated in most precise and unambiguous words. The manuscript submitted must contain the authors' estimation of precedent works, the aim of investigation, the original part and conclusions ensuring the understanding of the essence of results obtained and of their novelty. The unjustified use of new terms and professional slang is to be avoided.

Authors are asked to keep the following instructions:

1. Manuscripts can be submitted in Russian, Ukrainian, or English, at the desire of authors.

2. The manuscript should be submitted with the permission for publication given by the organisation where the work is done.

3. Manuscripts should be typed on a standard typewriter or on a printer, ***double-spaced***, in duplicate, with the left margin not less than 4 cm. Type tables, captions for illustrations and summaries (abstracts) on separate paper sheets. Summary (up to 0.5 page of typewritten text) is to be in Russian, Ukrainian, and English.

4. For papers, the volume should not exceed 15 typewritten pages, tables and figures included (the figures number not more than 5). For short communications and letters to the Editor, the volume should not exceed 3 pages and 2 figures. For letters to the Editor, the urgent publication necessity should be substantiated.

5. For reviews, the content and volume should be co-ordinated with the Editors, therefore, a review summary and structure are to be presented in advance.

6. References should be listed in the end of communication, numerated consecutively. The initials and names of all authors are to be listed if their number is less than four; otherwise, the first three authors must be listed followed by the remark "et al.".

The rules of the references list making is illustrated by the samples below:

1. V.V.Berestovsky, E.M.Lifshits, L.P.Pitayevsky, Quantum Electrodynamics [in Russian], Nauka, Moscow (1984), p.1.
2. A.M.Sergienko, R.I.Chernova, A.Ya.Sergienko, *FTT*, **30**, 835 (1988).
3. R.Brandley, J.M.Faber, C.N.Nelson, et al., *Phys.Rev.*, **A 18**, 1632 (1978).
4. A.N.Stirling and D.Watson, in: Progress of Low Temperature Physics, ed. by D.F.Brewer, North Holland, Amsterdam (1986), v.10, p.683.
5. K.D.Gromov, M.E.Landsberg, in : Abstr. of 10th All-Union Conf. on Low Temperature Physics [in Russian], (Tashkent 1986), Nauka, Moscow (1987), p.434.
6. N.V.Vasil'ev, Cand.Thesis (Phys.-Math. Sci.), Moscow State Univ., Moscow (1985).

7. The original issues must be always referenced instead of translated ones. If a Russian journal cited is translated and distributed abroad, please refer to the English version, if possible. Since the papers will be translated into English, the designations and indices accepted in English issues, i.e. only Roman and Greek letters, must be used (e.g. T_m but not $T_{пл}$ for melting point). Please avoid the complicated and confused sentences in original Russian (Ukrainian) text.

8. The figures are master-copied by scanning method, therefore, the Editors make special requirements to the originals quality (including the axes orthogonality, uniform lines width, the coordinate axes marking with inward-directed strokes, etc.). The size of plots and photos must not exceed 8 cm in width and 20 cm in height, and that of complex figures, not more than 16 cm in width. ***Photographs must show high contrast.*** Xerox copies of photos are not permitted. Legends

(arrows, designations, etc.) are to be made by hand on the one photos copy only. Figures must be identified on the back by author's name, few first words of the paper title and figure number. ***The Editors reserve the right to reject papers having low-quality illustrations.***

9. The precise addresses, names, full first names and patronyms of authors, office and/or home telephone numbers, fax, e-mail must be applied to the manuscript submitted. The author to whom the correspondence should be addressed must be pointed out. The paper original must be signed by all authors.

10. Two copies of proofs in Russian (Ukrainian) and English are sent to authors. These proofs signed by author(s) and marked by the date of signing are to be sent back to the Editors within three days.

Paper layout

Decimal Classification Index (on the left)

Paper Title

Authors' initials and names

Full name(s) of Organisation(s) where the work is done, post address(es) of Organisation(s)

Paper text according to the following general layout: introduction, experimental (including both the preparation and studying methods), results and discussion, conclusions, references list, figures, captions for figures, tables, summaries (in Ukrainian, Russian, and English), each item on a separate sheet of paper.

Recommendations to Authors Using the Computer Type-Setting

1. Two copies of paper typed clearly on the printer are submitted to the Editors. In this case, formulas are not to be marked, excluding capital and small letters having the same form, and also vectors. In other respects, the rules for the manuscript preparations are the same.

2. The paper text can be submitted also on a floppy-disk (with symbols and formulas excluded) prepared using the simple MULTI-EDIT editor or any ASCII editor. Therewith, word divisions, right justification , pageing, indentions, and other text draws-in are not permitted. Each line must begin with non-blank symbol, and words must be separated by one blank only; paragraphs, headings, formulas are to be separated by one empty line. The symbol * (asterisk) is to be placed for a footnote; the footnote text must be type-setted as a separate paragraph just below the current one.

3. Instead of formulas and symbols, as well as instead *Italic* and **bold Roman** letters, two symbols ## must be placed.

4. The figures to be scanned must be prepared with special care, taking into account the forthcoming scale change. Photos or half-tone pictures are to be submitted in sizes allowing for the reproduction in 1:1 scale (width not more than 8 cm, height not exceeding 20 cm).

Graphics can be submitted on a floppy-disk in any of the following formats: GEM/Dr. HALO DPE (.IMG), PC Paint brash (.PCX), TIFF (uncompressed variants), MAC Paint, CGM (.CGM), Autocad (.SLD), MAC PICT, EPS, HPGL, Lotus (.PIC), Windows Metafile (.WMF).

At the images preparation in such a form, the 300 point on inch resolution should be counted on for bit images, in that case, figures can be reproduced without modifications.

A camera ready master copy is prepared by the Editorial Board of **Functional Materials** using the software and technical support of **LASERUSS** Scientific Publishing Group.

Editor of English text: V.Ya. Shnol

Translated by: V.Ya. Shnol, T.M. Grishchenko

Computer Operators: V.Ya. Serebryanny, V.A. Tkachev, V.V. Shlakhturov, L.D. Patsenker, V.A. Zakorina

Proof–reader: E.G. Protsenko